UNIVERSITÉ DE MONTRÉAL

NUMERICAL VALIDATION OF ANALYTICAL HOMOGENIZATION MODELS FOR THE CASE OF RANDOMLY DISTRIBUTED AND ORIENTED ELLIPSOIDAL FIBERS REINFORCED COMPOSITES

ELIAS GHOSSEIN
DÉPARTEMENT DE GÉNIE MÉCANIQUE
ÉCOLE POLYTECHNIQUE DE MONTRÉAL

THÈSE PRÉSENTÉE EN VUE DE L'OBTENTION
DU DIPLÔME DE PHILOSOPHIÆ DOCTOR
(GÉNIE MÉCANIQUE)
SEPTEMBRE 2014

UNIVERSITÉ DE MONTRÉAL

ÉCOLE POLYTECHNIQUE DE MONTRÉAL

Cette thèse intitulée:

NUMERICAL VALIDATION OF ANALYTICAL HOMOGENIZATION MODELS FOR
THE CASE OF RANDOMLY DISTRIBUTED AND ORIENTED ELLIPSOIDAL FIBERS
REINFORCED COMPOSITES

présentée par: GHOSSEIN Elias
en vue de l'obtention du diplôme de: Philosophiæ Doctor
a été dûment acceptée par le jury d'examen constitué de:

M. BOUAANANI Najib, Ph.D., président
M. LÉVESQUE Martin, Ph.D., membre et directeur de recherche
M. BARTHELAT François, Ph.D., membre
M. BRENNER Renald, Ph.D., membre

DEDICATION

To my grandparents
Aida and Abou Gebran

To my parents
Alexa and Joseph

To my brother
Marc

To my second half
Pamela

Thank you for everything . . .

ACKNOWLEDGEMENTS

First, I would like to thank my supervisor Pr. Martin Lévesque for his trust and support throughout this thesis. His advice and constructive criticism guided me to perform a high quality work. During my PhD, I gained a scientific maturity and this was mainly thanks to him. Also, I want to thank Pr. Brenner, Pr. Barthelat and Pr. Prudhomme for being my committee members and Pr. Bouaanani for being the Jury President.

I owe special gratitude to the members of Laboratory for Multiscale Mechanics (LM2) research group. I would like to particularly thank Amine El-Mourid, Hadi Moussaddy, Maryam Pahlavan Pour, Behzad Rahmani and Farhad Mortazavi for their contributions and for numerous fruitful discussions all along this project.

I would like to acknowledge the contributions of the National Science and Engineering Research Council of Canada (NSERC) and the Fonds de Recherche du Québec – Nature et Technologies (FRQNT). Their financial support through scholarships made this project possible.

I would also like to thank the Fluids Dynamics Laboratory at Ecole Polytechnique de Montréal for sharing computational resources that greatly facilitated the tasks.

I would like to take this opportunity to thank my grandparents Aida and Abou Gebran, my parents Alexa and Joseph, as well as my brother Marc who devoted their entire lives to my success. Over the last four years, they provided me unconditional support during the good and bad times. My grandfather died in the first days of this thesis and I promised him to go through. It is thanks to his prayers that I reached my goal.

Last but not least, I would like to thank my one and only second half, Pamela, for her love and support throughout these past four years. She knew how to encourage me in the difficult times and she was patient in the times of intense stress and work. Pamela, without your presence in my life, I would not have done a PhD and this thesis would never have seen the day. I owe you my perseverance and my determination. Thank you for being in my life !

RÉSUMÉ

Le développement de nouveau matériaux composites peut s'avérer long et coûteux. Il serait alors pertinent d'avoir des outils capables de prédire le comportement mécanique de matériaux composites avant qu'ils ne soient réellement fabriqués. L'utilisation de tels outils permettrait de réduire le temps et les coûts reliés aux tests de certification. Plusieurs méthodes analytiques existent pour prédire les propriétés mécaniques de composites. Les plus connues sont la règle des mélanges et la théorie classique des laminés. Dans la plupart des cas, ces méthodes fournissent des prédictions inexactes puisque qu'elles ne prennent pas en considération toute l'information disponible reliée à la microstructure.

Les modèles d'homogénéisation analytiques prédisent les propriétés mécaniques effectives de matériaux hétérogènes en utilisant des informations reliées à la microstructure (les propriétés des phases, leur fraction volumique, la forme et l'orientation des renforts, etc.). Toutefois, il n'existe pas d'étude systématique et approfondie où l'on évalue la précision de ces modèles pour une vaste gamme de propriétés mécaniques et géométriques des phases. Dans le but de valider la performance des modèles analytiques, leurs prédictions doivent être comparées à celles obtenues par des méthodes numériques. Les différentes méthodes numériques utilisées dans la littérature sont coûteuses en terme de temps de calcul, ce qui a limité la gamme de composites étudiée. De plus, la plupart des études ont été réalisées sans avoir rigoureusement déterminé le Volume Élémentaire Représentatif (VER).

L'objectif principal de cette thèse était de valider la performance des modèles d'homogénéisation analytiques à prédire les propriétés mécaniques effectives et les statistiques des champs locaux de composites renforcés par des fibres elliptiques aléatoirement distribuées et orientées. Étant donnée qu'une grande campagne de validation était planifiée, un outil numérique complètement automatisé a été développé. Ce dernier a traité deux étapes indépendantes: i) la génération aléatoire des microstructures représentatives et ii) le calcul exact des propriétés effectives.

Les microstructures représentatives ont été générées en utilisant une approche basée sur la dynamique moléculaire. Un nouveau algorithme performant et efficace a été développé dans le but de générer des arrangements constitués d'ellipsoïdes aléatoirement distribués et orientés. L'algorithme proposé a été capable de générer tous les types d'ellipsoïdes à hautes fractions volumiques et/ou rapports de forme. Les propriétés effectives et les statistiques des champs locaux ont été obtenues avec précision en utilisant une technique basée sur les Transformées de Fourier Rapides (TFR).

Les prédictions de l'outil numérique ont été comparées à celles des modèles

d'homogénéisation analytiques les plus connus pour une vaste gamme de propriétés mécaniques des phases et de fractions volumiques et rapports de forme des fibres. La campagne de validation a impliqué un rigoureux processus de détermination du VER et approximativement 1800 différents composites à fibres elliptiques ont été étudiés.

Un domaine de validité a été attribué à chaque modèle analytique. Il a été montré qu'aucun modèle ne se distingue des autres comme étant le plus précis sur toute la gamme de propriétés mécaniques et géométriques des phases. Toutefois, si un seul modèle devait être choisi pour prédire les propriétés effectives et les statistiques des champs locaux de composites à fibres elliptiques aléatoirement distribuées et orientées, cette thèse recommande le modèle de Lielens. En effet, ce modèle a fournit des prédictions précises dans la plupart des cas étudiés.

Outre la validation complète et approfondie des modèles d'homogénéisation analytiques, la principale contribution de cette thèse est le développement de deux modèles d'interpolation. Ces modèles prédisent respectivement les propriétés effectives et les statistiques des champs locaux de composites renforcés par des fibres elliptiques aléatoirement distribuées et orientées. Ces modèles peuvent être une alternative aux modèles d'homogénéisation analytiques puisque leur précision dépasse celle de tout autre modèle publié dans la littérature.

ABSTRACT

The development of new composite materials can be a long and expensive process. It would therefore be relevant to have predictive tools that can predict the mechanical behavior of composites before their fabrication. Using these tools could lead to shorter certification time and cost reductions. Several analytical approaches exist for predicting the mechanical properties of composites. The best known are the Rule of Mixtures and the Classical Lamination Theory. In most cases, both approaches lead to inaccurate predictions since they do not take into account all the available information about the microstructure.

Analytical homogenization models rely on microstructural information (e.g., constituents properties, volume fraction, shape, orientation, etc.) to predict the effective mechanical properties of heterogeneous materials. However, no systematic and thorough study evaluates the accuracy of these models for a wide range of constituents mechanical and geometrical properties. In order to validate the performance of analytical models, their predictions should be compared to those obtained by numerical methods. The different numerical methods that have been used in the literature had a high computational cost, which has limited the investigated range of composites. Furthermore, most numerical studies were performed without conducting a rigorous Representative Volume Element (RVE) determination process.

The main purpose of this thesis was to validate the performance of analytical homogenization models at predicting the effective mechanical properties and local field statistics of randomly distributed and oriented ellipsoidal fibers reinforced composites. Since a large validation campaign was planned, a fully automated numerical tool was developed. The latter dealt with two independent steps: i) random generation of the representative microstructures and ii) accurate computation of the effective properties.

The representative microstructures were generated using a molecular dynamics approach. A new computationally-efficient algorithm was developed for generating packings of randomly distributed and oriented ellipsoids. The proposed algorithm was able to generate all types of ellipsoids with high volume fractions and/or aspect ratios. The effective properties and local field statistics were accurately computed using a Fast Fourier Transforms (FFT) based technique.

The predictions of the numerical tool were compared to those of the best known analytical homogenization models for a broad range of phases mechanical properties, fibers volume fractions and aspect ratios. The validation campaign involved a thorough and rigorous RVE determination process and approximately, 1800 different ellipsoidal fibers reinforced composites were studied.

A validity domain was attributed to each analytical model. It was found that no analytical homogenization model stands out of the others as being more accurate over the studied range of phases mechanical and geometrical properties. However, if a single model was to be chosen to predict the effective properties and local field statistics of ellipsoidal fibers reinforced composites, this thesis recommend the Lielens' model. Indeed, it was shown that this model was suitable in most of the studied cases.

Besides the thorough and comprehensive validation of analytical homogenization models, the main contribution of this thesis is the development of two interpolation models. These models predict respectively the effective properties and the local field statistics of randomly distributed and oriented ellipsoidal fibers reinforced composites. It was shown that these models could be an alternative to analytical homogenization models since their accuracy is the highest published so far.

TABLE OF CONTENTS

LIST OF TABLES

LIST OF FIGURES

LIST OF APPENDICES

LIST OF SYMBOLS AND ABBREVIATIONS

Latin symbols

$\mathbf{A}(\boldsymbol{x})$	Local strain localization tensor
$\mathbf{A}_i$	Average strain localization tensor over phase "i"
$\mathbf{B}(\boldsymbol{x})$	Local stress concentration tensor
$\mathbf{B}_i$	Average stress concentration tensor over phase "i"
c_i	Volume fraction of phase "i"
$\mathbf{C}_i$	Stiffness tensor of phase "i"
$\widetilde{\mathbf{C}}$	Effective stiffness tensor
$\mathbf{G}^0(\boldsymbol{x})$	Green operator
$\mathbf{I}$	Fourth order identity tensor
$\mathbf{J}$	Spherical projection tensor
$\mathbf{K}$	Deviatoric projection tensor
L	Edge length of a volume element
n	Number of realizations
$\boldsymbol{q}$	Quaternion of an ellipsoidal particle
$\boldsymbol{r}$	Position vector of an ellipsoidal particle
R	Aspect ratio of an axisymmetric ellipsoid
R_1	First aspect ratio of a scalene ellipsoid
R_2	Second aspect ratio of a scalene ellipsoid
$\mathbf{S}_i$	Compliance tensor of phase "i"
$\widetilde{\mathbf{S}}$	Effective compliance tensor
$\mathbf{S}^{\mathrm{E}}$	Eshelby's tensor
T	Quantile of the Student distribution
$\mathbf{T}$	Second-order orientation tensor
$\boldsymbol{v}$	Linear velocity vector of an ellipsoidal particle
v_f	Lielens' interpolation factor
V	Volume
$\boldsymbol{x}$	Point coordinates vector
$\boldsymbol{x}_c$	Coordinates of the contact point between two ellipsoids
Z	Target property

Greek symbols

δ_{iso}	Deviation from isotropy
$\boldsymbol{\varepsilon}(\boldsymbol{x})$	Local strain tensor
$< \boldsymbol{\varepsilon} >_i$	Strain first order moment within phase "i"
$< \boldsymbol{\varepsilon} \otimes \boldsymbol{\varepsilon} >_i$	Strain second order moment within phase "i"
$\boldsymbol{\varepsilon}^*$	Uniform stress-free strain
$\mathbf{E}$	Macroscopic strain tensor
κ_i	Bulk modulus of phase "i"
$\widetilde{\kappa}$	Effective bulk modulus
μ_i	Shear modulus of phase "i"
$\widetilde{\mu}$	Effective shear modulus
$\boldsymbol{\sigma}(\boldsymbol{x})$	Local stress tensor
$< \boldsymbol{\sigma} >_i$	Stress first order moment within phase "i"
$< \boldsymbol{\sigma} \otimes \boldsymbol{\sigma} >_i$	Stress second order moment within phase "i"
$\boldsymbol{\Sigma}$	Macroscopic stress tensor
(θ, ϕ, ψ)	Euler angles
$\boldsymbol{\omega}$	Angular velocity vector of an ellipsoidal particle
$\boldsymbol{\xi}$	Wave number in Fourier space

Abbreviations

2D	Two-dimensional
2OE	Second-order estimates
3D	Three-dimensional
3PB	Three-point bounds
Ben	Benveniste
EDMD	Event-driven molecular dynamics
ESCS	Effective self-consistent scheme
Esh.	Eshelby
FEM	Finite Element Method
FFT	Fast Fourier Transforms
GSC	Generalized self-consistent
GSCS	Generalized self-consistent scheme
HSB	Hashin-Shtrikman bounds
HSL	Hashin-Shtrikman lower bounds
HSU	Hashin-Shtrikman upper bounds

IDD	Interaction direct derivative
LI	Lielens
MD	Molecular dynamics
MPCs	Multi-Points Constraints
MT	Mori-Tanaka
NNL	Near-neighbor list
NT	Numerical tool
ODF	Orientation distribution function
PCW	Ponte-Castañeda and Willis
ROFRC	Randomly Oriented Fiber Reinforced Composites
RSA	Random Sequential Adsorption
RVE	Representative Volume Element
SC	Self-consistent
SCS	Self-consistent scheme
TDMD	Time-driven molecular dynamics
TOA	Third Order Approximation
TPM	Three-phase model

INTRODUCTION

Composite materials are increasingly used in the aerospace industry. For example, composites represent 50% of the total mass of the recent B-737 Boeing aircraft. The development of new composite materials can be expensive and time consuming. Simulation tools have been used by numerous authors for reducing the breadth of experimental campaigns required to obtain final products. Among various modeling techniques, homogenization relies on microstructural information to predict the effective mechanical properties of composites (the number of phases, their mechanical properties, their volume fractions, their shapes and spatial distributions, etc.).

In spite of the substantial benefits they offer, few analytical homogenization models are used in industry. Instead, the industry relies mainly on the simple Rule of Mixtures and on the Classical Lamination Theory, which lead in most cases to inaccurate predictions. The industry is then constrained to use unnecessarily high safety factors, which hinders the production of lightweight parts. This lack of confidence in predictive models is partly due to the fact that analytical homogenization models have not been thoroughly validated or verified.

Numerical homogenization is performed by simulating artificial loadings on microstructures that are representative of the bulk material. The response of the microstructure is computed using numerical techniques such as the Finite Element Method (FEM) and the Fast Fourier Transforms (FFT). Numerical homogenization offers the possibility of homogenizing any possible microstructure by modeling in detail the geometry of its constituents. Therefore, numerical homogenization can compute accurate local fields, unlike analytical homogenization where local fields are approximated. Nevertheless, the applicability of such an approach is limited due to its huge computational cost when dealing with complex microstructures (e.g., microstructures with high aspect ratio and/or volume fraction of fibers).

In order to assess the accuracy of analytical homogenization models, it is necessary to compare their predictions to those obtained by numerical methods. Furthermore, these methods should be fully automated if a large validation campaign is planned. Indeed, a comprehensive performance evaluation requires generating an important database of accurate effective properties. Therefore, it is of considerable interest to develop a robust and fully automated procedure for generating this database in order to reduce user input.

The main objective of this thesis is to develop a fully automated numerical tool for computing the exact mechanical properties of randomly distributed and oriented ellipsoidal fibers reinforced composites. The development of a numerical tool requires two independent

steps. First, representative microstructures of the composite should be randomly generated. Then, the local fields and effective mechanical properties must be accurately computed. The numerical tool is then used to validate the performance of existing analytical homogenization models at predicting effective responses as well as local stress/strains distributions.

This thesis is organized as follows. Chapter 1 presents a literature review on the analytical and numerical homogenization methods applicable to randomly distributed and oriented ellipsoidal fibers reinforced composites. This chapter also summarizes the works dealing with numerical validation of analytical models and highlights the existing gaps. Chapter 2 introduces the objectives of the thesis with respect to the findings of Chapter 1. The scientific approach as well as the publication strategy are presented in Chapter 3. The four articles resulting from this work are included in Chapters 4 to 7. Chapter 4 presents a rigorous study on the validation of analytical homogenization models for the case of spherical particles reinforced composites. In Chapter 5, a new computationally-efficient algorithm for generating random packings of hard ellipsoids is introduced. Chapter 6 studies thoroughly the accuracy of analytical models at predicting the effective properties of composites reinforced by randomly distributed and oriented ellipsoidal particles. Chapter 7 investigates the performance of the analytical models at predicting the local field statistics. Chapter 8 discusses the relationships between the articles and Chapter 9 presents complementary work performed during this project. The contributions from this thesis are finally summarized and topics for future studies are recommended.

CHAPTER 1

LITERATURE REVIEW

This Chapter introduces the basic principles of homogenization and presents the different analytical and numerical homogenization methods applicable to composites reinforced by randomly distributed and oriented ellipsoidal fibers. The various studies that have dealt with numerical validation of analytical models are also presented. The survey is limited to two-phase linearly elastic composites. Both matrix and reinforcements are assumed to be isotropic. Reinforcements are axisymmetric, monodisperse and perfectly bonded to the matrix.

1.1 Notations and conventions

Scalars and vectors are respectively denoted by letters (e.g., s, S, σ, Σ) and boldfaced lower case Latin letters (e.g., $\boldsymbol{s}$); second and fourth order tensors are respectively denoted by boldfaced Greek letters (e.g., $\boldsymbol{\sigma}$, $\boldsymbol{\Sigma}$) and boldfaced upper case Latin letters (e.g., $\mathbf{S}$). The Einstein summation convention has been adopted, unless specified otherwise.

1.2 Analytical homogenization

1.2.1 Basic principles

Homogenization models are based on the separation of scales between the overall mechanical response of the composite, belonging to the macroscopic scale, and the mechanical behavior of the heterogeneities, belonging to the microscopic scale (Bornert *et al.*, 2001). The purpose of homogenization is to derive the relationship between stress and strain at the macroscopic scale ($\boldsymbol{\Sigma}$ and $\mathbf{E}$) and those at the microscopic scale ($\boldsymbol{\sigma}(\boldsymbol{x})$ and $\boldsymbol{\varepsilon}(\boldsymbol{x})$), as shown in Figure 1.1. More specifically, homogenization computes the composite's effective stiffness tensor $\widetilde{\mathbf{C}}$, or compliance tensor $\widetilde{\mathbf{S}}$, such that:

$$\boldsymbol{\Sigma} = \widetilde{\mathbf{C}} : \mathbf{E} \tag{1.1a}$$

$$\mathbf{E} = \widetilde{\mathbf{S}} : \boldsymbol{\Sigma} \tag{1.1b}$$

It is possible to show that (Böhm, 1998):
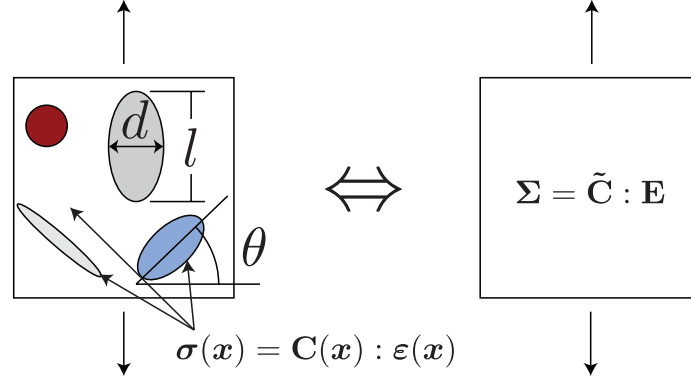
Figure 1.1 Illustration of the homogenization approach. Separation of scales between the mechanical behavior of the heterogeneities ($\boldsymbol{\sigma}(\boldsymbol{x})$ and $\boldsymbol{\varepsilon}(\boldsymbol{x})$), belonging to the microscopic scale, and the overall mechanical response of the composite ($\boldsymbol{\Sigma}$ and $\mathbf{E}$), belonging to the macroscopic scale.

$$< \boldsymbol{\varepsilon}(\boldsymbol{x}) > \, = \, \mathbf{E} \tag{1.2a}$$

$$< \boldsymbol{\sigma}(\boldsymbol{x}) > \, = \, \boldsymbol{\Sigma} \tag{1.2b}$$

where $< \cdot >$ denotes an average over the volume:

$$< \boldsymbol{f}(\boldsymbol{x}) > \, = \, \frac{1}{V} \int_V \boldsymbol{f}(\boldsymbol{x}) \mathrm{d}V \tag{1.3}$$

where V is the volume of the composite.

The relationship between the micro- and the macroscopic scale is given by the following equations:

$$\boldsymbol{\varepsilon}(\boldsymbol{x}) \, = \, \mathbf{A}(\boldsymbol{x}) : \mathbf{E} \tag{1.4a}$$

$$\boldsymbol{\sigma}(\boldsymbol{x}) \, = \, \mathbf{B}(\boldsymbol{x}) : \boldsymbol{\Sigma} \tag{1.4b}$$

where $\mathbf{A}(\boldsymbol{x})$ and $\mathbf{B}(\boldsymbol{x})$ denote the strain localization and the stress concentration tensors, respectively. The first moment of strains and stresses in phase "i" ($i = 1$ for the matrix and $i = 2$ for the reinforcements) can be expressed as (Hill, 1963):

$$< \boldsymbol{\varepsilon} >_i \, = \, < \mathbf{A}(\boldsymbol{x}) >_i : \mathbf{E} \, = \, \mathbf{A}_i : \mathbf{E} \tag{1.5a}$$

$$< \boldsymbol{\sigma} >_i \, = \, < \mathbf{B}(\boldsymbol{x}) >_i : \boldsymbol{\Sigma} \, = \, \mathbf{B}_i : \boldsymbol{\Sigma} \tag{1.5b}$$

where $< \cdot >_i$ denotes the volume average over phase "i" and $\mathbf{A}_i$ and $\mathbf{B}_i$ refer respectively to the average strain localization and stress concentration tensors within the phase.

Tensors $\mathbf{A}_i$ and $\mathbf{B}_i$ are related through Hill (1965):

$$< \mathbf{A}(\boldsymbol{x}) > \; = \; c_1 \mathbf{A}_1 + c_2 \mathbf{A}_2 \; = \; \mathbf{I} \tag{1.6a}$$

$$< \mathbf{B}(\boldsymbol{x}) > \; = \; c_1 \mathbf{B}_1 + c_2 \mathbf{B}_2 \; = \; \mathbf{I} \tag{1.6b}$$

where $\mathbf{I}$ is the fourth order identity tensor and c_i is the volume fraction of phase "i".

Using Eqs. (1.2) and (1.5), one can write (Böhm, 1998):

$$
\begin{aligned}
\Sigma \; &= \; < \boldsymbol{\sigma}(\boldsymbol{x}) > \\
&= \; c_1 < \boldsymbol{\sigma} >_1 + c_2 < \boldsymbol{\sigma} >_2 \\
&= \; c_1 \, \mathbf{C}_1 : < \boldsymbol{\varepsilon} >_1 + c_2 \, \mathbf{C}_2 : < \boldsymbol{\varepsilon} >_2 \\
&= \; \big(c_1 \, \mathbf{C}_1 : \mathbf{A}_1 + c_2 \, \mathbf{C}_2 : \mathbf{A}_2 \big) : \mathbf{E}
\end{aligned}
\tag{1.7a}
$$

and

$$
\begin{aligned}
\mathbf{E} \; &= \; < \boldsymbol{\varepsilon}(\boldsymbol{x}) > \\
&= \; c_1 < \boldsymbol{\varepsilon} >_1 + c_2 < \boldsymbol{\varepsilon} >_2 \\
&= \; c_1 \, \mathbf{S}_1 : < \boldsymbol{\sigma} >_1 + c_2 \, \mathbf{S}_2 : < \boldsymbol{\sigma} >_2 \\
&= \; \big(c_1 \, \mathbf{S}_1 : \mathbf{B}_1 + c_2 \, \mathbf{S}_2 : \mathbf{B}_2 \big) : \Sigma
\end{aligned}
\tag{1.7b}
$$

where $\mathbf{C}_i$ and $\mathbf{S}_i$ denote respectively the stiffness and compliance tensor of phase "i". Eqs. (1.1) and (1.7) lead to the effective stiffness and compliance tensors as:

$$\widetilde{\mathbf{C}} \; = \; c_1 \, \mathbf{C}_1 : \mathbf{A}_1 + c_2 \, \mathbf{C}_2 : \mathbf{A}_2 \tag{1.8a}$$

$$\widetilde{\mathbf{S}} \; = \; c_1 \, \mathbf{S}_1 : \mathbf{B}_1 + c_2 \, \mathbf{S}_2 : \mathbf{B}_2 \tag{1.8b}$$

Using Eqs. (1.6), Eqs. (1.8) can be written as:

$$\widetilde{\mathbf{C}} \; = \; \mathbf{C}_1 + c_2 \big(\mathbf{C}_2 - \mathbf{C}_1 \big) : \mathbf{A}_2 \tag{1.9a}$$

$$\widetilde{\mathbf{S}} \; = \; \mathbf{S}_1 + c_2 \big(\mathbf{S}_2 - \mathbf{S}_1 \big) : \mathbf{B}_2 \tag{1.9b}$$

For the special case of randomly distributed and oriented reinforcements, Benveniste (1987) has obtained the following expressions:

$$\widetilde{\mathbf{C}} \; = \; \mathbf{C}_1 + c_2 \Big\langle \big(\mathbf{C}_2 - \mathbf{C}_1 \big) : \mathbf{A}_2 \Big\rangle \tag{1.10a}$$

$$\widetilde{\mathbf{S}} \; = \; \mathbf{S}_1 + c_2 \Big\langle \big(\mathbf{S}_2 - \mathbf{S}_1 \big) : \mathbf{B}_2 \Big\rangle \tag{1.10b}$$

where $\langle \mathbf{X} \rangle$ represents orientation averaging of a given tensor $\mathbf{X}$, such as:

$$\left\langle \mathrm{X}_{mnop} \right\rangle \;=\; \frac{1}{2\pi^2} \int\limits_{-\pi}^{\pi}\int\limits_{0}^{\pi}\int\limits_{0}^{\pi/2} \omega_{mq}\omega_{nr}\omega_{os}\omega_{pt}\mathrm{X}_{qrst}\sin(\phi)\mathrm{d}\theta\mathrm{d}\phi\mathrm{d}\psi \tag{1.11}$$

where θ, ϕ and ψ refer to the Euler angles and $\boldsymbol{\omega}$ denotes the rotation tensor (Odegard *et al.*, 2003). Appendix A shows how to compute Eq. (1.11) analytically.

Eqs. (1.10) provide direct estimations for the effective tensors of composites reinforced by randomly distributed and oriented inclusions based on the knowledge of $\mathbf{A}_2$ or $\mathbf{B}_2$. Given the complexity of the problem, it is almost impossible to define accurately the tensors $\mathbf{A}_2$ and $\mathbf{B}_2$. Thus, the difference between analytical homogenization models lies in the estimation of these two tensors. These tensors are defined based on the assumptions introduced for each model, as discussed in Section 1.2.2.

Knowing the effective tensors of a composite and its macroscopic response for a given loading (i.e., $\boldsymbol{\Sigma}$ and $\mathbf{E}$), it is possible to obtain the second order moments of stresses and strains in each phase Castaneda and Suquet (1998):

$$< \boldsymbol{\varepsilon} \otimes \boldsymbol{\varepsilon} >_i \;=\; \frac{1}{c_i}\mathbf{E} : \frac{\partial \widetilde{\mathbf{C}}}{\partial \mathbf{C}_i} : \mathbf{E} \tag{1.12a}$$

$$< \boldsymbol{\sigma} \otimes \boldsymbol{\sigma} >_i \;=\; \frac{1}{c_i}\boldsymbol{\Sigma} : \frac{\partial \widetilde{\mathbf{S}}}{\partial \mathbf{S}_i} : \boldsymbol{\Sigma} \tag{1.12b}$$

Since the phases are isotropic, their stiffness and compliance tensors can be expressed as follows:

$$\mathbf{C}_i \;=\; 3\kappa_i\mathbf{J} + 2\mu_i\mathbf{K} \tag{1.13a}$$

$$\mathbf{S}_i \;=\; \frac{1}{3}\kappa_i^{-1}\mathbf{J} + \frac{1}{2}\mu_i^{-1}\mathbf{K} \tag{1.13b}$$

where κ_i and μ_i denote respectively the bulk and shear moduli of phase "i", while $\mathbf{J}$ and $\mathbf{K}$ are the classical spherical and deviatoric projection tensors. Using Eqs. (1.12) and (1.13), the following result can be obtained with the chain rule (Castaneda and Suquet, 1998):

$$\frac{1}{c_i}\mathbf{E} : \frac{\partial \widetilde{\mathbf{C}}}{\partial \kappa_i} : \mathbf{E} \;=\; 3 < \boldsymbol{\varepsilon} \otimes \boldsymbol{\varepsilon} >_i :: \mathbf{J} \tag{1.14a}$$

$$\frac{1}{c_i}\mathbf{E} : \frac{\partial \widetilde{\mathbf{C}}}{\partial \mu_i} : \mathbf{E} \;=\; 2 < \boldsymbol{\varepsilon} \otimes \boldsymbol{\varepsilon} >_i :: \mathbf{K} \tag{1.14b}$$

$$\frac{1}{c_i}\boldsymbol{\Sigma} : \frac{\partial \widetilde{\mathbf{S}}}{\partial \kappa_i^{-1}} : \boldsymbol{\Sigma} \;=\; \frac{1}{3} < \boldsymbol{\sigma} \otimes \boldsymbol{\sigma} >_i :: \mathbf{J} \tag{1.14c}$$

$$\frac{1}{c_i}\boldsymbol{\Sigma} : \frac{\partial \widetilde{\mathbf{S}}}{\partial \mu_i^{-1}} : \boldsymbol{\Sigma} \;=\; \frac{1}{2} < \boldsymbol{\sigma} \otimes \boldsymbol{\sigma} >_i :: \mathbf{K} \tag{1.14d}$$

where κ_i^{-1} and μ_i^{-1} denote respectively the inverse of the bulk and shear moduli of phase "i".

1.2.2 Analytical homogenization models

Voigt and Reuss bounds

In the Voigt model, it is assumed that the strain in each phase is equal to the macroscopic strain $\mathbf{E}$ (i.e., $\mathbf{A}(\boldsymbol{x}) = \mathbf{A}_i = \mathbf{I}$). In the Reuss model, it is assumed that the stress in each phase is equal to the macroscopic stress $\boldsymbol{\Sigma}$ (i.e., $\mathbf{B}(\boldsymbol{x}) = \mathbf{B}_i = \mathbf{I}$). These two models are therefore insensitive to the shape and orientation of the reinforcements. Indeed, their predictions depend only on the properties and the volume fraction of the phases. Furthermore, it can be shown that the model of Voigt provides an upper bound while the model of Reuss provides a lower bound on the mechanical properties of the composite (Bourgeois, 1994).

Eshelby's problem

The Eshelby's problem (Eshelby, 1957) is a pillar for most existing homogenization models. In this problem, an elliptical inclusion embedded in an infinite medium is considered, as shown in Figure 1.2. Initially, the inclusion is free of stress and strain and then subjected
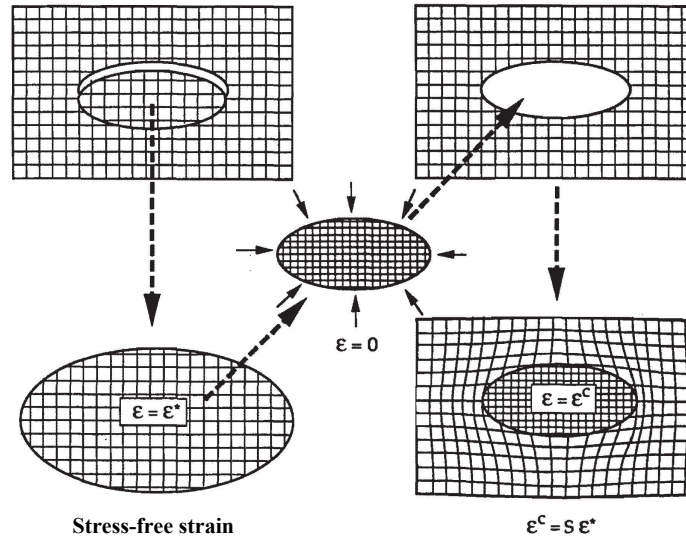
Figure 1.2 Illustration of the Eshelby's inclusion problem. An elliptical inclusion embedded in an infinite medium is subjected to a uniform stress-free strain $\boldsymbol{\varepsilon}^*$. The resulting strain field in the constrained inclusion is given by $\boldsymbol{\varepsilon}^c = \mathbf{S}^E : \boldsymbol{\varepsilon}^*$, where $\mathbf{S}^E$ is the Eshelby's tensor. (Bourgeois, 1994).

to a uniform stress-free strain $\boldsymbol{\varepsilon}^*$ (as a thermal deformation for example) and becomes constrained by the surrounding medium. Eshelby has shown that the resulting strain field $\boldsymbol{\varepsilon}^{\mathrm{c}}$ in the constrained inclusion is uniform and is given by:

$$\boldsymbol{\varepsilon}^{\mathrm{c}} = \mathbf{S}^{\mathrm{E}} : \boldsymbol{\varepsilon}^* \tag{1.15}$$

where $\mathbf{S}^{\mathrm{E}}$ is the Eshelby's tensor. This tensor depends on the mechanical properties of the infinite medium as well as on the geometrical properties of the inclusion. Expressions of $\mathbf{S}^{\mathrm{E}}$ for different inclusions shapes and material symmetries can be found in Mura (1987). Appendix B provides the expressions of $\mathbf{S}^{\mathrm{E}}$ for spherical and ellipsoidal inclusions embedded in an isotropic linearly elastic medium. For complex shapes and material symmetries, Eshelby's tensor can be numerically computed according to the methodology of Gavazzi and Lagoudas (1990).

Dilute solution of Eshelby

The first homogenization model based on Eshelby's theory assumes that the reinforcements are embedded in an infinite medium having the properties of the matrix. It is also assumed that the reinforcements are far from each other. Thus, this model is suitable for composites having a low volume fraction of inclusions. The strain localization tensor for Eshelby's dilute solution is (Eshelby, 1957):

$$\mathbf{A}_2^{\mathrm{Esh}} = \left[\mathbf{I} + \mathbf{S}_1^{\mathrm{E}} : \mathbf{C}_1^{-1} : \left(\mathbf{C}_2 - \mathbf{C}_1\right)\right]^{-1} \tag{1.16}$$

where $\mathbf{S}_1^{\mathrm{E}}$ is Eshelby's tensor computed using the matrix mechanical properties.

Bounds of Hashin-Shtrikman

Hashin and Shtrikman (1961) have established tighter bounds than those of Voigt and Reuss by using variational principles. These bounds apply to heterogeneous materials with isotropic constituents that exhibit an overall isotropic behavior. The strain localization tensors for the Hashin-Shtrikman lower (HSL) an upper (HSU) bounds are expressed by (Hashin, 1962; Hashin and Shtrikman, 1963):

$$\mathbf{A}_2^{\mathrm{HSL}} = \left[\mathbf{I} + \mathbf{S}_1^{\mathrm{E}^*} : \mathbf{C}_1^{-1} : \left(\mathbf{C}_2 - \mathbf{C}_1\right)\right]^{-1} \tag{1.17a}$$

$$\mathbf{A}_2^{\mathrm{HSU}} = \left[\mathbf{I} + \mathbf{S}_2^{\mathrm{E}^*} : \mathbf{C}_2^{-1} : \left(\mathbf{C}_1 - \mathbf{C}_2\right)\right]^{-1} \tag{1.17b}$$

where $\mathbf{S}_i^{\mathrm{E}^*}$ denotes Eshelby's tensor of a spherical inclusion embedded in a medium having the mechanical properties of phase "i".

Walpole (1966) reformulated the Hashin-Shtrikman bounds using energy principles. For aligned reinforcements, the strain localization tensors for the Hashin-Shtrikman-Walpole lower (HSWL) and upper (HSWU) bounds are expressed by (Walpole, 1966; Willis, 1977; Weng, 1992):

$$\mathbf{A}_2^{\mathrm{HSWL}} = \left[\mathbf{I} + \mathbf{S}_1^{\mathrm{E}} : \mathbf{C}_1^{-1} : \left(\mathbf{C}_2 - \mathbf{C}_1\right)\right]^{-1} \tag{1.18a}$$

$$\mathbf{A}_2^{\mathrm{HSWU}} = \left[\mathbf{I} + \mathbf{S}_2^{\mathrm{E}} : \mathbf{C}_2^{-1} : \left(\mathbf{C}_1 - \mathbf{C}_2\right)\right]^{-1} \tag{1.18b}$$

where $\mathbf{S}_i^{\mathrm{E}}$ is Eshelby's tensor computed using the properties of phase "i".

Self-consistent model

The self-consistent model was originally developed for polycrystals and has been extended to composites by the work of Budiansky (1965) and Hill (1965). This homogenization assumes that the reinforcements are immersed in an equivalent homogeneous medium having the effective properties of the composite. The strain localization tensor for the self-consistent model is given by:

$$\mathbf{A}_2^{\mathrm{SC}} = \left[\mathbf{I} + \widetilde{\mathbf{S}}^{\mathrm{E}} : \widetilde{\mathbf{C}}^{-1} : \left(\mathbf{C}_2 - \widetilde{\mathbf{C}}\right)\right]^{-1} \tag{1.19}$$

where $\widetilde{\mathbf{S}}^{\mathrm{E}}$ is Eshelby's tensor obtained by considering the effective composite as the infinite media. Since $\widetilde{\mathbf{S}}^{\mathrm{E}}$ and $\widetilde{\mathbf{C}}$ are initially unknown, the self consistent scheme is an implicit model that is iteratively solved.

Generalized self-consistent model

Christensen and Lo (1979) have developed a three-phase model to predict the shear effective properties of composites reinforced by spherical and cylindrical reinforcements. This model is based on the assumption that the inclusions are first immersed in the matrix and the assembly is then embedded in the effective medium having the sought properties. The model was subsequently reformulated by Benveniste (2008) and its application has been extended to multi-phase composites. Unlike the self-consistent scheme, this model is explicit.

Mori-Tanaka model

The Mori-Tanaka model (Mori and Tanaka, 1973) was initially developed to determine the average stress in the matrix of a composite having a high volume fraction of inclusions. In

this model, the reinforcements are embedded in an infinite medium having the properties of the matrix. The strain localization tensor for the Mori-Tanaka model is expressed as follows:

$$\mathbf{A}_2^{\text{MT}} = \mathbf{T} : \left[c_1\mathbf{I} + c_2\mathbf{T}\right]^{-1} \tag{1.20a}$$

where:

$$\mathbf{T} = \mathbf{A}^{\text{Esh}} = \left[\mathbf{I} + \mathbf{S}_1^{\text{E}} : \mathbf{C}_1^{-1} : \left(\mathbf{C}_2 - \mathbf{C}_1\right)\right]^{-1} \tag{1.20b}$$

Benveniste (1987) proposed a new formulation of the Mori-Tanaka model which is suitable for composites with randomly oriented fibers. He developed a model where orientation averaging is directly performed on $\mathbf{T}$. His estimate reads:

$$\widetilde{\mathbf{C}}^{\text{Ben}} = \mathbf{C}_1 + c_2\left\langle\left(\mathbf{C}_2 - \mathbf{C}_1\right) : \mathbf{T}\right\rangle : \left[c_1\mathbf{I} + c_2\langle\mathbf{T}\rangle\right]^{-1} \tag{1.21}$$

It should be noted that this model delivers non-symmetric effective tensors for many microstructures (e.g., reinforcements with different aspect ratios) (Ferrari, 1991; Benveniste *et al.*, 1991), which is physically invalid. However, since this study deals with inclusions of identical aspect ratios, Eq.(1.21) leads to symmetric tensors.

Lielens' model

Lielens *et al.* (1998) have developed a model that interpolates nonlinearly between the Hashin-Shtrikman-Walpole bounds for aligned reinforcements (Walpole, 1966; Willis, 1977; Weng, 1992). More specifically, this model interpolates the inverse of the strain localization tensor between the case where the stiffest phase is embedded in the more compliant phase and that where the most compliant phase is embedded in the stiffest phase (Tucker and Liang, 1999). The strain localization tensor is given by:

$$\mathbf{A}_2^{\text{LI}} = \hat{\mathbf{A}}^{\text{LI}} : \left[c_1\mathbf{I} + c_2\hat{\mathbf{A}}^{\text{LI}}\right]^{-1} \tag{1.22a}$$

where:

$$\hat{\mathbf{A}}^{\text{LI}} = \left\{\left(1 - v_f\right)\left[\hat{\mathbf{A}}^{\text{lower}}\right]^{-1} + v_f\left[\hat{\mathbf{A}}^{\text{upper}}\right]^{-1}\right\}^{-1}, \tag{1.22b}$$

v_f is the interpolation factor and is related to the inclusions volume fraction (Lielens *et al.*, 1998; Tucker and Liang, 1999):

$$v_f = \frac{1}{2}c_2(1 + c_2) \tag{1.22c}$$

$\hat{\mathbf{A}}^{\text{lower}}$ and $\hat{\mathbf{A}}^{\text{upper}}$ are computed as:

$$\hat{\mathbf{A}}^{\text{lower}} = \mathbf{A}_2^{\text{HSWL}} = \left[\mathbf{I} + \mathbf{S}_1^{\text{E}} : \mathbf{C}_1^{-1} : \left(\mathbf{C}_2 - \mathbf{C}_1\right)\right]^{-1} \tag{1.22d}$$

$$\hat{\mathbf{A}}^{\text{upper}} = \mathbf{A}_2^{\text{HSWU}} = \left[\mathbf{I} + \mathbf{S}_2^{\text{E}} : \mathbf{C}_2^{-1} : \left(\mathbf{C}_1 - \mathbf{C}_2\right)\right]^{-1} \tag{1.22e}$$

Ponte-Castañeda and Willis model

Castaneda and Willis (1995) developed a model to estimate the effective properties by using the variational formulation of Hashin and Shtrikman (1962a,b). In this model, the reinforcements are embedded in spherical safety cells, as shown in Figure 1.3. The model is physically valid if the spherical cells do not overlap. For a composite consisting of an isotropic matrix and randomly oriented isotropic ellipsoidal inclusions, the effective stiffness tensor is obtained as follows:

$$\widetilde{\mathbf{C}}^{\text{PCW}} = \mathbf{C}_1\left\{\mathbf{I} - c_2\left[\left\langle\mathbf{A}^{\text{PCW}}\right\rangle^{-1} + c_2\mathbf{S}_1^{\text{E}^*}\right]^{-1}\right\} \tag{1.23a}$$

where $\mathbf{S}_1^{\text{E}^*}$ is Eshleby's tensor of a spherical inclusion computed using the matrix as the infinite media. $\mathbf{A}^{\text{PCW}}$ is given by the following relation:

$$\mathbf{A}^{\text{PCW}} = -\left[\mathbf{S}_1^{\text{E}} - \left(\mathbf{C}_1 - \mathbf{C}_2\right)^{-1}\mathbf{C}_1\right]^{-1} \tag{1.23b}$$

The range of physically valid volume fractions is limited to (Castaneda and Willis, 1995):
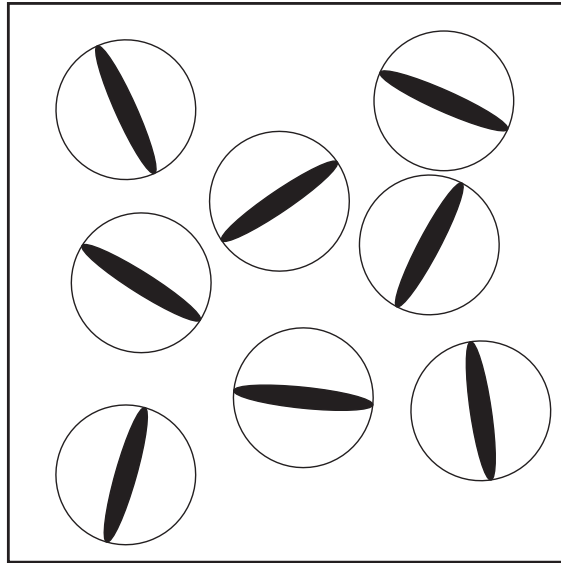
Figure 1.3 Model of Ponte-Castañeda and Willis (PCW): randomly oriented ellipsoidal inclusions embedded in spherical safety cells.

$$c_2 \leq \begin{cases} 1/R^2 & \text{if} \quad R \geq 1 \\ 1/R & \text{if} \quad R < 1 \end{cases} \qquad \text{with} \qquad R = a/b \qquad (1.24)$$

where R denotes the ellipsoids aspect ratio defined as the ratio between the length of the radius along the symmetry axis (a) over the length of the equatorial radius (b). For example, for ellipsoidal reinforcements with an aspect ratio of 10, the volume fraction limit is 1%. Hu and Weng (2000) have shown that the Ponte-Castañeda and Willis model violates the bounds of Hashin-Shtrikman for volume fractions higher than the physical limit given by Eq. (1.24).

1.3   Numerical homogenization

Numerical homogenization is used to accurately compute the local fields and the effective properties of heterogeneous materials. For randomly distributed and oriented fibers reinforced composites, numerical homogenization is performed in three steps:

1)   A representative microstructure of the studied composite is randomly generated;

2)   The local fields and the effective properties of the generated microstructure are accurately computed;

3)   Steps 1) and 2) are repeated within the Representative Volume Element (RVE) determination process.

Existing algorithms for generating random microstructures are first described in the following sub-sections. Then, the different numerical techniques for computing the local fields and the effective properties of a single microstructure are presented. The section summarizes the different methods available in the literature for determining the RVE.

1.3.1   Generation of random microstructures

Random Sequential Adsorption (RSA) algorithm

The Random Sequential Adsorption (RSA) algorithm (Rintoul and Torquato, 1997) is certainly the most widely used algorithm for generating random microstructures. At the beginning of the computation, the position of a reinforcement is randomly selected. Then, the position of another reinforcement is drawn and the contact is checked between both reinforcements. If there is interference, the position of the second reinforcement is drawn again until there is no contact with the first. The process is repeated until the desired number of reinforcement and volume fraction are reached. Several authors have used this algorithm and have struggled to reach high volume fractions (Segurado and Llorca, 2002;
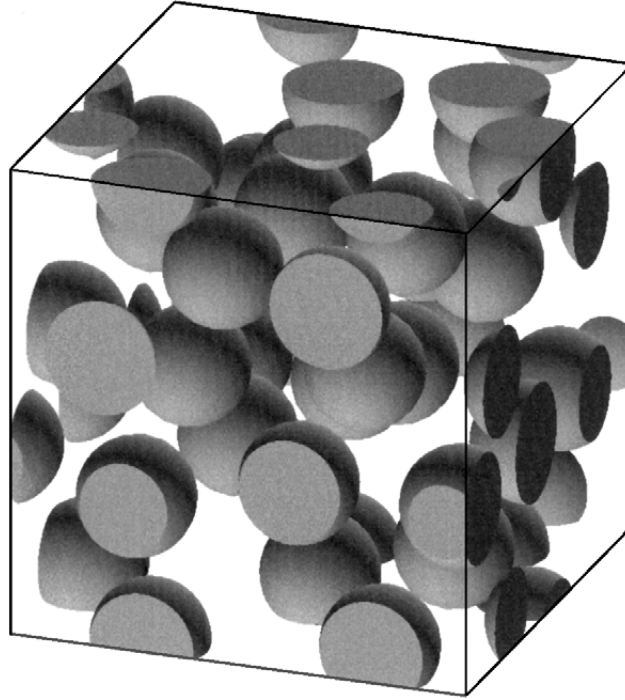
Figure 1.4 Microstructure generated using Random Sequential Adsorption (RSA) algorithm. Number of spheres = 30. Volume fraction = 25%. (Segurado and Llorca, 2002).

Barello and Lévesque, 2008; Kari *et al.*, 2007b). In its simplest form, this algorithm can generate volume fractions of approximately 30% for identical spherical particles. Moreover, when the desired number of reinforcements is high, the computation time becomes important.

Figure 1.4 shows a microstructure generated using the RSA algorithm, including 30 spherical particles with a volume fraction of 25% (Segurado and Llorca, 2002).

Modified RSA algorithm

An improved version of the RSA algorithm was proposed by Segurado and Llorca (2002). A unit cell having a volume fraction lower than the desired value is first generated with the RSA algorithm. The cell is then compressed in several steps and the reinforcements positions and volumes are updated at each compression stage. However, this compression leads to reinforcements interpenetration. It is therefore necessary to check for reinforcements overlapping at each compression stage. If two reinforcements overlap, one of them is displaced along a random vector. If the reinforcements are still in interference, the reinforcement is placed in its original position and the process is repeated until the two inclusions no longer intersect. The simulation continues until the target volume fraction is reached. This modification in the RSA algorithm allows for denser packings than with the original version

(around 50% for identical spherical particles). Nevertheless, the computation time remains important.

Molecular dynamics algorithm

Lubachevsky and Stillinger (1990) proposed an algorithm based on molecular dynamics. This algorithm was originally applied to discs (2D) and spheres (3D) (Lubachevsky *et al.*, 1991). The main idea of the algorithm is as follows. All inclusions are randomly created in the unit cell but have a null volume. Each inclusion has also a random velocity vector. The particles are then set in motion and their volumes gradually increase. Binary collisions are checked at each iteration. When a binary collision occurs, the velocities of the two concerned particles are updated according to the kinetic energy conservation principle. Furthermore, if the unit cell must be periodic (see Section 1.3.2), collisions between particles and the cell faces must be checked. Indeed, if a particle leaves the cell through a face, it must appear from the opposite side to meet the periodicity conditions. The simulation stops when the desired volume fraction is reached. This algorithm is more efficient than the RSA and the modified RSA algorithms since it can generate very dense packings in a low computation time. For example, a packing of 30 identical spheres with a volume fraction of 60% can be generated in less than 10 seconds. It was also possible to reach a volume fraction of 74% (Ghossein and Levesque, 2012), which is close to the theoretical maximum dense packing for monodisperse spheres ($\approx 74.05\%$). This type of algorithm is called event-driven molecular dynamics (EDMD) where a sequence of discrete events are predicted and processed. Other authors (Allen *et al.*, 1989) have used a time-driven molecular dynamics (TDMD) approach where time is divided into small increments and, at each step time, differential equations based on Newton's law are integrated. TDMD algorithm are much easier to implement than EDMD but are far less efficient, especially for high densities.

Molecular dynamics algorithm for non spherical inclusions

The works of Lubachevsky and Stillinger have been extended by Donev *et al.* (2005a) to the case of non spherical particles within an EDMD framework. In most cases, the collision time between inclusions is computed numerically. Since this step requires numerous computations, Donev et al. introduced the near-neighbor list (NNL) concept to avoid computing unnecessary collisions. Each particle has a bounding neighborhood and collision between a pair of particles is checked if their bounding neighborhoods overlap. This method is very useful for aspherical inclusions and speeds up considerably the algorithm. The latter was applied to ellipses (2D) and ellipsoids (3D) (Donev *et al.*, 2005b). To calculate the colli-
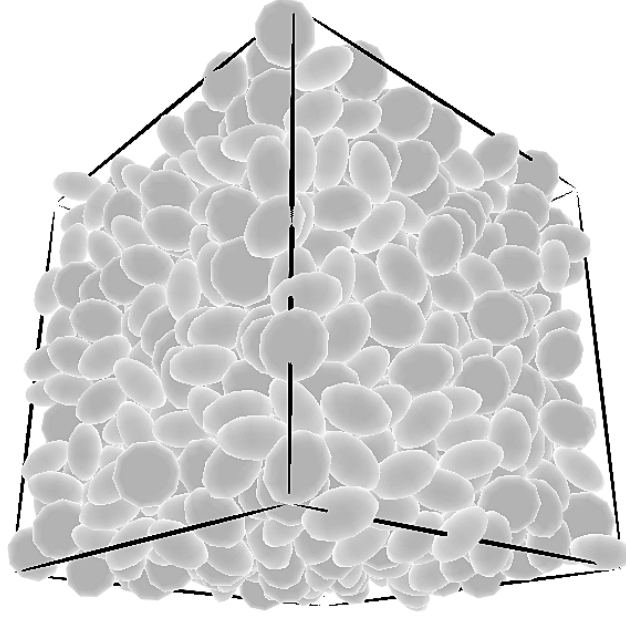
Figure 1.5 Packing of oblate ellipsoids generated using the molecular dynamics algorithm proposed by Donev *et al.* (2005a,b). Number of ellipsoids = 1000. Volume fraction = 70%. Aspect ratio = 1.9. (Donev, 2006).

sion time between two ellipsoids, the authors made use of the overlap potentials (Perram and Wertheim, 1985; Perram *et al.*, 1996). The collision time t_c between two moving ellipsoids is the first root of the overlap potential $F(t)$ that represents the maximum of a certain parametric function $f(t, \lambda)$:

$$t_c = \min(t)$$
$$\text{such that } F(t) = 0 \;\; \text{and} \;\; t \geq 0 \tag{1.25}$$
$$\text{where } F(t) = \max_{0 \leq \lambda \leq 1} f(t, \lambda)$$

Since the maximum of $f(t, \lambda)$ cannot be computed analytically, the problem takes the form of two optimization subproblems, which can make the algorithm less computationally-efficient.

Figure 1.5 shows a packing generated using the molecular dynamics algorithm proposed by Donev *et al.* (2005a,b). The packing contains 1000 oblate ellipsoids with an aspect ratio of 1.9 and a volume fraction of 70% (Donev, 2006).

1.3.2 Local fields and effective properties of a single microstructure

Several numerical methods can be used to compute the local fields and the effective properties of a 3D microstructure. The most known techniques are the Finite Element Method

(FEM) and the Fast Fourier Transforms (FFT). In this section, a brief description of these two methods is presented. A listing of some other numerical methods can be found in Böhm (1998) and Pierard (2006).

Finite Element Method (FEM)

The FEM is certainly the most widely used technique for computing the local stress and strain fields of a given microstructure (Llorca *et al.*, 2000; Bohm *et al.*, 2002; Segurado and Llorca, 2002; Kari *et al.*, 2007b; Barello and Lévesque, 2008; Klusemann and Svendsen, 2010; Cojocaru and Karlsson, 2010; El-Mourid *et al.*, 2012; Pahlavanpour *et al.*, 2013; Moussaddy *et al.*, 2013b). In this method, a unit cell is meshed with elements and boundary conditions are applied. The problem is then solved and the stress and strain fields are obtained in each element. The required mesh size depends on the number of reinforcements within the unit cell, their volume fraction and aspect ratio, as well as the mechanical properties contrasts between the inclusions and the matrix.

Figure 1.6 shows the meshing of two different unit cells. The first (Figure 1.6a) contains randomly distributed spherical particles while the second (Figure 1.6b) contains randomly distributed voids. The volume fraction in both cells is 20%.

The main advantage of the FEM is that it allows for a non-uniform discretization of the

(a)   (b)
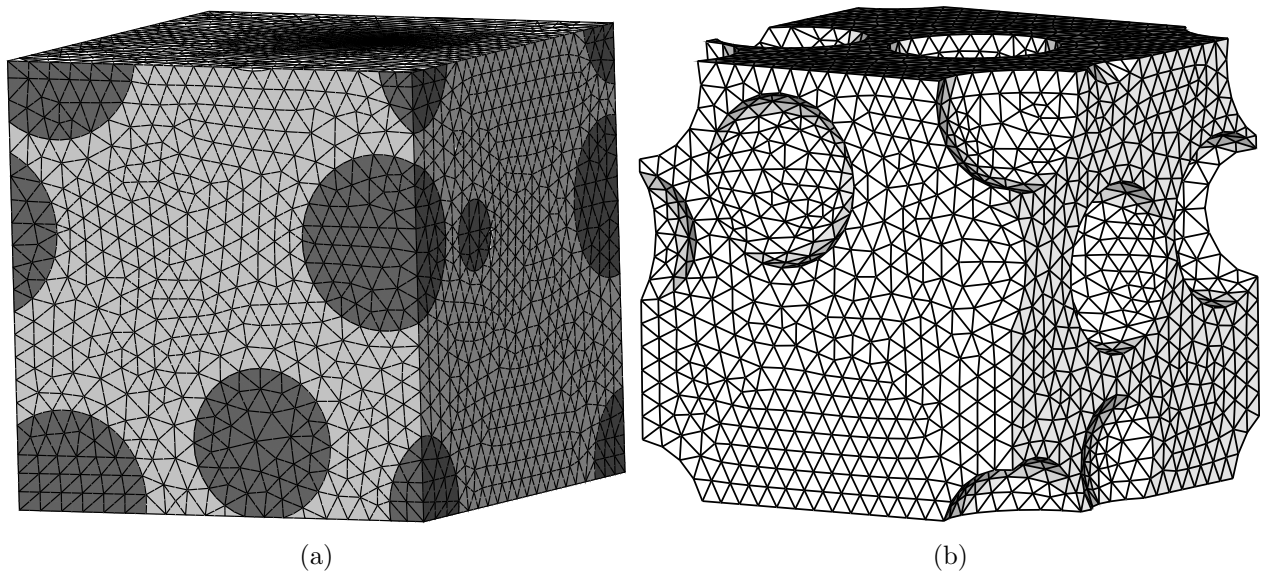
Figure 1.6 Meshing of a unit cell. (a) Randomly distributed spherical particles with a volume fraction of 20%. (b) Randomly distributed voids with a volume fraction of 20%. (Klusemann and Svendsen, 2010).

microstructure permitting different levels of mesh refinements in different parts of the unit cell. Moreover, different shapes of elements (e.g., cubic, tetrahedrons) can be used, enabling the representation of reinforcements with complex shapes. However, despite the robustness of the FEM, it cannot be fully automated since the meshing operation usually requires user input, especially for large volume fractions and/or aspect ratios.

Fast Fourier Transforms (FFT)

Moulinec and Suquet (1998) have proposed an algorithm based on Fast Fourier Transforms (FFT) that computes the local fields in composites. The algorithm consists of discretizing the microstructures into voxels and solving, in each voxel, the constitutive law in Fourier space. The constitutive law is iteratively solved until the stress and strain fields converge within a prescribed tolerance. The main advantage of this technique is that it does not require meshing, and therefore has the potential to be completely automated. However, the FFT-based technique requires a uniform discrectization of the microstructure into equal size voxels. Therefore, the number of voxels required to adequately represent microstructures with high aspect ratio and/or volume fraction of fibers could become very important. Moreover, this method converges slowly for high mechanical properties contrast between the matrix and reinforcements.

Eyre and Milton (1999) proposed an accelerated version of this algorithm by applying it to electrostatic problems. The main advantage of this new version is that it converges faster for high mechanical properties contrasts. However, the computational cost of an iteration in the accelerated scheme is important when compared to that of the basic scheme. This is due to the fact that at each iteration, the FFT function is called three times in the accelerated scheme against twice in the basic scheme.

The common point in the previous algorithms lies in the fact that convergence is impossible for infinite mechanical properties contrasts between reinforcements and matrix (rigid inclusions, porous phases, etc.). In order to solve this issue, Michel *et al.* (2000, 2001) proposed a modification to the basic scheme by introducing a Lagrange multiplier. The authors applied their new algorithm to voided materials and to rigidly reinforced composites. Convergence was reached in both cases.

In order to optimize the computation time, Moulinec and Suquet (2003a) proposed the following:

⊙ For low mechanical properties contrasts, the basic scheme should be used;

⊙ For high contrasts, the accelerated scheme of Eyre and Milton should be used;

⊙ For infinite contrasts, the algorithm based on augmented Lagrangian should be used.

Effective properties of a single microstructure

Whatever the numerical method used to compute the local fields, the effective properties are derived from the volume averaged stresses and strains:

$$\mathbf{\Sigma} \;=\; <\boldsymbol{\sigma}(\boldsymbol{x})> \;=\; \widetilde{\mathbf{C}} :<\boldsymbol{\varepsilon}(\boldsymbol{x})> \;=\; \widetilde{\mathbf{C}} : \mathbf{E} \tag{1.26}$$

where $<\cdot>$ denotes an average over the volume, which is equivalent to an average over all elements (FEM) or voxels (FFT-based technique). Using the major and minor symmetry properties of elasticity tensors, Eq. (1.26) can be written in a matrix notation as:

$$\begin{bmatrix} \Sigma_{11} \\ \Sigma_{22} \\ \Sigma_{33} \\ \sqrt{2}\,\Sigma_{23} \\ \sqrt{2}\,\Sigma_{13} \\ \sqrt{2}\,\Sigma_{12} \end{bmatrix} = \begin{bmatrix} \widetilde{C}_{1111} & \widetilde{C}_{1122} & \widetilde{C}_{1133} & \sqrt{2}\widetilde{C}_{1123} & \sqrt{2}\widetilde{C}_{1113} & \sqrt{2}\widetilde{C}_{1112} \\ \widetilde{C}_{2211} & \widetilde{C}_{2222} & \widetilde{C}_{2233} & \sqrt{2}\widetilde{C}_{2223} & \sqrt{2}\widetilde{C}_{2213} & \sqrt{2}\widetilde{C}_{2212} \\ \widetilde{C}_{3311} & \widetilde{C}_{3322} & \widetilde{C}_{3333} & \sqrt{2}\widetilde{C}_{3323} & \sqrt{2}\widetilde{C}_{3313} & \sqrt{2}\widetilde{C}_{3312} \\ \sqrt{2}\widetilde{C}_{2311} & \sqrt{2}\widetilde{C}_{2322} & \sqrt{2}\widetilde{C}_{2333} & 2\widetilde{C}_{2323} & 2\widetilde{C}_{2313} & 2\widetilde{C}_{2312} \\ \sqrt{2}\widetilde{C}_{1311} & \sqrt{2}\widetilde{C}_{1322} & \sqrt{2}\widetilde{C}_{1333} & 2\widetilde{C}_{1323} & 2\widetilde{C}_{1313} & 2\widetilde{C}_{1312} \\ \sqrt{2}\widetilde{C}_{1211} & \sqrt{2}\widetilde{C}_{1222} & \sqrt{2}\widetilde{C}_{1233} & 2\widetilde{C}_{1223} & 2\widetilde{C}_{1213} & 2\widetilde{C}_{1212} \end{bmatrix} \begin{bmatrix} E_{11} \\ E_{22} \\ E_{33} \\ \sqrt{2}\,E_{23} \\ \sqrt{2}\,E_{13} \\ \sqrt{2}\,E_{12} \end{bmatrix} \tag{1.27}$$

The six columns of the effective elastic tensor can be computed by independently applying six orthogonal macroscopic deformation states $\mathbf{E}$ on the unit cell (e.g., three pure longitudinal and three pure shear deformations). For example, to calculate the first column, a deformation is applied in the first principal direction (E_{11}). The five other columns are determined similarly. Thus, six independent simulations are required to find the complete stiffness tensor.

For the case of randomly distributed and oriented ellipsoidal fibers reinforced composites, the effective medium is considered quasi-isotropic (Benveniste, 1987) and hence, is defined by two independent moduli: the effective bulk modulus $\widetilde{\kappa}$ and the effective shear modulus $\widetilde{\mu}$. These moduli can be computed from $\widetilde{\mathbf{C}}$ using the following relations:

$$\widetilde{\kappa} \;=\; \frac{\widetilde{C}_{mmnn}}{9} \tag{1.28a}$$

$$\widetilde{\mu} \;=\; \frac{3\widetilde{C}_{mnmn} - \widetilde{C}_{mmnn}}{30} \tag{1.28b}$$

Note that Eqs. (1.28) rely on the invariant components of $\widetilde{\mathbf{C}}$ (i.e., C_{mmnn} and C_{mnmn}).

Boundary conditions

Homogenization using FEM can be performed under any set of boundary conditions. Applying different boundary conditions on the same microstructure can yield different effective

properties. By choosing appropriate boundary conditions, one can compute more accurate estimations of the effective properties.

Uniform traction boundary conditions are given by (Huet, 1990):

$$\boldsymbol{\sigma}(\boldsymbol{x}) \cdot \boldsymbol{n} = \boldsymbol{\Sigma} \cdot \boldsymbol{n} \qquad \forall\, \boldsymbol{x} \in V^S \tag{1.29}$$

where V^S is the surface of the volume element and $\boldsymbol{n}$ is the normal vector at position $\boldsymbol{x}$ on V^S. Uniform displacement boundary conditions are such that (Huet, 1990):

$$\boldsymbol{u}(\boldsymbol{x}) = \mathbf{E} \cdot \boldsymbol{x} \qquad \forall\, \boldsymbol{x} \in V^S \tag{1.30}$$

where $\boldsymbol{u}(\boldsymbol{x})$ is the displacement vector.

Huet (1990) has shown that uniform traction boundary conditions underestimate the effective properties and more precisely lead to a lower bound, while uniform displacement boundary conditions overestimate the effective properties and lead to an upper bound.

On the other hand Gusev (1997) and Kanit *et al.* (2003) have shown that periodic boundary conditions deliver more accurate estimations of the effective properties for a smaller computational effort. Periodic boundary conditions can be applied on the microstructure by assuming the following relation (Michel *et al.*, 1999):

$$\boldsymbol{u}(\boldsymbol{x}) = \mathbf{E} \cdot \boldsymbol{x} + \boldsymbol{u}^*(\boldsymbol{x}) \tag{1.31}$$

where $\boldsymbol{u}^*(\boldsymbol{x})$ is a periodic fluctuation that takes the same value at a pair of homologous points located on opposite faces of the unit cell (i.e., two points that share two of their coordinates).

Periodic boundary conditions are an integral part of the FFT-based technique. However, applying periodic boundary conditions in the FEM is a more complex process. First, like in the FFT formulation, the unit cell must be periodic, i.e., a particle that intersects a face of the unit cell continues from the opposite face (see Figure 1.6a). Second, the meshing must also be periodic. A periodic mesh implies that exactly homologous nodes should be located at each two opposite faces. The periodic conditions could be then applied by coupling the displacement of each pair of homologous nodes (Bohm *et al.*, 2002; Barello and Lévesque, 2008):

$$\boldsymbol{u}(\boldsymbol{x}_2) - \boldsymbol{u}(\boldsymbol{x}_1) = \mathbf{E} : (\boldsymbol{x}_2 - \boldsymbol{x}_1) \tag{1.32}$$

where $\boldsymbol{x}_1$ and $\boldsymbol{x}_2$ denotes the coordinates of homologous nodes located on opposites faces. This can be achieved by applying Multi-Points Constraints (MPCs) on each pair of homologous nodes.

1.3.3 RVE determination

Numerous works dealt with the definition of RVE (Hill, 1963; Sab, 1992; Drugan and Willis, 1996; Gusev, 1997; Kanit *et al.*, 2003; Ostoja-Starzewski, 2006). The suggested definitions are based on the microstructure morphology and/or its physical behavior. The RVE definitions may be different depending on the application domain. Since the aim of homogenization is to compute accurate effective properties, the works as in those of Kanit *et al.* (2003); Kari *et al.* (2007a); Barello and Lévesque (2008); Moussaddy *et al.* (2013b); Pahlavanpour *et al.* (2013, 2014) have adopted the physical RVE definition in which a RVE is a volume element that computes the same target properties as the bulk material (Gusev, 1997).

In theory, a volume element is exactly representative of a random media when it contains an infinity of heterogeneities (Ostoja-Starzewski, 2002). For a finite volume, the RVE cannot be reached exactly but with a predefined error tolerance. Kanit *et al.* (2003) proposed a RVE definition which is not characterized by a single finite volume, but by an ensemble of r random finite volumes containing N heterogeneities each. As a first step, r random volume elements are generated and the target properties of each are computed. All generated volume elements have the same microstructural properties (i.e., constituents properties, inclusions volume fraction, inclusions aspect ratio, and number of represented heterogeneities). The required number of realizations r is determined using a criterion based on the confidence interval of the target properties (Kanit *et al.*, 2003):

$$\frac{\text{CI}\big[\bar{Z}\big]}{\bar{\bar{Z}}} \leq \epsilon_r \qquad (1.33)$$

where $\bar{Z}$ is the arithmetic mean of the target property Z over r realizations, $\text{CI}\big[\bar{Z}\big]$ is the width of the confidence interval of $\bar{Z}$ and ϵ_r is a predefined tolerance.

The procedure is then repeated for increasing numbers of heterogeneities (while keeping constant the other microstructural properties). Several criteria have been proposed to determine the required number of heterogeneities N to reach the RVE (Gusev, 1997; Ostoja-Starzewski, 1999; Terada *et al.*, 2000; Kanit *et al.*, 2003; Stroeven *et al.*, 2004; Ostoja-Starzewski, 2006; Trias *et al.*, 2006). The *stability criterion* is the most commonly used. It is based on the stability of the ensemble average of the target property over increments of N (Gusev, 1997):

$$\frac{\big|\bar{Z}^{(N_2)} - \bar{Z}^{(N_1)}\big|}{\bar{Z}^{(N_1)}} \leq \epsilon_N \qquad \text{with} \qquad N_2 > N_1 \qquad (1.34)$$

where $\bar{Z}^{(N_j)}$ refers to the arithmetic mean of the desired property Z for an ensemble of volume elements containing N_j heterogeneities each, while ϵ_N is a given tolerance.

The value of N for which this criterion is met depends on the applied boundary conditions.
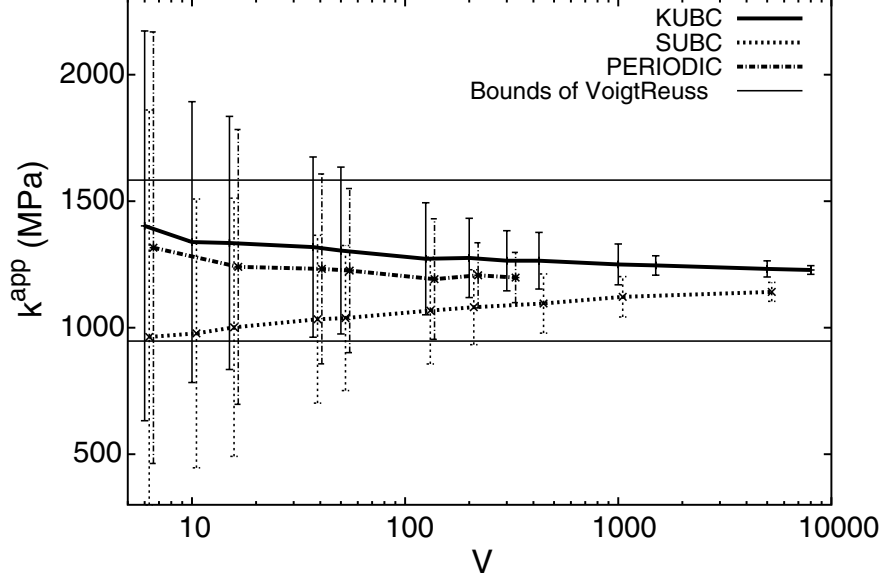
Figure 1.7 Effective bulk modulus of a voronoï microstructure as a function of the volume size V measured by the number of grains included. Three types of boundary conditions are considered: periodic (PERIODIC), uniform displacement (KUBC) and uniform traction (SUBC) boundary conditions. For clarity, the error bars are slightly shifted around each studied volume size V. (Kanit *et al.*, 2003).

Figure 1.7 shows the variation of the effective bulk modulus of a voronoï microstructure as a function of the volume size measured by the number of grains included (Kanit *et al.*, 2003). Three types of boundary conditions were studied: periodic, uniform displacement and uniform traction boundary conditions. It is observed that the convergence of effective properties was reached faster under periodic boundary conditions.

Moussaddy *et al.* (2013b) showed that the *stability criterion* does not provide accurate results when the fibers aspect ratio is higher than 30. The authors proposed another criterion to determine the required number of heterogeneities N: the *averaging variations criterion*. First, the arithmetic and the harmonic means of the target property Z over r realizations are computed:

$$\bar{Z} \;=\; \frac{1}{r} \sum_{k=1}^{r} Z_k \tag{1.35a}$$

$$\bar{\bar{Z}} \;=\; \left(\frac{1}{r} \sum_{k=1}^{r} \frac{1}{Z_k} \right)^{-1} \tag{1.35b}$$

where Z_k is the target property of the kth realization.

The average property is then computed by averaging both means:

$$\hat{Z} = \frac{\bar{Z} + \bar{\bar{Z}}}{2} \tag{1.36}$$

It is possible to demonstrate that:

$$\bar{\bar{Z}} \leq \hat{Z} \leq \bar{Z} \tag{1.37}$$

Equality in Eq. (1.37) is met only if all realizations lead to the same value of Z. The *averaging variations criterion* states that the difference between $\hat{Z}$ and any of $\bar{Z}$ and $\bar{\bar{Z}}$ must be within a given tolerance:

$$\max\left(\frac{|\hat{Z} - \bar{Z}|}{\hat{Z}}, \frac{|\hat{Z} - \bar{\bar{Z}}|}{\hat{Z}}\right) \leq \epsilon_N \tag{1.38}$$

1.4   Numerical works and validation of analytical models

Very few studies dealt with the validation of analytical homogenization models for the case of randomly distributed and oriented fibers reinforced composites. This section summarizes the different works that evaluate the accuracy of analytical models at predicting the effective mechanical properties, as well as the local field statistics.

1.4.1   Prediction of the effective mechanical properties

Spherical particles reinforced composites

Spherical particles reinforced composites are the most studied microstructures in the literature. Several authors have studied the case of isotropic elastic spheres randomly distributed in an isotropic elastic matrix and compared their numerical predictions against various analytical models estimates (Gusev, 1997; Llorca *et al.*, 2000; Segurado and Llorca, 2002; Pierard *et al.*, 2004; Marur, 2004; Segurado and LLorca, 2006; Sun *et al.*, 2007; Kari *et al.*, 2007b; Klusemann and Svendsen, 2010; Cojocaru and Karlsson, 2010). Others authors have investigated the case of isotropic elastic spherical particles distributed in an isotropic elastoplastic matrix (Bohm and Han, 2001; Han *et al.*, 2001; Bohm *et al.*, 2002). Barello and Lévesque (2008) have evaluated the accuracy of homogenization models for the case of linearly viscoelastic spherical particles reinforced composites with incompressible phases.

The common point in all these works is that only the effect of the particles volume fraction on the homogenization models accuracy has been studied. Most authors have varied the spheres volume fraction up to 60% and compared their numerical results to the analytical models predictions. No study has investigated the effect of the phases mechanical properties contrast on the analytical models performance. Indeed, the numerical simulations
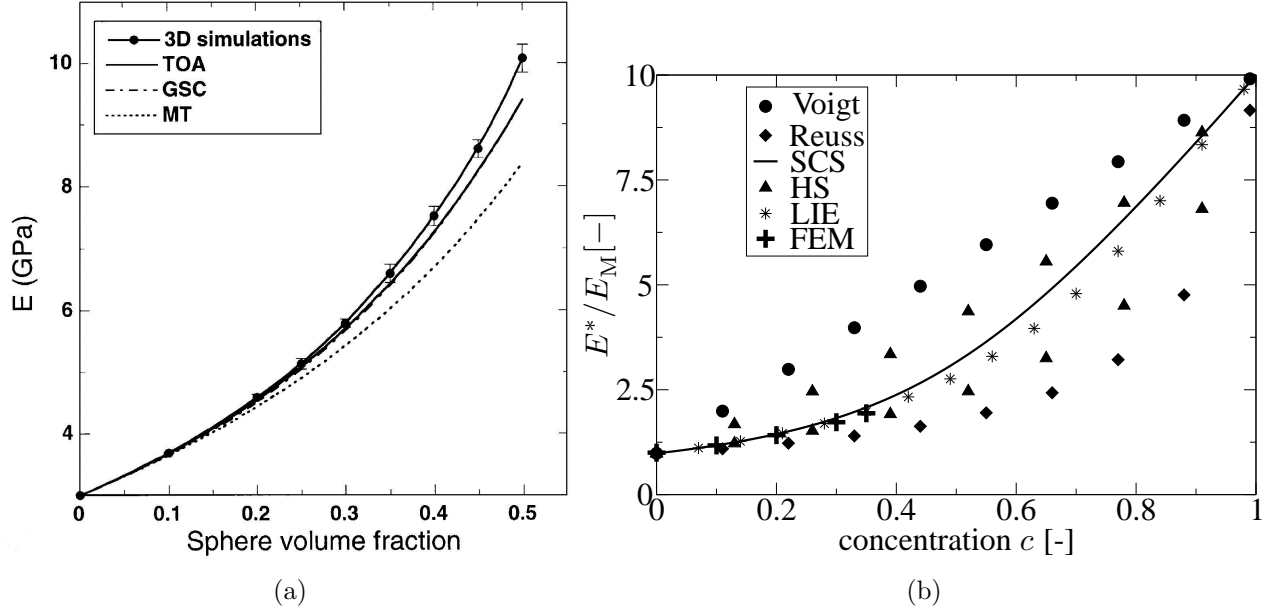
Figure 1.8 Effective Young's modulus of spherical particles reinforced composites for different inclusions volume fractions. (a) Comparison between the FEM results and the predictions of the Third Order Approximation (TOA), the generalized self-consistent model (GSC) and the Mori-Tanaka model (MT). Phases properties contrast: 23.(Segurado and Llorca, 2002). (b) Comparison between the FEM results and the Voigt-Reuss bounds, the Hashin-Shtrikman bounds (HS) and the predictions of the self-consistent scheme (SCS) and the Lielens' model (LIE). Phases properties contrast: 10.(Klusemann and Svendsen, 2010).

were performed for a fixed value of contrast (typically between 5 and 60), which does not allow to define rigorously a validity domain for each analytical model. Moreover, most studies have considered the same contrast for the bulk and shear moduli (i.e., $\kappa_2/\kappa_1 = \mu_2/\mu_1$), which leads to constituents with identical Poisson's ratio. This assumption has restricted the studied range of microstructures.

Figure 1.8 presents the results of two studies where the performance of analytical homogenization models at predicting the effective Young's modulus of spherical particles reinforced composites was evaluated (Segurado and Llorca, 2002; Klusemann and Svendsen, 2010). The authors compared their FEM results to the predictions of several analytical models for different spheres volume fractions.

The first study (Figure 1.8a) reveals that the predictions of the Third Order Approximation (TOA) and the generalized self-consistent model (GSC) were the most accurate. The authors concluded that Mori-Tanaka (MT) predictions were accurate only for volume fractions lower than 30%. The second study (Figure 1.8b) reveals that the Lielens' model delivered the most accurate estimates. However, since the numerical computations were lim-

ited to a volume fraction of 35%, it was not possible to generalize this statement for higher volume fractions.

Furthermore, the effect of the phases mechanical properties contrast on the analytical models accuracy was not deeply investigated. Indeed, the comparisons were performed for a fixed value of contrast (23 in the first study and 10 in the second). Different conclusions could be drawn for higher properties contrasts.

Fibers reinforced composites

No study rigorously and thoroughly dealt with the evaluation of analytical models accuracy for short fiber reinforced composites over a wide range of phases mechanical properties, fibers volume fractions and aspect ratios, in three dimensions. Tucker and Liang (1999) compared the predictions of a limited number of models against finite element simulations for aligned fibers reinforced composites. Other works have studied the case of Randomly Oriented Fiber Reinforced Composites (ROFRC) (Bohm *et al.*, 2002; Lusti and Gusev, 2004; Kari *et al.*, 2007a; Hua and Gu, 2013; Mortazavi *et al.*, 2013; Moussaddy, 2013). Some of these studies dealt with a very narrow range of fibers aspect ratio (≤ 5) (Bohm *et al.*, 2002; Hua and Gu, 2013). Others have limited their works to low reinforcements volume fractions ($\leq 3\%$), and eluded the rigorous evaluation of the RVE (Lusti and Gusev, 2004; Mortazavi *et al.*, 2013).

In their study on aligned short-fiber composites, Tucker and Liang (1999) found that Lielens' and Mori-Tanaka models provided the best predictions of effective properties. However, their numerical simulations did not allow to choose the most accurate model since they were limited to a volume fraction of 20% and a phases properties contrast of 30.

Bohm *et al.* (2002) compared their numerical results to the self-consistent scheme and Mori-Tanaka/Benveniste model for the case of a metal matrix reinforced by randomly oriented short fibers. They found a good agreement between the numerical and analytical predictions. Nevertheless, their analysis was performed on three random microstructures without determining rigorously the RVE.

Duschlbauer *et al.* (2006) studied the case of composites reinforced by planar random fibers. The authors showed that Mori-Tanaka/Benveniste model was adequate for predicting the thermoelastic properties of such composites, but it was the only investigated model. Furthermore, their work was limited to a volume fraction of 21%, an aspect ratio of 10 and a phases properties contrast less than 10.

In their work on microstructures with randomly dispersed short fibers, Kari *et al.* (2007a) found that the self-consistent model provided the best estimates of the effective properties. However, their simulations were performed with a phases properties contrast of 6.4, which

did not allow to deeply investigate the models performance.

Moussaddy (2013) found that Lielens' model was the best suited model to predict the effective bulk modulus of ROFRC for volume fractions over 5%. The author also showed that no model accurately predicted the effective shear moduli for volume fractions over 5%. However, his study was limited to the case where fibers were completely stiffer than the matrix (i.e., $\kappa_2 \geq \kappa_1$ and $\mu_2 \geq \mu_1$). The other cases were not investigated.

1.4.2 Prediction of the local field statistics

The capabilities of analytical homogenization models at predicting local field statistics have been studied by a limited number of authors. The approach typically consisted of computing local fields for specific microstructures submitted to specific load cases, computing scalar equivalent stresses/strains and compare them with those predicted by analytical models. For example, Moulinec and Suquet (2003b); Brenner and Masson (2005); Idiart and Castaneda (2007b); Rekik *et al.* (2007); Buryachenko (2011); Doghri *et al.* (2011); Corcolle *et al.* (2012); Lahellec and Suquet (2013) studied composites while Idiart *et al.* (2006); Idiart and Castaneda (2007b); Rekik *et al.* (2007); Idiart *et al.* (2009); Rekik *et al.* (2012) were interested in rigidly reinforced and porous composites. Other studies dealt with the computation of intragranular field fluctuations in polycrystals (Lebensohn *et al.*, 2004, 2005b,a, 2007; Castelnau *et al.*, 2006, 2008; Brenner *et al.*, 2009; Montagnat *et al.*, 2013).

However, all of the above-mentioned studies focused on very specific microstructures submitted to very specific load cases, which led to load dependent conclusions (see Appendix C for more details). Such approaches could provide erroneous observations and cannot, therefore, be used to draw general conclusions regarding the accuracy of analytical models at predicting local field statistics.

CHAPTER 2

OBJECTIVES AND RATIONALE

2.1 Rationale of the thesis

Based on the literature review, the rationale of this thesis can be explained as follow:

⊙ No rigorous and comprehensive study has evaluated the performance of exiting analytical homogenization models at predicting the effective mechanical properties of randomly distributed and oriented ellipsoidal fibers reinforced composites, for a wide range of phases mechanical properties, fibers volume fractions and aspect ratios.

⊙ In the few works that dealt with the evaluation of analytical models accuracy, only the effect of the fibers volume fraction and/or aspect ratio has been studied. No study has investigated the effect of the phases mechanical properties contrast on the homogenization models accuracy.

⊙ Numerical homogenization studies were limited to low volume fractions and/or aspect ratios due to the challenges related to the random generation process. Although the molecular dynamics algorithm proposed by Lubachevsky and Stillinger (1990) works well when generating packings of hard spherical particles, there is no computationally-efficient algorithm that can generate packings of hard ellipsoids at high volume fractions and aspect ratios. Indeed, the algorithm proposed by Donev *et al.* (2005a) has a high computational cost since the determination of binary collisions times relied on two optimization subproblems, which makes the algorithm less efficient. Developing a new computationally-efficient algorithm becomes then necessary to extend the range of achievable microstructures.

⊙ Most numerical studies were performed without conducting a rigorous RVE determination process due its computational burden. Published works deal with a limited number of volume elements without performing a statistical analysis to ensure that the RVE was achieved. It is therefore possible to question the validity of some published results.

⊙ No study has validated the analytical models performance at predicting local field statistics by using a load independent approach. In all studies, numerical field statistics were computed for microstructures submitted to specific load cases and compared to those predicted by analytical models. Statements and conclusions were

therefore load dependent, and the presented results cannot be used as a benchmark for evaluating the accuracy of analytical models at predicting the local field statistics.

2.2 Objectives of the thesis

The main objective of this thesis is to validate the accuracy of analytical homogenization models at predicting the effective mechanical properties and the local field statistics of randomly distributed and oriented ellipsoidal fibers reinforced composites. This main objective is divided into three specific objectives:

1) **Assessment of analytical models at predicting the effective properties of spherical particles reinforced composites**

   The objective is to find the most suitable analytical model to predict the effective properties of randomly distributed spherical particles reinforced composites, depending on the phases mechanical properties contrast and spheres volume fraction. A fully automated numerical tool was developed and the effective properties were accurately computed for a wide range of phases mechanical properties and particles volume fractions. The predictions of the numerical tool were compared to the analytical models estimates and a validity domain was attributed to each model.

2) **Assessment of analytical models at predicting the effective properties of ellipsoidal fibers reinforced composites**

   The objective is to study the performance of analytical homogenization models at predicting the effective properties of randomly distributed and oriented ellipsoidal fibers reinforced composites. First, a new computationally-efficient algorithm able to generate random packings of hard ellipsoids at high volume fractions and aspect ratios was developed. The algorithm was then integrated in the numerical tool developed previously and the effective properties of ellipsoidal fibers reinforced composites were computed for a wide range of phases mechanical and geometrical properties. Comparisons between numerical and analytical predictions quantified the effect of the phases mechanical properties contrast, the fibers volume fraction and the fibers aspect ratio on the analytical models accuracy.

3) **Assessment of analytical models at predicting the local field statistics of ellipsoidal fibers reinforced composites**

   The objective is to evaluate the accuracy of analytical models at predicting the local field statistics of randomly distributed and oriented ellipsoidal fibers reinforced composites (including spherical and ellipsoidal particles), and more specifically the intraphase first and second order moments. First, load independent properties di-

rectly related to the first and second order moments were defined. These load independent properties were then computed numerically for a wide range of phase mechanical properties contrasts, fibers volume fractions and aspect ratios. The numerical results were compared to the predictions of a range of analytical models and the most suitable model to predict the intraphase first and second order moments was identified.

CHAPTER 3

SCIENTIFIC APPROACH

Four research articles were prepared in order to achieve the objectives stated in Chapter 2. The following lines describes each article as well as its context with respect to the three specific objectives.

3.1 Article 1: A fully automated numerical tool for a comprehensive validation of homogenization models and its application to spherical particles reinforced composites

This paper presents a fully automated numerical tool for computing the accurate effective properties of two-phase linearly elastic composites reinforced by randomly distributed spherical particles. Virtual microstructures were randomly generated using an algorithm based on molecular dynamics. Composites effective properties were computed using a technique based on Fast Fourier Transforms (FFT). The predictions of the numerical tool were compared to those of analytical homogenization models for a broad range of phases mechanical properties contrasts and spheres volume fractions.

The main contributions and findings of this paper are:

⊙ A new fully automated numerical tool that can compute accurately the effective properties of randomly distributed spherical particles reinforced composites.

⊙ A database that contains the effective properties of 320 different spherical particles reinforced composites. In due course, this database might replace analytical homogenization models.

⊙ A rigorous assessment of several analytical homogenization models for the case of spherical particles reinforced composites.

⊙ None of the tested analytical models provides accurate estimates for the whole studied range of contrasts and volume fractions.

⊙ No analytical homogenization model stands out of the others as being more accurate over the investigated range of volume fractions and contrasts.

This article was published in the "International Journal of Solids and Structures", volume 49, issues 11–12, pages 1387–1398 in March 2012. This journal publishes research in the field

of the mechanics of solids and structures. This article was written almost entirely by the author of this thesis.

3.2 Article 2: Random generation of periodic hard ellipsoids based on molecular dynamics: a computationally-efficient algorithm

This paper presents a computationally-efficient algorithm for generating random periodic packings of hard ellipsoids. The algorithm is based on molecular dynamics where the ellipsoids are set in translational and rotational motion and their volumes gradually increase. Binary collision times are computed by simply finding the roots of a nonlinear function. In addition, an original and efficient method to compute the collision time between an ellipsoid and a cube face is proposed. The algorithm can generate all types of ellipsoids (prolate, oblate and scalene) with very high aspect ratios (i.e., > 10).

The main contributions and findings of this paper are:

⊙ The binary collision times are computed by simply finding the roots of a nonlinear function, which is a more efficient and simple technique than that presented by Donev *et al.* (2005a,b).

⊙ The paper puts more emphasis on periodic packings and presents a novel and efficient technique to compute the collision time between an ellipsoid and a cell face.

⊙ The necessary steps for processing the impact between two ellipsoids are well established and can be used for any types of ellipsoids (prolate, oblate, scalene).

⊙ It is the first time that ellipsoids packings with high aspect ratios (i.e., > 10) are presented in the literature.

⊙ The algorithm is comprehensive and well documented. Detailed pseudo-codes are given so the algorithm can be easily implemented by other researchers.

This article was published in the "Journal of Computational Physics", volume 253, pages 471–490 in July 2013. This journal treats the computational aspects of physical problems and presents techniques for the numerical solution of mathematical equations arising in all areas of physics. This article was written almost entirely by the author of this thesis.

3.3 Article 3: A comprehensive validation of analytical homogenization models: the case of ellipsoidal particles reinforced composites

This paper presents a rigorous and exhaustive evaluation of the analytical homogenization models accuracy for the case of randomly distributed and oriented ellipsoidal fibers reinforced

composites. Artificial random microstructures were generated using a molecular dynamics algorithm. Numerical effective properties were computed using a Fast Fourier Transforms (FFT) based technique. The numerical predictions were compared to those of the analytical models for a wide range of phases mechanical properties, fibers volume fractions and aspect ratios. The validation campaign involved a rigorous Representative Volume Element (RVE) determination process and approximately, 66000 simulations were performed.

The main contributions and findings of this paper are:

- ⊙ Similar results were obtained for prolate and oblate ellipsoidal fibers. In both cases, the analytical models show similar trends and have almost the same accuracy.

- ⊙ Contrasts between phases mechanical properties are the most influential parameters on the analytical models accuracy, followed by the fibers volume fraction.

- ⊙ In the investigated range of properties, Lielens' is the most accurate model provided that the ellipsoids are stiffer than the matrix.

- ⊙ For microstructures with high fibers aspect ratio, the Mori-Tanaka/Benveniste model could be an alternative to Lielens' model when predicting the effective shear modulus, especially when the fibers are not completely stiffer than the matrix (i.e., $\kappa_2 \leq \kappa_1$ and $\mu_2 \geq \mu_1$).

- ⊙ A new interpolation model has been developed and it can be seen as a substitute to analytical models.

This article was published in "Mechanics of Materials", volume 75, pages 135–150 in April 2014. This journal publishes research on general constitutive behavior of advanced technological and natural materials as well as on macroscopic predictions based on microscopic models. This article was written almost entirely by the author of this thesis.

3.4 Article 4: Homogenization models for predicting local field statistics in ellipsoidal fibers reinforced composites: Comparisons and validations

This paper validates the performance of analytical homogenization models at predicting the local field statistics in randomly distributed and oriented ellipsoidal fibers reinforced composites. The numerical validation was based on a newly introduced load independent metric, which allowed to formulate general conclusions. A large validation campaign was conducted and the Representative Volume Element (RVE) was rigorously determined for each combination of phases mechanical properties, fibers volume fraction and aspect ratio. The load independent properties computed numerically were compared to those predicted by a range of analytical models.

The main contributions and findings of this paper are:

- ⊙ The accuracy of analytical homogenization models is more sensitive to the fibers volume fraction than to their aspect ratio when predicting the first and second order moments.

- ⊙ For low mechanical properties contrasts, Mori-Tanaka and Mori-Tanaka/Benveniste are the most suitable models to predict the first order moments as well as the intra-matrix second order moments. For high contrasts, Lielens' model provides the most accurate predictions.

- ⊙ Regarding the intra-fiber second order moments, the predictions of the self-consistent scheme are the most accurate in the investigated range of contrasts and volume fractions, provided that the fibers aspect ratio is low. For fibers with high aspect ratio, Lielens' model has the highest accuracy among the studied models.

- ⊙ A new interpolation model that delivers accurate estimates of the mean and covariance tensors of the intraphase stress fields.

This article was submitted to the "International Journal of Solids and Structures" on July 16, 2014. This journal publishes research in the field of the mechanics of solids and structures. This article was written almost entirely by the author of this thesis.

CHAPTER 4

ARTICLE 1: A FULLY AUTOMATED NUMERICAL TOOL FOR A COMPREHENSIVE VALIDATION OF HOMOGENIZATION MODELS AND ITS APPLICATION TO SPHERICAL PARTICLES REINFORCED COMPOSITES

4.1   Abstract

This paper presents a fully automated numerical tool for computing the accurate effective properties of two-phase linearly elastic composites reinforced by randomly distributed spherical particles. Virtual microstructures were randomly generated by an algorithm based on molecular dynamics. Composites effective properties were computed using a technique based on Fast Fourier Transforms (FFT). The predictions of the numerical tool were compared to those of analytical homogenization models for a broad range of phases mechanical properties contrasts and spheres volume fractions. It is found that none of the tested analytical models provides accurate estimates for the whole range of contrasts and volume fractions tested. Furthermore, no analytical homogenization models stands out of the others as being more accurate for the investigated range of volume fractions and contrasts. The new fully automated tool provides a unique means for computing, once and for all, the accurate properties of composites over a broad range of microstructures. In due course, the database generated with this tool might replace analytical homogenization models.

4.2   Introduction

Determination of composites' effective elastic properties is a classical solid mechanics problem. Homogenization models estimate or bound the mechanical properties of composites using information related to the properties of the constituent phases, their geometry and their spatial distribution. The bounds of Hashin and Shtrikman (1963) (HSB), the self-consistent scheme (SCS) (Budiansky, 1965; Hill, 1965), the Mori-Tanaka (MT) model (Mori and Tanaka, 1973; Benveniste, 2008), the general self-consistent scheme (GSCS) of Christensen and Lo (1979), the second-order estimates (2OE), the three-point bounds (3PB) and the third order approximation (TOA) proposed by Torquato (1991, 1998), the model of

Lielens *et al.* (1998), the effective self-consistent scheme (ESCS) and the interaction direct derivative (IDD) developed by Zheng and Du (2001), are some examples.

These models predictive capabilities have been evaluated numerically by numerous authors, for very specific and limited configurations (see Section 4.3.3). However, to the knowledge of the authors, no study focused on conducting a systematic and thorough evaluation of existing homogenization models' accuracy. As a result, the range of microstructures over which homogenization models deliver predictions of given accuracies is not rigorously defined. A comprehensive performance evaluation requires generating an important database of "accurate" effective properties. It is of considerable interest to develop a robust and fully automated procedure for generating this database in order to reduce user input.

The main objective of this paper is to present a fully automated numerical tool for validating the performance of analytical homogenization models for composites reinforced by randomly distributed spherical particles. The paper is organized as follows: Section 4.3 reviews the different methods for generating random microstructures and computing composites effective properties. Section 4.4 presents the algorithms implemented in this study for generating randomly distributed spherical particles microstructures. Section 4.5 presents the code used to calculate the effective properties. The methodology adopted to conduct the validation campaign is introduced in Section 4.6. A comprehensive validation of several homogenization models is carried out in Section 4.7. The predictions of these models are compared to the numerical predictions of the validation tool, followed by a discussion and analysis of the results.

Unless specified otherwise, the following convention has been adopted: scalars and vectors are respectively denoted by lower case letters (i.e. a, α) and boldfaced lower case latin letters (i.e. $\boldsymbol{a}$); second and fourth order tensors are respectively denoted by boldfaced lower case greek letters (i.e. $\boldsymbol{\alpha}$) and boldfaced upper case latin letters (i.e. $\mathbf{A}$).

4.3   Background

4.3.1   Generation of random microstructures

Most artificial microstructures found in the literature were generated using the Random Sequential Adsorption (RSA) algorithm (Rintoul and Torquato, 1997). In this algorithm, the position of the first reinforcement is randomly generated. The position of a second reinforcement is subsequently drawn. If both reinforcements are in contact, the second reinforcement position is redrawn until it does not interfere with the first. The process is repeated until the desired volume fraction and number of reinforcements are reached. Several authors have used this algorithm and had difficulties to reach high volume fractions ($> 30\%$). Some au-

thors (Segurado and Llorca, 2002; Kari *et al.*, 2007b; Barello and Lévesque, 2008) developed improved versions of the RSA algorithm to reach higher volume fractions, at the expense of an increased computational cost.

Lubachevsky and Stillinger (1990) proposed an algorithm based on molecular dynamics and they applied it for disks and spheres (Lubachevsky *et al.*, 1991). The basic ideas of their algorithm are as follows. All particles are initially created but they all have a null volume. The spherical particles are put in motion and their radius increases throughout the computation. The spheres can collide with each other or with the faces of the cell. The simulation ends when the desired volume fraction is reached. This algorithm can achieve high volume fractions, up to the theoretical dense packing, for a low computational cost.

4.3.2   Computation of composites effective properties.

Finite element method is the most commonly used numerical method for obtaining composites effective properties. The technique consists of meshing a Representative Volume Element (RVE) of the microstructure, imposing boundary conditions and solving for the stresses and strains. The effective properties are computed from the relation between the volume averaged stress and strain tensors. Although this method has been successfully used by many authors (see Table 4.1), it cannot be fully automated since the meshing operation usually requires user input.

Moulinec and Suquet (1998) have proposed an alternative method involving Fast Fourier Transforms (FFT). The method relies on the solution of Lippman-Schwinger equation (Kröner, 1972) in Fourier space. The solution of this equation determines the stress and strain fields in the composite. The effective properties are then computed as with the finite element method. An accelerated version of this algorithm was proposed by Eyre and Milton (1999). This technique has two main advantages. First, it does not require any meshing, and hence, has the potential to be automated. Second, it is much faster than the finite element method for linearly elastic problems (Michel *et al.*, 1999). In addition, the method imposes periodic boundary conditions, which allows it to efficiently converge towards the RVE (Kanit *et al.*, 2003).

If random microstructures are considered, the effective properties of different composites should be evaluated according to the rigorous procedure presented by Kanit *et al.* (2003). In this procedure, for given numbers of represented reinforcements, several microstructures are randomly generated and the effective properties are computed for each of them. The number of simulations is considered adequate when the effective properties are known within a given confidence interval, whose width is below a certain threshold. The process is repeated for an increasing number of reinforcements and the RVE is obtained when the average effective

properties converge.

4.3.3 Summary of existing works on the effective properties of spherical particles reinforced composites

Table 4.1 summarizes the various studies which dealt with effective properties computation for randomly distributed spherical particles reinforced composites using finite element method. Only the case of two-phase composites with perfect interphase and non-overlapping spheres was considered. For each case, the type of microstructure studied, the range of volume fractions and constituent phases mechanical properties contrasts are specified. The

Table 4.1 Summary of previous study dealing with the computation of randomly distributed spherical particles reinforced composites' effective properties

Author(s)	Microstructure studied	Volume fractions	Contrasts E_2/E_1	Analytical models
Gusev (1997).	Isotropic elastic matrix and spheres*	26.78%	23	Not available.
Llorca *et al.* (2000).	Isotropic elastic matrix and spheres*	up to 50%	4 & 60	MT, SCS, GSCS.
Bohm and Han (2001).	Isotropic elastic spheres in an isotropic elastoplastic matrix*	20%	6	HSB, 3PB, 2OE, MT, GSCS.
Han *et al.* (2001).	Isotropic elastic spheres in an isotropic elastoplastic matrix*	20%	6	HSB, 3PB, MT, SCS, GSCS.
Bohm *et al.* (2002).	Isotropic elastic spheres in an isotropic elastoplastic matrix*	15%	6	HSB, 3PB, MT, SCS, GSCS.
Segurado and Llorca (2002).	Isotropic elastic matrix and spheres	up to 50%	23 & ∞	MT, GSCS, TOA.
Pierard *et al.* (2004).	Isotropic elastic matrix and spheres*	15 to 52%	23	Voigt, Reuss, HSB, MT, Lielens.
Marur (2004).	Isotropic elastic matrix and spheres*	up to 40%	23	Three-phase model (TPM).
Segurado and LLorca (2006).	Isotropic elastic matrix and spheres*	15%	6	MT, SCS, TOA.
Sun *et al.* (2007).	Isotropic elastic matrix and spheres	10 to 60%	44	HSB, MT.
Kari *et al.* (2007b).	Isotropic elastic matrix and spheres	10 to 60%	6	HSB, 3PB, MT, SCS, GSCS, TOA.
Barello and Lévesque (2008).	Incompressible isotropic viscoelastic matrix and spheres	10 to 25%	10 & 100	MT, SCS, TOA.
Klusemann and Svendsen (2010).	Isotropic elastic matrix and spheres	up to 35%	up to 20 & ∞	Voigt, Reuss, HSB, MT, SCS, Lielens, ESCS, IDD.
Cojocaru and Karlsson (2010).	Isotropic elastic matrix and spheres	5 to 25%	6	HSB, SCS.

contrast is defined as $\frac{E_2}{E_1}$, where E is Young's modulus and subscripts 2 and 1 refer to the reinforcing and matrix phases, respectively. For clarity, the contrast values were rounded up to the unit. The symbol "*" in the field "*Microstructure studied*" means that the paper partially focused on determining the effective properties of composites reinforced by spherical particles. The models listed in the "*Analytical models*" column are those against which the authors compared their predictions.

Table 4.1 reveals that most authors studied the effect of the volume fraction on analytical homogenization models accuracy. Very few studies dealt with the effect of the mechanical properties contrast on homogenization models accuracy. In addition, all the authors considered constituents having very similar Poisson's ratios.

4.4   Random generation of periodic spherical particles

The algorithm for generating the random microstructures used in this study is inspired on that proposed by Lubachevsky and Stillinger (1990). The algorithm was implemented in MATLAB. A fixed number of particles having a null volume were created in a unitary cube at the beginning of the computation. A random velocity vector was also assigned to each particle. The spheres were then put in motion and their radius increase according to a growth rule. The goal of the algorithm was to compute the time at which either one of the following events occurred: collision between two spheres (Algorithm 4.2) or collision between one sphere and at least one of the cell faces (Algorithm 4.3). If two particles collided, their new respective velocity were computed using the kinetic energy principle (Algorithm 4.4). However, spheres hitting one of the cell faces were copied periodically on the opposite faces (4.5) in order to meet the periodicity requirement of Moulinec and Suquet' (1998) algorithm. The computation ended when the desired volume fraction was reached.

Algorithm 4.1 presents the main program that calls Algorithms 4.2 to 4.5 (see Appendix 4.A). In addition, the following paragraphs detail the various subroutines. Detailed descriptions are given, so that the code can be reproduced by other researchers. In the algorithm description, the following convention is adopted, unless otherwise specified: a symbol with an index represents a unique entity for each sphere (i.e., α_i). A symbol with a superscript represents an entity that changes from one calculation step to another (i.e., α^n).

4.4.1   Detection of binary collisions

The collision time t between two particles i and j satisfies the following equation:

$$\|\Delta \boldsymbol{r}^n + \Delta \boldsymbol{v}^n t\| = \left[(R_i^n + R_j^n) + (a_i + a_j)t \right] \tag{4.1}$$

where

$$\Delta \boldsymbol{r}^n = \boldsymbol{r}_i^n - \boldsymbol{r}_j^n \tag{4.2a}$$

$$\Delta \boldsymbol{v}^n = \boldsymbol{v}_i^n - \boldsymbol{v}_j^n \tag{4.2b}$$

Eq. (4.1) leads to a quadratic equation in t, of the form:

$$\alpha t^2 + 2\beta t + \gamma = 0 \tag{4.3}$$

where

$$\alpha = \|\Delta \boldsymbol{v}^n\|^2 - (a_i + a_j)^2 \tag{4.4a}$$

$$\beta = \Delta \boldsymbol{r}^n \cdot \Delta \boldsymbol{v}^n - (R_i^n + R_j^n)(a_i + a_j) \tag{4.4b}$$

$$\gamma = \|\Delta \boldsymbol{r}^n\|^2 - (R_i^n + R_j^n)^2 \tag{4.4c}$$

The various steps for determining the next collision time between two spheres are summarized in Algorithm 4.2.

4.4.2 Detection of collisions with the cube cell faces

Collision times must be computed between each sphere i and the cube faces that do not intersect i. The collision time between a sphere and a cell face is given by the following equation:

$$\tau_{ik} = \begin{cases} \left[R_i^n - r_i^n(k) \right] \left[v_i^n(k) - a_i \right]^{-1} & \text{for } k \in \{1, 2, 3\} \\[2ex] \left[L - r_i^n(k-3) - R_i^n \right] \left[v_i^n(k-3) + a_i \right]^{-1} & \text{for } k \in \{4, 5, 6\} \end{cases} \tag{4.5}$$

where $r_i^n(m)$ and $v_i^n(m)$ refers respectively to the mth term of vectors $\boldsymbol{r}_i^n$ and $\boldsymbol{v}_i^n$. Eq. (4.5) computes the collision time with faces located at $x_1 = 0$, $x_2 = 0$ and $x_3 = 0$ ($k = 1$, $k = 2$ and $k = 3$ respectively) and with faces located at $x_1 = L$, $x_2 = L$ and $x_3 = L$ ($k = 4$, $k = 5$ and $k = 6$ respectively). The steps required to compute the next collision time between a particle and a cubic cell face are outlined in Algorithm 4.3.

4.4.3 Post-collision particles velocities update

Figure 4.1 shows two colliding spheres. Their velocities before collision are divided into two components: one parallel and one perpendicular to the line connecting their centers. The
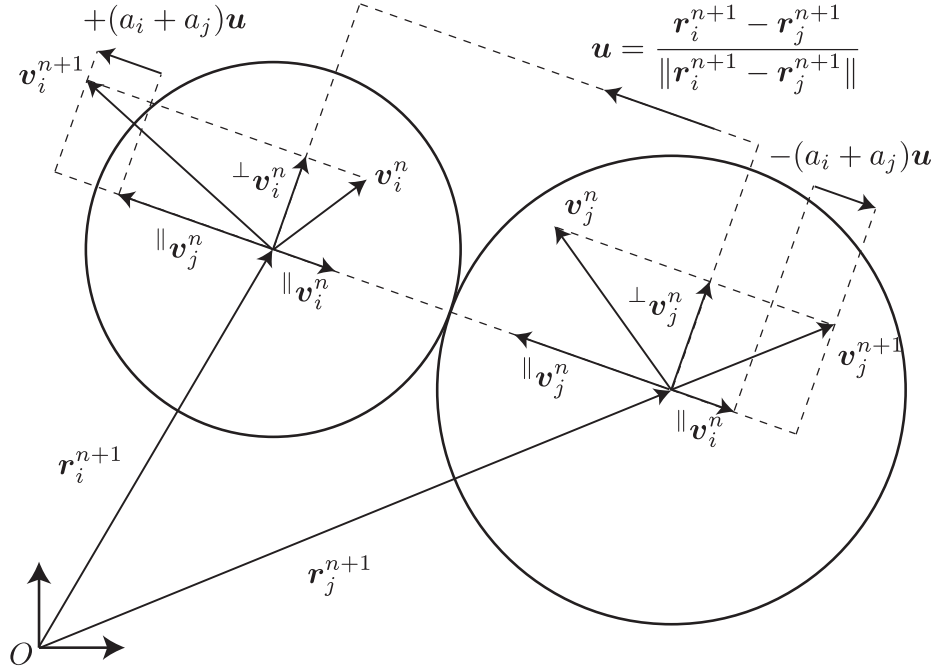
Figure 4.1 Two colliding spheres.

perpendicular components are preserved during the collision. The parallel components are interchanged while adding the effect of the radius growth rate. The spheres velocities after collision are computed by adding respectively the new parallel and perpendicular components. Details of the procedure are presented in Algorithm 4.4.

4.4.4 Creation of periodic particles following their collision with the cubic cell faces

When a sphere i collides with one or more cube faces, periodic spheres must be created on opposite sides. The number of periodic spheres created depends on the number of faces that intersect the sphere i. Each periodic particle has a position vector denoted by $^p\boldsymbol{r}_i^{n+1}$ and a velocity vector denoted by $^p\boldsymbol{v}_i^{n+1}$. Each periodic sphere has the same velocity as particle i but is offset from it by a vector $\boldsymbol{h}$. $\boldsymbol{h} = (a, b, c)$ where a, b and c can take the values of $\{0, L, -L\}$, depending on which face the periodic particle appears. More details are given in Algorithm 4.5.

4.4.5 Examples of random microstructures

For illustration purposes, assemblies of 100 spheres with a volume fraction of 50% were generated in less than 25 seconds using MATLAB 2011a on an Intel i7 Quad Core, 1.60 GHz,
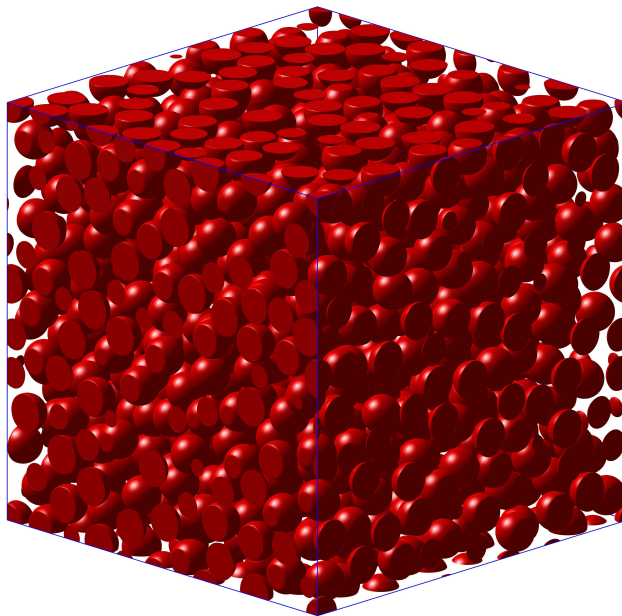
Figure 4.2 A packing of 1000 spherical particles randomly distributed in a periodic unit cell. Volume fraction = 40%. For presentation purposes, the parts of the spheres outside the cell were cut.

8 GB RAM. The algorithm also reached a volume fraction of 74% which approaches the theoretical maximum dense packing arrangement for spheres of identical size ($\frac{\pi}{3\sqrt{2}} \approx 74.05\%$). Figure 4.2 shows 1000 identical spherical particles randomly distributed in an elementary cube for a volume fraction of 40%.

4.5 Determination of composites effective properties with FFT

The effective properties properties were determined using the algorithm proposed in (Moulinec and Suquet, 1998; Michel *et al.*, 1999) and accelerated by the works of Eyre and Milton (1999). The following subsections present the outline of this algorithm.

4.5.1 Discretization of the microstructure

The microstructure was discretized into $N \times N \times N$ cubic voxels. Only the parts of the spheres inside the cell were considered. A material was assigned to each voxel. The rule of arbitration has been chosen as follows. Nine points uniformly distributed were considered in each voxel. If the majority of the points belonged to a sphere, then the entire voxel was assigned the mechanical properties of the spherical particles. Otherwise, the voxel had the properties of the matrix. Then, the volume fraction of voxels belonging to the spheres was computed. The discretization was adjusted until the volume fraction reached the microstruc-

(a)   (b)
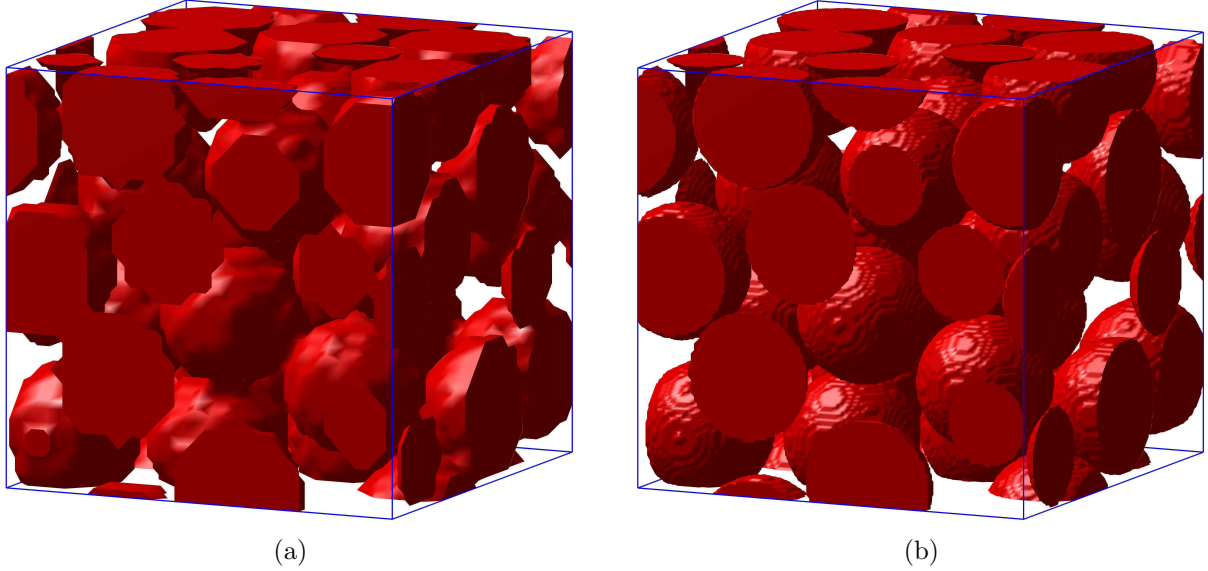
Figure 4.3 Discretization of an elementary volume containing 30 spherical reinforcements for a volume fraction of 50%. (a) $32 \times 32 \times 32$ voxels. (b) $128 \times 128 \times 128$ voxels.

ture's volume fraction, within a certain accuracy. Convergence in terms of voxels number is discussed in detail in Section 4.5.

Figure 4.3 shows an example of discretized microstructures with two different grids. In Figure 4.3a, the resolution is $32 \times 32 \times 32$ and the relative error on the volume fraction was 0.16%. However, in Figure 4.3b, a resolution of $128 \times 128 \times 128$ led to a relative error on volume fraction of $4.77 \times 10^{-4}\%$.

4.5.2   Calculation of effective properties

The main steps of the algorithm used for computing the effective properties of composites are presented here. Algorithm 4.6 lists the various operations implemented in this study. Specific information is given in the following paragraphs. For more details, consult (Moulinec and Suquet, 1998; Michel *et al.*, 1999; Eyre and Milton, 1999).

In this algorithm, $\boldsymbol{x}_d$ represents the coordinates of voxels in real space while $\boldsymbol{\xi}_d$ represents the wave numbers in Fourier space. The Fast Fourier Transforms and its inverse are respectively represented by $\mathcal{FFT}$ and $\mathcal{FFT}^{-1}$. Two types of errors were used to assess convergence: the equilibrium error (ϵ_{eq}) calculated in Fourier space and the compatibility error (ϵ_{comp}).

In the algorithm, $\mathbf{C}^0$ denotes the stiffness tensor of the reference material computed from κ^0 and μ^0 which represent respectively the bulk and shear modulus of the reference

material (see Moulinec and Suquet (1998) for more details). A Green operator was that for an isotropic elastic reference material and was given as in Fourier space (Mura, 1987):

$$\mathrm{G}^0_{ijkl}(\boldsymbol{\xi}) = \frac{1}{4\mu^0\|\boldsymbol{\xi}\|^2}\left(\delta_{ki}\xi_l\xi_j + \delta_{li}\xi_k\xi_j + \delta_{kj}\xi_l\xi_i + \delta_{lj}\xi_k\xi_i\right) - \frac{\lambda^0 + \mu^0}{\mu^0\left(\lambda^0 + 2\mu^0\right)}\frac{\xi_i\xi_j\xi_k\xi_l}{\|\boldsymbol{\xi}\|^4} \qquad (4.6)$$

where λ^0 is the Lamé modulus of the reference material and δ denotes Kronecker's delta.

Composites' homogenized properties were computed from the volume averaged stresses and strains. These two entities are related according the following equation:

$$< \boldsymbol{\sigma}(\boldsymbol{x}) > = \widetilde{\mathbf{C}} : < \boldsymbol{\varepsilon}(\boldsymbol{x}) > \qquad (4.7)$$

where $< \cdot >$ means an average over the volume and $\widetilde{\mathbf{C}}$ is the unknown effective tensor. For each realization, $\widetilde{\mathbf{C}}$ was not strictly isotropic because a finite number of spheres was simulated. Consequently, the effective bulk and shear modulus for each realization were obtained as follows:

$$\widetilde{\mu} = \frac{\widetilde{\mathrm{C}}_{1212} + \widetilde{\mathrm{C}}_{1313} + \widetilde{\mathrm{C}}_{2323}}{3} \qquad (4.8a)$$

$$\widetilde{\kappa}_i = \widetilde{\mathrm{C}}_{iiii} - \frac{4}{3}\widetilde{\mu} \qquad \text{for } i \in \{1, 2, 3\} \qquad (4.8b)$$

$$\widetilde{\kappa}_{1+i+j} = \widetilde{\mathrm{C}}_{iijj} + \frac{2}{3}\widetilde{\mu} \qquad \text{for } (i, j) \in \left\{(1, 2), (1, 3), (2, 3)\right\} \qquad (4.8c)$$

$$\widetilde{\kappa} = \frac{1}{6}\sum_{i=1}^{6}\widetilde{\kappa}_i \qquad (4.8d)$$

The algorithm' implementation was validated by comparing its predictions against those obtained by finite elements (not shown here). Identical results (within 0.9%) were obtained.

4.5.3 Parallelization of the algorithm

Effective properties were computed by imposing 6 orthogonally different displacement strain field (when expressed as per the modified Voigt notation). For example, the first column was determined by imposing a strain in the first principal direction (ε_{11}). The other five columns were computed in an equivalent manner. Thus, Algorithm 6 can be called six times independently, which renders its parallelization computationally-efficient. The computation time was divided by almost 6 when computations were performed on 6 independent workers.

Table 4.2 provides the approximate computation time as a function of the number of voxels, for $\mu_1 = \kappa_1 = 1$ and $\mu_2 = \kappa_2 = 10$. The microstructure contained 60 spheres with a

Table 4.2 Approximate computation time as a function of the number of voxels. $\mu_1 = \kappa_1 = 1$ and $\mu_2 = \kappa_2 = 10$. Number of spheres = 60. Volume fraction = 30%. Calculations were performed using MATLAB 2011a on an Intel(R) Xeon(R) Dual Core, 2.40 GHz, 48 GB RAM and parallelized on 6 local workers.

Voxels number	Computation time (seconds)		
	Discretization	Calculation of effective properties	Total
$32 \times 32 \times 32$	0.62	1.36	1.98
$64 \times 64 \times 64$	2.49	10.51	13.00
$128 \times 128 \times 128$	16.96	104.42	121.38

volume fraction of 30%. Calculations were performed using MATLAB 2011a on an Intel(R) Xeon(R) Dual Core, 2.40 GHz, 48 GB RAM and parallelized on 6 local workers.

4.6   Validation campaign

The accuracy of homogenization models was evaluated for composites made of an isotropic matrix reinforced with isotropic spherical particles. Four parameters were defined: $\rho_1 = \frac{\mu_2}{\mu_1}$, $\rho_2 = \frac{\kappa_1}{\mu_1}$, $\rho_3 = \frac{\kappa_2}{\mu_1}$ and ν_f. ρ_i represent the normalized contrast with respect to the matrix shear modulus and ν_f represent the spheres volume fraction. ρ_i took values of $\{1, 10, 100, 1000\}$ while ν_f took values of $\{0.1, 0.2, 0.3, 0.4, 0.5\}$. Effective properties were therefore obtained for 320 different materials. For each combination of these variables, three types of convergence were studied. First, the convergence of the stress and strain fields was checked for each realization. Second, statistical confidence intervals on the mean effective properties were computed for each given number of particles represented. For a fixed number of spheres, the number of realizations was increased until the width of the confidence interval was below a prescribed threshold. Third, the RVE was determined by increasing the number of spheres and by comparing the confidence intervals of the respective effective properties. Implementation of these three convergences are described in the following subsections.

4.6.1   Convergence of the stress/strain fields

A convergence analysis in terms of number of voxels was performed. A tolerance of 2% was used on the effective shear and bulk modulus as a criterion of convergence. Let N be the number of voxels along the cube side. N was initially set to $N = 32$ and doubled. If the results converged for $N = 64$, the simulation stopped. If convergence was not reached, N was increased to $N = 128$. For the tested range of contrasts and volume fraction, most cases converged with 128^3 voxels or less.
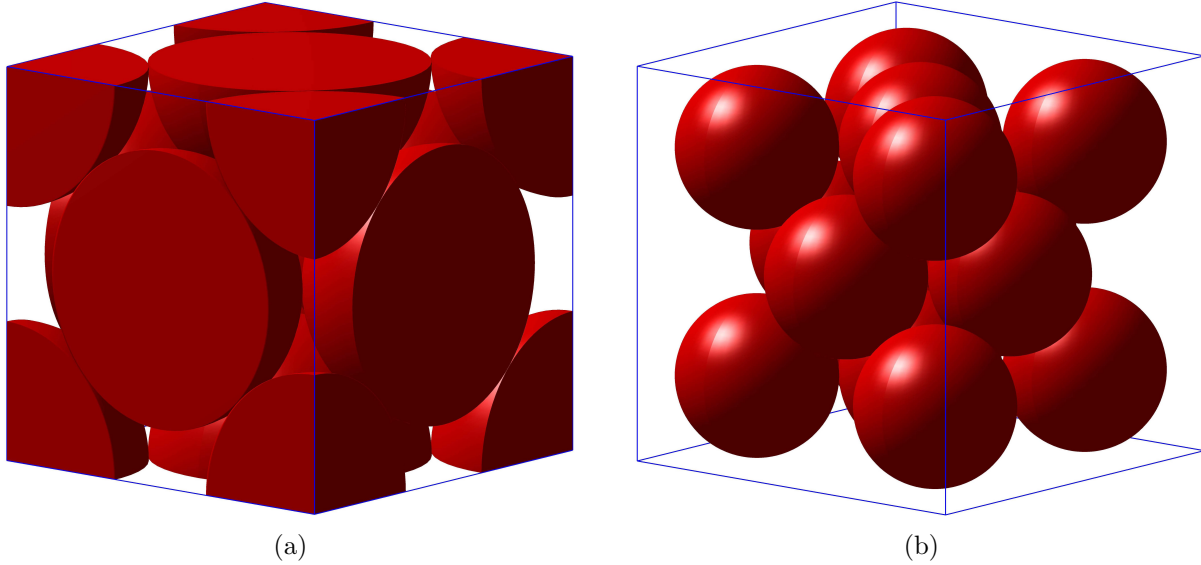
Figure 4.4 (a) Compact arrangement with a volume fraction of spheres equal to $\frac{\pi}{3\sqrt{2}}$ ($\approx$ 74.05%). (b) Compact arrangement diluted to 50% volume fraction of spheres.

However there were cases in which 128^3 voxels were not sufficient. It was therefore necessary to discretize the microstructure with 256^3 voxels. This discretization requires considerable computational resources. In order to avoid running calculations for such large models, the following approach was defined. For each combination of contrasts where convergence did not occur at 128^3 voxels, a convergence analysis was performed on a compact microstructure where $\nu_f = 50\%$. To obtain this microstructure, the most compact arrangement was considered with a volume fraction of spheres equal to $\frac{\pi}{3\sqrt{2}} \approx 0.74$ (see Figure 4.4a). Then, this arrangement was diluted into the matrix until the volume fraction of spheres reached 50%, as shown in Figure 4.4b. It was assumed that this type of microstructure was the worst case because the stress and strain fields present high gradients. Therefore, it was assumed that if convergence in terms of voxels was reached for this type of microstructure, it would also be reached for any other random microstructures with a spheres volume fraction lower than or equal to 50%, for the same values of ρ_i.

For the combinations of $\{\rho_i, \nu_f\}$ where convergence was not reached for 128^3 voxels, convergence was tested on the compact microstructure for $N = \{128, 160, 256\}$. If convergence occurred at $N = 160$, 160^3 voxels were used for the generated random microstructures. If convergence was reached at $N = 256$, microstructures were discretized in 256^3 voxels. For most cases, a discretization of 160^3 voxels was sufficient. Only 6 cases out of the 320 required 256^3 voxels to converge.

4.6.2 Effective properties convergence

The mechanical properties were computed using the methodology proposed by Kanit *et al.* (2003). For each number of spheres, the number of simulations n was considered sufficient if the following inequality was satisfied:

$$\max_{x=\widetilde{\kappa},\widetilde{\mu}} \frac{T^{n-1}_{(1-\alpha/2)} S_x}{\bar{x}\sqrt{n}} \leq 0.01 \tag{4.9}$$

where T is the quantile of the Student distribution with $(n-1)$ degrees of freedom, S is an estimate of the standard deviation of x and $(1-\alpha)$ is the desired confidence level. For this study, $1-\alpha = 0.95$. It should be noted that in each case, a minimum of six simulations were realized.

4.6.3 Convergence of the RVE

The procedure described in Section 4.6.2 was repeated for an increasing number of spheres. The RVE was defined as the number of represented spheres above which the effective property did not significantly change, in statistical terms, with the computed confidence intervals of Section 4.6.2. The final effective properties were those calculated for the RVE.
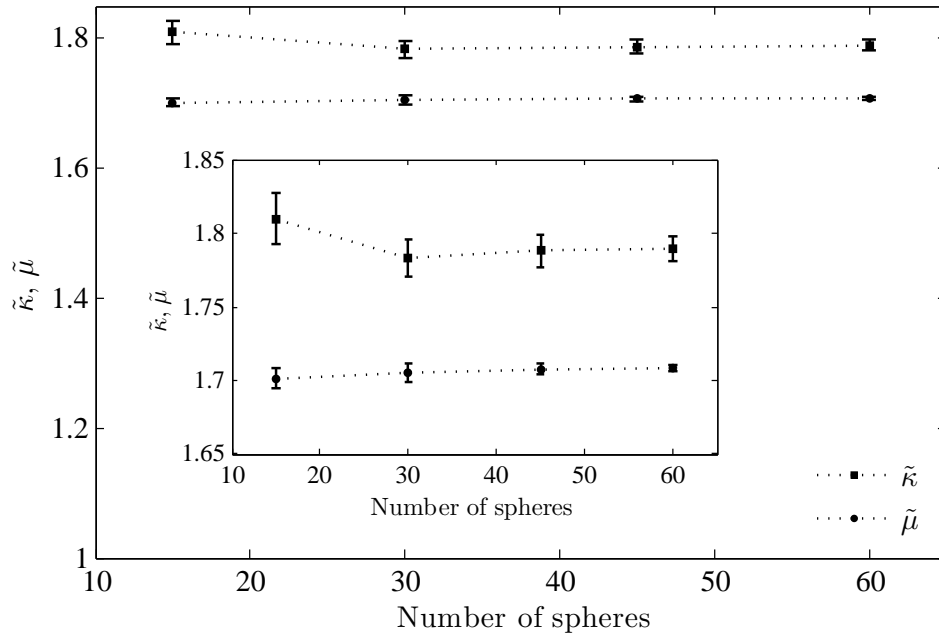
Figure 4.5 Effective properties as a function of the number of represented reinforcements (15, 30, 45 and 60 spheres). $\mu_1 = \kappa_1 = 1$, $\mu_2 = \kappa_2 = 10$ and $\nu_f = 0.3$. The error bars represent a 95% confidence interval on the mean value.

For illustration purposes, Figure 4.5 shows the mean effective moduli, along with their 95% confidence intervals, as a function of the number of represented reinforcements for a typical case ($\mu_1 = \kappa_1 = 1$, $\mu_2 = \kappa_2 = 10$ and $v_f = 0.3$).

4.7   Results and discussion

Properties $\widetilde{\kappa}$ and $\widetilde{\mu}$ computed with the numerical tool (NT) for several contrasts and volume fractions were compared to the predictions of several analytical homogenization models: Mori-Tanaka (MT), self-consistent scheme (SCS), general self consistent scheme(GSCS), Lielens and third order approximation (TOA). MATLAB built-in cubic spline interpolation was used to interpolate between the 320 generated data points. This interpolation was used in the following plots.

The results are shown for the case where the reinforcements are stiffer than the matrix ($\kappa_2 \geq \kappa_1$ and $\mu_2 \geq \mu_1$) and for the case where ($\kappa_2 \leq \kappa_1$ and $\mu_2 \geq \mu_1$). For each case, the shear modulus of the matrix was set to 1 and results are presented for volume fractions of 10%, 30% and 50% .

4.7.1   Spheres stiffer than the matrix ($\kappa_2 \geq \kappa_1$ and $\mu_2 \geq \mu_1$)

For this case, κ_1 was set to 1 and contrasts ρ_1 and ρ_3 were simultaneously varied from 1 to 1000. This led to constituents with constant Poisson's ratio.

For a volume fraction of 10% (Figure 4.6), predictions are satisfactory for all the studied models. For $\widetilde{\kappa}$, SCS and Lielens provide the most accurate predictions. For $\widetilde{\mu}$, SCS seems to be the most accurate model.

Figure 4.7 shows that the model predictions deviate from the accurate solution when the volume fraction of spheres is 30%, especially for high contrasts. In this area, MT, GSCS and TOA models underestimate the accurate solution while the SCS overestimates it. For low contrasts ($\rho_{1,3} \leq 70$ for $\widetilde{\kappa}$ and $\rho_{1,3} \leq 20$ for $\widetilde{\mu}$), TOA is the most accurate. However, for high contrasts ($\rho_{1,3} \geq 70$ for $\widetilde{\kappa}$ and $\rho_{1,3} \geq 20$ for $\widetilde{\mu}$), Lielens is the most accurate model.

The same behavior is observed when the volume fraction of spherical particles is 50% (Figure 4.8). However, the predictions of SCS diverge very rapidly when the contrasts ratios increase. SCS is not adequate for predicting the properties of such composites with high contrasts and volume fractions. For low contrasts ($\rho_{1,3} \leq 10$), all models lead to similar predictions while for high contrasts ($\rho_{1,3} \geq 70$ for $\widetilde{\kappa}$ and $\rho_{1,3} \geq 40$ for $\widetilde{\mu}$), it seems that Lielens delivers predictions having less discrepancy. It is interesting to note that all models except SCS predict a plateau when $\rho_{1,3} \geq 100$. This is not the case for the accurate solution.

4.7.2 Spheres stiffer than the matrix in terms of shear only ($\kappa_2 \leq \kappa_1$ and $\mu_2 \geq \mu_1$)

For this case, κ_2 was set to 1 and contrasts ρ_1 and ρ_2 were simultaneously varied from 1 to 1000. Therefore, the Poisson's ratios of the two phases are not identical and their difference increases with increasing contrast.

It is important to note that, for this specific case, the predictions of Lielens are not shown in the plots. Indeed, our implementation of Lielens model relies on an interpolation between the strain localization tensors used for computing Hashin and Shtrikman lower and upper bounds (see Eqs. (25) and (26) in (Lielens *et al.*, 1998)). When the matrix is more compliant than the reinforcements (i.e. when $\mu_1 \leq \mu_2$ and $\kappa_1 \leq \kappa_2$ simultaneously), the lower bound corresponds to the estimation of Mori-Tanaka. When the matrix is stiffer than the reinforcements (i.e. when $\mu_1 \geq \mu_2$ and $\kappa_1 \geq \kappa_2$ simultaneously), the upper bound corresponds to the Mori-Tanaka estimation. As a result, if the matrix is more compliant than the reinforcements, the Lielens estimation will always be stiffer than that of Mori-Tanaka and if the matrix is the stiffest part, the Lielens estimation will be more compliant than that of Mori-Tanaka. However, when the matrix is neither more compliant or stiffer than the reinforcements (i.e. when $\mu_1 \leq \mu_2$ and $\kappa_1 \geq \kappa_2$ or $\mu_1 \geq \mu_2$ and $\kappa_1 \leq \kappa_2$) Lielens model becomes inapplicable. For example, consider the case where $\mu_1 \leq \mu_2$ and $\kappa_1 \geq \kappa_2$. Consider further that the Mori-Tanaka estimation is computed with μ_m, μ_f, κ_m and κ_f where subscripts m and f refer to the matrix and fiber phases, respectively. Then, for this specific case, the upper Hashin-Shtrikman Bound (HSB) would be computed with the Mori-Tanaka estimation by setting $\mu_m = \mu_2$, $\mu_f = \mu_1$, $\kappa_m = \kappa_1$ and $\kappa_f = \kappa_2$ and the lower HSB would be computed with the Mori-Tanaka estimation be setting $\mu_m = \mu_1$, $\mu_f = \mu_2$, $\kappa_m = \kappa_2$ and $\kappa_f = \kappa_1$. The two HSB are computed for materials that do not really exist because they are a combination of both the matrix and reinforcement properties. Therefore, for the cases where the matrix is neither more compliant or stiffer than the reinforcements, Lielens model doest not make physical sense. As a result, for theses cases, the predictions of Lielens model were not compared with the accurate solution.

Figure 4.9 shows that for a volume fraction of 10%, all models are accurate. For high contrasts ($\rho_{1,2} \geq 70$ for $\widetilde{\kappa}$ and $\rho_{1,2} \geq 30$ for $\widetilde{\mu}$), most models deliver inaccurate predictions. In this area, MT, GSCS and TOA underestimate the effective properties. For this low volume fraction of spheres, SCS is the most accurate model. To better understand the difference in behavior between both plots in Figure 4.9, μ_2 was set to 10 and only ρ_2 was varied from 1 to 1000, as shown in Figure 4.10. For $\widetilde{\kappa}$, a behavior similar to that of Figure 4.9a was observed. $\widetilde{\mu}$ remained almost constant as a function of κ_1. $\widetilde{\mu}$ is therefore fairly insensitive to a variation of κ_1. The opposite behavior was observed when κ_1 was fixed instead of μ_2 (not shown here). Therefore, the shape shown in Figure 4.6a is typical of the case where $\kappa_2 \geq \kappa_1$ while that of

Figure 4.9a is typical of the case where $\kappa_2 \leq \kappa_1$. It should be noted that cases where $\mu_2 \leq \mu_1$ were not studied in this work and further works are needed to confirm that plots similar to that of Figure 4.9a would be obtained for these cases.

Similar behavior is observed in Figure 4.11 where the volume fraction of spheres is 30%. However, SCS is less accurate at this volume fraction than it was at 10%. For $\widetilde{\kappa}$, TOA is the most accurate model, while for $\widetilde{\mu}$, GSCS is the closest to the interpolation curve.

When the spheres and the matrix are in equal proportions (Figure 4.12), the predictions of SCS diverge rapidly from the interpolation curve. The behavior of this model is therefore similar to that shown in Figure 4.8. For low contrasts ($\rho_{1,2} \leq 30$ for $\widetilde{\kappa}$ and $\rho_{1,2} \leq 70$ for $\widetilde{\mu}$), TOA is the most accurate model for the two effective moduli. However, for high contrasts ($\rho_{1,2} \geq 70$), predictions of GSCS are the closest to the accurate effective shear modulus. For $\widetilde{\kappa}$, there is no model that accurately represents the accurate solution. Finally, it is important to note that the accurate effective properties do not reach a plateau in the investigated range of contrasts while all models (except SCS) predict a convergence of properties for $\rho_{1,2} \geq 500$.

4.7.3 Maximum relative error induced by each analytical model

Tables 4.3 and 4.4 present the maximum relative error made by each analytical model when predicting respectively $\widetilde{\kappa}$ and $\widetilde{\mu}$. This relative error ϵ was computed as:

$$\epsilon = \max_{i \in \{1,2,\ldots,320\}} \left| \frac{f_i^m - f_i^e}{f_i^e} \right| \tag{4.10}$$

where f refers to either $\widetilde{\kappa}$ or $\widetilde{\mu}$, superscripts m and e denote respectively the predictions of the analytical models and the numerical tool, while subscript i refers to one of the predictions

Table 4.3 Maximum relative error (ϵ) induced by each analytical model when predicting $\widetilde{\kappa}$ for 320 different combinations of contrasts ratios and spheres volume fractions (except for Lielens model where only 200 cases were considered). $[a, b, c]$ means that $\{\rho_1, \rho_2, \rho_3\} = \{10^a, 10^b, 10^c\}$.

| Models | Volume fractions | | | | | | | | | |
| | 10% | | 20% | | 30% | | 40% | | 50% | |
	ϵ	$[a, b, c]$	ϵ	$[a, b, c]$	ϵ	$[a, b, c]$	ϵ	$[a, b, c]$	ϵ	$[a, b, c]$
MT	17%	$[3, 3, 0]$	24%	$[3, 3, 0]$	31%	$[3, 3, 0]$	40%	$[3, 3, 0]$	52%	$[3, 3, 0]$
SCS	4%	$[1, 3, 0]$	18%	$[2, 3, 0]$	45%	$[2, 3, 0]$	97%	$[2, 3, 0]$	588%	$[3, 0, 3]$
GSCS	17%	$[3, 3, 0]$	24%	$[3, 3, 0]$	31%	$[3, 3, 0]$	40%	$[3, 3, 0]$	52%	$[3, 3, 0]$
Lielens	1%	$[3, 0, 3]$	5%	$[0, 0, 3]$	12%	$[0, 0, 3]$	23%	$[0, 0, 3]$	42%	$[0, 0, 3]$
TOA	15%	$[3, 3, 0]$	20%	$[3, 3, 0]$	26%	$[3, 3, 0]$	35%	$[3, 3, 0]$	47%	$[3, 3, 0]$

Table 4.4 Maximum relative error (ϵ) induced by each analytical model when predicting $\widetilde{\mu}$ for 320 different combinations of contrasts ratios and spheres volume fractions (except for Lielens model where only 200 cases were considered). $[a, b, c]$ means that $\{\rho_1, \rho_2, \rho_3\} = \{10^a, 10^b, 10^c\}$.

| Models | Volume fractions | | | | | | | | | |
| | 10% | | 20% | | 30% | | 40% | | 50% | |
	ϵ	$[a, b, c]$	ϵ	$[a, b, c]$	ϵ	$[a, b, c]$	ϵ	$[a, b, c]$	ϵ	$[a, b, c]$
MT	6%	$[3, 3, 3]$	17%	$[3, 3, 3]$	32%	$[3, 3, 3]$	53%	$[3, 3, 3]$	72%	$[3, 3, 3]$
SCS	2%	$[3, 3, 3]$	5%	$[2, 3, 1]$	29%	$[3, 3, 2]$	291%	$[3, 3, 3]$	930%	$[3, 3, 3]$
GSCS	5%	$[3, 3, 3]$	12%	$[3, 3, 3]$	19%	$[3, 2, 2]$	28%	$[3, 3, 3]$	45%	$[3, 0, 3]$
Lielens	8%	$[3, 3, 0]$	17%	$[3, 3, 0]$	25%	$[3, 3, 0]$	41%	$[3, 3, 3]$	60%	$[3, 3, 3]$
TOA	4%	$[3, 3, 3]$	11%	$[3, 3, 3]$	22%	$[3, 3, 3]$	41%	$[3, 3, 3]$	61%	$[3, 3, 3]$

among the 320 generated data points (except for Lielens model where only 200 cases were considered).

The relative errors are rounded to the unit. For each volume fraction, the combination of contrasts for which the maximum error was induced is specified. The tables show that the error made by each model increases with the volume fraction. In addition, errors are always induced for high contrasts.

When considering $\widetilde{\kappa}$, if $\epsilon < 10\%$ was defined as an acceptable threshold, only Lielens and SCS scheme for a volume fraction of 10% would meet the criteria for the whole ranges of specified contrasts. For a volume fraction of 20%, only Lielens meet the accuracy criteria. It is seen that Lielens leads to the lowest value of ϵ for all studied volume fractions. Thus, for predicting $\widetilde{\kappa}$, Lielens model is the most accurate model provided that the spheres are completely stiffer than the matrix.

As for $\widetilde{\mu}$, and for $\epsilon < 10\%$, all models meet the criteria when the volume fraction is 10%. This is not the case for a volume fraction of 20% where only SCS satisfies the accuracy criteria. In addition, it is shown that SCS leads to the lowest value of ϵ for volume fractions of 10% and 20%, while GSCS leads to the lowest ϵ for volume fractions of 30%, 40% and 50%.

This shows that no analytical homogenization model stands out of the others as being more accurate over the whole range of volume fractions and contrasts investigated.

4.7.4 Computations of validity domains for specific models

It is of considerable interest to identify the range of contrasts and volume fractions for which a given analytical homogenization model delivers predictions where ϵ is below a pre-

scribed threshold. For example, when $\kappa_1 = \mu_1 = 1$, Figure 4.13 shows the range of κ_2 and μ_2 for which $\epsilon \leq 0.1$, for both $\widetilde{\kappa}$ and $\widetilde{\mu}$ and for different volume fractions. It should be noted that for this very specific case, $\epsilon \leq 0.1$ for volume fractions of 10% and 20%, for the whole range of contrasts studied. For higher volume fractions, Figure 4.13 shows that the area covered by the range of validity decreases as the volume fraction increases.

Similarly, Figure 4.14 compares the range of validity of MT and TOA models for $\epsilon \leq 0.1$, for a volume fraction of 50% and for $\kappa_1 = \mu_1 = 1$. It can be seen that TOA outperforms MT in this specific case.

These simple analyses exemplify the usefulness of generating an important database of artificial composites. Similar comparisons could be generated for identifying the most suitable model under specific conditions.

4.8 Conclusion

The contributions of this study are as follows:

- ⊙ A fully automated numerical tool that can generate random microstructures constituted of randomly distributed spheres into a matrix and compute their mechanical effective properties.

- ⊙ Computation of the effective properties for 320 different spherical particles reinforced composites over a broad range of contrasts and volume fractions.

- ⊙ A rigorous validation of several analytical homogenization models for the case of spherical particles reinforced composites.

The interpolation algorithm is computationally-efficient and combining it with an expanding database will most likely lead to more accurate predictions than any other existing analytical homogenization model. In due course, this database could be an alternative to homogenization models for specific microstructures.

Generating the 320 data points presented in this paper required approximately 6 months of computations on an average of 3 multi-core computers. Indeed, around 16,800 different simulations were performed for accurately computing the 320 effective properties (taking into account all the convergence analysis performed). The authors seek collaborations with other researchers in order to expand their database. Ongoing works are dealing with the case of random ellipsoids. Other microsctructures could also be studied.

If many teams worldwide unite their efforts in a concerted manner, effective properties for a wide range of composites will be computed, once and for all. Such an intensive verification of analytical homogenization models could provide the required confidence levels for their widespread integration in high technology industry.

Acknowledgments

Appendix 4.A Algorithms pseudo-code

Algorithm 4.1 Main Program

1: Define a cube of side L oriented along $x_1-x_2-x_3$ axes. Set a corner as origin.

2: Define a number of spheres, noted by N and a desired volume fraction, noted by $\mathcal{V}^f$.

3: **for** each sphere i **do**

4:     Assign a random position vector $\boldsymbol{r}_i^0$.

5:     Assign a random velocity vector $\boldsymbol{v}_i^0$.

6:     Assign a radius $R_i^0 = 0$ and radius growth rate $a_i = 0.1$.

7: **end for**

8: Initialize time $t^0 = 0$ and actual volume fraction $\mathcal{V}^0 = 0$.

9: **while** $\mathcal{V}^n < \mathcal{V}^f$ **do**

10:     Compute t_c using Algorithm 4.2.

11:     Compute t_s using Algorithm 4.3.

12:     Compute $\Delta t^n = \min(t_c, t_s)$.

13:     Move all spheres to time $t^{n+1} = t^n + \Delta t^n$.

14:     **for** each particle i **do**

15:         Update the position: $\boldsymbol{r}_i^{n+1} = \boldsymbol{r}_i^n + \boldsymbol{v}_i^n \Delta t^n$.

16:         Update the radius: $R_i^{n+1} = R_i^n + a_i \Delta t^n$.

17:     **end for**

18:     **if** $\Delta t^n = t_c$ **then**

19:         Update the velocities of the concerned particles using Algorithm 4.4.

20:     **else if** $\Delta t^n = t_s$ **then**

21:         Create periodic image(s) of the concerned particle using Algorithm 4.5.

22:     **end if**

23:     Compute the new volume fraction: $\mathcal{V}^{n+1} = \frac{1}{L^3} \sum\limits_{i=1}^{N} \frac{4}{3}\pi (R_i^{n+1})^3$.

24: **end while**

25: Perform a scaling by reducing the spheres radii in order to reach $\mathcal{V}^{n+1} = \mathcal{V}^f$.

Algorithm 4.2 Detection of binary collisions

1: **for** each pair of particles i and j (including periodic images) **do**
2:     Compute $\Delta \boldsymbol{r}^n$ and $\Delta \boldsymbol{v}^n$ using Eqs. (4.2).
3:     Compute α, β and γ using Eqs. (4.4).
4:     **if** $(\beta \leq 0$ or $\alpha < 0)$ and $\beta^2 - \alpha\gamma \geq 0$ **then**
5:         $\tau_{ij} = \alpha^{-1}\left[-\beta - \sqrt{\beta^2 - \alpha\gamma}\right].$
6:     **else if** $(\beta > 0$ and $\alpha \geq 0)$ or $\beta^2 - \alpha\gamma < 0$ **then**
7:         No collision.
8:     **end if**
9: **end for**
10: Select the minimum time $t_c = \min(\tau_{ij})$.

Algorithm 4.3 Detection of collisions with the cube cell faces

1: **for** each particle i **do**
2:     **for** $k = 1 \rightarrow k = 6$ **do**
3:         **if** particle i does not intersect the kth face of the cube **then**
4:             Compute τ_{ik} using Eqs. (4.5).
5:         **end if**
6:     **end for**
7:     Keep only positive times.
8: **end for**
9: Select the minimum time $t_s = \min(\tau_{ik})$.

<div align="center">Algorithm 4.4 Post-collision particles velocities update</div>

1: Assume that i and j are the spheres that collided.

2: Compute unit vector: $\boldsymbol{u} = (\boldsymbol{r}_i^{n+1} - \boldsymbol{r}_j^{n+1}) \, / \, \|\boldsymbol{r}_i^{n+1} - \boldsymbol{r}_j^{n+1}\|$.

3: Decompose the velocity of each particle into two components: $(^{\|}\boldsymbol{v})$ and $(^{\perp}\boldsymbol{v})$.

4: $^{\|}\boldsymbol{v}_z^n = (\boldsymbol{v}_z^n \cdot \boldsymbol{u})\boldsymbol{u}$ and $^{\perp}\boldsymbol{v}_z^n = \boldsymbol{v}_z^n - {}^{\|}\boldsymbol{v}_z^n$ where $z = \{i, j\}$.

5: Compute the new velocity for each particle:

6: $\boldsymbol{v}_i^{n+1} = \left[{}^{\|}\boldsymbol{v}_j^n + (a_i + a_j)\boldsymbol{u} \right] + {}^{\perp}\boldsymbol{v}_i^n$.

7: $\boldsymbol{v}_j^{n+1} = \left[{}^{\|}\boldsymbol{v}_i^n - (a_i + a_j)\boldsymbol{u} \right] + {}^{\perp}\boldsymbol{v}_j^n$.

8: **if** particle i has P periodic images $(P \neq 0)$ **then**

9:     **for** $p = 1 \rightarrow p = P$ **do**

10:         $^{p}\boldsymbol{v}_i^{n+1} = \boldsymbol{v}_i^{n+1}$.

11:     **end for**

12: **end if**

13: **if** particle j has Q periodic images $(Q \neq 0)$ **then**

14:     **for** $q = 1 \rightarrow q = Q$ **do**

15:         $^{q}\boldsymbol{v}_j^{n+1} = \boldsymbol{v}_j^{n+1}$.

16:     **end for**

17: **end if**

Algorithm 4.5 Creation of periodic particles following their collision with the cubic cell faces

---

1: Suppose that particle i collided with m faces.

2: **if** $m = 1$ **then**

3:     $P = 1$.

4: **else if** $m = 2$ **then**

5:     $P = 3$.

6: **else if** $m = 3$ **then**

7:     $P = 7$.

8: **end if**

9: Create P periodic images of sphere i.

10: **for** $p = 1 \rightarrow p = P$ **do**

11:     $^{p}\boldsymbol{r}_i^{n+1} = \boldsymbol{r}_i^{n+1} + \boldsymbol{h}$.

12:     $^{p}\boldsymbol{v}_i^{n+1} = \boldsymbol{v}_i^{n+1}$.

13: **end for**

Algorithm 4.6 Computing the effective properties using FFT

1: Initialize the strain field $\boldsymbol{\varepsilon}^0(\boldsymbol{x}_d) = \boldsymbol{\psi}$, $\forall \boldsymbol{x}_d \in V$, where $\boldsymbol{\psi}$ denotes the average tensor of the periodic strain field to be imposed.

2: Compute $\kappa^0 = -\sqrt{\kappa_1 \kappa_2}$ and $\mu^0 = -\sqrt{\mu_1 \mu_2}$.

3: Compute $\mathbf{C}^0$ using κ^0 and μ^0.

4: Compute $\mathbf{G}^0$ using Eq. (4.6).

5: Let $\mathbf{C}(\boldsymbol{x}_d)$ be the stiffness tensor of a given voxel.

6: Initialize $\epsilon_{eq} = 1$ and $\epsilon_{comp} = 1$.

7: **while** $\max(\epsilon_{eq}, \epsilon_{comp}) > 10^{-4}$ **do**

8:     **if** $\epsilon_{comp} < 10^{-4}$ **then**

9:         $\boldsymbol{\sigma}^n(\boldsymbol{x}_d) = \mathbf{C}(\boldsymbol{x}_d) : \boldsymbol{\varepsilon}^n(\boldsymbol{x}_d)$.

10:         $\hat{\boldsymbol{\sigma}}^n = \mathcal{FFT}(\boldsymbol{\sigma}^n)$.

11:         Compute $\epsilon_{eq} = \|\hat{\boldsymbol{\sigma}}^n(\mathbf{0})\|^{-1} \sqrt{< \|\boldsymbol{\xi}_d \cdot \hat{\boldsymbol{\sigma}}^n(\boldsymbol{\xi}_d)\|^2 >}$ where $< \cdot >$ represents an average over all voxels.

12:     **end if**

13:     $\boldsymbol{\tau}^n(\boldsymbol{x}_d) = \big(\mathbf{C}(\boldsymbol{x_d}) + \mathbf{C}^0\big) : \boldsymbol{\varepsilon}^n(\boldsymbol{x}_d)$.

14:     $\hat{\boldsymbol{\tau}}^n = \mathcal{FFT}(\boldsymbol{\tau}^n)$.

15:     $\hat{\boldsymbol{\varepsilon}}^n_{comp}(\boldsymbol{\xi}_d) = \mathbf{G}^0(\boldsymbol{\xi}_d) : \hat{\boldsymbol{\tau}}^n(\boldsymbol{\xi}_d)$, $\forall \boldsymbol{\xi}_d \neq 0$ and $\hat{\boldsymbol{\varepsilon}}^n_{comp}(\mathbf{0}) = \boldsymbol{\psi}$.

16:     $\boldsymbol{\varepsilon}^n_{comp} = \mathcal{FFT}^{-1}(\hat{\boldsymbol{\varepsilon}}^n_{comp})$.

17:     Compute $\epsilon_{comp} = \|\boldsymbol{\psi}\|^{-1} \sqrt{< \|\boldsymbol{\varepsilon}^n(\boldsymbol{x}_d) - \boldsymbol{\varepsilon}^n_{comp}(\boldsymbol{x}_d)\|^2 >}$.

18:     $\boldsymbol{\varepsilon}^{n+1}(\boldsymbol{x}_d) = \boldsymbol{\varepsilon}^n(\boldsymbol{x}_d) - 2\big(\mathbf{C}(\boldsymbol{x}_d) - \mathbf{C}^0\big)^{-1} : \mathbf{C}^0 : \big(\boldsymbol{\varepsilon}^n_{comp}(\boldsymbol{x}_d) - \boldsymbol{\varepsilon}^n(\boldsymbol{x}_d)\big)$.

19: **end while**
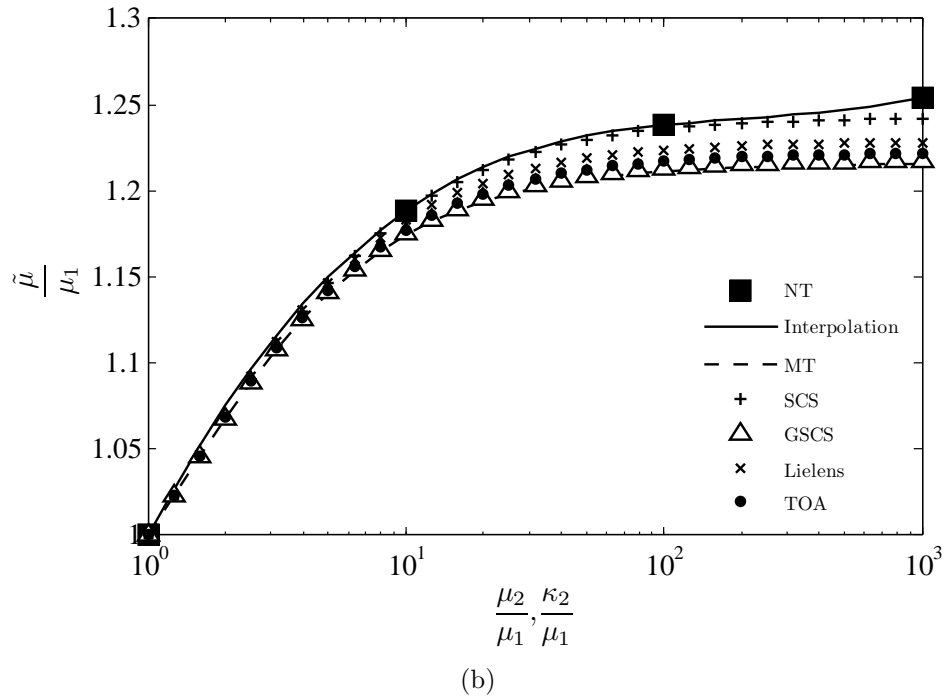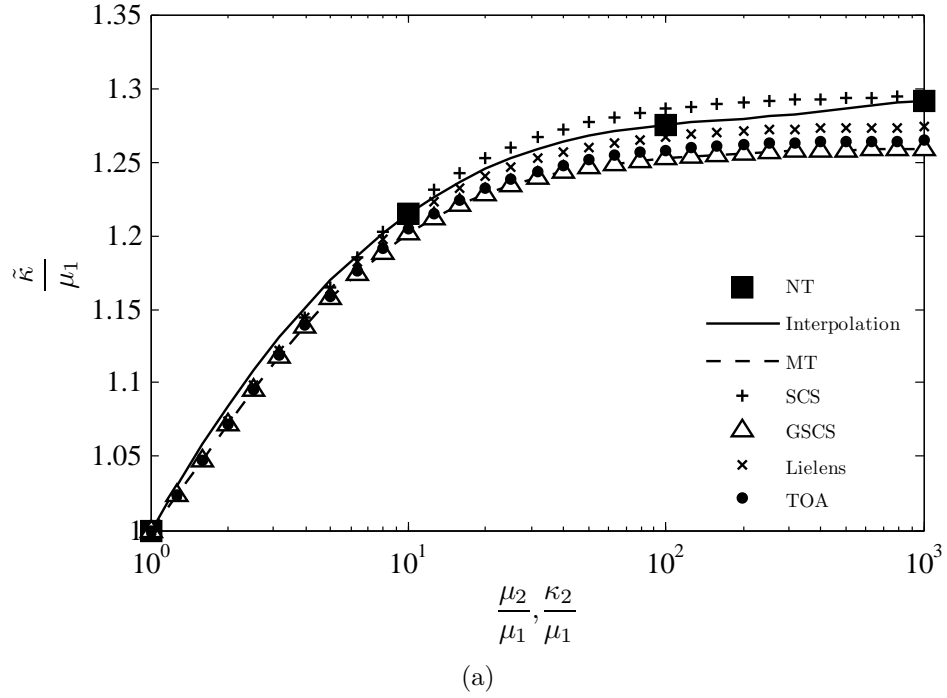
Figure 4.6 Comparison between the mechanical properties predicted with the numerical tool (NT) and those predicted by analytical models: Mori-Tanaka (MT), self-consistent scheme (SCS), general self-consistent scheme (GSCS), Lielens and third order approximation (TOA). The volume fraction of inclusions is 10%. $\mu_1 = \kappa_1 = 1$. (a) Normalized bulk modulus. (b) Normalized shear modulus.
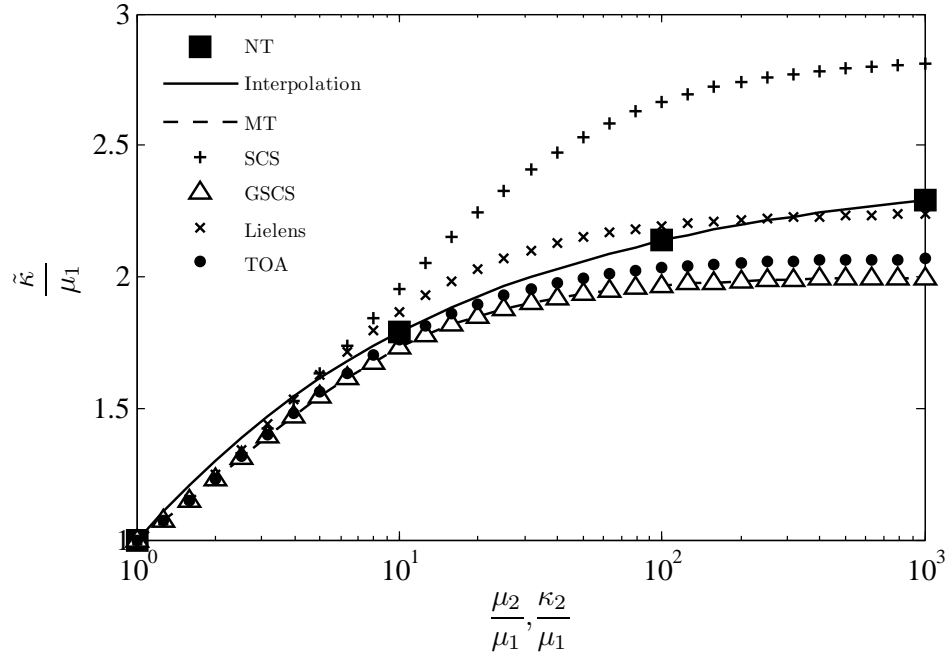
(a)
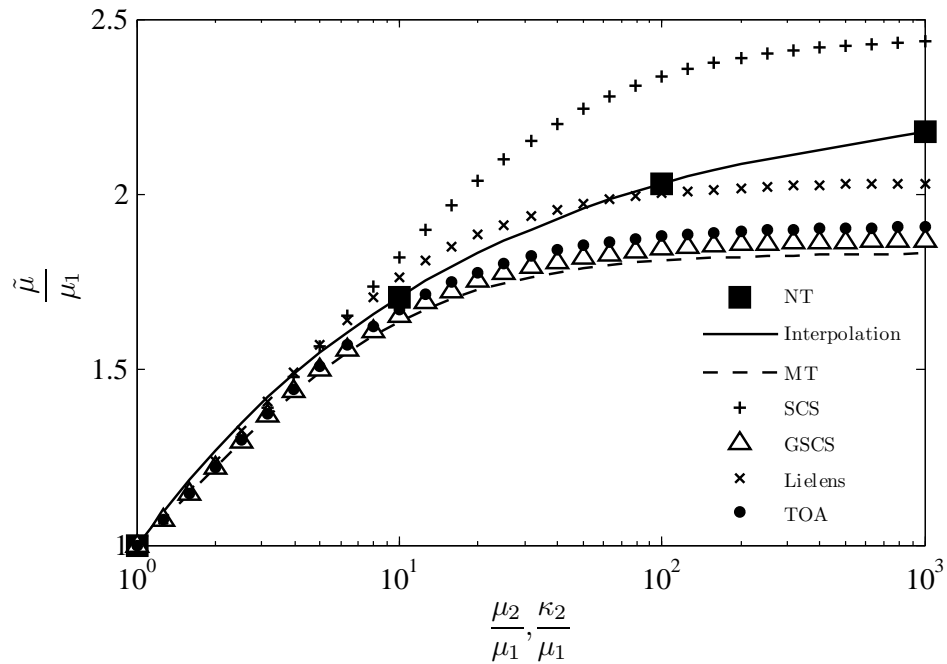
(b)

Figure 4.7 Comparison between the mechanical properties predicted with the numerical tool (NT) and those predicted by analytical models: Mori-Tanaka (MT), self-consistent scheme (SCS), general self-consistent scheme (GSCS), Lielens and third order approximation (TOA). The volume fraction of inclusions is 30%. $\mu_1 = \kappa_1 = 1$. (a) Normalized bulk modulus. (b) Normalized shear modulus.
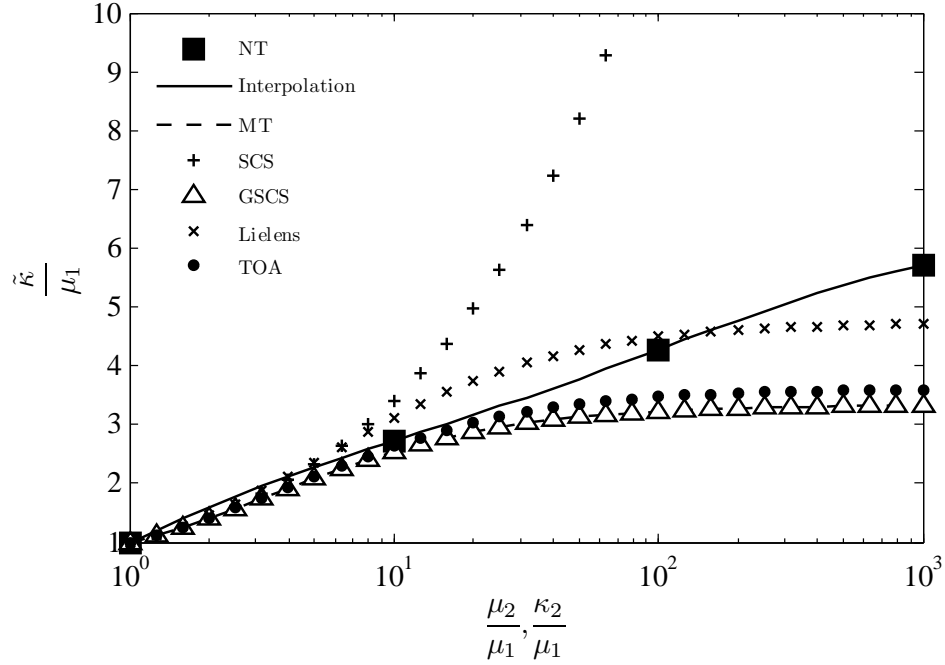
(a)
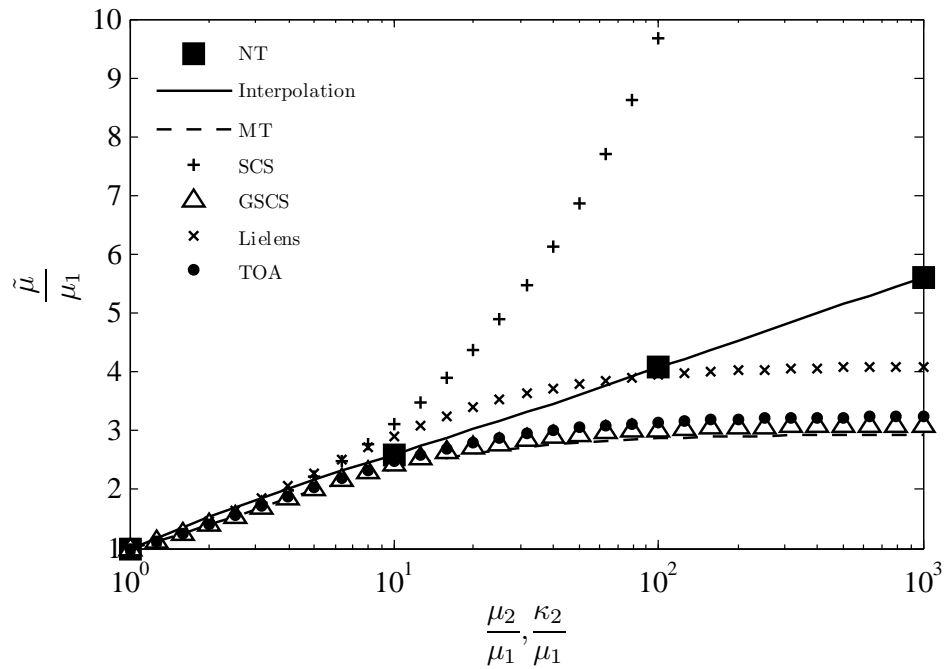
(b)

Figure 4.8 Comparison between the mechanical properties predicted with the numerical tool (NT) and those predicted by analytical models: Mori-Tanaka (MT), self-consistent scheme (SCS), general self-consistent scheme (GSCS), Lielens and third order approximation (TOA). The volume fraction of inclusions is 50%. $\mu_1 = \kappa_1 = 1$. (a) Normalized bulk modulus. (b) Normalized shear modulus.
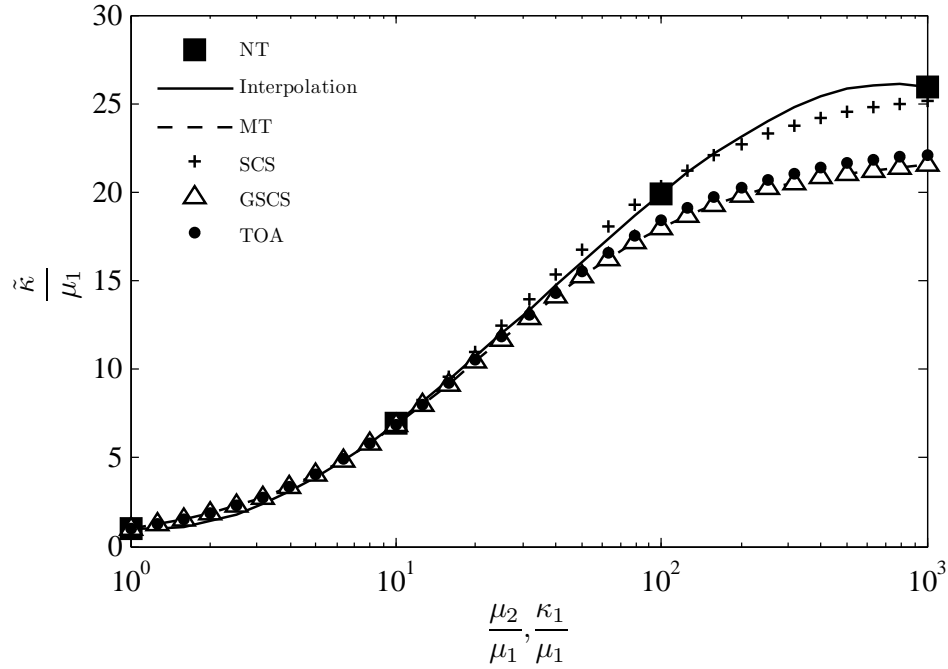
(a)
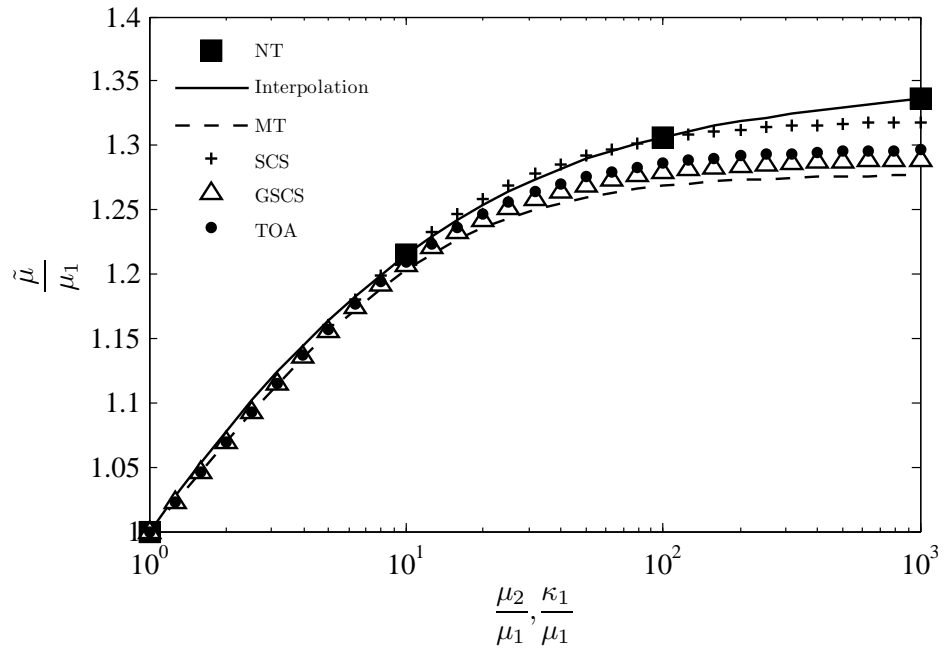
(b)

Figure 4.9 Comparison between the mechanical properties predicted with the numerical tool (NT) and those predicted by analytical models: Mori-Tanaka (MT), self-consistent scheme (SCS), general self-consistent scheme (GSCS) and third order approximation (TOA). The volume fraction of inclusions is 10%. $\mu_1 = \kappa_2 = 1$. (a) Normalized bulk modulus. (b) Normalized shear modulus.
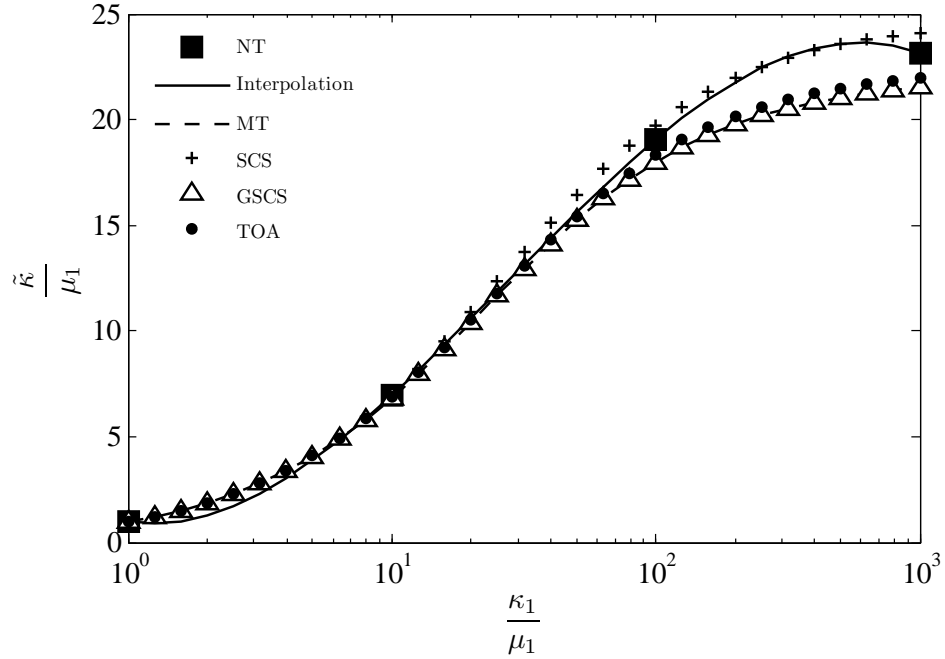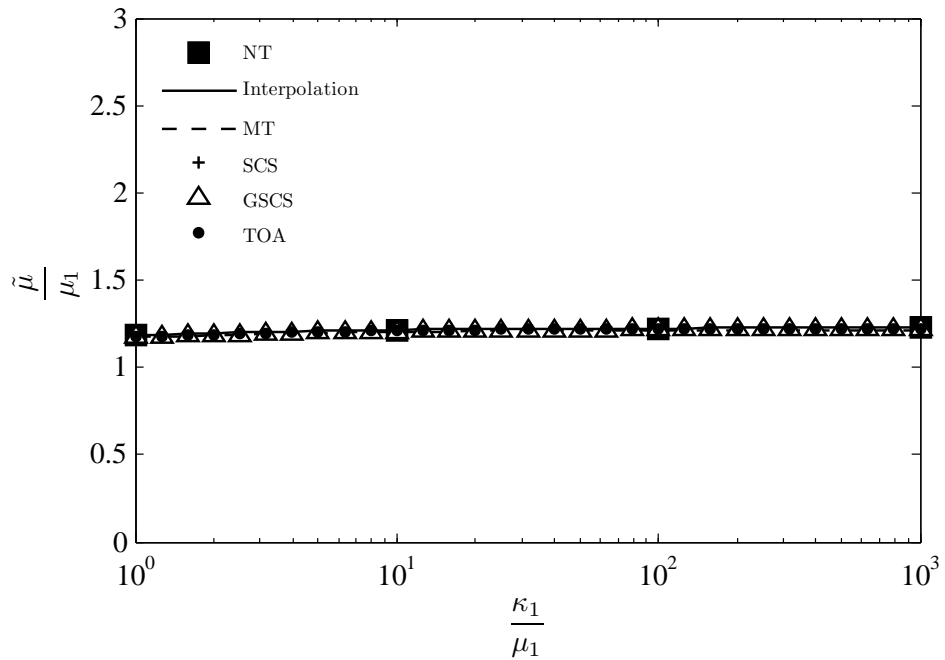
Figure 4.10 Comparison between the mechanical properties predicted with the numerical tool (NT) and those predicted by analytical models: Mori-Tanaka (MT), self-consistent scheme (SCS), general self-consistent scheme (GSCS) and third order approximation (TOA). The volume fraction of inclusions is 10%. $\mu_1 = \kappa_2 = 1$ and $\mu_2 = 10$. (a) Normalized bulk modulus. (b) Normalized shear modulus.
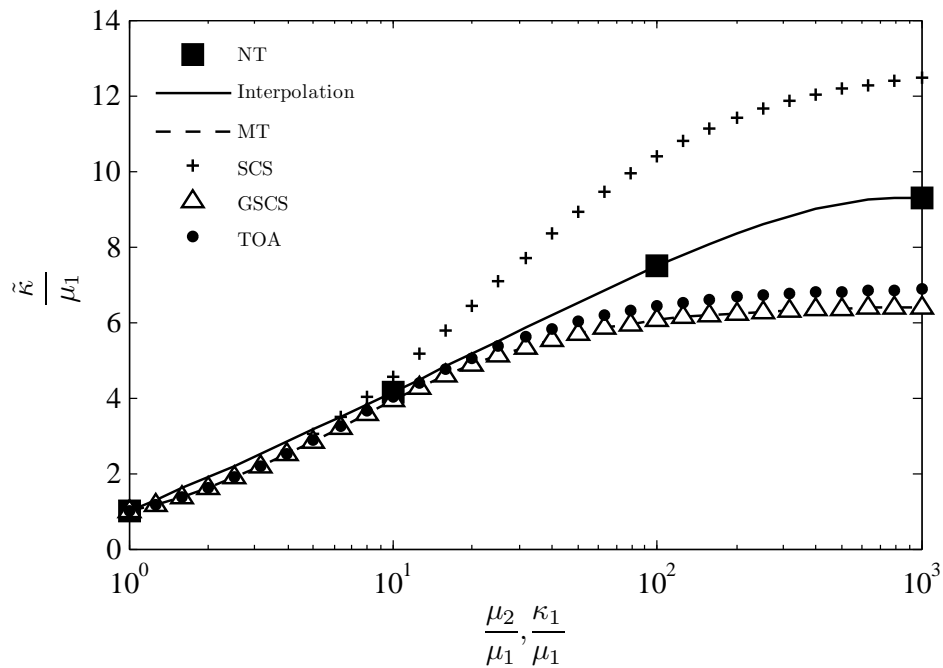
(a)
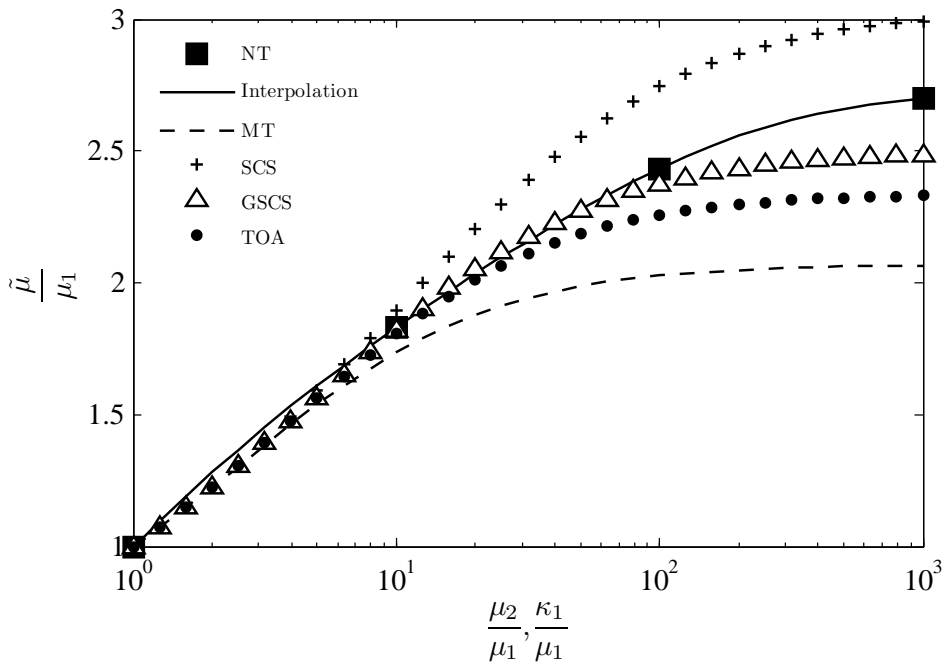
(b)

Figure 4.11 Comparison between the mechanical properties predicted with the numerical tool (NT) and those predicted by analytical models: Mori-Tanaka (MT), self-consistent scheme (SCS), general self-consistent scheme (GSCS) and third order approximation (TOA). The volume fraction of inclusions is 30%. $\mu_1 = \kappa_2 = 1$. (a) Normalized bulk modulus. (b) Normalized shear modulus.
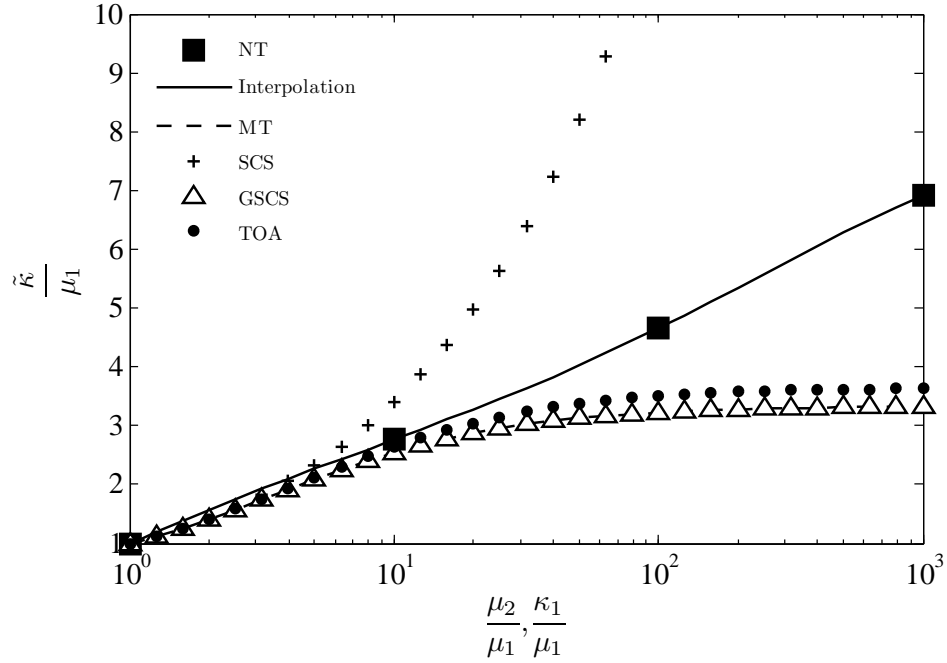
(a)
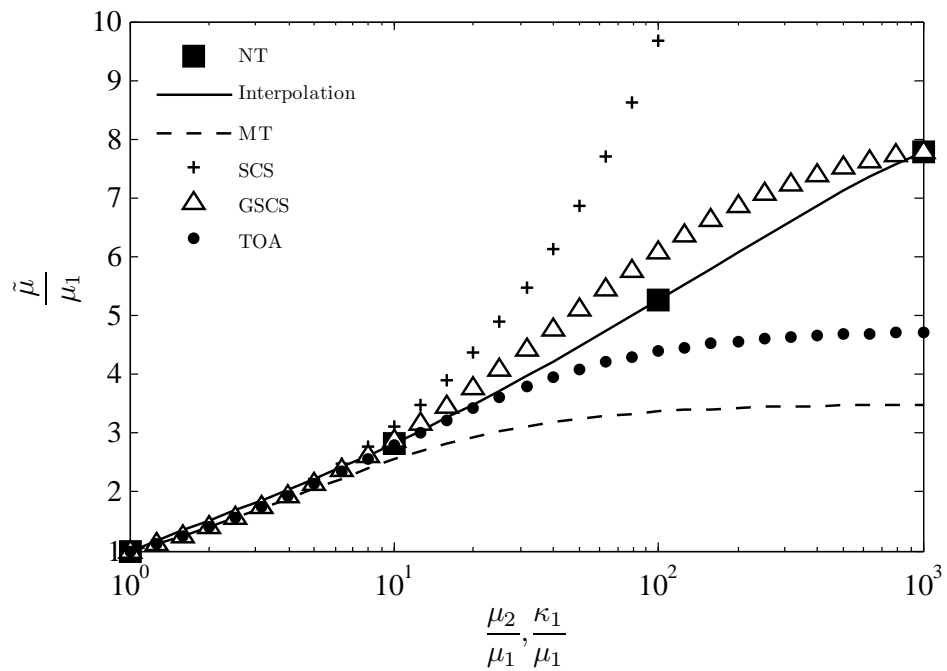
(b)

Figure 4.12 Comparison between the mechanical properties predicted with the numerical tool (N.T) and those predicted by analytical models: Mori-Tanaka (MT), self-consistent scheme (SCS), general self-consistent scheme (GSCS) and third order approximation (TOA). The volume fraction of inclusions is 50%. $\mu_1 = \kappa_2 = 1$. (a) Normalized bulk modulus. (b) Normalized shear modulus.
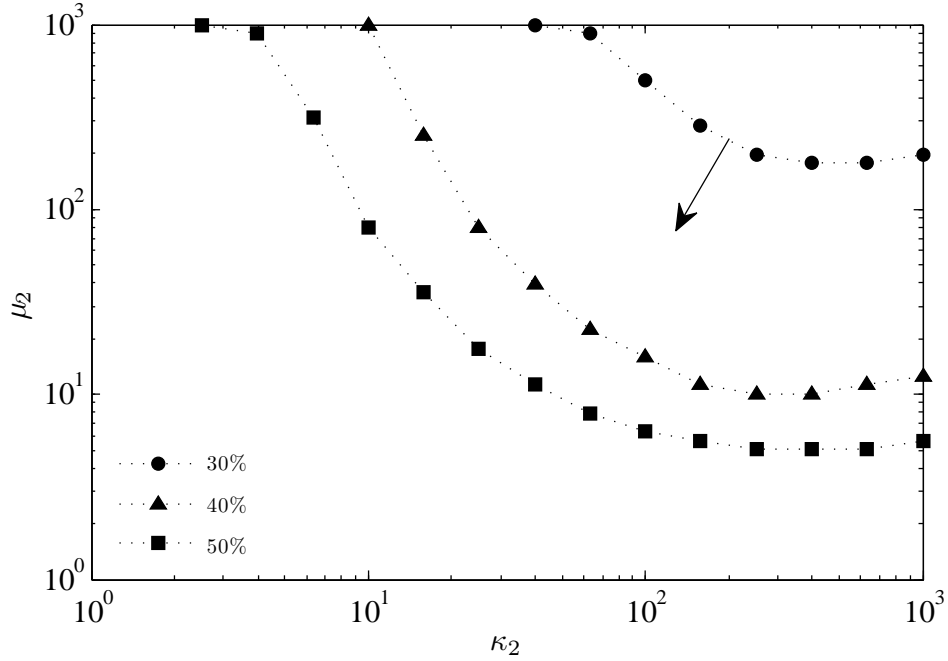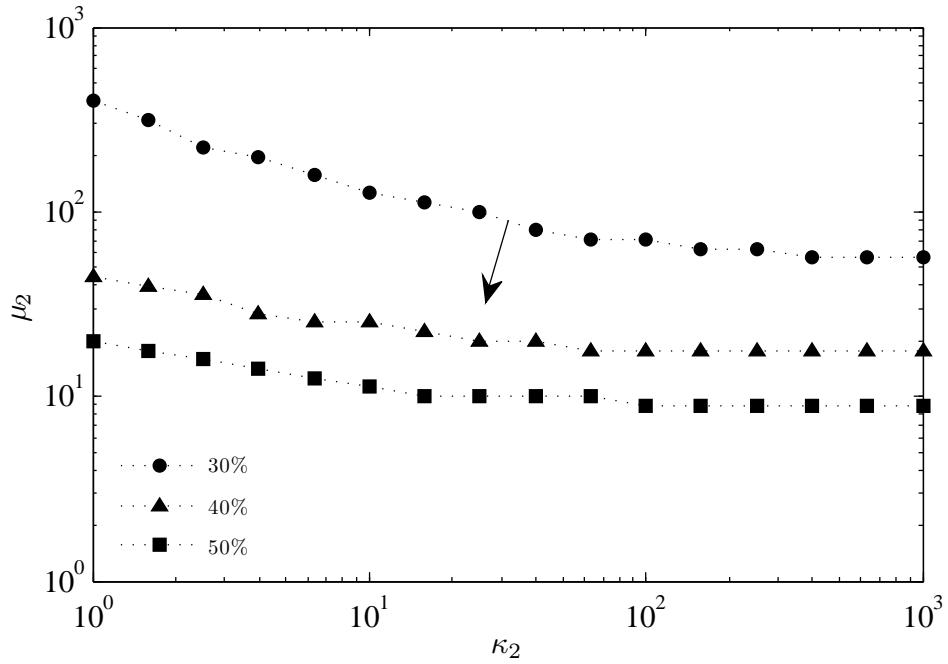
Figure 4.13 Mori-Tanaka (MT) range of validity for $\epsilon \leq 10\%$ and for $\kappa_1 = \mu_1 = 1$. The arrow indicates the validity domain. (a) Validity range on the effective bulk modulus. (b) Validity range on the effective shear modulus.
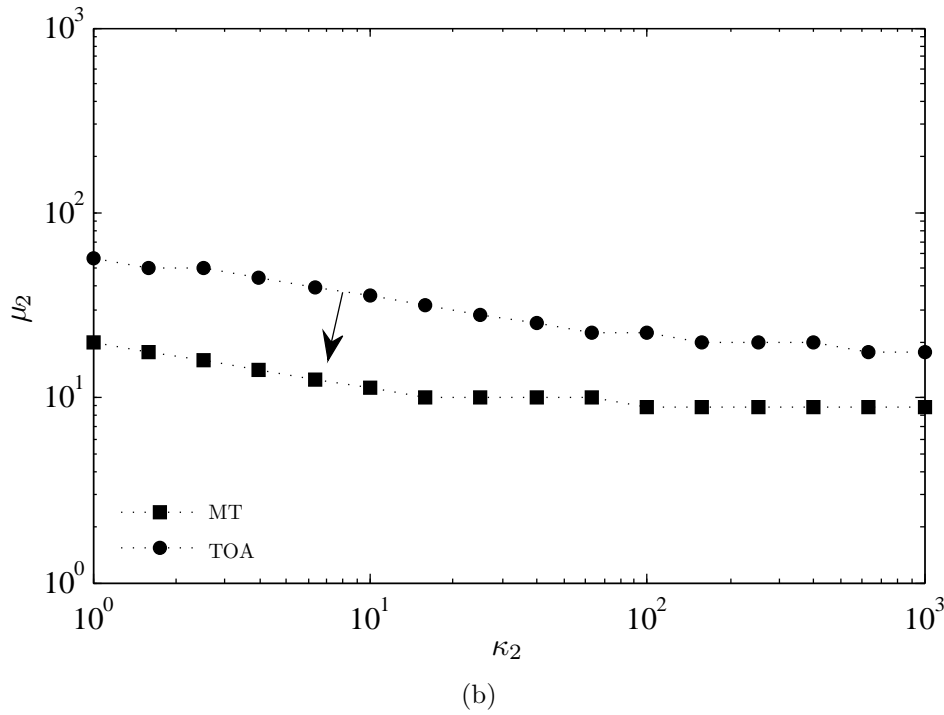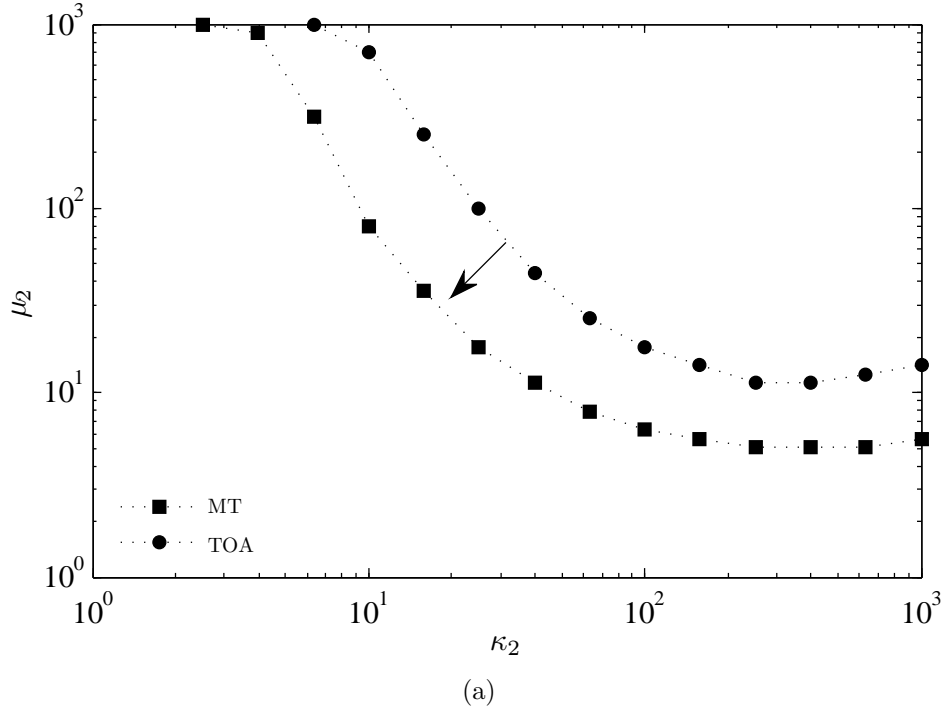
Figure 4.14 Range of validity of Mori-Tanaka (MT) and third order approximation (TOA) for $\epsilon \leq 10\%$, for a volume fraction of 50% and for $\kappa_1 = \mu_1 = 1$. The arrow indicates the validity domain. (a) Validity range on the effective bulk modulus. (b) Validity range on the effective shear modulus.

CHAPTER 5

ARTICLE 2: RANDOM GENERATION OF PERIODIC HARD ELLIPSOIDS BASED ON MOLECULAR DYNAMICS: A COMPUTATIONALLY-EFFICIENT ALGORITHM

5.1 Abstract

This paper presents a computationally-efficient algorithm for generating random periodic packings of hard ellipsoids. The algorithm is based on molecular dynamics where the ellipsoids are set in translational and rotational motion and their volumes gradually increase. Binary collision times are computed by simply finding the roots of a nonlinear function. In addition, an original and efficient method to compute the collision time between an ellipsoid and a cube face is proposed. The algorithm can generate all types of ellipsoids (prolate, oblate and scalene) with very high aspect ratios (i.e., > 10). It is the first time that such packings are reported in the literature. Orientations tensors were computed for the generated packings and it has been shown that ellipsoids had a uniform distribution of orientations. Moreover, it seems that for low aspect ratios (i.e., ≤ 10), the volume fraction is the most influential parameter on the algorithm CPU time. For higher aspect ratios, the influence of the latter becomes as important as the volume fraction. All necessary pseudo-codes are given so that the reader can easily implement the algorithm.

5.2 Introduction

Random packings are found in several physics and engineering fields. Several studies relied on random packings to simulate the behavior of molecular fluids (Gray *et al.*, 1984; Kolafa and Nezbeda, 1987). They are also widely used in numerical homogenization of random media (Torquato, 2002; Ghossein and Levesque, 2012) where periodic boundary conditions are usually imposed since they lead to smaller Representative Volume Elements (RVEs) (Kanit *et al.*, 2003). When the effective properties are computed from the finite element technique, the imposition of periodic boundary conditions requires the unit cell to be periodic. In this case, the random packings must also be periodic.

Several types of random packings were studied in the literature : hard spherical particles (Ghossein and Levesque, 2012; Segurado and Llorca, 2002; Barello and Lévesque, 2008), cylin-

ders (Iorga *et al.*, 2008; Redenbach and Vecchio, 2011), ellipsoids (Man *et al.*, 2005; Bezrukov and Stoyan, 2006; Buchalter and Bradley, 2007), spherocylinders (Allen *et al.*, 1989; Williams and Philipse, 2003; Zhao *et al.*, 2012), etc. Following the work of Lubachevsky and Stillinger (1990), algorithms based on molecular dynamics (MD) have become increasingly popular due to their computational efficiency with respect to algorithms where the particles are generated sequentially (Rintoul and Torquato, 1997). Algorithms that generate random packings of spherical particles are now well established (Lubachevsky *et al.*, 1991; Lubachevsky, 1991). They rely on simple equations and, in most cases, analytical solutions exist. This is not the case for non-spherical models where numerical methods are usually needed. Donev *et al.* (2005a) proposed an efficient algorithm that relies on the near-neighbor list (NNL) method to improve the binary collisions computation time. This algorithm was tested for generating random packings that contain ellipses and ellipsoids (Donev *et al.*, 2005b). However, the technique used to determine the collision time between two ellipsoids may not be computationally-efficient. Indeed, the collision time between two moving ellipsoids is the first non-zero time value for which the maximum of a certain function is equal to zero. Since the maximum of this function is computed numerically, the problem could be computationally expensive. In addition, the authors considered periodic packings but without detailing the method for computing the collision between an ellipsoid and a cell face.

The aim of this paper is to present a fully detailed computationally-efficient algorithm for generating random periodic packings of hard ellipsoids. Special emphasis is put on obtaining a computationally efficient algorithm that can deal with general ellipsoids.

The paper is structured as follows: Section 5.3 reviews the different techniques for generating random packings. Section 5.4 presents some preliminaries on the mathematical representation of an ellipsoid oriented in space. The random generation algorithm is detailed in Section 5.5. Section 5.6 describes the method for evaluating the orientations dispersion of random ellipsoids. The performance of the algorithm is discussed in Section 5.7. Several examples of random packings are also presented.

The following convention has been adopted, unless specified otherwise: scalars are denoted by lower case letters (i.e. a, α); column vectors and matrices are respectively denoted by boldfaced lower case letters (i.e. $\boldsymbol{a}$, $\boldsymbol{\alpha}$) and boldfaced upper case Latin letters (i.e. $\mathbf{A}$). " $\times$ " denotes a vector product.

5.3 Background

5.3.1 Existing algorithms for generating random packings

The Random Sequential Adsorption (RSA) algorithm (Rintoul and Torquato, 1997) is

certainly the most widely used algorithm for generating random packings. At the beginning of the computation, the position of a particle is randomly selected. Then, the position of another particle is drawn and the contact is checked between both particles. If there is interference, the position of the second particle is drawn again until there is no contact with the first. The process is repeated until the desired number of particles and volume fraction are reached. Several authors (Segurado and Llorca, 2002; Barello and Lévesque, 2008; Kari *et al.*, 2007b) have used this algorithm and have struggled to reach high volume fractions. In its simplest form, this algorithm can generate volume fractions of approximately 30% for identical spherical particles.

An improved version of the RSA algorithm was proposed by Segurado and Llorca (2002). A unit cell having a volume fraction lower than the desired value is first generated with the RSA algorithm. The cell is then compressed in several steps and the particles positions and volumes are updated at each compression stage. However, this compression leads to particles interpenetration. It is therefore necessary to check for particles overlapping at each compression stage. If two particles touch, one of them is displaced along a random vector. If the particles are still in interference, the particle is placed in its original position and the process is repeated until the two inclusions no longer intersect. The simulation continues until the target volume fraction is reached. This modification in the RSA algorithm allows for denser packings than with the original version (around 50% for identical spherical particles).

Lubachevsky and Stillinger (1990) proposed an algorithm based on molecular dynamics. This algorithm was originally applied to discs (2D) and spheres (3D) (Lubachevsky *et al.*, 1991). The main idea of the algorithm is as follows. All inclusions are randomly created in the unit cell but have a null volume. Each inclusion has also a random velocity vector. The particles are then set in motion and their volumes gradually increase. Two types of events are checked at each iteration: binary collisions and collisions between particles and the cell faces. When a binary collision occurs, the velocities of the two concerned particles are updated according to the kinetic energy conservation principle. However, if a particle leaves the cell through a face, it must appear from the opposite side to meet the periodicity conditions. The simulation stops when the desired volume fraction is reached. This algorithm is more efficient than the RSA and the modified RSA algorithm since it can generate very dense packings in a low computation time. For example, a packing of 30 identical spheres with a volume fraction of 62% can be generated in less than 10 seconds. It was also possible to reach a volume fraction of 74% (Ghossein and Levesque, 2012), which is close to the theoretical maximum dense packing for spheres of identical size ($\approx 74.05\%$). This type of algorithm is called event-driven molecular dynamics (EDMD) where a sequence of discrete events are predicted and processed. Other authors (Allen *et al.*, 1989) have used a time-driven molecular

dynamics (TDMD) approach where time is divided into small increments and, at each step time, differential equations based on Newton's law are integrated. TDMD algorithm is much easier to implement than EDMD but is far less efficient, especially for high densities.

The works of Lubachevsky and Stillinger have been extended by Donev *et al.* (2005a) to the case of non spherical particles within an EDMD framework. In most cases, the collision time between inclusions is computed numerically. Since this step requires numerous computations, Donev et al. introduced the near-neighbor list (NNL) concept to avoid computing unnecessary collisions. Each particle has a bounding neighborhood and collision between a pair of particles is checked if their bounding neighborhoods overlap. This method is very useful for very aspherical inclusions and speeds up considerably the algorithm. The latter was applied to ellipses (2D) and ellipsoids (3D) (Donev *et al.*, 2005b). To calculate the collision time between two ellipsoids, the authors made use of the overlap potentials (Perram and Wertheim, 1985; Perram *et al.*, 1996). The collision time between two moving ellipsoids is the first root of the overlap potential $F(t)$ that represents the maximum of a certain parametric function $f(t, \lambda)$, i.e., $F(t) = \max_{0 \leq \lambda \leq 1} f(t, \lambda)$. Since the maximum of $f(t, \lambda)$ cannot be computed analytically, the problem takes the form of two optimization subproblems, which can make the algorithm less computationally-efficient.

Wang *et al.* (2001) have developed an algebraic condition for defining the relative configuration of two static ellipsoids (separate, tangent or overlapping). Choi *et al.* (2003, 2009) have used this condition to develop a continuous collision detection algorithm based on the Bézier clipping technique. However, their algorithm is only applicable to ellipsoids moving under rational motions (motions defined by rational function of time). Jia *et al.* (2011) extended their work for ellipsoids moving under arbitrary motions by using a symbolic approach. In this method, the collision time between two ellipsoids is computed by finding the roots of a function. This technique is discussed in Section 5.5.2.

5.3.2   Orientation tensor

Random packings of ellipsoids are characterized by an Orientation Distribution Function that provides the probability of an inclusion to be oriented along a given vector. The nature (e.g. isotropic, transversely isotropic) of an ODF can be characterized with orientation tensors.

In a global coordinate system $Oe_1e_2e_3$, the orientation of each ellipsoid is defined by its two Euler angles, θ and ϕ (it is assumed that the ellipsoids have an axis of revolution). θ is the angle between e_3 and the ellipsoid's major axis, while ϕ is the angle between e_1 and the projection of the ellipsoid's major axis in the Oe_1e_2 plane. All possible orientations can be described when $0 \leq \theta \leq \pi$ and $0 \leq \phi \leq 2\pi$.

The second-order orientation tensor of a packing containing N ellipsoids is computed as follows (Advani and Tucker, 1987) :

$$\mathrm{T}_{mn} = \left\langle w_m^i w_n^i \right\rangle \tag{5.1a}$$

where

$$\begin{cases} w_1^i &= \sin\theta^i \cos\phi^i \\ w_2^i &= \sin\theta^i \sin\phi^i \\ w_3^i &= \cos\theta^i \end{cases} \tag{5.1b}$$

and $\langle \cdot \rangle$ denotes the unweighted average over the N ellipsoids. It should be noted that $\mathrm{tr}(\mathbf{T}) = 1$. In the case of isotropic packings, the orientation tensor is equal to $\frac{1}{3}\mathbf{I}$, where $\mathbf{I}$ is the identity matrix.

5.4   Representation of an ellipsoid

In this section, the mathematical representation of an ellipsoid is defined. The methodology used to determine the configuration of an ellipsoid at time $(t+\Delta t)$ from its configuration at time t is also presented.

5.4.1   Static ellipsoid

Let i be an ellipsoid oriented in space and defined in a global coordinate system $Oe_1e_2e_3$. Let vector $\boldsymbol{r}_{(t)}^i$ denote the position of the ellipsoid's center O' at time t. Let the local coordinate system $Oe'_1e'_2e'_3$ be aligned along the principal axes of i. The equation of the ellipsoid in its local coordinate system can be written as :

$$\boldsymbol{x'}^\top \mathbf{A'}_{(t)}^{i} \boldsymbol{x'} = 0 \tag{5.2a}$$

where

$$\mathbf{A'}_{(t)}^{i} = \begin{bmatrix} \left(a_{(t)}^i\right)^{-2} & 0 & 0 & 0 \\ 0 & \left(b_{(t)}^i\right)^{-2} & 0 & 0 \\ 0 & 0 & \left(c_{(t)}^i\right)^{-2} & 0 \\ 0 & 0 & 0 & -1 \end{bmatrix} \tag{5.2b}$$

and $a_{(t)}^i$, $b_{(t)}^i$ and $c_{(t)}^i$ represent the length of the semi-principal axes. It should be noted that $\boldsymbol{x'} = \{x_1, x_2, x_3, w\}^\top$ are the homogeneous coordinates of a point in space. It is the equivalent of the point $\boldsymbol{x'} = \left\{\frac{x_1}{w}, \frac{x_2}{w}, \frac{x_3}{w}\right\}^\top$ in Cartesian coordinates.

The mathematical representation of i in the global system is obtained with rotation matrices. Normalized quaternions are used for this purpose instead of Euler angles because they are more stable numerically (Eberly, 2002) . The orientation of i at time t can be defined as a rotation of an angle $\Omega^i_{(t)}$ around an axis oriented along a unit vector $\boldsymbol{u}^i_{(t)}$. The quaternion of i, consisting of a scalar $\alpha^i_{(t)}$ and a vector $\boldsymbol{\psi}^i_{(t)}$, is written as follows :

$$\boldsymbol{q}^i_{(t)} = \left[\alpha^i_{(t)}, \boldsymbol{\psi}^i_{(t)}\right] = \left[\cos\frac{\Omega^i_{(t)}}{2}, \left(\sin\frac{\Omega^i_{(t)}}{2}\right)\boldsymbol{u}^i_{(t)}\right] \tag{5.3}$$

Since $\left\|\boldsymbol{u}^i_{(t)}\right\| = 1$, $\left\|\boldsymbol{q}^i_{(t)}\right\| = \left(\alpha^i_{(t)}\right)^2 + \left\|\boldsymbol{\psi}^i_{(t)}\right\|^2 = 1$ (i.e. the quaternion $\boldsymbol{q}^i_{(t)}$ is normalized).

Quaternions have the property that if the ellipsoid undergoes a motion defined by the quaternion $\boldsymbol{q_1} = \left[\alpha_1, \boldsymbol{\psi_1}\right]$, followed by a movement defined by the quaternion $\boldsymbol{q_2} = \left[\alpha_2, \boldsymbol{\psi_2}\right]$, the total motion of the ellipsoid can be summarized in a single quaternion $\boldsymbol{q_{12}}$, such that :

$$\boldsymbol{q_{12}} = [\alpha_{12}, \boldsymbol{\psi_{12}}] = \left[\alpha_1\alpha_2 - \boldsymbol{\psi_1}^\top\boldsymbol{\psi_2}, \alpha_1\boldsymbol{\psi_2} + \alpha_2\boldsymbol{\psi_1} - \boldsymbol{\psi_1} \times \boldsymbol{\psi_2}\right] \tag{5.4}$$

The rotation matrix can be obtained from the quaternion as follows :

$$\mathbf{R}^i_{(t)} = \left[2\left(\alpha^i_{(t)}\right)^2 - 1\right]\mathbf{I} + 2\boldsymbol{\psi}^i_{(t)}\boldsymbol{\psi}^{i\top}_{(t)} + 2\alpha^i_{(t)}\mathbf{S}^i_{(t)} \tag{5.5a}$$

where $\mathbf{I}$ is the identity matrix and $\mathbf{S}^i_{(t)}$ is given by :

$$\mathbf{S}^i_{(t)} = \begin{bmatrix} 0 & -\psi^i_{(t)}[3] & \psi^i_{(t)}[2] \\ \psi^i_{(t)}[3] & 0 & -\psi^i_{(t)}[1] \\ -\psi^i_{(t)}[2] & \psi^i_{(t)}[1] & 0 \end{bmatrix} \tag{5.5b}$$

where $\psi^i_{(t)}[k]$ refers to the kth term of vector $\boldsymbol{\psi}^i_{(t)}$.

In homogeneous coordinates, the transition from $Oe'_1e'_2e'_3$ to $Oe_1e_2e_3$ is performed directly by combining rotation and translation :

$$\boldsymbol{x} = \mathbf{M}^i_{(t)}\,\boldsymbol{x'} \tag{5.6a}$$

where

$$\mathbf{M}^i_{(t)} = \begin{bmatrix} \mathbf{R}^i_{(t)} & \boldsymbol{r}^i_{(t)} \\ \mathbf{0}^\top & 1 \end{bmatrix} \quad\Leftrightarrow\quad \left(\mathbf{M}^i_{(t)}\right)^{-1} = \begin{bmatrix} \left(\mathbf{R}^i_{(t)}\right)^\top & -\left(\mathbf{R}^i_{(t)}\right)^\top\boldsymbol{r}^i_{(t)} \\ \mathbf{0}^\top & 1 \end{bmatrix} \tag{5.6b}$$

Using Eqs. (5.2a) and (5.6a), the ellipsoid equation in the global coordinate system becomes:

$$\boldsymbol{x}^\top \mathbf{A}_{(t)}^i \, \boldsymbol{x} = 0 \tag{5.7a}$$

where

$$\mathbf{A}_{(t)}^i = \left(\mathbf{M}_{(t)}^i\right)^{-\top} \mathbf{A}_{(t)}^{\prime i} \left(\mathbf{M}_{(t)}^i\right)^{-1} \tag{5.7b}$$

where $\left(\mathbf{M}_{(t)}^i\right)^{-\top}$ denotes the inverse of $\left(\mathbf{M}_{(t)}^i\right)^{\top}$.

5.4.2   Moving and growing ellipsoid

Let i be an ellipsoid whose configuration at a given time t is determined by its position vector $\boldsymbol{r}_{(t)}^i$, its quaternion $\boldsymbol{q}_{(t)}^i$ and the lengths of its semi-principle axes $\{a_{(t)}^i, b_{(t)}^i, c_{(t)}^i\}$. Moreover, i has linear and angular velocity vectors, denoted respectively by $\boldsymbol{v}^i$ and $\boldsymbol{\omega}^i$. The objective is to find the configuration of ellipsoid i at time $(t + \Delta t)$, i.e. $\boldsymbol{r}_{(t+\Delta t)}^i$, $\boldsymbol{q}_{(t+\Delta t)}^i$ and $\{a_{(t+\Delta t)}^i, b_{(t+\Delta t)}^i, c_{(t+\Delta t)}^i\}$, while considering that i grows gradually over the time. The new position of the ellipsoid's center at that instant is given by :

$$\boldsymbol{r}_{(t+\Delta t)}^i = \boldsymbol{r}_{(t)}^i + \boldsymbol{v}^i \Delta t \tag{5.8}$$

The new lengths of the semi-principle axes are :

$$\begin{cases} a_{(t+\Delta t)}^i &= a_{(t)}^i + a_0^i \Delta t \\ b_{(t+\Delta t)}^i &= b_{(t)}^i + b_0^i \Delta t \\ c_{(t+\Delta t)}^i &= c_{(t)}^i + c_0^i \Delta t \end{cases} \tag{5.9}$$

where a_0^i, b_0^i and c_0^i represent the semi-principle axes growth rates.

During the time interval Δt, the ellipsoid has rotated by an angle $\Omega^i = \|\boldsymbol{\omega}\| \Delta t$ about an axis oriented along the unit vector $\boldsymbol{u}^i = \boldsymbol{\omega}/\|\boldsymbol{\omega}\|$. The quaternion associated with this motion, denoted by $\boldsymbol{q}_{\Delta t}$, can be written as :

$$\boldsymbol{q}_{\Delta t}^i = [\alpha_{\Delta t}^i , \boldsymbol{\psi}_{\Delta t}^i] = \left[\cos\left(\frac{\|\boldsymbol{\omega}^i\|\Delta t}{2}\right) , \left(\sin\left(\frac{\|\boldsymbol{\omega}^i\|\Delta t}{2}\right)\right)\frac{\boldsymbol{\omega}^i}{\|\boldsymbol{\omega}^i\|}\right] \tag{5.10}$$

Using Eq. (5.4), the quaternion at time $(t + \Delta t)$ becomes:

$$\begin{aligned} \boldsymbol{q}_{(t+\Delta t)}^i &= \left[\alpha_{(t+\Delta t)}^i , \boldsymbol{\psi}_{(t+\Delta t)}^i\right] \\ &= \left[\alpha_{(t)}^i \alpha_{\Delta t}^i - \boldsymbol{\psi}_{(t)}^{i\top} \boldsymbol{\psi}_{\Delta t}^i , \; \alpha_{(t)}^i \boldsymbol{\psi}_{\Delta t}^i + \alpha_{\Delta t}^i \boldsymbol{\psi}_{(t)}^i - \boldsymbol{\psi}_{(t)}^i \times \boldsymbol{\psi}_{\Delta t}^i\right] \end{aligned} \tag{5.11}$$

By knowing the position and the quaternion at time $(t + \Delta t)$, it is possible to deduce the rotation matrix $\mathbf{R}^i_{(t+\Delta t)}$ and the transition matrix $\mathbf{M}^i_{(t+\Delta t)}$ from Eqs. (5.5) and (5.6b). Finally, the equation of the ellipsoid in the coordinate system $O\boldsymbol{e}_1\boldsymbol{e}_2\boldsymbol{e}_3$ at time $(t + \Delta t)$ is given by:

$$\boldsymbol{x}^\top \mathbf{A}^i_{(t+\Delta t)} \, \boldsymbol{x} = 0 \tag{5.12a}$$

where

$$\mathbf{A}^i_{(t+\Delta t)} = \left(\mathbf{M}^i_{(t+\Delta t)}\right)^{-\top} \mathbf{A'}^i_{(t+\Delta t)} \left(\mathbf{M}^i_{(t+\Delta t)}\right)^{-1} \tag{5.12b}$$

The matrix $\mathbf{A'}^i_{(t+\Delta t)}$ is calculated with Eq. (5.2b) using the lengths of the semi-principal axes at time $(t + \Delta t)$ obtained with Eq. (5.9)

The algorithm we implemented to define the state of an ellipsoid at time $(t + \Delta t)$ from its state at time t is presented in Appendix 5.A (see Algorithm 5.2).

5.5 Proposed new algorithm

5.5.1 Algorithm outline

At the beginning of the simulation, N ellipsoids are randomly created into a cube of side L. The ellipsoids volumes are initially null. Each ellipsoid has a random linear and angular velocity, as well as a random quaternion (i.e. orientation). The semi-principle axes growth rates $\{a_0, b_0, c_0\}$ are chosen such that $b_0 = a_0/R_1$ and $c_0 = a_0/R_2$, where R_1 and R_2 denotes respectively the two aspect ratios that are input in the algorithm. It was found, after trials and errors, that $a_0 = 0.1$ led to good results. The elliptical particles are then put in translational and rotational motion and their volumes gradually increase. At each step, two types of collisions are checked and computed: binary collision between two ellipsoids and collision between a particle and a cube face. If the first type of collision occurs, the linear and angular velocities of the involved particles are updated. However, if an ellipsoid intersects a cube face, its periodic image is created on the opposite side. The algorithm stops when the volume fraction $\mathcal{V}_f$ is reached.

The principal steps of the algorithm are summarized in Algorithm 5.1.

5.5.2 Collision times between ellipsoids

Overlap detection between two static ellipsoids

Let i and j be two ellipsoids at time t with the respective equations $\boldsymbol{x}^\top \mathbf{A}^i_{(t)} \, \boldsymbol{x} = 0$ and $\boldsymbol{x}^\top \mathbf{A}^j_{(t)} \, \boldsymbol{x} = 0$. Introduce the characteristic equation of i and j as :

$$\det(\lambda \mathbf{A}^i_{(t)} + \mathbf{A}^j_{(t)}) = p_{1(t)}\lambda^4 + p_{2(t)}\lambda^3 + p_{3(t)}\lambda^2 + p_{4(t)}\lambda + p_{5(t)} = 0 \qquad (5.13)$$

Algorithm 5.3 details the computation of coefficients $p_{k(t)}$ from matrices $\mathbf{A}^i_{(t)}$ and $\mathbf{A}^j_{(t)}$ (Choi et al., 2009).

Eq. (5.13) is a 4th-order polynomial and has therefore four roots. Wang et al. (2001) showed that two of the roots are always real and negative. In addition, the authors have established a relationship between the nature of the other two roots and the configuration of the two ellipsoids. They have shown that :

  i) i and j are separate if Eq. (5.13) admits two negative and two positive roots.

  ii) i and j are externally tangent if Eq. (5.13) admits two negative roots and a double positive root.

  iii) i and j overlap in all other cases.

Therefore, the next collision time between two moving ellipsoids is the first moment where condition ii) is met. The problem takes the form of an eigenvalue optimization and can be relatively challenging to solve. It would be more efficient to determine the relationship between the coefficients p_k which ensures the presence of a positive double root.

Jia et al. (2011) have identified a relationship between the coefficients $p_{k(t)}$ and the ellipsoids configuration (separate, externally tangent or overlap). The technique is based on the Sylvester-Habicht matrix of the characteristic equation and its first derivative (Basu et al., 2006). Five coefficients $\{\eta_{1(t)}, \eta_{2(t)}, \eta_{3(t)}, \eta_{4(t)}, \eta_{5(t)}\}$ are computed from the coefficients $p_{k(t)}$ (see Algorithm 5.4). The configuration of ellipsoids i and j at time t is then determined according to the value of $\eta_{k(t)}$. All possible combinations of $\eta_{k(t)}$ are summarized in Table 5.1 (see (Jia et al., 2011) for more details).

Table 5.1 Relation between the coefficients $\eta_{k(t)}$ and the ellipsoids configuration at time t.

Cases	$\eta_{1(t)}$	$\eta_{2(t)}$	$\eta_{3(t)}$	$\eta_{4(t)}$	$\eta_{5(t)}$	Ellipsoids configuration
1	$= 0$	> 0	> 0		> 0	separate
2	> 0	> 0			> 0	separate
3	$= 0$	> 0	< 0		> 0	externally tangent
4	$= 0$	$= 0$		< 0	> 0	externally tangent
5	For all other cases					overlap

Computing the first collision time between two moving ellipsoids

Table 5.1 shows that $\eta_1 = 0$ when two ellipsoids are externally tangent. Algorithm 5.5 details the implementation of function $\eta_{1(t+\Delta t)}$ that provides the value of coefficient η_1 for any value of Δt. Once the function $\eta_{1(t+\Delta t)}$ is implemented, the procedure to compute the first collision time is as follows. First, all the roots of $\eta_{1(t+\Delta t)}$ are computed numerically. This can be done with the algorithm of (Brent, 2002) which combines the bisection method, the secant method and the inverse quadratic interpolation. Then, all computed values of Δt are sorted in ascending order and the collision time t_c is the smallest Δt value that satisfies case 3 or 4 in Table 5.1.

This technique is very efficient since computing the roots of function $\eta_{1(t+\Delta t)}$ is usually very fast, and in most cases, there are only two.

Contact point between the two ellipsoids

Once t_c is computed, it is possible to find the four roots of the characteristic equation $\det(\lambda \mathbf{A}^i_{(t+t_c)} + \mathbf{A}^j_{(t+t_c)}) = 0$, corresponding to the eigenvalues of the matrix $\left(\mathbf{A}^i_{(t+t_c)}\right)^{-1} \mathbf{A}^j_{(t+t_c)}$. Among these four roots, there is a positive double root denoted by λ_0. The homogeneous coordinates of the point of contact $\boldsymbol{x}_c$ are the solution of the following equation (Choi *et al.*, 2009) :

$$\left(\lambda_0 \mathbf{A}^i_{(t+t_c)} - \mathbf{A}^j_{(t+t_c)}\right)\boldsymbol{x}_c = 0 \tag{5.14}$$

where $\boldsymbol{x}_c$ corresponds to the eigenvector of the matrix $\left(\mathbf{A}^i_{(t+t_c)}\right)^{-1} \mathbf{A}^j_{(t+t_c)}$ associated with the eigenvalue λ_0.

Improving the computation time of binary collisions

At each iteration, all binary collision times are saved. During an iteration, the collision time between two ellipsoids is calculated only if the velocities of at least one ellipsoid have changed since the last iteration or if one ellipsoid is a new periodic image that was created in the previous iteration. Indeed, if the velocities of a pair of ellipsoids has not changed, the collision time between this pair can be derived from the collision time obtained at the previous iteration. It suffices to subtract from the latter the time spent between the last two iterations.

Furthermore, the algorithm for finding the next binary collisions can be improved if it is possible to avoid computing collisions that are unlikely to occur. First, the concept of bounding spheres is introduced. Two ellipsoids cannot collide if their respective bounding spheres will never overlap. At time t, the bounding sphere of ellipsoid i, denoted by BS_i,

has the same position $r^i_{(t)}$ and the same linear velocity v^i as the latter. The radius and the radius growth rate of BS_i are respectively given by $R^i_{(t)} = \max\left(a^i_{(t)}, b^i_{(t)}, c^i_{(t)}\right)$ and $R^i_0 = \max\left(a^i_0, b^i_0, c^i_0\right)$. Two bounding spheres BS_i and BS_j are in contact if :

$$\left\|r^i_{(t)} - r^j_{(t)}\right\| \le R^i_{(t)} + R^j_{(t)} \tag{5.15}$$

If Eq. (5.15) is satisfied, the collision time between the two bounding spheres, denoted by t^{BS}_c, is set to 0. Otherwise, the collision time between BS_i and BS_j is given by (Ghossein and Levesque, 2012) :

$$t^{BS}_c = \begin{cases} \gamma_1^{-1}\left[-\gamma_2 - \sqrt{\gamma_2^2 - \gamma_1\gamma_3}\right] & \text{if} \quad (\gamma_2 \le 0 \ \text{ or } \ \gamma_1 < 0) \ \text{ and } \ \gamma_2^2 - \gamma_1\gamma_3 \ge 0 \\ \text{No collision} & \text{if} \quad (\gamma_2 > 0 \ \text{ and } \ \gamma_1 \ge 0) \ \text{ or } \ \gamma_2^2 - \gamma_1\gamma_3 < 0 \end{cases} \tag{5.16a}$$

where

$$\begin{cases} \gamma_1 &= \left\|v^i - v^j\right\|^2 - \left(R^i_0 + R^j_0\right)^2 \\ \gamma_2 &= \left(r^i_{(t)} - r^j_{(t)}\right)^\top \left(v^i - v^j\right) - \left(R^i_{(t)} + R^j_{(t)}\right)\left(R^i_0 + R^j_0\right) \\ \gamma_3 &= \left\|r^i_{(t)} - r^j_{(t)}\right\|^2 - \left(R^i_{(t)} + R^j_{(t)}\right)^2 \end{cases} \tag{5.16b}$$

Collision between ellipsoids i and j is computed only if BS_i and BS_j overlap or will collide after a certain time. The main advantage of using the bounding spheres method is that the collision between two spheres is computed analytically unlike ellipsoids where the collision time is obtained numerically. In addition, the algorithm stores the minimum collision time ($t_{\min}$) obtained whenever a pair of ellipsoids has been checked. Therefore, the computation of collisions between ellipsoids i and j is performed if the collision time between BS_i and BS_j is lower than the minimum time stored, i.e. $t^{BS}_c < t_{\min}$.

The algorithm uses also the near-neighbor list (NNL) concept introduced by Donev *et al.* (2005a). The neighborhood of an ellipsoid i, denoted by N_i, is also an ellipsoid which is concentric with i and has the same parameters as the latter. The only difference lies in the length of the semi-principle axes of N_i which are equal to $\{\mu a^i_{(t)}, \mu b^i_{(t)}, \mu c^i_{(t)}\}$, where μ is a scale factor. The value of μ was set to 1.2 in the algorithm. It is possible to reduce the value of μ during the course of the simulation such that $\mu \to 1$ near the jamming point. The collision between a pair of ellipsoids i and j is checked only if their respective neighborhood N_i and N_j overlap or are externally tangent. This reduces considerably the number of collisions to compute. Overlap between N_i and N_j at time t is checked analytically by computing their five coefficients $\eta_k(t)$ using Algorithm 5.5 and by deducing their configuration with Table 5.1.

Algorithm 5.6 details the next binary collision time computation while considering the

bounding spheres and the NNL concepts. The algorithm provides also the coordinates of the contact point $\boldsymbol{x}_c$.

5.5.3 Collision time between ellipsoids and the cube faces

Intersection between a stationary ellipsoid and a cube face

Let i be an ellipsoid at time t defined by the equation $\boldsymbol{x}^\top \mathbf{A}^i_{(t)} \boldsymbol{x} = 0$. $\mathbf{A}^i_{(t)}$ can be written as :

$$\mathbf{A}^i_{(t)} = \begin{bmatrix} \mathbf{B}^i_{(t)} & \frac{1}{2}\boldsymbol{d}^i_{(t)} \\ \frac{1}{2}\boldsymbol{d}^i_{(t)}{}^\top & F^i_{(t)} \end{bmatrix} \tag{5.17}$$

where $\mathbf{B}^i_{(t)}$ is a 3×3 matrix and $\boldsymbol{d}^i_{(t)}$ is a 3×1 vector. The ellipsoid equation becomes :

$$\boldsymbol{x}^\top \mathbf{B}^i_{(t)} \boldsymbol{x} + \boldsymbol{d}^i_{(t)}{}^\top \boldsymbol{x} + F^i_{(t)} = 0 \tag{5.18}$$

where $\boldsymbol{x}$ denotes Cartesian coordinates. It should be noted that $\mathbf{B}^i_{(t)}$ is symmetric and positive definite since Eq (5.18) is the equation of an ellipsoid.

Computation of the intersection equation between i and a cube face $x_k = \beta$ ($k \in \{1, 2, 3\}$ and $\beta \in \{0, L\}$) can be accomplished through a change of variables from 3D coordinates ($\boldsymbol{x}$) to 2D coordinates ($\boldsymbol{x}^*$). The transformation can be written as follows :

$$\boldsymbol{x} = \mathbf{P}\boldsymbol{x}^* + \boldsymbol{p} \tag{5.19a}$$

where

$$\begin{cases} \boldsymbol{x} &= \{x_1, x_2, x_3\}^\top \\ \boldsymbol{x}^* &= \{x_l, x_m\}^\top \\ \mathbf{P} &= [\boldsymbol{e}_l, \boldsymbol{e}_m] \\ \boldsymbol{p} &= \beta \boldsymbol{e}_k \end{cases} \quad l, m \in \{1, 2, 3\} \quad ; \quad l < m \quad ; \quad l \neq k \neq m \tag{5.19b}$$

For example, if the cube face equation is $x_1 = L$, Eq. (5.19a) becomes :

$$\begin{Bmatrix} x_1 \\ x_2 \\ x_3 \end{Bmatrix} = \begin{bmatrix} 0 & 0 \\ 1 & 0 \\ 0 & 1 \end{bmatrix} \begin{Bmatrix} x_2 \\ x_3 \end{Bmatrix} + \begin{Bmatrix} L \\ 0 \\ 0 \end{Bmatrix} \tag{5.20}$$

Combination of Eqs. (5.18) and (5.19a) yields the portion of i that intersect the cube's face and leads to :

$$g_{(t)}(\boldsymbol{x}^*) = \boldsymbol{x}^{*\top} \mathbf{B}_{(t)}^{i*} \boldsymbol{x}^* + \boldsymbol{d}_{(t)}^{i*\top} \boldsymbol{x}^* + F_{(t)}^{i*} = 0 \tag{5.21a}$$

where

$$\begin{cases} \mathbf{B}_{(t)}^{i*} &= \mathbf{P}^\top \mathbf{B}_{(t)}^i \mathbf{P} \\[4pt] \boldsymbol{d}_{(t)}^{i*} &= 2\mathbf{P}^\top \mathbf{B}_{(t)}^i \boldsymbol{p} + \mathbf{P}^\top \boldsymbol{d}_{(t)}^i \\[4pt] F_{(t)}^{i*} &= \boldsymbol{p}^\top \mathbf{B}_{(t)}^i \boldsymbol{p} + \boldsymbol{d}_{(t)}^{i\top} \boldsymbol{p} + F_{(t)}^i \end{cases} \tag{5.21b}$$

The intersection of an ellipsoid with a plane is an ellipse, a point or the empty set. To determine the nature of the intersection, it is necessary to identify the number of solutions that satisfy Eq. (5.21a). Since $\mathbf{B}_{(t)}^{i*}$ is positive definite, $g_{(t)}(\boldsymbol{x}^*)$ is a quadratic convex function which has a global minimum. The minimum of the function, denoted by $\boldsymbol{x}_{\min}^*$, is derived by setting $\nabla_{\boldsymbol{x}^*}\left[g_{(t)}(\boldsymbol{x}^*)\right] = 0$ and leads to :

$$\boldsymbol{x}_{\min}^* = -\frac{1}{2}\left(\mathbf{B}_{(t)}^{i*}\right)^{-1}\boldsymbol{d}_{(t)}^{i*} \tag{5.22}$$

The minimum value of $g_{(t)}(\boldsymbol{x}^*)$, denoted by $g_{(t)}^\dagger$, is therefore given by :

$$g_{(t)}^\dagger = g_{(t)}(\boldsymbol{x}_{\min}^*) = -\frac{1}{4}\boldsymbol{d}_{(t)}^{i*\top}\left(\mathbf{B}_{(t)}^{i*}\right)^{-1}\boldsymbol{d}_{(t)}^{i*} + F_{(t)}^{i*} \tag{5.23}$$

The intersection type depends on the value of $g_{(t)}^\dagger$:

i) If $g_{(t)}^\dagger < 0$, $g_{(t)}(\boldsymbol{x}^*)$ crosses zero at various points. Therefore Eq. (5.21a) has several solutions and the intersection is an ellipse.

ii) If $g_{(t)}^\dagger = 0$, $g_{(t)}(\boldsymbol{x}^*)$ crosses zero at a single point. Therefore Eq. (5.21a) has a unique solution and the intersection is a point.

iii) If $g_{(t)}^\dagger > 0$, $g_{(t)}(\boldsymbol{x}^*)$ does not cross zero. Therefore Eq. (5.21a) has no solution and the intersection is the empty set.

First collision time between an ellipsoid and a cube face

The collision time between an ellipsoid i and a cube face can be computed by determining the first value t_s such that $g_{(t+t_s)}^\dagger = 0$. First, the function $g_{(t+\Delta t)}^\dagger$ is implemented (see Algorithm 5.7). The roots of $g_{(t+\Delta t)}^\dagger$ are then computed using the Brent algorithm and the smallest Δt value corresponds to the next collision time.

Improvement of the next collision time computation efficiency

As in the case of binary collisions, the collision time between an ellipsoid and a cube face

is computed only if the velocities of the ellipsoid have changed since the previous iteration. It is also possible to improve the performance of the algorithm by using the concept of bounding spheres. An ellipsoid i cannot collide with a cube face if its bounding sphere BS_i will never touch this face. At time t, BS_i is in contact with the cube face $x_k = \beta$ if :

$$\begin{cases} r^i_{(t)}[k] - R^i_{(t)} \leq \beta & \text{if} \quad \beta = 0 \\ r^i_{(t)}[k] + R^i_{(t)} \geq \beta & \text{if} \quad \beta = L \end{cases} \tag{5.24}$$

If Eq. (5.24) is satisfied, the collision time between BS_i and the cube face $x_k = \beta$, denoted by t_s^{BS}, is set to 0. Otherwise, t_s^{BS} is given by (Ghossein and Levesque, 2012) :

$$t_s^{BS} = \begin{cases} \left[R^i_{(t)} - r^i_{(t)}[k] \right] \left[v^i_{(t)}[k] - R^i_0 \right]^{-1} & \text{if} \quad \beta = 0 \\ \left[\beta - R^i_{(t)} - r^i_{(t)}[k] \right] \left[v^i_{(t)}[k] + R^i_0 \right]^{-1} & \text{if} \quad \beta = L \end{cases} \tag{5.25}$$

Given that the algorithm stores the minimum time $(t_{\min})$ obtained whenever a collision between an ellipsoid and a cube face has been processed, the collision between an ellipsoid i and a cube face $x_k = \beta$ is computed only if $t_s^{BS} < t_{\min}$.

Algorithm 5.8 details the computation of the next collision time between an ellipsoid and a cube face while considering the bounding sphere concept.

5.5.4 Updating linear and angular velocities after impact

Let i and j be two ellipsoids that collide at time $t = t_c$. The linear ($\boldsymbol{v}^{i-}$ and $\boldsymbol{v}^{j-}$) and angular ($\boldsymbol{\omega}^{i-}$ and $\boldsymbol{\omega}^{j-}$) velocities before collision are known. The objective is to determine the linear and angular velocities after impact, i.e. $\boldsymbol{v}^{i+}$, $\boldsymbol{v}^{j+}$, $\boldsymbol{\omega}^{i+}$ and $\boldsymbol{\omega}^{j+}$. A system of 12 equations should be defined in order to find these 12 unknowns. Friction is assumed negligible at the contact surface.

First, the unit normal vector $\boldsymbol{n}$ at the contact point $\boldsymbol{x}_c$ is computed. $\boldsymbol{n}$ is defined as going from i to j (see Figure 5.1) and is given by :

$$\boldsymbol{n} = \frac{\nabla \left(\boldsymbol{x}^\top \mathbf{A}^i_{(t)} \boldsymbol{x} \right)}{\left\| \nabla \left(\boldsymbol{x}^\top \mathbf{A}^i_{(t)} \boldsymbol{x} \right) \right\|} = \frac{2\mathbf{B}^i_{(t)} \boldsymbol{x}_c + \boldsymbol{d}^i_{(t)}}{\left\| 2\mathbf{B}^i_{(t)} \boldsymbol{x}_c + \boldsymbol{d}^i_{(t)} \right\|} \tag{5.26}$$

where $\mathbf{B}^i_{(t)}$ and $\boldsymbol{d}^i_{(t)}$ are computed from Eq. (5.17).

Two other unit vectors $\boldsymbol{t_1}$ and $\boldsymbol{t_2}$ are defined such that $\boldsymbol{t_1}$, $\boldsymbol{t_2}$ and $\boldsymbol{n}$ form an orthonormal basis in $\mathbb{R}^3$. The kinematics theory used to model the impact is based on the linear and
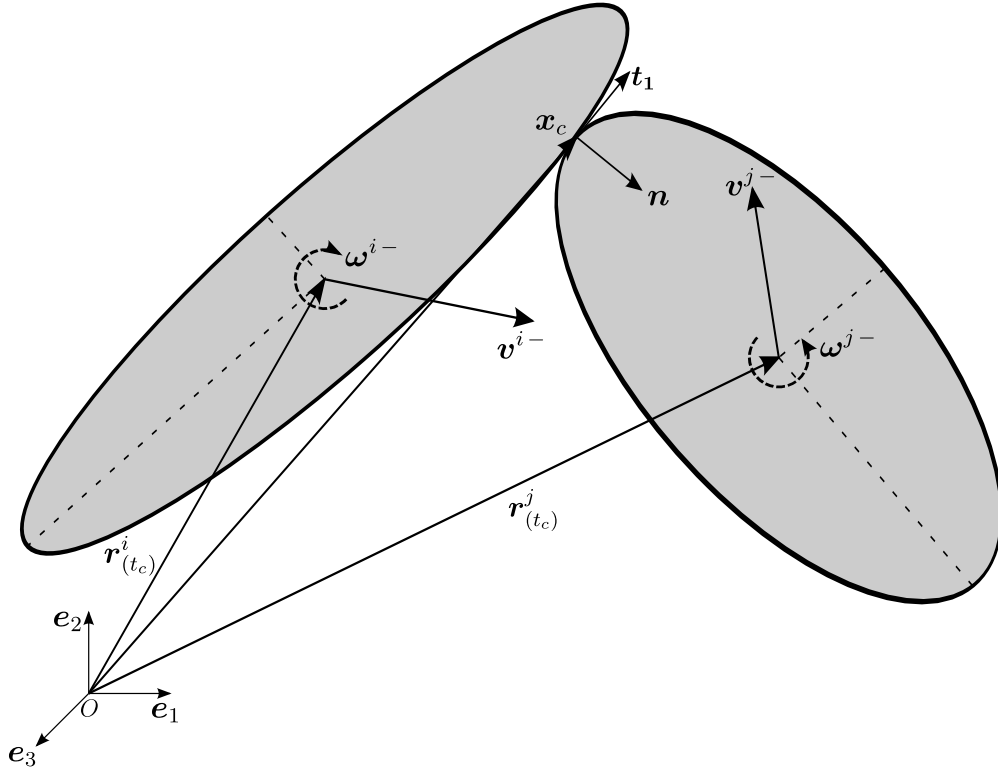
Figure 5.1 Two colliding ellipsoids at time $t_c - \delta t$. $\boldsymbol{n}$ is defined as going from i to j. Vector $\boldsymbol{t_2}$ (not shown) is perpendicular to $\boldsymbol{n}$ and $\boldsymbol{t_1}$ such that $\boldsymbol{t_1} \times \boldsymbol{t_2} = \boldsymbol{n}$.

angular momentum conservation and is detailed below.

Ellipsoid mass and moment of inertia

Assuming a unit density, the mass and the moment of inertia of an ellipsoid i are given by :

$$m^i_{(t)} = \frac{4}{3}\pi a^i_{(t)} b^i_{(t)} c^i_{(t)} \tag{5.27a}$$

$$\mathbf{H'}^i_{(t)} = \frac{m^i_{(t)}}{5} \begin{bmatrix} \left(b^i_{(t)}\right)^2 + \left(c^i_{(t)}\right)^2 & 0 & 0 \\ 0 & \left(a^i_{(t)}\right)^2 + \left(c^i_{(t)}\right)^2 & 0 \\ 0 & 0 & \left(a^i_{(t)}\right)^2 + \left(b^i_{(t)}\right)^2 \end{bmatrix} \tag{5.27b}$$

The moment of inertia given by Eq. (5.27b) is expressed in the ellipsoids local coordinate system. The rotation matrix $\mathbf{R}^i_{(t)}$ can be used to calculate the moment of inertia expression in the global coordinate system as :

$$\mathbf{H}^i_{(t)} = \mathbf{R}^i_{(t)} \mathbf{H}'^i_{(t)} \left(\mathbf{R}^i_{(t)} \right)^\top \tag{5.28}$$

Governing equations

For each ellipsoid, the linear momentum along $\boldsymbol{t_1}$ and $\boldsymbol{t_2}$ is conserved during the impact. This allows to write the following four equations :

$$m^r_{(t)} \boldsymbol{v}^{r+\top} \boldsymbol{t_1} = m^r_{(t)} \boldsymbol{v}^{r-\top} \boldsymbol{t_1} \qquad r = \{i, j\} \tag{5.29a}$$

$$m^r_{(t)} \boldsymbol{v}^{r+\top} \boldsymbol{t_2} = m^r_{(t)} \boldsymbol{v}^{r-\top} \boldsymbol{t_2} \qquad r = \{i, j\} \tag{5.29b}$$

In addition, the total linear momentum along $\boldsymbol{n}$ is conserved :

$$m^i_{(t)} \boldsymbol{v}^{i+\top} \boldsymbol{n} + m^j_{(t)} \boldsymbol{v}^{j+\top} \boldsymbol{n} = m^i_{(t)} \boldsymbol{v}^{i-\top} \boldsymbol{n} + m^j_{(t)} \boldsymbol{v}^{j-\top} \boldsymbol{n} \tag{5.30}$$

Furthermore, the angular momentum about the contact point $\boldsymbol{x}_c$ is conserved during the impact for each ellipsoid. It is then possible to define six new equations :

$$\mathbf{H}^r_{(t)} \boldsymbol{\omega}^{r+} + m^r_{(t)} \left[(\boldsymbol{r}^r_{(t)} - \boldsymbol{x}_c) \times \boldsymbol{v}^{r+} \right] = \mathbf{H}^r_{(t)} \boldsymbol{\omega}^{r-} + m^r_{(t)} \left[(\boldsymbol{r}^r_{(t)} - \boldsymbol{x}_c) \times \boldsymbol{v}^{r-} \right] \quad r = \{i, j\} \tag{5.31}$$

The last equation is obtained by applying the coefficient of restitution along $\boldsymbol{n}$ while considering the effect of the ellipsoids growth rate. This equation can be written as :

$$\boldsymbol{v}^{c+\top} \boldsymbol{n} = -e \left(\boldsymbol{v}^{c-\top} \boldsymbol{n} \right) - 2 \left[\max \left(a^i_0, b^i_0, c^i_0 \right) + \max \left(a^j_0, b^j_0, c^j_0 \right) \right] \tag{5.32a}$$

where $e = 1$ for a perfect elastic collision. $\boldsymbol{v}^{c-}$ and $\boldsymbol{v}^{c+}$ denote the closing velocities of the contact point of i with respect to that of j, before and after collision respectively :

$$\begin{cases} \boldsymbol{v}^{c-} &= \left[\boldsymbol{v}^{i-} + \boldsymbol{\omega}^{i-} \times (\boldsymbol{x}_c - \boldsymbol{r}^i_{(t)}) \right] - \left[\boldsymbol{v}^{j-} + \boldsymbol{\omega}^{j-} \times (\boldsymbol{x}_c - \boldsymbol{r}^j_{(t)}) \right] \\ \\ \boldsymbol{v}^{c+} &= \left[\boldsymbol{v}^{i+} + \boldsymbol{\omega}^{i+} \times (\boldsymbol{x}_c - \boldsymbol{r}^i_{(t)}) \right] - \left[\boldsymbol{v}^{j+} + \boldsymbol{\omega}^{j+} \times (\boldsymbol{x}_c - \boldsymbol{r}^j_{(t)}) \right] \end{cases} \tag{5.32b}$$

Eqs. (5.29), (5.30), (5.31) and (5.32) form a system of 12 linear equations that can be easily solved to obtain $\boldsymbol{v}^{i+}$, $\boldsymbol{v}^{j+}$, $\boldsymbol{\omega}^{i+}$ and $\boldsymbol{\omega}^{j+}$.

Algorithm 5.9 summarizes the steps needed to compute the velocities after collision.

5.5.5 Post-collision with the cube faces: creation of periodic ellipsoids

When an ellipsoid intersects with a cube face, its periodic image must appear on the opposite side. The number of periodic images varies depending on the number of faces that

intersect ellipsoid i. Each periodic image of i has the same quaternion and the same linear and angular velocities as i. The offset between i and one of its periodic particles is given by the vector βe_k, where $\beta \in \{L, -L\}$ and $k \in \{1, 2, 3\}$, depending on which face the periodic particle appears.

Algorithm 5.10 describes the creation of periodic particles when an ellipsoid is in contact with one or more cube faces.

5.6 Orientations distributions of the generated packings

Orientation tensors were computed using Eqs (5.1) to verify the orientations distributions in the generated packings. θ and ϕ were obtained from the quaternions. If an ellipsoid i has the quaternion $q^i = [\alpha^i, \psi^i]$, its angles θ^i and ϕ^i are given by:

$$\theta^i = \frac{\pi}{2} - \sin^{-1}\left(2\big(\alpha^i \psi^i[2] - \psi^i[1]\psi^i[3]\big)\right) \tag{5.33a}$$

$$\phi^i = \tan2^{-1}\left(2\big(\alpha^i \psi^i[3] + \psi^i[1]\psi^i[2]\big), 1 - 2\big(\psi^i[2]^2 + \psi^i[3]^2\big)\right) \tag{5.33b}$$

Define the ratio $\rho^n = \lambda_{\max}^n / \lambda_{\min}^n$, where $\lambda_{\max}$ and $\lambda_{\min}$ denotes respectively the maximum and minimum eigenvalue of the orientation tensor and n a given realization of a random packing. Let $\bar{\rho}$ be the average value of the ρ^n. In the sequel, an ensemble of packings was considered isotropic when $\bar{\rho} \approx 1$ since $\rho^n \geq 1$.

5.7 Results and discussion

5.7.1 Examples of ellipsoids packings

Figures 5.2, 5.3, 5.4 and 5.5 show several examples of periodic packings generated with the algorithm presented in this paper. Figure 5.2a shows a packing containing 100 prolate ellipsoids ($R_1 = R_2 = 3$) with a volume fraction of 40%. Prolate ellipsoids are also shown in Figure 5.2b, but where the aspect ratios are much higher ($R_1 = R_2 = 40$) and $\mathcal{V}_f = 10\%$. Figure 5.3 presents two examples of oblate ellipsoids. Figure 5.3a shows a packing containing 100 ellipsoids occupying 40% of the space and with aspect ratios $R_1 = 3$ and $R_2 = 1$ while Figure 5.3b illustrates a packing containing 50 ellipsoids particles with aspect ratios $R_1 = 20$ and $R_2 = 1$ and a volume fraction of 15%. The algorithm can also generate ellipsoids that do not have an axis of revolution (asymmetric or scalene ellipsoids) as shown in Figure 5.4. Figure 5.4a shows 100 scalene ellipsoids with a volume fraction of 30% and aspect ratios of $R_1 = 2$ and $R_2 = 5$. Figure 5.4b shows a packing containing 1000 asymmetric ellipsoids at a volume fraction of 20% where $R_1 = 4$ and $R_2 = 0.5$. Finally, it is possible to generate

ellipsoids particles with random aspect ratios. Figure 5.5a shows 50 polydisperse ellipsoids with a volume fraction of 30% and where R_1 and R_2 range from 1 to 5. Figure 5.5b illustrates a packing of 125 ellipsoids occupying 20% of the space and where $0.1 \leq R_1, R_2 \leq 2$.

5.7.2 Orientations dispersion in the generated packings

The distribution of the packings were characterized with the orientation tensors. Two cases were considered. In the first, the ellipsoids had aspect ratios $R_1 = 2$ and $R_2 = 2$ and the volume fraction was set to 30%. In the second case, the ellipsoids occupied 10% of the space and had higher aspect ratios : $R_1 = 10$ and $R_2 = 10$. For each case, six ellipsoids numbers N were studied, namely $\{10, 25, 50, 100, 200, 500\}$.

Figure 5.6 shows the evolution of the ratio $\bar{\rho}$ as a function of N and 10 realizations. For both cases, it can be seen that $\bar{\rho} \to 1$ when N is large enough. In addition, the 95% confidence intervals are tighter as N increases. This shows that the packings generated by the algorithm are totally random and the ellipsoids orientations dispersion is uniform, even for higher aspect ratios. This will remain true even if $R_1, R_2 > 10$. Indeed, when the aspect ratios are high, it is necessary to generate smaller particles to obtain a uniform orientations distribution, and therefore, a greater number of particles for a fixed volume fraction.

5.7.3 Algorithm performance

Table 5.2 gives the maximum volume fraction reached as a function of aspect ratios R_1 and R_2 for prolate and oblate ellipsoids. During a simulation, it is considered that the maximum volume fraction is reached when the increase in the latter, after 50 successive iterations, is less

Table 5.2 Maximum volume fraction reached as a function of aspect ratios R_1 and R_2. For each case, the minimum number of ellipsoids necessary to obtain a uniform distribution of orientations is given. Approximative CPU times (averaged over 10 runs) are also indicated.

R_1	Prolate ellipsoids ($R_2 = R_1$)			Oblate ellipsoids ($R_2 = 1$)		
	$\mathcal{V}_f$	N	t_{CPU} (s)	$\mathcal{V}_f$	N	t_{CPU} (s)
2	60%	30	54.3	60%	30	52.7
5	55%	45	69.9	55%	45	65.2
10	30%	90	48.6	30%	60	39.3
20	20%	175	112.5	20%	75	47.8
30	10%	175	104.9	10%	90	53.7
40	10%	310	181.3	10%	100	92.8

than 0.1%. It is obvious that the maximum volume fraction reached decreases when the aspect ratios increase. In addition, the volume fractions limit values are identical for both prolate and oblate ellipsoids. When $R_1, R_2 \leq 10$, results are similar to those reported by Donev *et al.* (2005b). However, the authors did not present any results for which $R_1, R_2 > 10$. This is the first time that such results are reported in the literature.

Table 5.2 also provides, for each packing, the minimum number of particles required to obtain a uniform distribution of orientations. These values have been determined by varying the number of particles and by computing, for each number, the ratio ρ^n for each of the 10 random realizations. The number of particle N was considered sufficient when $\bar{\rho}$ was close to 1 (see Sections 5.6 and 5.7.2 for more details). An average CPU time (t_{CPU}) is also given for each combination of aspect ratios and volume fraction.

Donev *et al.* (2005b) reported that the binary collision computation took about 2 ms using Fortran 95 on a 1666 MHz Athlon running Linux. The proposed algorithm uses about 0.07 ms per ellipsoid binary collision using MATLAB 2011a on an Intel i7 Quad Core, 1.60 GHz, 8 GB RAM. The time saving between the two algorithm is much more important than the improvement in terms of processor. This is due to the fact that in the proposed algorithm, the collision time is obtained by finding the zero of a function while in that proposed by Donev et al, the collision time is obtained by solving two optimization subproblems. Finally, the proposed algorithm takes about 0.02 ms to compute the collision time between an ellipsoid and a cube face.

To better evaluate the influence of various parameters on the algorithm computation time, Figures 5.7, 5.8, and 5.9 show the variation of CPU time (averaged over 10 runs) with the number of particles, the volume fraction and the aspect ratio. Results are only presented for prolate ellipsoids since similar results were obtained for oblate ellipsoids. Figure 5.7 shows t_{CPU} as a function of the number of ellipsoids, for different combinations of volume fractions and aspect ratios. It seems that t_{CPU} varies linearly (on a log-log scale) with N, for $N > 100$. The average slope for the five different combinations is 1.5. Thus, $t_{\mathrm{CPU}} \propto N^{1.5}$. Figure 5.8 shows t_{CPU} as a function of the volume fraction, for a fixed aspect ratio ($R_1 = R_2 = 2$). A trend similar to that shown in Figure 5.7 is observed, whatever the number of particles N. However, the average slope is approximately 2.6, which means that $t_{\mathrm{CPU}} \propto \mathcal{V}_f^{2.6}$. Therefore, t_{CPU} seems to be more sensitive to the volume fraction than to the number of particles (for the studied ranges). On the other hand, Figure 5.9 shows that when $R_1 \leq 10$, $t_{\mathrm{CPU}} \propto R_1^{0.6}$. However, for high aspect ratios (i.e., $R_1 > 10$), $t_{\mathrm{CPU}} \propto R_1^{2.8}$. One could conclude that the aspect ratio has a negligible effect on the CPU time when its value is low (i.e. ≤ 10). This parameter becomes as dominant as the volume fraction when its value is quite high (i.e., > 10).

5.8   Conclusion

The main contribution of this paper is a detailed computationally-efficient MD algorithm for generating random packings of periodic ellipsoids. The specific contributions of this paper are :

- ⊙ The binary collision times are computed by simply finding the roots of a nonlinear function, which is a more efficient and simple technique than that presented by Donev *et al.* (2005a,b).

- ⊙ The paper puts more emphasis on periodic packings and presents a novel and efficient technique to compute the collision time between an ellipsoid and a cell face.

- ⊙ The necessary steps for processing the impact between two ellipsoids are well established and can be used for any types of ellipsoids (prolate, oblate, scalene).

- ⊙ It is the first time that ellipsoids packings with high aspect ratios (i.e., $R_1, R_2 > 10$) are presented in the literature.

- ⊙ The algorithm is comprehensive and well documented. Detailed pseudo-codes are given so the algorithm can be easily implemented by other researchers.

Computation of the orientation tensors has shown a uniform dispersion of the ellipsoids orientations in the generated packings.

Finally, packings generated with this algorithm will be used in numerical homogenization where it would be possible to study the effect of fibers orientation and aspect ratios on the mechanical effective properties of ellipsoidal (i.e., 3D) particles reinforced composites.

Acknowledgments

Appendix 5.A   Algorithms pseudo-code

Algorithm 5.1 Main Algorithm.

Input: N, R_1, R_2, $\mathcal{V}_f$

Output: $\{a, b, c\}$, $\boldsymbol{r}$ and $\boldsymbol{q}$ of all ellipsoids

. . . .

1: Define a cube of side L. Set a corner as origin.

2: **for** $i = 1 \to N$ **do**

3:      Assign a random position vector $\boldsymbol{r}^i_{(0)}$.

4:      Assign a random quaternion vector $\boldsymbol{q}^i_{(0)} = \left[\alpha^i_{(0)}, \boldsymbol{\psi}^i_{(0)} \right]$.

5:      Assign a random linear $\left(\boldsymbol{v}^i_{(0)} \right)$ and angular $\left(\boldsymbol{\omega}^i_{(0)} \right)$ velocity vector.

6:      Assign the semi-principle axis growth rate $a^i_0 = 0.1$.

7:      Compute $b^i_0 = a^i_0 / R_1$ and $c^i_0 = a^i_0 / R_2$.

8: **end for**

9: Initialize the actual volume fraction $\mathcal{V}_{(0)} = 0$.

10: **while** $\mathcal{V}_{(t)} < \mathcal{V}_f$ **do**

11:      Compute t_c using Algorithm 5.6.

12:      Compute t_s using Algorithm 5.8.

13:      Compute $\Delta t = \min(t_c, t_s)$.

14:      **for** $i = 1 \to N$ **do**

15:          Move the particle i from time t to time $(t + \Delta t)$ using Algorithm 5.2.

16:      **end for**

17:      **if** $\Delta t = t_c$ **then**

18:          Update the velocities of the concerned particles using Algorithm 5.9.

19:      **else if** $\Delta t = t_s$ **then**

20:          Create periodic image(s) of the concerned particle using Algorithm 5.10.

21:      **end if**

22:      Compute the new volume fraction: $\mathcal{V}_{(t+\Delta t)} = \dfrac{1}{L^3} \displaystyle\sum_{i=1}^{N} \dfrac{4}{3} \pi a^i_{(t+\Delta t)} b^i_{(t+\Delta t)} c^i_{(t+\Delta t)}$.

23:      $t \leftarrow t + \Delta t$.

24: **end while**

25: Perform a scaling by reducing $\left\{ a^i_{(t+\Delta t)}, b^i_{(t+\Delta t)}, c^i_{(t+\Delta t)} \right\}$ in order to reach $\mathcal{V}_{(t+\Delta t)} = \mathcal{V}_f$.

Algorithm 5.2 Moving an ellipsoid i between time t and time $(t + \Delta t)$

Input: $r^i_{(t)}$, $q^i_{(t)} = \left[\alpha^i_{(t)}, \psi^i_{(t)}\right]$, v^i, ω^i, $\left\{a^i_{(t)}, b^i_{(t)}, c^i_{(t)}\right\}$, $\left\{a^i_0, b^i_0, c^i_0\right\}$, Δt

Output: $\left\{a^i_{(t+\Delta t)}, b^i_{(t+\Delta t)}, c^i_{(t+\Delta t)}\right\}$, $r^i_{(t+\Delta t)}$, $q^i_{(t+\Delta t)}$, $\mathbf{A}^i_{(t+\Delta t)}$, $\mathbf{R}^i_{(t+\Delta t)}$, $\mathbf{M}^i_{(t+\Delta t)}$

....

1: Compute the new position $r^i_{(t+\Delta t)}$ using Eq. (5.8).
2: Compute $a^i_{(t+\Delta t)}$, $b^i_{(t+\Delta t)}$ and $c^i_{(t+\Delta t)}$ using Eq. (5.9).
3: Compute the quaternion $q^i_{\Delta t}$ using Eq. (5.10).
4: Compute the quaternion $q^i_{(t+\Delta t)}$ using Eq. (5.11).
5: Compute $\mathbf{R}^i_{(t+\Delta t)}$ and $\mathbf{M}^i_{(t+\Delta t)}$ using Eqs. (5.5) and (5.6b).
6: Compute $\mathbf{A}'^i_{(t+\Delta t)}$ using Eq. (5.2b).
7: Compute $\mathbf{A}^i_{(t+\Delta t)}$ using Eq. (5.12b).

Algorithm 5.3 Computing the coefficients $p_{k(t)}$ of Eq. (5.13) for ellipsoids i and j

Input: $\mathbf{M}^i_{(t)}$, $\left\{a^i_{(t)}, b^i_{(t)}, c^i_{(t)}\right\}$, $\mathbf{A}^j_{(t)}$.

Output: $p_{k(t)}$

....

1: Compute $\mathbf{C} = \left(\mathbf{M}^i_{(t)}\right)^\top \mathbf{A}^j_{(t)} \left(\mathbf{M}^i_{(t)}\right)$.
2: Let $\delta_1 = \left(1/a^i_{(t)}\right)^2$, $\delta_2 = \left(1/b^i_{(t)}\right)^2$ and $\delta_3 = \left(1/c^i_{(t)}\right)^2$.
3: Compute $p_{1(t)} = -\delta_1 \delta_2 \delta_3$.
4: Compute $p_{2(t)} = -\left(\delta_2 \delta_3 C_{11} + \delta_1 \delta_3 C_{22} + \delta_1 \delta_2 C_{33} - \delta_1 \delta_2 \delta_3 C_{44}\right)$.
5: Compute $p_{3(t)} = \delta_1 \delta_2 \left(C_{33} C_{44} - C_{34} C_{43}\right) + \delta_2 \delta_3 \left(C_{11} C_{44} - C_{14} C_{41}\right) + \delta_1 \delta_3 \left(C_{22} C_{44} - C_{24} C_{42}\right) + \delta_1 \left(C_{23} C_{32} - C_{22} C_{33}\right) + \delta_2 \left(C_{13} C_{31} - C_{11} C_{33}\right) + \delta_3 \left(C_{12} C_{21} - C_{11} C_{22}\right)$.
6: Compute $p_{4(t)} =$
$\delta_1 \left(C_{22} C_{33} C_{44} - C_{22} C_{34} C_{43} - C_{33} C_{42} C_{24} - C_{44} C_{32} C_{23} + C_{32} C_{24} C_{43} + C_{42} C_{23} C_{34}\right) +$
$\delta_2 \left(C_{11} C_{33} C_{44} - C_{11} C_{34} C_{43} - C_{33} C_{14} C_{41} - C_{44} C_{13} C_{31} + C_{31} C_{14} C_{43} + C_{41} C_{13} C_{34}\right) +$
$\delta_3 \left(C_{11} C_{22} C_{44} - C_{11} C_{24} C_{42} - C_{22} C_{14} C_{41} - C_{44} C_{12} C_{21} + C_{21} C_{14} C_{42} + C_{41} C_{12} C_{24}\right) +$
$C_{11} C_{23} C_{32} + C_{22} C_{13} C_{31} + C_{33} C_{12} C_{21} - C_{11} C_{22} C_{33} - C_{21} C_{13} C_{32} - C_{31} C_{12} C_{23}$.
7: Compute $p_{5(t)} = \det\left(\mathbf{A}^j_{(t)}\right)$.

Algorithm 5.4 Computing the coeffcients $\eta_{k(t)}$ for ellipsoids i and j

Input: $p_{k(t)}$

Output: $\eta_{k(t)}$

....

1: Compute $\bar{p}_1 = -p_{2(t)}/(4p_{1(t)})$, $\bar{p}_2 = p_{3(t)}/(6p_{1(t)})$, $\bar{p}_3 = -p_{4(t)}/(4p_{1(t)})$ and $\bar{p}_4 = p_{5(t)}/p_{1(t)}$.

2: Compute $\beta_1 = \left(\bar{p}_4 - \bar{p}_1\bar{p}_3\right) + 3\left(\bar{p}_2^2 - \bar{p}_1\bar{p}_3\right)$.

3: Compute $\beta_2 = -\bar{p}_3\left(\bar{p}_3 - \bar{p}_1\bar{p}_2\right) - \bar{p}_4\left(\bar{p}_1^2 - \bar{p}_2\right) - \bar{p}_2\left(\bar{p}_2^2 - \bar{p}_1\bar{p}_3\right)$.

4: Compute $\eta_{1(t)} = \beta_1^3 - 27\beta_2^2$.

5: Compute $\eta_{2(t)} = -9\left(\bar{p}_3 - \bar{p}_1\bar{p}_2\right)^2 + 27\left(\bar{p}_1^2 - \bar{p}_2\right)\left(\bar{p}_2^2 - \bar{p}_1\bar{p}_3\right) - 3\left(\bar{p}_4 - \bar{p}_1\bar{p}_3\right)\left(\bar{p}_1^2 - \bar{p}_2\right)$.

6: Compute $\eta_{3(t)} = \beta_1\left(\bar{p}_3 - \bar{p}_1\bar{p}_2\right) - 3\bar{p}_1\beta_2$.

7: Compute $\eta_{4(t)} = -\left(\bar{p}_4 - \bar{p}_1\bar{p}_3\right)$.

8: Compute $\eta_{5(t)} = \left(\bar{p}_1^2 - \bar{p}_2\right)$.

Algorithm 5.5 Function $\eta_{k(t+\Delta t)}$ for ellipsoids i and j

Input: Δt

Output: $\eta_{k(t+\Delta t)}$

....

1: Compute $\left\{a^i_{(t+\Delta t)}, b^i_{(t+\Delta t)}, c^i_{(t+\Delta t)}\right\}$ and $\mathbf{M}^i_{(t+\Delta t)}$ for ellipsoid i using Algorithm 5.2.

2: Compute $\mathbf{A}^j_{(t+\Delta t)}$ for ellipsoid j using Algorithm 5.2.

3: Compute $p_{k(t+\Delta t)}$ using Algorithm 5.3.

4: Compute $\left\{\eta_{1(t+\Delta t)}, \eta_{2(t+\Delta t)}, \eta_{3(t+\Delta t)}, \eta_{4(t+\Delta t)}, \eta_{5(t+\Delta t)}\right\}$ using Algorithm 5.4.

Algorithm 5.6 Finding the next binary collision time (Part 1)

Input: $\{a_{(t)}, b_{(t)}, c_{(t)}\}$, $\{a_0, b_0, c_0\}$, $\boldsymbol{r}_{(t)}$, $\boldsymbol{q}_{(t)}$, $\boldsymbol{v}$, $\boldsymbol{\omega}$ of all ellipsoids
Output: t_c, $\boldsymbol{x}_c$

. . . .

1: Set $t_{\min} = $ `realmax` and $\mu = 1.2$.
2: **for** $i = 1 \to N - 1$ (including periodic ellipsoids) **do**
3:     **for** $j = i + 1 \to N$ (including periodic ellipsoids) **do**
4:         **if** $\boldsymbol{v}^i$ or $\boldsymbol{v}^j$ have changed since last iteration **then**
5:             Compute $R^r_{(t)} = \max\left(a^r_{(t)}, b^r_{(t)}, c^r_{(t)}\right)$ and $R^r_0 = \max\left(a^r_0, b^r_0, c^r_0\right)$ where $r = \{i, j\}$.
6:             Compute t^{BS}_c using Eqs. (5.15) and (5.16).
7:             **if** $0 \le t^{BS}_c < t_{\min}$ **then**
8:                 Define ellipsoids N_i and N_j using μ.
9:                 Compute $\eta_{k(t)}$ for N_i and N_j using Algorithm 5.5 (use $\Delta t = 0$).
10:                **if** N_i and N_j are externally tangent or overlap **then**
11:                    $\text{test}_1 = $ `true`.
12:                **else**
13:                    $\text{test}_1 = $ `false`.
14:                **end if**
15:             **else**
16:                $\text{test}_1 = $ `false`.
17:             **end if**
18:             **if** $\text{test}_1 = $ `true` **then**
19:                Define the function $\eta_{1(t+\Delta t)}$ using Algorithm 5.5.
20:                Compute all roots of $\eta_{1(t+\Delta t)}$: $\Delta t_1 < \Delta t_2 < \ldots < \Delta t_n$.
21:                $\text{test}_2 = $ `false`.
22:                **for** $p = 1 \to n$ **do**
23:                   Compute $\eta_{k(t+\Delta t_p)}$ for i and j using Algorithm 5.5.
24:                   **if** $\left\{\eta_{1(t+\Delta t_p)} = 0,\ \eta_{2(t+\Delta t_p)} > 0,\ \eta_{3(t+\Delta t_p)} < 0 \text{ and } \eta_{5(t+\Delta t_p)} > 0\right\}$ or
$\left\{\eta_{1(t+\Delta t_p)} = 0,\ \eta_{2(t+\Delta t_p)} = 0,\ \eta_{4(t+\Delta t_p)} < 0 \text{ and } \eta_{5(t+\Delta t_p)} > 0\right\}$ **then**
25:                     Compute $t_{\min} = \min(\Delta t_p, t_{\min})$.
26:                     $\text{test}_2 = $ `true`.
27:                     **break**
28:                   **end if**
29:                **end for**

Algorithm 5.6 Finding the next binary collision time (Part 2)

30:                **if** $\text{test}_2 = $ `false` **then**

31:                    **Return** No collision between i and j.

32:                **end if**

33:            **else**

34:                **Return** No collision between i and j.

35:                **end if**

36:         **else**

37:             Deduce the binary collision time Δt from last iteration.

38:             Compute $t_{\min} = \min(\Delta t, t_{\min})$.

39:         **end if**

40:      **end for**

41: **end for**

42: Set $t_c = t_{\min}$.

43: Compute $\mathbf{A}^i_{(t+t_c)}$ and $\mathbf{A}^i_{(t+t_c)}$ using Algorithm 5.2.

44: Compute the eigenvalues of matrix $\left(\mathbf{A}^i_{(t+t_c)}\right)^{-1}\mathbf{A}^j_{(t+t_c)}$.

45: Search for the double positive eigenvalue λ_0.

46: Compute $\boldsymbol{x}_c$ using Eq. (5.14).

Algorithm 5.7 Function $g^{\dagger}_{(t+\Delta t)}$ between an ellipsoid i and a cube face $x_k = \beta$

Input: Δt

Output: $g^{\dagger}_{(t+\Delta t)}$

. . . .

1: Compute $\mathbf{A}^i_{(t+\Delta t)}$ using Algorithm 5.2.

2: Deduce $\mathbf{B}^i_{(t+\Delta t)}$, $\boldsymbol{d}^i_{(t+\Delta t)}$ and $F^i_{(t+\Delta t)}$ using Eq. (5.17).

3: Compute $\mathbf{P}$ and $\boldsymbol{p}$ using Eq. (5.19b).

4: Compute $\mathbf{B}^{i*}_{(t+\Delta t)}$, $\boldsymbol{d}^{i*}_{(t+\Delta t)}$ and $F^{i*}_{(t+\Delta t)}$ using Eq. (5.21b).

5: Compute $g^{\dagger}_{(t+\Delta t)}$ using Eq. (5.23).

Algorithm 5.8 Finding the next collision time between an ellipsoid and a cube face

Input: $\left\{a_{(t)}, b_{(t)}, c_{(t)}\right\}$, $\left\{a_0, b_0, c_0\right\}$, $\boldsymbol{r}_{(t)}$, $\boldsymbol{q}_{(t)}$, $\boldsymbol{v}$, $\boldsymbol{\omega}$ of all ellipsoids
Output: t_s

....

1: Set $t_{min} = \texttt{realmax}$.
2: **for** $i = 1 \rightarrow N$ **do**
3:      Compute $R^i_{(t)} = \max\left(a^i_{(t)}, b^i_{(t)}, c^i_{(t)}\right)$ and $R^i_0 = \max\left(a^i_0, b^i_0, c^i_0\right)$.
4:      **for** $k = 1 \rightarrow 3$ **do**
5:          **for** $\beta = \{0, L\}$ **do**
6:             **if** $\boldsymbol{v}^i$ has changed since last iteration **then**
7:                 **if** particle i does not intersect the cube face $x_k = \beta$ **then**
8:                     Compute t^{BS}_s using Eqs. (5.24) and (5.25).
9:                     **if** $0 \leq t^{BS}_s < t_{\min}$ **then**
10:                         Define the function $g^{\dagger}_{(t+\Delta t)}$ using Algorithm 5.7.
11:                         Compute all n roots of $g^{\dagger}_{(t+\Delta t)}$: $\Delta t_1 < \Delta t_2 < \ldots < \Delta t_n$.
12:                         **if** $n \neq 0$ **then**
13:                           Compute $t_{\min} = \min(\Delta t_1, t_{\min})$.
14:                         **else**
15:                           **Return** No collision between i and $x_k = \beta$.
16:                         **end if**
17:                   **else**
18:                       **Return** No collision between i and $x_k = \beta$.
19:                   **end if**
20:               **end if**
21:           **else**
22:               Deduce the collision time Δt from last iteration.
23:               Compute $t_{\min} = \min(\Delta t, t_{\min})$.
24:           **end if**
25:          **end for**
26:      **end for**
27: **end for**
28: Set $t_s = t_{\min}$.

Algorithm 5.9 Computing velocities after impact at time $t = t_c$

Input: $\boldsymbol{r}^i_{(t)}$, $\boldsymbol{r}^j_{(t)}$, $\boldsymbol{q}^i_{(t)}$, $\boldsymbol{q}^j_{(t)}$, $\boldsymbol{v}^{i-}$, $\boldsymbol{v}^{j-}$, $\boldsymbol{\omega}^{i-}$, $\boldsymbol{\omega}^{j-}$, $\{a^i_{(t)}, b^i_{(t)}, c^i_{(t)}\}$, $\{a^j_{(t)}, b^j_{(t)}, c^j_{(t)}\}$, $\{a^i_0, b^i_0, c^i_0\}$, $\{a^j_0, b^j_0, c^j_0\}$, $\boldsymbol{x}_c$

Output: $\boldsymbol{v}^{i+}$, $\boldsymbol{v}^{j+}$, $\boldsymbol{\omega}^{i+}$, $\boldsymbol{\omega}^{j+}$

. . . .

1: Compute $\mathbf{A}^r_{(t)}$, $\mathbf{R}^r_{(t)}$ using Algorithm 5.2, where $r = \{i, j\}$.

2: Compute $\boldsymbol{n}$ using Eq. (5.26).

3: Compute $\boldsymbol{t_1}$ and $\boldsymbol{t_2}$ such that $\boldsymbol{t_1} \times \boldsymbol{t_2} = \boldsymbol{n}$.

4: Compute $m^r_{(t)}$ and $\mathbf{H}''^r_{(t)}$ using Eq. (5.27a) and (5.27b), where $r = \{i, j\}$.

5: Compute $\mathbf{H}^r_{(t)}$ using Eq. (5.28), where $r = \{i, j\}$.

6: Define the linear equations system using Eqs. (5.29), (5.30), (5.31) and (5.32).

7: Solve the equations system to find $\boldsymbol{v}^{i+}$, $\boldsymbol{v}^{j+}$, $\boldsymbol{\omega}^{i+}$ and $\boldsymbol{\omega}^{j+}$.

8: **if** ellipsoid i has P^i periodic image(s) $(P^i \neq 0)$ **then**

9:      **for** $p = 1 \to P^i$ **do**

10:           $\boldsymbol{v}^p = \boldsymbol{v}^{i+}$.

11:           $\boldsymbol{\omega}^p = \boldsymbol{\omega}^{i+}$.

12:      **end for**

13: **end if**

14: **if** ellipsoid j has P^j periodic image(s) $(P^j \neq 0)$ **then**

15:      **for** $p = 1 \to P^j$ **do**

16:           $\boldsymbol{v}^p = \boldsymbol{v}^{j+}$.

17:           $\boldsymbol{\omega}^p = \boldsymbol{\omega}^{j+}$.

18:      **end for**

19: **end if**

Algorithm 5.10 Creation of periodic images following the collision between a particle and the cube faces at time $t = t_s$

Input: $\boldsymbol{r}^i_{(t)}$, $\boldsymbol{q}^i_{(t)}$, $\boldsymbol{v}^i$, $\boldsymbol{\omega}^i$, $\left\{a^i_{(t)}, b^i_{(t)}, c^i_{(t)}\right\}$, $\left\{a^i_0, b^i_0, c^i_0\right\}$

Output: Periodic particles of ellipsoid i

. . . .

1: Suppose that particle i collided with m faces.

2: **if** $m = 1$ **then**

3:     $P^i = 1$.

4: **else if** $m = 2$ **then**.

5:     $P^i = 3$.

6: **else if** $m = 3$ **then**

7:     $P^i = 7$.

8: **end if**

9: Create P^i periodic image(s) of ellipsoid i.

10: **for** $p = 1 \rightarrow P^i$ **do**

11:     $\boldsymbol{r}^p_{(t)} = \boldsymbol{r}^i_{(t)} + \beta\boldsymbol{e}_k$ where $\beta \in \{L, -L\}$ and $k \in \{1, 2, 3\}$.

12:     $\boldsymbol{q}^p_{(t)} = \boldsymbol{q}^i_{(t)}$.

13:     $\boldsymbol{v}^p = \boldsymbol{v}^i$.

14:     $\boldsymbol{\omega}^p = \boldsymbol{\omega}^i$.

15: **end for**

(a)

(b)
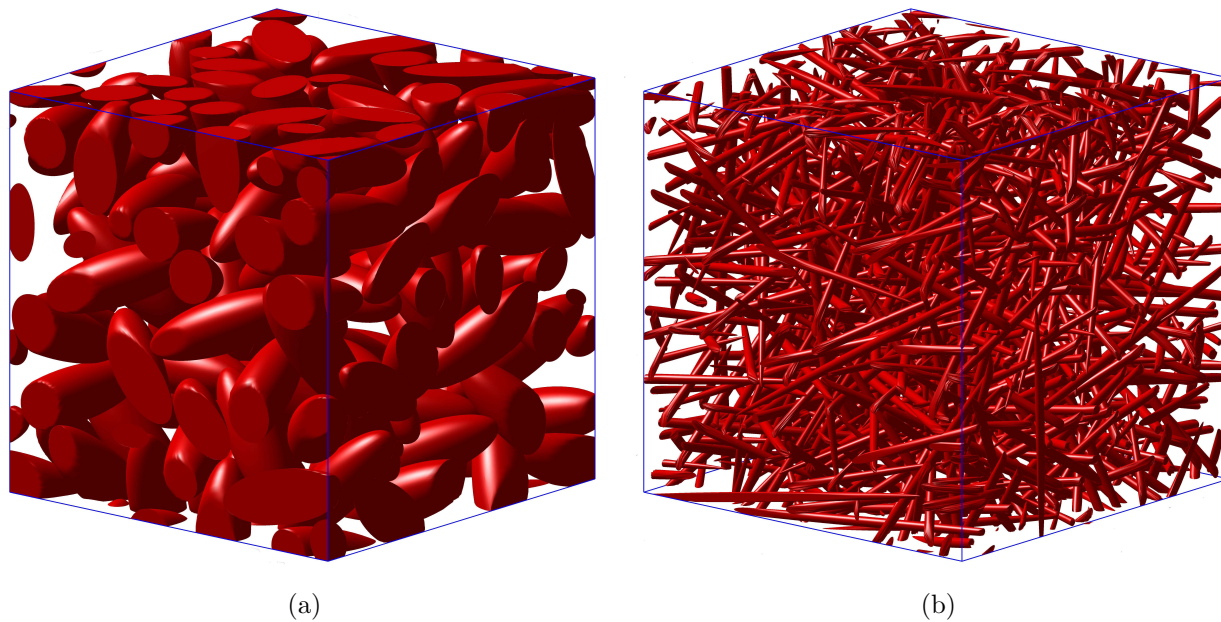
Figure 5.2 Random packings of prolate ellipsoids. (a) $N = 100$, $R_1 = 3$, $R_2 = 3$, $\mathcal{V}_f = 40\%$. (b) $N = 300$, $R_1 = 40$, $R_2 = 40$, $\mathcal{V}_f = 10\%$.

(a)

(b)
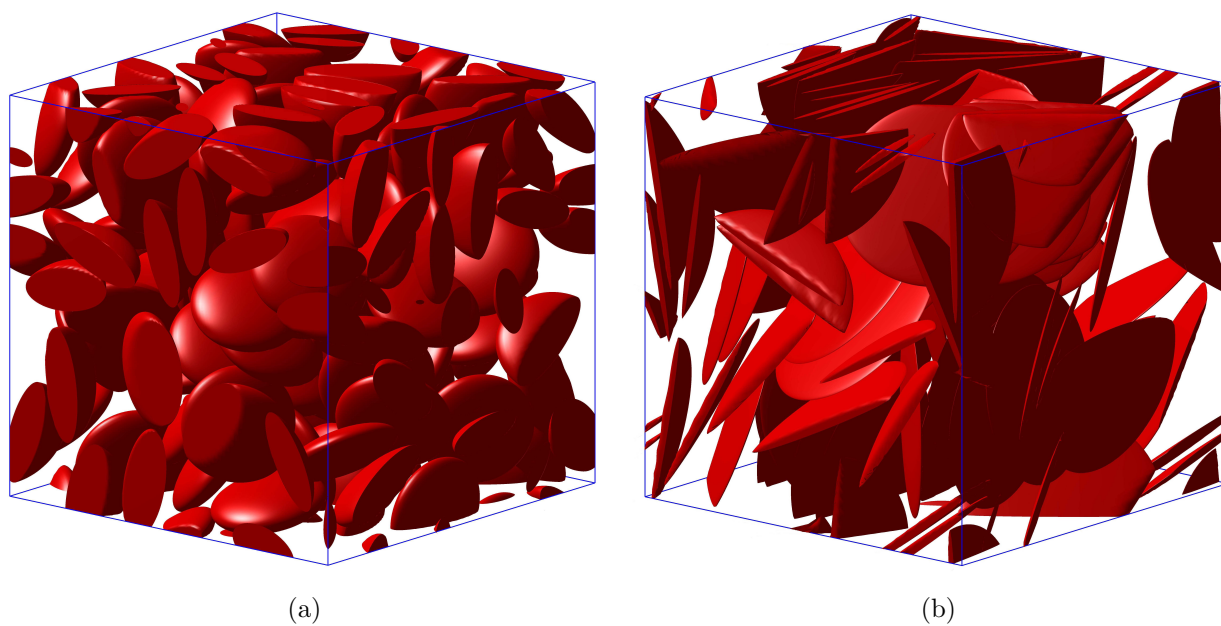
Figure 5.3 Random packings of oblate ellipsoids. (a) $N = 100$, $R_1 = 3$, $R_2 = 1$, $\mathcal{V}_f = 40\%$. (b) $N = 50$, $R_1 = 20$, $R_2 = 1$, $\mathcal{V}_f = 15\%$.
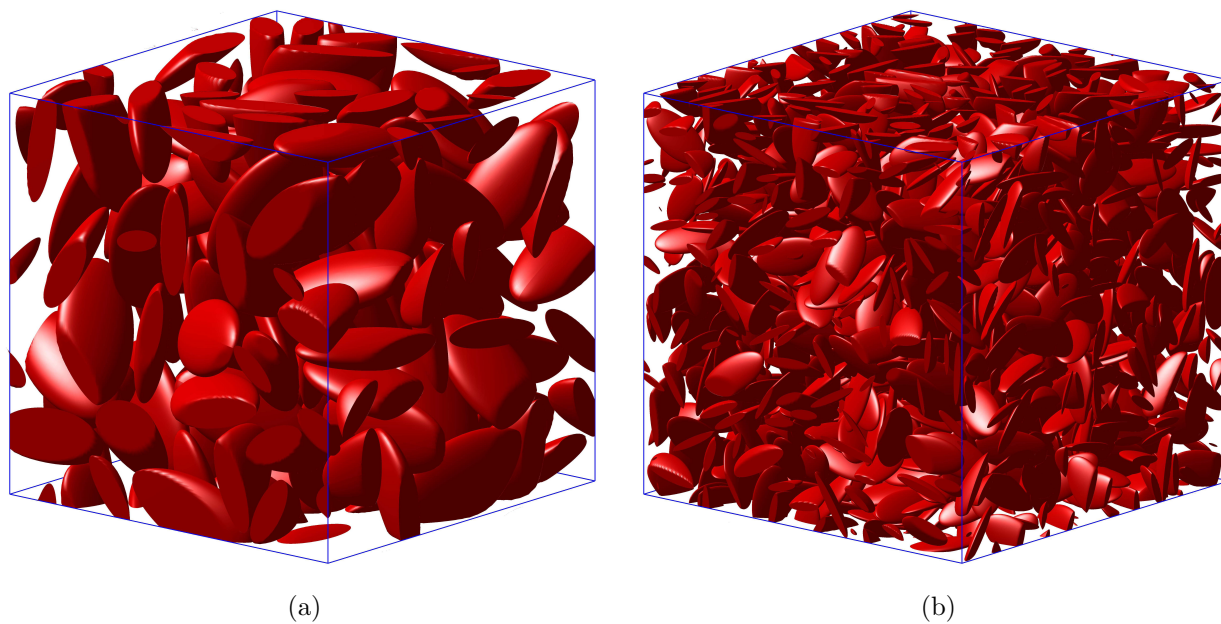
Figure 5.4 Random packings of scalene ellipsoids. (a) $N = 100$, $R_1 = 2$, $R_2 = 5$, $\mathcal{V}_f = 30\%$. (b) $N = 1000$, $R_1 = 4$, $R_2 = 0.5$, $\mathcal{V}_f = 20\%$.
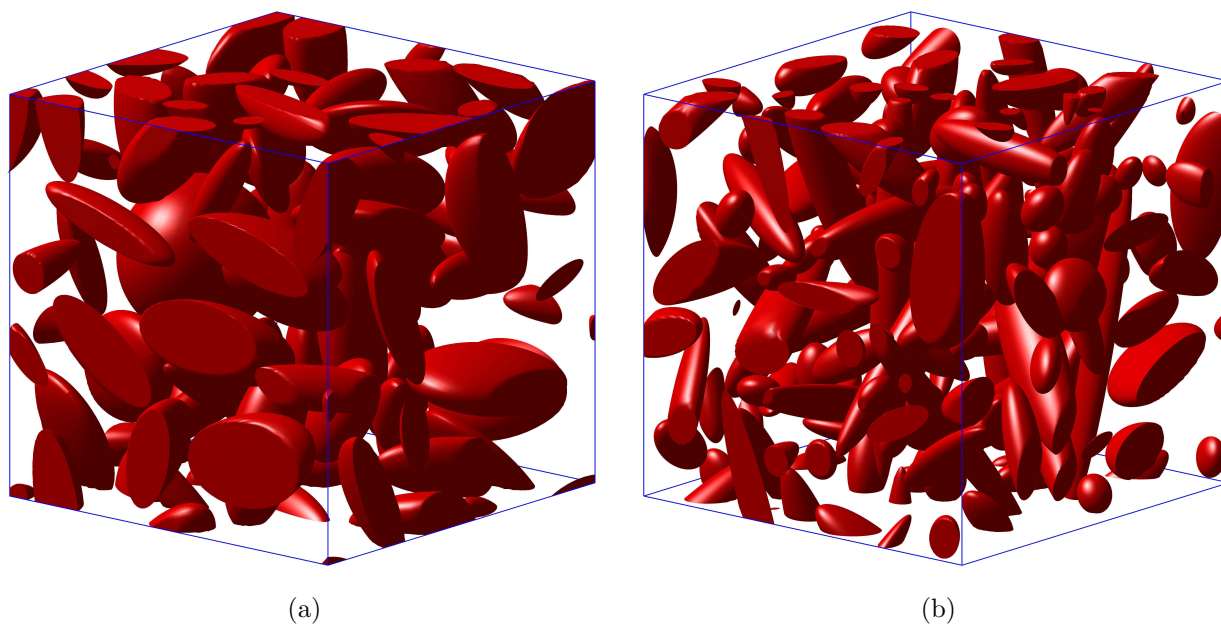
Figure 5.5 Random packings of polydisperse ellipsoids. (a) $N = 50$, $1 \leq R_1, R_2 \leq 5$, $\mathcal{V}_f = 30\%$. (b) $N = 125$, $0.1 \leq R_1, R_2 \leq 2$, $\mathcal{V}_f = 20\%$.
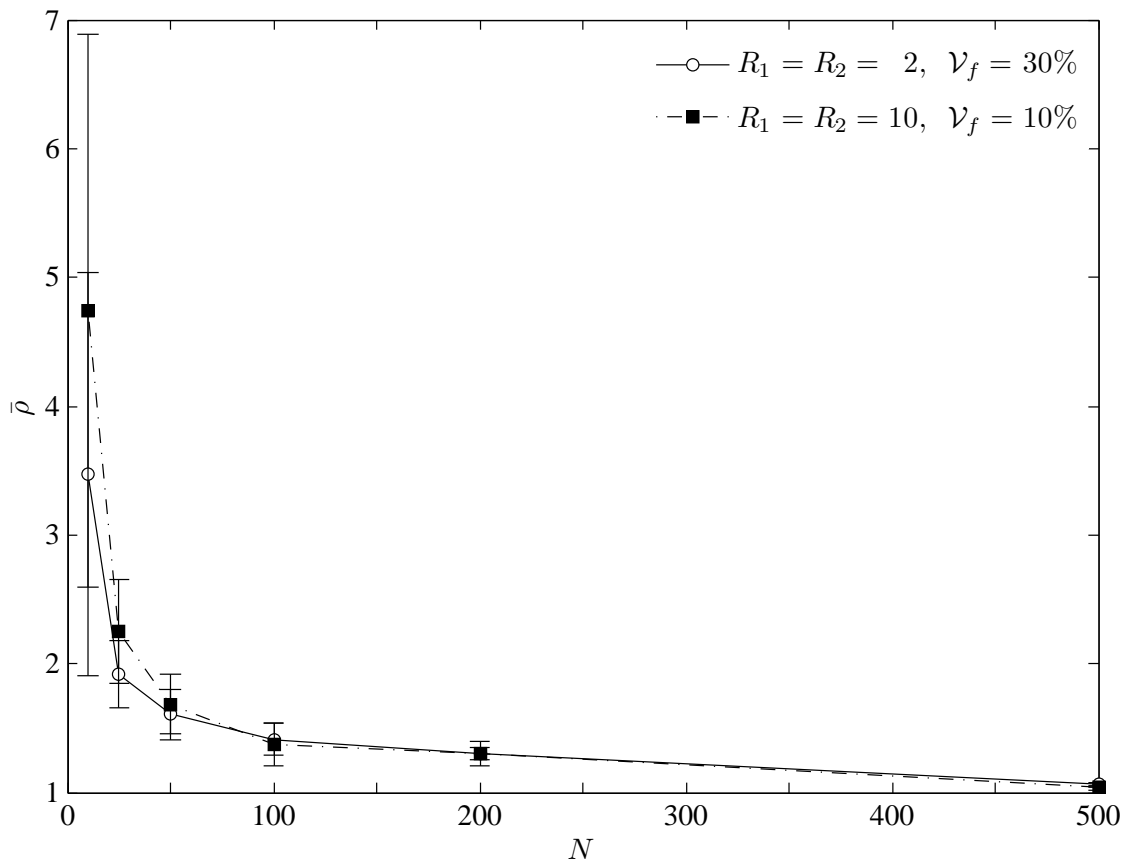
Figure 5.6 Ratio $\bar{\rho}$ as a function of the ellipsoids number N. Each point represents the mean value obtained for 10 random realizations. 95% confidence intervals are shown.
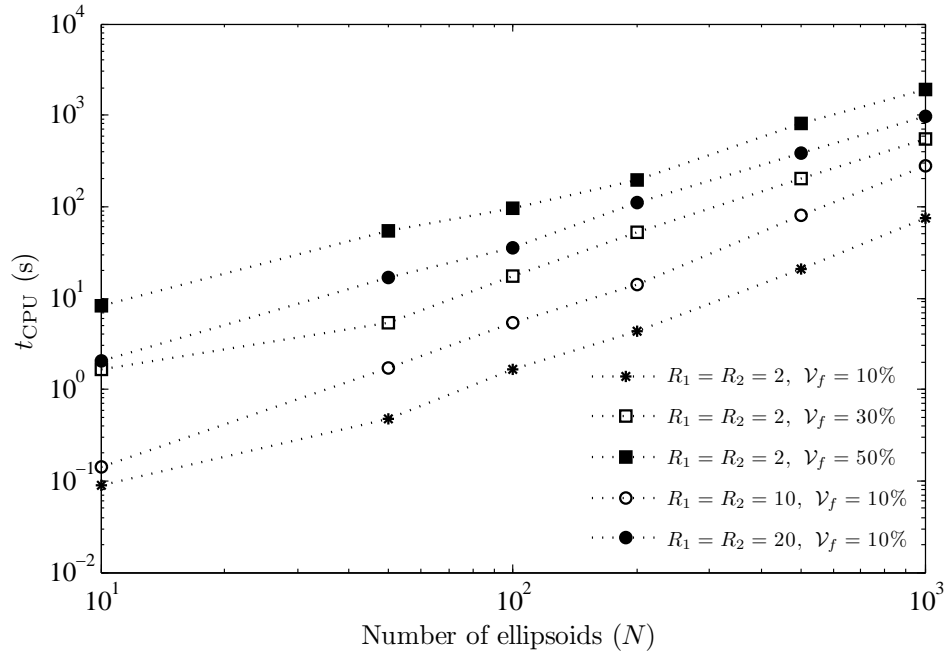
Figure 5.7 CPU time (averaged over 10 realizations) as a function of the ellipsoids number (prolate).
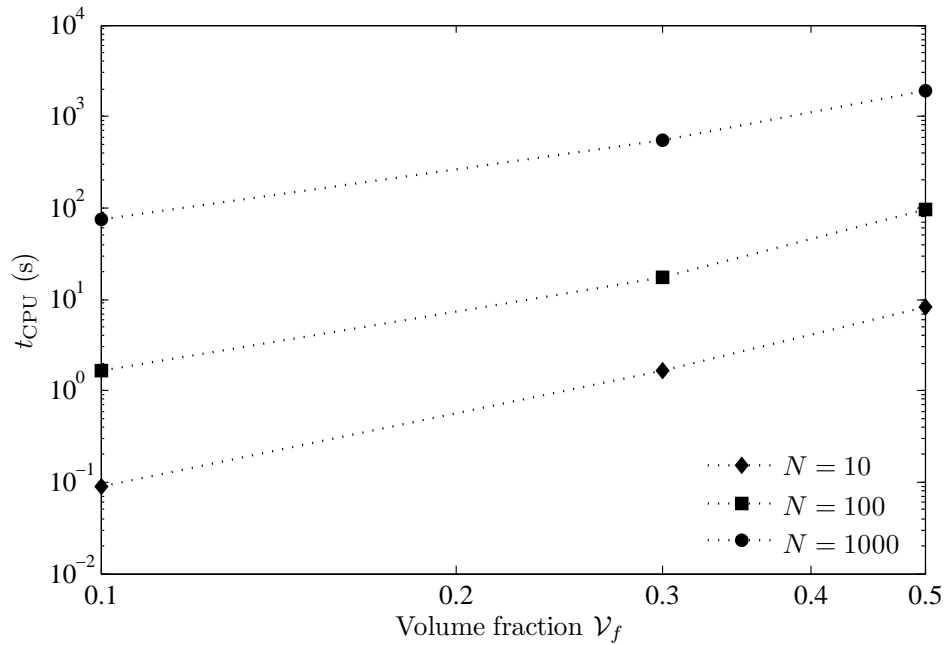
Figure 5.8 CPU time (averaged over 10 realizations) as a function of the volume fraction for prolate ellipsoids. $R1 = 2$, $R_2 = 2$.
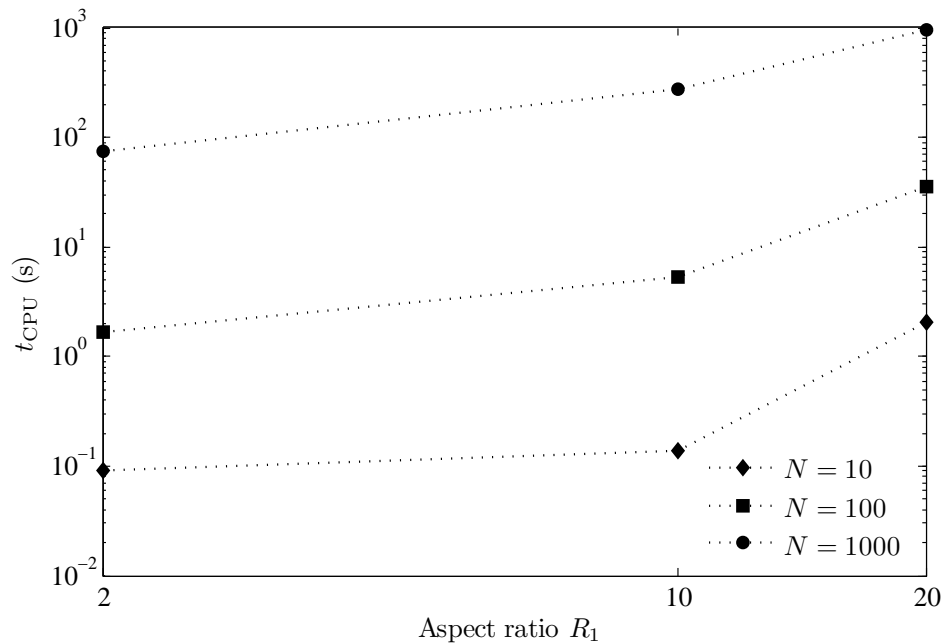
Figure 5.9 CPU time (averaged over 10 realizations) as a function of the aspect ratio for prolate ellipsoids. $\mathcal{V}_f = 10\%$.

CHAPTER 6

ARTICLE 3: A COMPREHENSIVE VALIDATION OF ANALYTICAL HOMOGENIZATION MODELS: THE CASE OF ELLIPSOIDAL PARTICLES REINFORCED COMPOSITES

E. Ghossein and M. Lévesque (2014). *Mechanics of Materials*, 75, pp. 135–150.

6.1   Abstract

This paper presents a rigorous and exhaustive evaluation of the analytical homogenization models accuracy for the case of randomly distributed and oriented ellipsoidal fibers reinforced composites. Artificial random microstructures were generated using a molecular dynamics (MD) algorithm. Numerical effective properties were computed using a Fast Fourier Transforms (FFT) based technique. The numerical predictions were compared to those of the analytical models for a wide range of phases mechanical properties, fibers volume fractions and aspect ratios. The validation campaign involved a rigorous Representative Volume Element (RVE) determination process and approximately, 66000 simulations were performed. The results show that the analytical models accuracy is more sensitive to the mechanical properties contrasts than to the fibers volume fraction and aspect ratio. Among all the studied models, Lielens' model remains the most accurate, especially for high contrasts and volume fractions. For high aspect ratio fibers, Lielens's model and Beveniste's interpretation of the Mori-Tanaka model provide similar estimates, especially when predicting the effective shear modulus. In this case, the latter could be an alternative to Lielens' model, especially for composites where the fibers are not completely stiffer than the matrix. All conclusions of this study apply to both prolate and oblate ellipsoidal fibers.

6.2   Introduction

Homogenization models rely on microstructural information (e.g., constituents properties, volume fractions, shapes, orientations, etc.) to predict the effective properties of heterogeneous materials. Several analytical homogenization models have been developed for predicting the mechanical properties of ellipsoidal fibers reinforced composites, such as the dilute solution of Eshelby (Eshelby, 1957), the Hashin-Shtrikman bounds (Hashin, 1962; Hashin and Shtrikman, 1963), the self-consistent scheme (Budiansky, 1965; Hill, 1965), the Mori-Tanaka

model (Mori and Tanaka, 1973; Benveniste, 1987), the model of Ponte Castaneda and Willis (Castaneda and Willis, 1995) and Lielens' model (Lielens *et al.*, 1998), among others.

To the knowledge of the authors, no study rigorously and thoroughly dealt with the performance evaluation of these models for a wide range of phases mechanical properties, fibers volume fractions and aspect ratios, in three dimensions. Tucker and Liang (1999) compared the predictions of a limited number of models against finite element simulations for aligned fibers reinforced composites. Other works have studied the case of Randomly Oriented Fiber Reinforced Composites (ROFRC) (Bohm *et al.*, 2002; Lusti and Gusev, 2004; Kari *et al.*, 2007a; Mortazavi *et al.*, 2013; Moussaddy *et al.*, 2013a) and spherical particles reinforced composites (Bohm and Han, 2001; Pierard *et al.*, 2004; Marur, 2004; Kari *et al.*, 2007b; Klusemann and Svendsen, 2010; Cojocaru and Karlsson, 2010; Ghossein and Levesque, 2012). Several researchers were also interested in the validity domains of micromechanical models when predicting the elastic properties of microstructures with aligned and randomly oriented clay platelets (Sheng *et al.*, 2004; Hbaieb *et al.*, 2007; Figiel and Buckley, 2009; Pahlavanpour *et al.*, 2013). These studies dealt with a very narrow range of fiber/matrix rigidity contrasts, i.e., Young's modulus of the fibers divided by the Young's modulus of the matrix, for isotropic constituents, lower than 30 (Bohm and Han, 2001; Pierard *et al.*, 2004; Marur, 2004; Sheng *et al.*, 2004; Kari *et al.*, 2007a,b; Cojocaru and Karlsson, 2010) and fibers aspect ratio, i.e., length divided by diameter inferior to 5 (Bohm *et al.*, 2002; Hua and Gu, 2013). Furthermore, some authors have limited their work to low reinforcements volume fractions ($\leq 3\%$), and eluded the rigorous evaluation of the Representative Volume Element (RVE) (Lusti and Gusev, 2004; Mortazavi *et al.*, 2013).

The aim of this paper is to rigorously and thoroughly validate the performance of analytical homogenization models for two-phase composites reinforced by randomly distributed and oriented ellipsoidal fibers with a fully automated numerical procedure based on Fast Fourier Transforms (FFT) (Moulinec and Suquet, 1998). The paper is organized as follows: Section 6.3 presents a literature review on analytical and numerical homogenization. The first part reviews the different analytical homogenization models for predicting the elastic properties of ellipsoidal particles reinforced composites. The second presents the main algorithms used in the literature for generating random microstructures, as well as the different numerical techniques for computing their effective properties. Section 6.4 summarizes the algorithms implemented in the numerical tool for generating ellipsoidal fibers reinforced microstructures. The algorithm used to compute the effective properties is presented in Section 6.5. Section 6.6 describes the methodology adopted for the validation campaign. A rigorous and comprehensive validation of several homogenization models is performed in Section 6.7. Effective properties predicted by analytical models are compared to those obtained numerically. A

discussion and analysis of the results concludes the paper.

The Einstein summation convention has been adopted, unless specified otherwise. Lower case letters (e.g., a, α) and boldfaced lower case Latin letters (e.g., $\boldsymbol{a}$) denote respectively scalars and vectors; boldfaced lower case Greek letters (e.g., $\boldsymbol{\alpha}$) and boldfaced upper case Latin letters (e.g., $\mathbf{A}$) denote respectively second and fourth order tensors.

6.3 Background

6.3.1 Analytical homogenization models

The overall elasticity tensor of a two-phase composite is given by:

$$\widetilde{\mathbf{C}} = \mathbf{C}_1 + c_2\Big\langle \big(\mathbf{C}_2 - \mathbf{C}_1\big) : \mathbf{A} \Big\rangle \tag{6.1}$$

where $\mathbf{C}_i$ and c_i denote respectively the stiffness tensor and the volume fraction of phase "i" while $\mathbf{A}$ denotes the strain-localization tensor related to each model. Subscripts "1" and "2" refer to the matrix and fibers, respectively, and $\langle \mathbf{M} \rangle$ represents orientation averaging of a given tensor $\mathbf{M}$, such as:

$$\big\langle \mathrm{M}_{ijkl} \big\rangle = \frac{1}{2\pi^2} \int\limits_{-\pi}^{\pi} \int\limits_{0}^{\pi} \int\limits_{0}^{\pi/2} \omega_{im}\omega_{jn}\omega_{ko}\omega_{lp}\mathrm{M}_{mnop} \sin(\phi)\mathrm{d}\theta\mathrm{d}\phi\mathrm{d}\psi \tag{6.2}$$

where θ, ϕ and ψ refers to the Euler angles and $\boldsymbol{\omega}$ denotes the rotation tensor (Odegard et $al.$, 2003).

The strain-localization tensor for Eshelby's dilute solution is (Eshelby, 1957):

$$\mathbf{A}^{\mathrm{Esh}} = \Big[\mathbf{I} + \mathbf{S}_1 : \mathbf{C}_1^{-1} : \big(\mathbf{C}_2 - \mathbf{C}_1\big)\Big]^{-1} \tag{6.3}$$

where $\mathbf{I}$ is the identity tensor. $\mathbf{S}_1$ is Eshelby's tensor computed using the matrix mechanical properties and depends on the ellipsoidal fibers aspect ratios.

The strain-localization tensor for the self-consistent model is given by (Budiansky, 1965; Hill, 1965):

$$\mathbf{A}^{\mathrm{SC}} = \Big[\mathbf{I} + \widetilde{\mathbf{S}} : \widetilde{\mathbf{C}}^{-1} : \big(\mathbf{C}_2 - \widetilde{\mathbf{C}}\big)\Big]^{-1} \tag{6.4}$$

where $\widetilde{\mathbf{S}}$ is Eshelby's tensor obtained by considering the effective composite as the infinite media. Since $\widetilde{\mathbf{S}}$ and $\widetilde{\mathbf{C}}$ are initially unknown, the self consistent scheme is an implicit model that is iteratively solved.

In the Mori-Tanaka model, $\mathbf{A}$ is written as (Mori and Tanaka, 1973):

$$\mathbf{A}^{\mathrm{MT}} = \mathbf{T} : \left[c_1\mathbf{I} + c_2\mathbf{T}\right]^{-1} \tag{6.5a}$$

where:

$$\mathbf{T} = \mathbf{A}^{\mathrm{Esh}} = \left[\mathbf{I} + \mathbf{S}_1 : \mathbf{C}_1^{-1} : \left(\mathbf{C}_2 - \mathbf{C}_1\right)\right]^{-1} \tag{6.5b}$$

Weng (1992, 1990, 1984) has shown that for ellipsoidal reinforcements, the Mori-Tanaka model is equivalent to the Hashin-Shtrikman-Walpole lower bound (Walpole, 1966; Willis, 1977; Weng, 1992).

Benveniste (1987) proposed a new formulation of the Mori-Tanaka model which is suitable for composites with randomly oriented fibers. He developed a one-step method where the orientation averaging is directly performed on tensor $\mathbf{T}$. His estimate reads:

$$\widetilde{\mathbf{C}}^{\mathrm{Ben}} = \mathbf{C}_1 + c_2\left\langle\left(\mathbf{C}_2 - \mathbf{C}_1\right) : \mathbf{T}\right\rangle : \left[c_1\mathbf{I} + c_2\langle\mathbf{T}\rangle\right]^{-1} \tag{6.6}$$

It should be noted that this model delivers non-symmetric effective tensors for many microstructures (e.g., reinforcements with different aspect ratios) (Ferrari, 1991; Benveniste *et al.*, 1991), which is physically invalid. However, since this study deals with inclusions of identical aspect ratios, Eq.(6.6) leads to symmetric tensors.

Lielens *et al.* (1998) have developed a model that interpolates nonlinearly between the Hashin-Shtrikman-Walpole bounds for aligned reinforcements (Walpole, 1966; Willis, 1977; Weng, 1992). More specifically, this model interpolates the inverse of the strain-localization tensor between the case where the stiffest phase is embedded in the more compliant phase and that where the most compliant phase is embedded in the stiffest phase (Tucker and Liang, 1999). $\mathbf{A}$ is given by:

$$\mathbf{A}^{\mathrm{LI}} = \hat{\mathbf{A}}^{\mathrm{LI}} : \left[c_1\mathbf{I} + c_2\hat{\mathbf{A}}^{\mathrm{LI}}\right]^{-1} \tag{6.7a}$$

where:

$$\hat{\mathbf{A}}^{\mathrm{LI}} = \left\{\left(1 - v_f\right)\left[\hat{\mathbf{A}}^{\mathrm{lower}}\right]^{-1} + v_f\left[\hat{\mathbf{A}}^{\mathrm{upper}}\right]^{-1}\right\}^{-1}, \tag{6.7b}$$

v_f is the interpolation factor and is related to the inclusions volume fraction (Lielens *et al.*, 1998; Tucker and Liang, 1999):

$$v_f = \frac{1}{2}c_2(1 + c_2), \tag{6.7c}$$

$\hat{\mathbf{A}}^{\mathrm{lower}}$ and $\hat{\mathbf{A}}^{\mathrm{upper}}$ are computed as:

$$\hat{\mathbf{A}}^{\mathrm{lower}} = \left[\mathbf{I} + \mathbf{S}_1 : \mathbf{C}_1^{-1} : \left(\mathbf{C}_2 - \mathbf{C}_1\right)\right]^{-1} \tag{6.7d}$$

$$\hat{\mathbf{A}}^{\mathrm{upper}} = \left[\mathbf{I} + \mathbf{S}_2 : \mathbf{C}_2^{-1} : \left(\mathbf{C}_1 - \mathbf{C}_2\right)\right]^{-1} \tag{6.7e}$$

where $\mathbf{S}_2$ is Eshelby's tensor computed by using the fibers properties as the infinite media.

6.3.2 Numerical homogenization

Random microstructures generation

Most artificial random microstructures found in the literature were generated by the Random Sequential Adsorption (RSA) algorithm (Rintoul and Torquato, 1997), and its modifications (Segurado and Llorca, 2002). The main disadvantage of this algorithm is the difficulty to generate microstructures with high number of fibers and volume fraction in a reasonable computational time (Segurado and Llorca, 2002; Barello and Lévesque, 2008). Lubachevsky and Stillinger (1990) proposed an algorithm based on molecular dynamics (MD) that can achieve high volume fractions, up to the theoretical packing limit, for spherical particles in a very short computation time (Ghossein and Levesque, 2012). Donev *et al.* (2005b) relied on the principles of MD algorithms to generate random packings of elliptical (2D) and ellipsoidal (3D) particles. Ghossein and Levesque (2013) have proposed a modified version of their algorithm that can generate all types of ellipsoids (prolate, oblate, scalene) with high aspect ratios (i.e., > 10) in a computationnally efficient manner.

Computation of composites effective properties

Most of the published works dealing with the computation of composites effective properties relied on the Finite Element Method (FEM) (Llorca *et al.*, 2000; Bohm *et al.*, 2002; Segurado and Llorca, 2002; Kari *et al.*, 2007b; Barello and Lévesque, 2008; Klusemann and Svendsen, 2010; Cojocaru and Karlsson, 2010; El-Mourid *et al.*, 2012; Pahlavanpour *et al.*, 2013; Moussaddy *et al.*, 2013b). However, this technique cannot be fully automated since the meshing operation usually requires user input, especially for large volume fractions and/or aspect ratios.

Moulinec and Suquet (1998) have proposed an algorithm that computes the effective properties of composites based on Fast Fourier Transforms (FFT). The algorithm consists of discretizing the microstructures into voxels and solving, in each voxel, the constitutive law in Fourier space. The mechanical properties are then deduced from the volume averaged stresses and strains over all the voxels. The technique was accelerated by the work of Eyre and Milton (1999). The advantage of this method stems from its rate of convergence and the fact that it does not require meshing. Furthermore, this method imposes periodic boundary conditions, which allows it to efficiently converge towards the RVE (Kanit *et al.*, 2003).
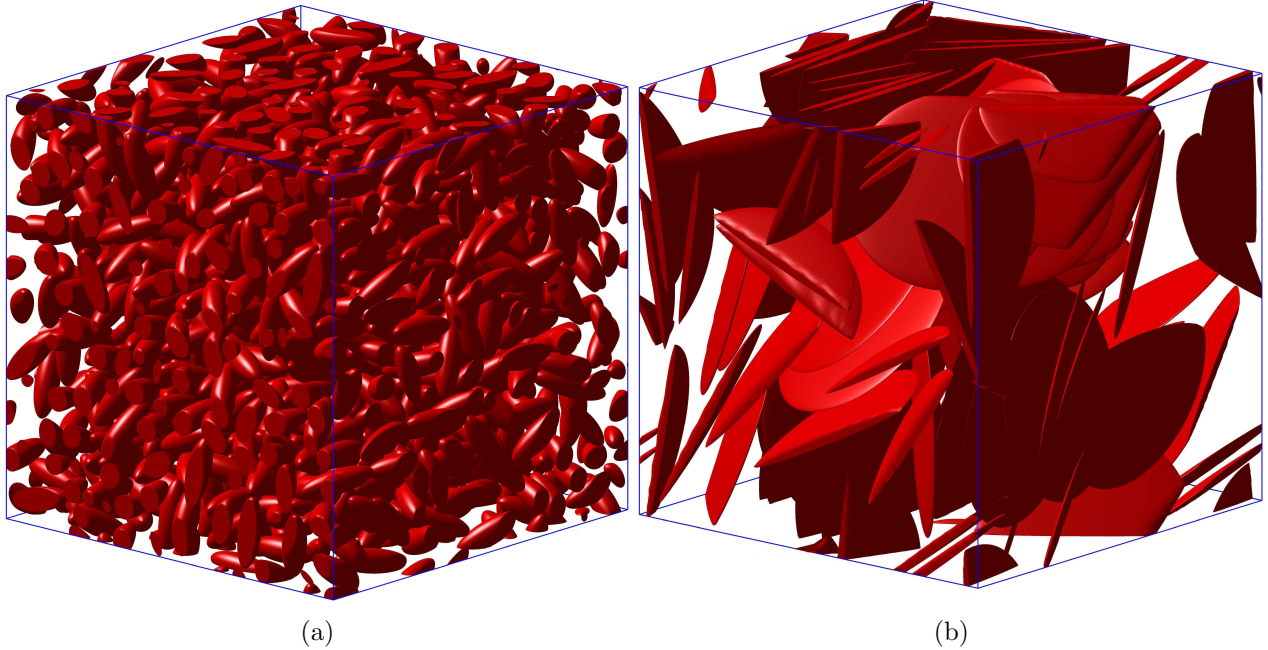
Figure 6.1 (a) Random microstructure containing 1000 prolate ellipsoids. Volume fraction = 30%. $R_1 = R_2 = 3$. (b) Random microstructure containing 50 oblate ellipsoids. Volume fraction = 15%. $R_1 = 20$, $R_2 = 1$.

6.4 Generation of periodic ellipsoidal particles volume elements

The algorithm of Ghossein and Levesque (2013) was used to generate a wide range of microstructures. Two aspect ratios were defined: $R_1 = a_i/b_i$ and $R_2 = a_i/c_i$, where $\{a_i, b_i, c_i\}$ denote the semi-principal axes length of ellipsoid i. A minimal distance of $10^{-3}L$ was imposed between two ellipsoids, where L is the cube's length. Figure 6.1a shows a periodic packing 1000 prolate ellipsoids with a volume fraction of 30% and an aspect ratio of 3 ($R_1 = R_2 = 3$). Figure 6.1b shows a periodic packing containing 50 oblate ellipsoids with an aspect ratio of 20 ($R_1 = 20$, $R_2 = 1$) and a volume fraction of 15%. These two packings were generated in less than 20 seconds on an Intel i7 Quad Core running at 1.60 GHz and with 8 GB of RAM.

6.5 Computation of composites effective properties using FFT

The effective properties of the generated microstructures were computed using the technique of Moulinec and Suquet (1998) and accelerated with the algorithm of Eyre and Milton (1999).

The microstructure was discretized into $N \times N \times N$ cubic voxels. For each voxel, a material was assigned by adopting the following rules of arbitration: the position of 9 points uniformly

(a)   (b)
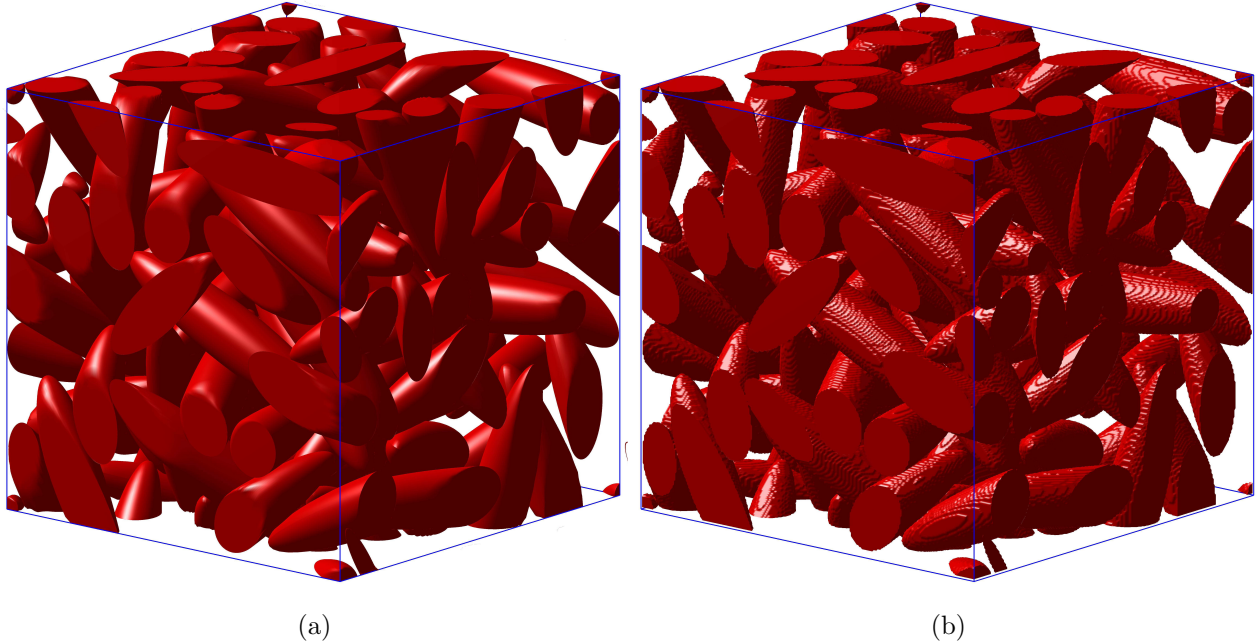
Figure 6.2 Discretization of a random microstructure on a grid of $256 \times 256 \times 256$ voxels. Number of ellipsoids = 60. Volume fraction = 40%. $R_1 = R_2 = 5$. (a) Generated microstructure. (b) Discretized microstructure.

distributed was verified. If most of the points belonged to an ellipsoid, then the properties of the ellipsoidal fibers were assigned to the voxel. Otherwise, the voxel was considered to be matrix. Figure 6.2 shows an example of discretization of a random composite containing 60 prolate ellipsoids with a volume fraction of 40% and an aspect ratio of 5. $256 \times 256 \times 256$ voxels were used to represent the microstructure.

The effective properties were derived from the volume averaged stresses and strains. The complete details of the numerical implementation of the algorithms for computing the stresses and strains fields can be found in (Ghossein and Levesque, 2012). The effective stiffness tensor $\widetilde{\mathbf{C}}$ was computed from:

$$< \boldsymbol{\sigma}(\boldsymbol{x}) > = \widetilde{\mathbf{C}} : < \boldsymbol{\varepsilon}(\boldsymbol{x}) > \tag{6.8}$$

where $< \cdot >$ denotes an average over the volume. The six columns of the stiffness tensor (in modified Voigt notation) were computed independently by imposing a periodic strain field in a particular direction. For example, to calculate the first column, a periodic deformation was applied in the first principal direction (ε_{11}). The five other columns were determined similarly. Since the algorithm had to be called six times independently, the calculations have been parallelized on six local workers using an Intel(R) Xeon(R) Dual Core running at 2.40 GHz and with 48 GB of RAM.

Following the determination of $\widetilde{\mathbf{C}}$, the effective bulk and shear moduli were computed as:

$$\widetilde{\kappa} = \frac{\widetilde{C}_{iijj}}{9} \tag{6.9a}$$

$$\widetilde{\mu} = \frac{3\widetilde{C}_{ijij} - \widetilde{C}_{iijj}}{30} \tag{6.9b}$$

Eqs. (6.9) were used to take into account all the components of $\widetilde{\mathbf{C}}$ since the latter was not strictly isotropic.

6.6 Validation campaign

Macroscopically isotropic composites made of randomly oriented isotropic ellipsoidal fibers distributed into an isotropic matrix were considered. A wide range of mechanical properties, volume fractions and fibers aspect ratios were studied. Table 6.1 summarizes all the studied combinations of volume fractions and aspect ratios.

For each combination of aspect ratio and volume fraction, three mechanical properties contrasts were simulated, namely: $\rho_1 = \frac{\mu_2}{\mu_1}$, $\rho_2 = \frac{\kappa_1}{\mu_1}$ and $\rho_3 = \frac{\kappa_2}{\mu_1}$, where the ρ_i were varied independently and took the values of $\{1, 10, 50, 100\}$.

The mechanical properties were evaluated according to the methodology of Kanit *et al.* (2003). The size of the RVE was determined for each combination of contrasts, volume fraction and aspect ratio as follows. Mechanical properties were computed for several random realizations having the same constituent properties, fibers aspect ratio, fibers volume fraction and the same number of represented ellipsoids. The number of simulations n was considered sufficient when the half width of a 95% confidence interval was less than 1% of the average value of the sought property. This is equivalent to satisfy the following inequality:

Table 6.1 Studied range of aspect ratios and volume fractions for prolate and oblate ellipsoidal fibers.

Prolate ($R_1 = R_2$)		Oblate ($R_2 = 1$)	
Aspect ratios	Volume fractions (%)	Aspect ratios	Volume fractions (%)
$R_1 = R_2 = 2$	$\{10, 20, 30, 40, 50\}$	$R_1 = 2$	$\{10, 20, 30, 40, 50\}$
$R_1 = R_2 = 5$	$\{10, 20, 30, 40\}$	$R_1 = 5$	$\{10, 20, 30\}$
$R_1 = R_2 = 10$	$\{10, 20\}$	$R_1 = 10$	$\{10, 20\}$
$R_1 = R_2 = 20$	$\{10\}$	$R_1 = 20$	$\{10\}$

$$\max_{x=\widetilde{\kappa},\widetilde{\mu}} \frac{T_{1-\alpha/2}^{n-1} S_x}{\bar{x}\sqrt{n}} \leq 0.01 \quad , \quad n \geq 6 \tag{6.10}$$

where T is the quantile of the Student distribution with $(n-1)$ degrees of freedom, S is an estimate of the standard deviation of x and $(1-\alpha)$ is the confidence level (i.e., $1-\alpha = 0.95$).

The procedure was repeated for increasing numbers of ellipsoids (while keeping constant the constituent properties, fibers volume fraction and aspect ratio). Starting with volume elements containing 15 particles each, 15 ellipsoids were added between each volume element size until the mean of the effective properties converged to an approximate asymptotic value (less than 2% variation from one ellipsoids number increment to the next). The RVE was then reached and the resulting mechanical properties were considered to be the exact properties of the composite. Moussaddy *et al.* (2013b) showed that this procedure provides accurate results when the fibers aspect ratio is lower than 30, which is the case in this study.

Based on the distribution and orientations of the reinforcements, the RVE should be isotropic. Moussaddy *et al.* (2013b) have demonstrated that the convergence of properties over volume element size increments, as describe above, can lead to erroneous results for large aspect ratio fibers. They have demonstrated that relying on a deviation from isotropy criterion led to a much more robust evaluation of effective properties. Several methods have been proposed in the literature for computing the deviation from isotropy. Some authors considered only the independent terms of the stiffness tensors (i.e., $\widetilde{C}_{1111}$, $\widetilde{C}_{1122}$ and $\widetilde{C}_{1212}$) (Zener and Siegel, 1949; Chung and Buessem, 1967; Spoor *et al.*, 1995; Ranganathan and Ostoja-Starzewski, 2008) while others have proposed formulations that do not take into account the vanishing terms (Bucataru and Slawinski, 2009; Moussaddy *et al.*, 2013b). This can lead to inaccuracy in the isotropy error measurement since these terms are not necessarily zero in the homogenized tensor $\widetilde{\mathbf{C}}$.

The deviation from isotropy was calculated for all the volume elements computed in this work as a validation for the results delivered by the convergence of effective properties described above. The deviation from isotropy of tensor $\widetilde{\mathbf{C}}$ was evaluated by using the following methodology. First, an isotropic stiffness tensor was calculated from the effective moduli $\widetilde{\kappa}$ and $\widetilde{\mu}$ as:

$$\mathbf{C}^* = 3\widetilde{\kappa}\mathbf{J} + 2\widetilde{\mu}\mathbf{K} \tag{6.11a}$$

where $\mathbf{J}$ and $\mathbf{K}$ are the isotropic projectors. The deviation from isotropy of $\widetilde{\mathbf{C}}$, denoted by δ_{iso}, was then computed as:

$$\delta_{\text{iso}} = \frac{\sum\limits_{i=1}^{6} |\lambda_i|}{\sum\limits_{i=1}^{6} \lambda_i^*} \tag{6.11b}$$

where λ_i and λ_i^* denote respectively the eigenvalues of $\left(\widetilde{\mathbf{C}} - \mathbf{C}^*\right)$ and $\mathbf{C}^*$ (in modified Voigt notation). This methodology was adopted since it takes into account all the terms of $\widetilde{\mathbf{C}}$. In addition, δ_{iso} is related to the strain energy mean error since it relies on the eigenvalues.

In total, 1472 different ellipsoidal fibers reinforced composites were studied and approximately 66000 simulations were performed. δ_{iso} was computed for each realization. Figure 6.3 shows the statistical distribution of δ_{iso}. If all 66000 simulations are considered (Figure 6.3a), δ_{iso} has a mean and maximum value of 2.4% and 11.2%, respectively. Theses values are reduced respectively to 1.3% and 5.2% if only the realizations at RVE size are examined (about 20000 simulations, including 13000 at a contrast of 100) (Figure 6.3b). Figure 6.3 provides also the 99$^{\text{th}}$ percentile of δ_{iso}. For all the simulations, $\delta_{\text{iso}}^{99^{\text{th}}} = 7.6\%$, whereas $\delta_{\text{iso}}^{99^{\text{th}}} = 3.9\%$ for only those at the RVE. These results show that the stiffness tensors obtained in this campaign are almost isotropic and were considered as acceptable for this work.

It should be noted that for each combination of contrasts, volume fraction, aspect ratio and number of fibers, a convergence analysis in terms of number of voxels was performed when computing the effective properties with the FFT method. N was initially set to $N = 32$ and doubled until both effective moduli converged. A tolerance of 2% was used as a criterion of convergence. This convergence analysis was performed for the first 6 realizations. The largest required value of N was then used for all the other generated microstructures having the same combination of mechanical and geometrical properties.

6.7   Results and discussion

The predictions of the dilute solution of Eshelby (Eshelby), the model of Mori-Tanaka (MT), the self-consistent scheme (SCS), Lielens' model and the model of Benveniste (MT/Benveniste) were compared to the exact solution given by the numerical tool (NT). Furthermore, the numerical results were interpolated using a MATLAB built-in cubic spline interpolation. The Hashin-Shtrikman bounds (HSB) are also shown in the plots to verify that the numerical and analytical predictions lie between these bounds. Results are shown for the case of prolate and oblate ellipsoidal fibers.

It should be noted that the accuracy of the Ponte Castaneda and Willis (PCW) model was not studied in this paper. It has been shown that this model has a limited range of allowable volume fractions ($c_2 \leq 1/R_1^2$ for prolate ellipsoids and $c_2 \leq 1/R_1$ for oblate

ellipsoids) (Castaneda and Willis, 1995). When exceeding the volume fraction limit, the PCW model violates the bounds of Hashin-Shtrikman (Hu and Weng, 2000).

6.7.1 Prolate ellipsoidal fibers

For all cases studied in this section, κ_1 was set to 1 and contrasts ρ_1 and ρ_3 were varied simultaneously from 1 to 100.

Figure 6.4 shows the results for a volume fraction of 10% and an aspect ratio of 2. It can be seen that every model delivers acceptable predictions, even for high mechanical properties contrasts. The figure suggests that Lielens' model delivers the most accurate predictions for $\widetilde{\kappa}$ and the SCS provides the most accurate estimates for $\widetilde{\mu}$.

Figure 6.5 shows the results for the same types of ellipsoids but for a volume fraction of 30%. It can be seen that the dilute solution of Eshelby deviates from the accurate solution. The other models deliver accurate estimates for low contrasts ($\rho_{1,3} \leq 10$). For higher contrasts, Lielens's model is the only accurate model. MT and MT/Benveniste models underestimate while the SCS overestimates the effective properties.

The same trend is observed when the inclusions volume fraction reaches 50%, as depicted in Figure 6.6. However, the SCS diverges rapidly when $\rho_{1,3} \geq 10$. Thus, it seems that the SCS is not an appropriate model to predict the properties of dense ellipsoidal particles reinforced microstructures. All models led to accurate predictions for $\rho_{1,3} \leq 10$. When $10 \leq \rho_{1,3} \leq 50$, Lielens's model remains the most accurate among the studied models. However, for higher contrasts ($\rho_{1,3} \geq 50$), no model provides acceptable estimates. Moreover, all models, except the SCS, predict a plateau, which is not the case for the numerical solution. It should be noted that similar results were reported for the case of spherical particles reinforced composites (Ghossein and Levesque, 2012) and for cylindrical fibers of very high aspect ratios (Moussaddy et al., 2013a).

Figures 6.7 and 6.8 show the results for aspect ratios of 10 and 20, respectively, and for volume fractions of 10%. For both cases, all models, except the SCS, provide accurate estimates for $\widetilde{\kappa}$ and $\widetilde{\mu}$, even when $\rho_{1,3} \geq 50$. The SCS is only accurate when $\rho_{1,3} \leq 30$. It is interesting to note that, for both aspect ratios, the numerical and analytical predictions do not reach a plateau in the investigated range of contrasts. Further works are needed to determine the contrasts at which an asymptotic effective property is reached.

According to these results, it seems that the accuracy of the analytical models is more sensitive to the fibers volume fraction than to their aspect ratio. However, the contrasts between the fibers and the matrix remain the most influent parameters on the homogenization models performance. Indeed, when the contrasts are low (i.e., ≤ 10), the analytical models predict the effective properties accurately, even for high volume fractions (up to 50%).

6.7.2 Oblate ellipsoidal fibers

The same analysis as that performed for the prolate ellipsoids was performed for the oblate ellipsoids.

Figures 6.9 to 6.13 show trends very similar to those obtained for the case of prolate ellipsoids. In overall, Lielens's model seems to be the most accurate model. Furthermore, the contrasts between the phases are the most influential parameters on the analytical models performance, followed by the fibers volume fraction. The only difference found is that for an aspect ratio of 10 and 20 (Figures 6.12 and 6.13), the effective properties reach a plateau for a contrast value around 100, which was not the case for prolate ellipsoids.

6.7.3 Maximum relative error for each analytical model

Tables 6.2 and 6.3 provide the maximum relative error ϵ induced by each homogenization model when predicting the effective moduli $\widetilde{\kappa}$ and $\widetilde{\mu}$. ϵ was computed as:

$$\epsilon = \max_{i \in \{1,2,...,1472\}} \left| \frac{p_i^{\mathrm{ana}} - p_i^{\mathrm{num}}}{p_i^{\mathrm{num}}} \right| \tag{6.12}$$

where p denotes either $\widetilde{\kappa}$ or $\widetilde{\mu}$, "num" and "ana" refers respectively to the numerical and analytical predictions, while subscript i refers to one of the predictions among the 1472 different microstructures studied in this work. For Lielens' model, ϵ was computed only for the cases where $\kappa_2 \geq \kappa_1$ and $\mu_2 \geq \mu_1$ since this model is only valid when the fibers are stiffer than the matrix (Ghossein and Levesque, 2012).

The relative errors are rounded to the unit. The values of contrasts ρ_i for which ϵ was induced are specified for each combination of volume fraction and aspect ratio. Results are only presented for prolate ellipsoids since similar values were obtained for oblate particles.

Tables 6.2a and 6.2b provide the maximum errors as a function of the particles volume fraction for $\widetilde{\kappa}$ and $\widetilde{\mu}$. The ellipsoids aspect ratio was set to 2. In both cases, the error made by each model increases with the volume fraction. Moreover, errors always occur for high contrasts. For both moduli, if $\epsilon < 10\%$ was defined as an acceptable threshold, all studied models would meet the accuracy criteria for a volume fraction of 10%. When the inclusions volume fraction is 20%, only Lielens' and the SCS meet the criteria. For a volume fraction greater than 30%, the accuracy criteria is not met by any model. From the results presented in Tables 6.2, Lielens' model seems to be the most accurate model when predicting $\widetilde{\kappa}$ and $\widetilde{\mu}$, provided that the ellipsoids are stiffer than the matrix.

Tables 6.3a and 6.3b present the maximum errors as a function of the ellipsoids aspect ratio. The volume fraction was fixed to 10%. For all models, the error increases with the

aspect ratio but not as significantly as observed in Tables 6.2a and 6.2b. If the SCS is excluded from the analysis, the maximum error is 15% in the studied range of properties. This shows that the ellipsoids aspect ratio has less influence on the models accuracy than the volume fraction. It is interesting to note that, for high aspect ratios (i.e., ≥ 10), the predictions of MT and MT/Benveniste are no longer similar, especially when predicting $\widetilde{\mu}$. Among these two models, MT/Benveniste seems more suitable for composites reinforced by fibers of high aspect ratios. This finding is relevant since MT and MT/Benveniste have been used in the literature under the name of Mori-Tanaka without specifying which of the two models has been used. This study clarifies the differences between the two models and identifies the best suited model for randomly oriented ellipsoidal particles reinforced composites. Finally, Lielens' and MT/Benveniste models have similar accuracies when predicting $\widetilde{\mu}$. As for $\widetilde{\kappa}$, Lielens' is the most accurate model.

6.7.4 Comparison with other studies

It should be noted that some of the observations made in this paper have been reported in other studies, but none has succeeded to prove them definitively. In their study on aligned short-fiber composites, Tucker and Liang (1999) found that Lielens' and MT models provided the best predictions of effective properties. However, their numerical simulations did not allow to choose the most accurate model among these two since their computations were limited to a volume fraction of 20% and a rigidity contrast of 30.

Bohm *et al.* (2002) compared their numerical results to the SCS and MT/Benveniste model for the case of a metal matrix reinforced by randomly oriented short fibers. They found a good agreement between the numerical and analytical predictions. Nevertheless, their analysis was performed on three random microstructures without determining rigorously the RVE.

Duschlbauer *et al.* (2006) studied the case of composites reinforced by planar random fibers. The authors showed that MT/Benveniste was adequate for predicting the thermoelastic properties of such composites, but it was the only investigated model. Furthermore, their work was limited to a volume fraction of 21%, an aspect ratio of 10 and a rigidity contrasts less than 10.

In their work on microstructures with randomly dispersed short fibers, Kari *et al.* (2007a) found that the SCS provided the best estimates of the effective properties. However, their simulations were performed with a Young's modulus contrast of 6.4, which did not allow to deeply investigate the models performance. Indeed, the results presented in this paper show that for this range of contrasts, all models provide accurate predictions and the difference between their estimations is negligible.

Moussaddy *et al.* (2013a) found that Lielens' model was the best suited model to pre-

dict the effective bulk modulus of ROFRC for volume fractions over 5%, which is also the case for ellipsoidal fibers reinforced composites. However, the authors showed that no model accurately predicted $\widetilde{\mu}$ for volume fractions over 5%. Since their study was limited to the case where fibers were completely stiffer than the matrix, it is possible to question the validity of this statement. Indeed, their works did not allow them to observe that MT and MT/Benveniste models have no longer the same accuracy when $\kappa_2 \leq \kappa_1$ and $\mu_2 \geq \mu_1$, and that the latter could replace Lielens's model for this specific type of composites, especially when predicting $\widetilde{\mu}$.

6.8   Conclusion

The main conclusions of this study are:

⊙ Similar results were obtained for prolate and oblate ellipsoidal fibers. In both cases, the analytical models show similar trends and have almost the same accuracy.

⊙ Contrasts between phases mechanical properties are the most influential parameters on the analytical models accuracy, followed by the fibers volume fraction.

⊙ In the investigated range of properties, Lielens' is the most accurate model provided that the ellipsoids are stiffer than the matrix.

⊙ For microstructures with high fibers aspect ratio, MT/Benveniste could be an alternative to Lielens' model when predicting $\widetilde{\mu}$, especially if the fibers are not completely stiffer than the matrix (i.e., $\kappa_2 \leq \kappa_1$ and $\mu_2 \geq \mu_1$).

If a single model was to be chosen for predicting the effective properties of ellipsoidal fibers reinforced composites, this study suggests that it should be Lielens' model. For low aspect ratios (i.e., ≤ 2), its accuracy is 9% for volume fractions up to 20% and rigidity contrasts up to 100. For low volume fractions (i.e., $\leq 10\%$), Lielens' model is accurate to 7% for aspect ratios up to 20 and mechanical properties contrasts up to 100.

Furthermore, an interpolation model has been developed in this paper and it can be seen as a substitute to analytical models. Its numerical execution is as quick as analytical models but its accuracy is the highest published so far.

Acknowledgments

Table 6.2a Relative error (ϵ) of each analytical model as a function of the ellipsoids volume fraction. The given values correspond to the maximum errors induced when predicting $\widetilde{\kappa}$ for 1472 different ellipsoidal particles reinforced composites. $R_1 = R_2 = 2$. $[a, b, c]$ means that $\{\rho_1, \rho_2, \rho_3\} = \{10^a, 10^b, 10^c\}$.

Models	Volume fractions									
	10%		20%		30%		40%		50%	
	$\epsilon(\%)$	$[a, b, c]$	$\epsilon(\%)$	$[a, b, c]$	$\epsilon(\%)$	$[a, b, c]$	$\epsilon(\%)$	$[a, b, c]$	$\epsilon(\%)$	$[a, b, c]$
MT	9	$[2, 2, 0]$	14	$[2, 2, 0]$	18	$[2, 2, 0]$	32	$[2, 2, 0]$	53	$[2, 2, 0]$
MT/Ben.	9	$[2, 2, 0]$	14	$[2, 2, 0]$	18	$[2, 2, 0]$	32	$[2, 2, 0]$	53	$[2, 2, 0]$
SCS	1	$[2, 0, 2]$	9	$[2, 0, 2]$	30	$[2, 0, 2]$	56	$[2, 0, 2]$	69	$[2, 0, 2]$
Lielens	1	$[0, 0, 2]$	5	$[0, 0, 2]$	12	$[0, 0, 2]$	23	$[0, 0, 2]$	40	$[0, 0, 2]$
Eshelby	4	$[2, 0, 2]$	12	$[2, 0, 2]$	23	$[2, 0, 2]$	46	$[2, 0, 2]$	53	$[2, 0, 2]$

Table 6.2b Relative error (ϵ) of each analytical model as a function of the ellipsoids volume fraction. The given values correspond to the maximum errors induced when predicting $\widetilde{\mu}$ for 1472 different ellipsoidal particles reinforced composites. $R_1 = R_2 = 2$. $[a, b, c]$ means that $\{\rho_1, \rho_2, \rho_3\} = \{10^a, 10^b, 10^c\}$.

Models	Volume fractions									
	10%		20%		30%		40%		50%	
	$\epsilon(\%)$	$[a, b, c]$	$\epsilon(\%)$	$[a, b, c]$	$\epsilon(\%)$	$[a, b, c]$	$\epsilon(\%)$	$[a, b, c]$	$\epsilon(\%)$	$[a, b, c]$
MT	4	$[2, 2, 2]$	11	$[2, 2, 2]$	22	$[2, 2, 2]$	43	$[2, 2, 2]$	61	$[2, 2, 2]$
MT/Ben.	4	$[2, 2, 2]$	11	$[2, 2, 2]$	22	$[2, 2, 2]$	43	$[2, 2, 2]$	61	$[2, 2, 2]$
SCS	1	$[2, 2, 2]$	8	$[2, 2, 2]$	31	$[2, 2, 2]$	70	$[2, 2, 2]$	93	$[2, 2, 2]$
Lielens	3	$[2, 2, 2]$	6	$[2, 2, 2]$	13	$[2, 2, 2]$	29	$[2, 2, 2]$	46	$[2, 2, 2]$
Eshelby	6	$[2, 2, 2]$	18	$[2, 2, 2]$	34	$[2, 2, 2]$	56	$[2, 2, 2]$	75	$[2, 2, 2]$

Table 6.3a Relative error (ϵ) of each analytical model as a function of the ellipsoids aspect ratio. The given values correspond to the maximum errors induced when predicting $\widetilde{\kappa}$ for 1472 different ellipsoidal particles reinforced composites. Volume fraction = 10%. $[a, b, c]$ means that $\{\rho_1, \rho_2, \rho_3\} = \{10^a, 10^b, 10^c\}$.

Models	Aspect ratios							
	$R_1 = R_2 = 2$		$R_1 = R_2 = 5$		$R_1 = R_2 = 10$		$R_1 = R_2 = 20$	
	$\epsilon(\%)$	$[a, b, c]$	$\epsilon(\%)$	$[a, b, c]$	$\epsilon(\%)$	$[a, b, c]$	$\epsilon(\%)$	$[a, b, c]$
MT	9	$[2, 2, 0]$	10	$[2, 2, 0]$	12	$[2, 2, 0]$	14	$[2, 2, 0]$
MT/Ben.	9	$[2, 2, 0]$	9	$[2, 2, 0]$	10	$[2, 2, 0]$	12	$[2, 2, 0]$
SCS	1	$[2, 0, 2]$	6	$[2, 0, 2]$	14	$[2, 0, 2]$	30	$[2, 0, 2]$
Lielens	1	$[0, 0, 2]$	2	$[0, 0, 2]$	2	$[0, 0, 2]$	3	$[0, 0, 2]$
Eshelby	4	$[2, 0, 2]$	6	$[2, 0, 2]$	7	$[2, 0, 2]$	7	$[2, 0, 2]$

Table 6.3b Relative error (ϵ) of each analytical model as a function of the ellipsoids aspect ratio. The given values correspond to the maximum errors induced when predicting $\widetilde{\mu}$ for 1472 different ellipsoidal particles reinforced composites. Volume fraction = 10%. $[a, b, c]$ means that $\{\rho_1, \rho_2, \rho_3\} = \{10^a, 10^b, 10^c\}$.

Models	Aspect ratios							
	$R_1 = R_2 = 2$		$R_1 = R_2 = 5$		$R_1 = R_2 = 10$		$R_1 = R_2 = 20$	
	$\epsilon(\%)$	$[a, b, c]$	$\epsilon(\%)$	$[a, b, c]$	$\epsilon(\%)$	$[a, b, c]$	$\epsilon(\%)$	$[a, b, c]$
MT	4	$[2, 2, 2]$	5	$[2, 2, 2]$	8	$[2, 2, 2]$	15	$[2, 2, 2]$
MT/Ben.	4	$[2, 2, 2]$	5	$[2, 2, 2]$	6	$[2, 2, 2]$	7	$[2, 2, 2]$
SCS	1	$[2, 2, 2]$	3	$[2, 2, 2]$	11	$[2, 2, 2]$	23	$[2, 2, 2]$
Lielens	3	$[2, 2, 2]$	3	$[2, 2, 2]$	6	$[2, 2, 2]$	7	$[2, 2, 2]$
Eshelby	6	$[2, 2, 2]$	7	$[2, 2, 2]$	9	$[2, 2, 2]$	9	$[2, 2, 2]$
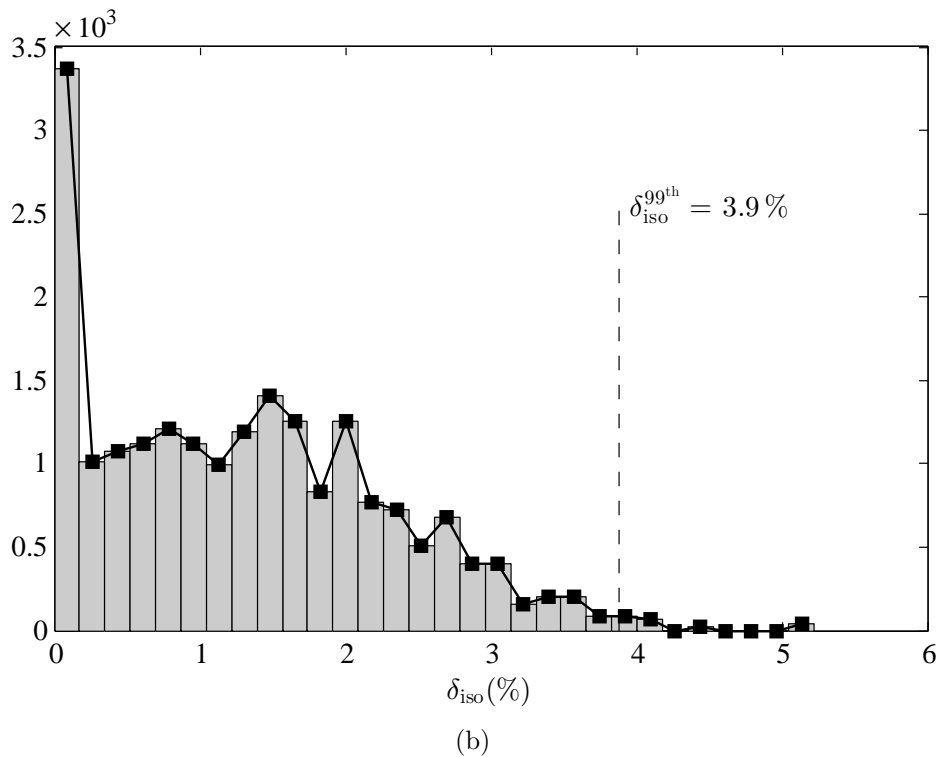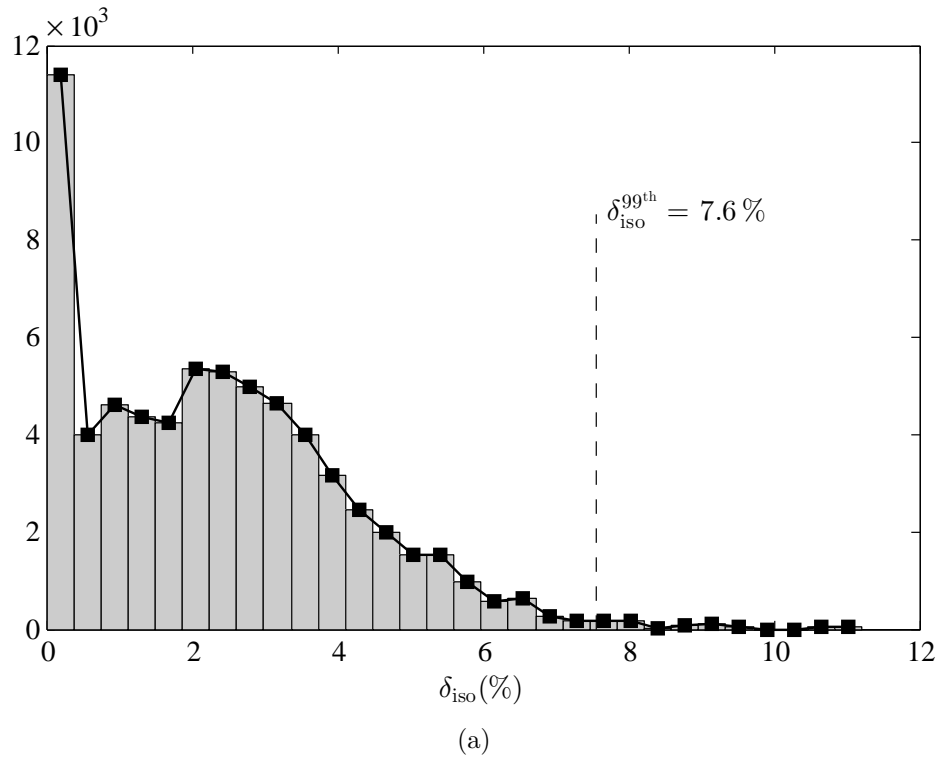
Figure 6.3 Statistical distribution of the deviation from isotropy δ_{iso}. The dashed line represents the 99th percentile. (a) Case where all the 66000 realizations are considered. (b) Case where only the realizations at RVE size are considered (about 20000 simulations).
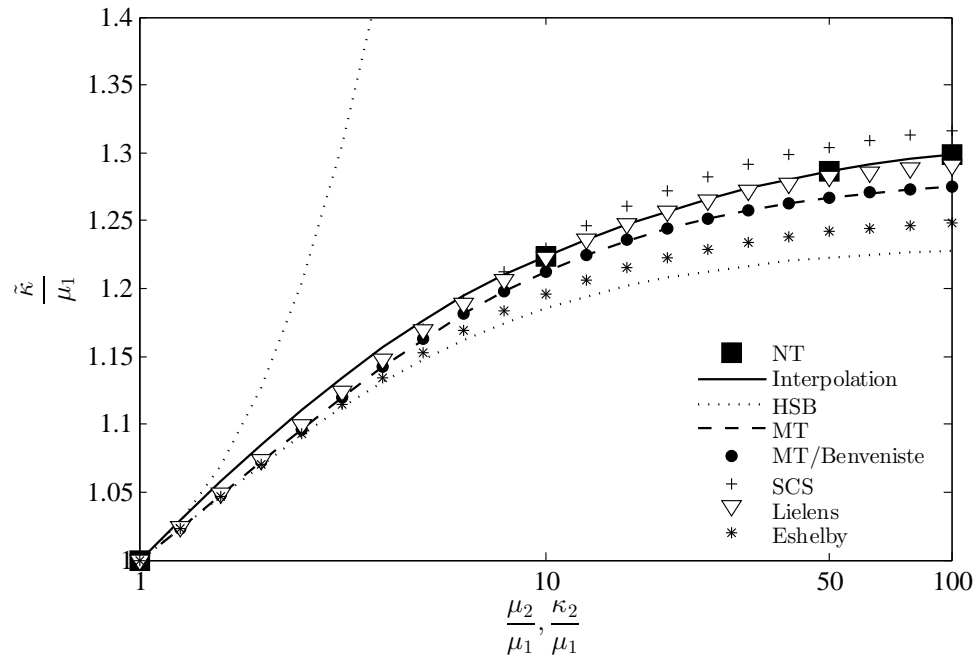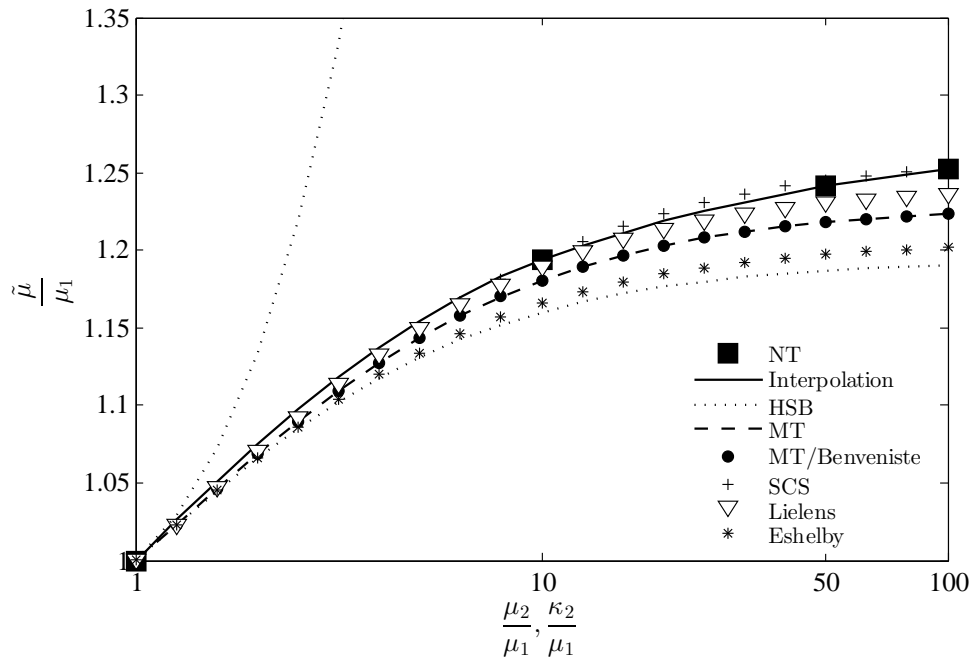
Figure 6.4 Comparison between the mechanical properties obtained with the numerical tool (NT) and those predicted by the analytical models: Hashin-Shtrikman Bounds (HSB), Mori-Tanaka (MT), Benveniste model (MT/Benveniste), self-consistent scheme (SCS), Lielens and the dilute solution of Eshelby (Eshelby). Volume fraction $= 10\%$. $R_1 = R_2 = 2$. $\kappa_1 = \mu_1 = 1$. (a) Normalized effective bulk modulus. (b) Normalized effective shear modulus.

Figure 6.5 Comparison between the mechanical properties obtained with the numerical tool (NT) and those predicted by the analytical models: Hashin-Shtrikman Bounds (HSB), Mori-Tanaka (MT), Benveniste model (MT/Benveniste), self-consistent scheme (SCS), Lielens and the dilute solution of Eshelby (Eshelby). Volume fraction = 30%. $R_1 = R_2 = 2$. $\kappa_1 = \mu_1 = 1$. (a) Normalized effective bulk modulus. (b) Normalized effective shear modulus.

Figure 6.6 Comparison between the mechanical properties obtained with the numerical tool (NT) and those predicted by the analytical models: Hashin-Shtrikman Bounds (HSB), Mori-Tanaka (MT), Benveniste model (MT/Benveniste), self-consistent scheme (SCS), Lielens and the dilute solution of Eshelby (Eshelby). Volume fraction = 50%. $R_1 = R_2 = 2$. $\kappa_1 = \mu_1 = 1$. (a) Normalized effective bulk modulus. (b) Normalized effective shear modulus.

(a)

(b)

Figure 6.7 Comparison between the mechanical properties obtained with the numerical tool (NT) and those predicted by the analytical models: Hashin-Shtrikman Bounds (HSB), Mori-Tanaka (MT), Benveniste model (MT/Benveniste), self-consistent scheme (SCS), Lielens and the dilute solution of Eshelby (Eshelby). Volume fraction = 10%. $R_1 = R_2 = 10$. $\kappa_1 = \mu_1 = 1$. (a) Normalized effective bulk modulus. (b) Normalized effective shear modulus.
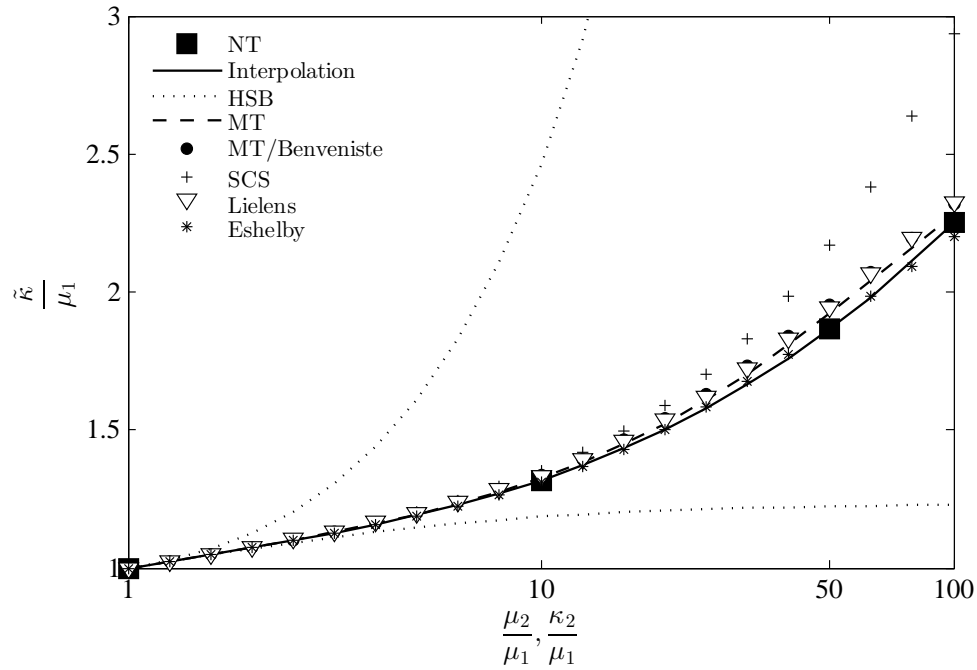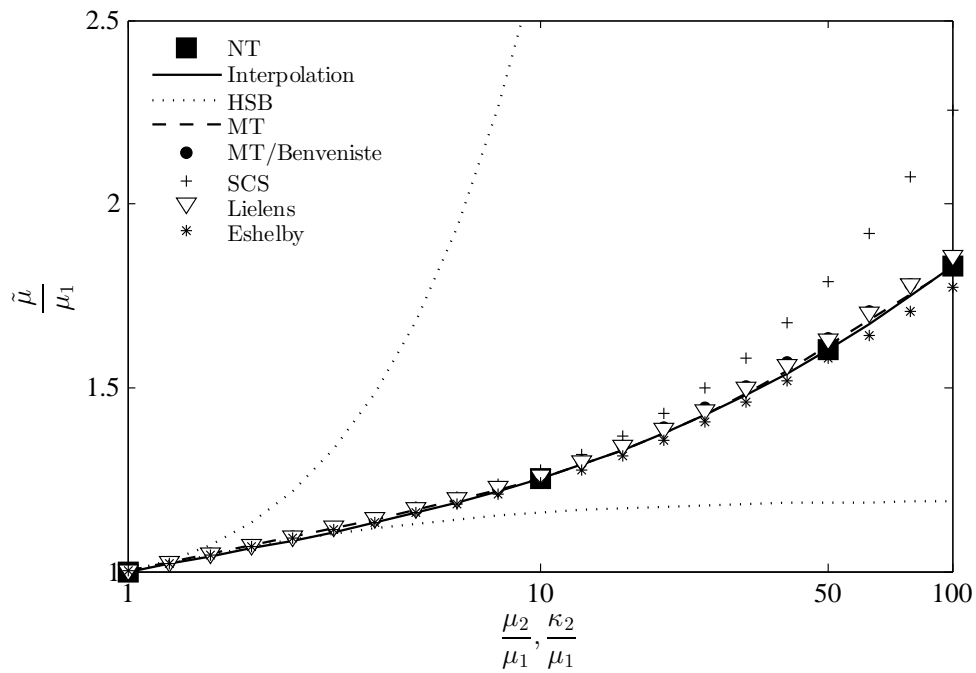
Figure 6.8 Comparison between the mechanical properties obtained with the numerical tool (NT) and those predicted by the analytical models: Hashin-Shtrikman Bounds (HSB), Mori-Tanaka (MT), Benveniste model (MT/Benveniste), self-consistent scheme (SCS), Lielens and the dilute solution of Eshelby (Eshelby). Volume fraction = 10%. $R_1 = R_2 = 20$. $\kappa_1 = \mu_1 = 1$. (a) Normalized effective bulk modulus. (b) Normalized effective shear modulus.
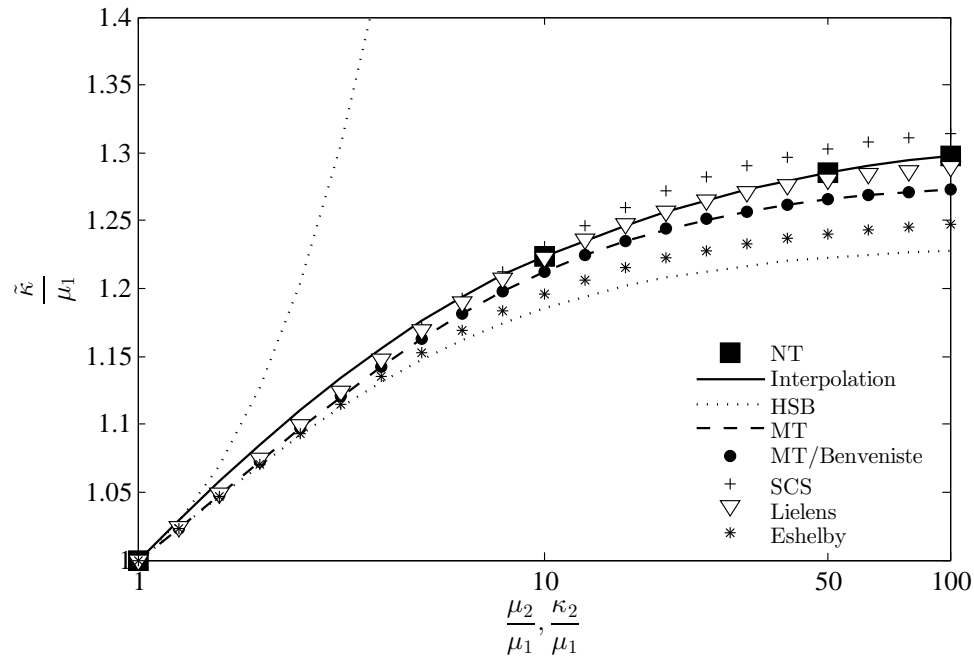
(a)
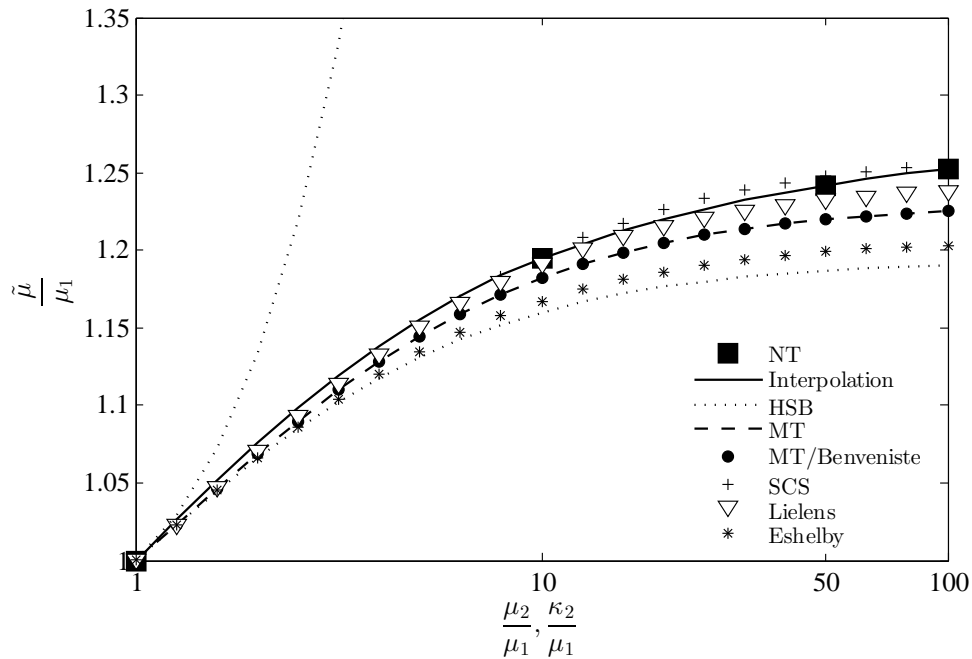
(b)

Figure 6.9 Comparison between the mechanical properties obtained with the numerical tool (NT) and those predicted by the analytical models: Hashin-Shtrikman Bounds (HSB), Mori-Tanaka (MT), Benveniste model (MT/Benveniste), self-consistent scheme (SCS), Lielens and the dilute solution of Eshelby (Eshelby). Volume fraction = 10%. $R_1 = 2$, $R_2 = 1$. $\kappa_1 = \mu_1 = 1$. (a) Normalized effective bulk modulus. (b) Normalized effective shear modulus.
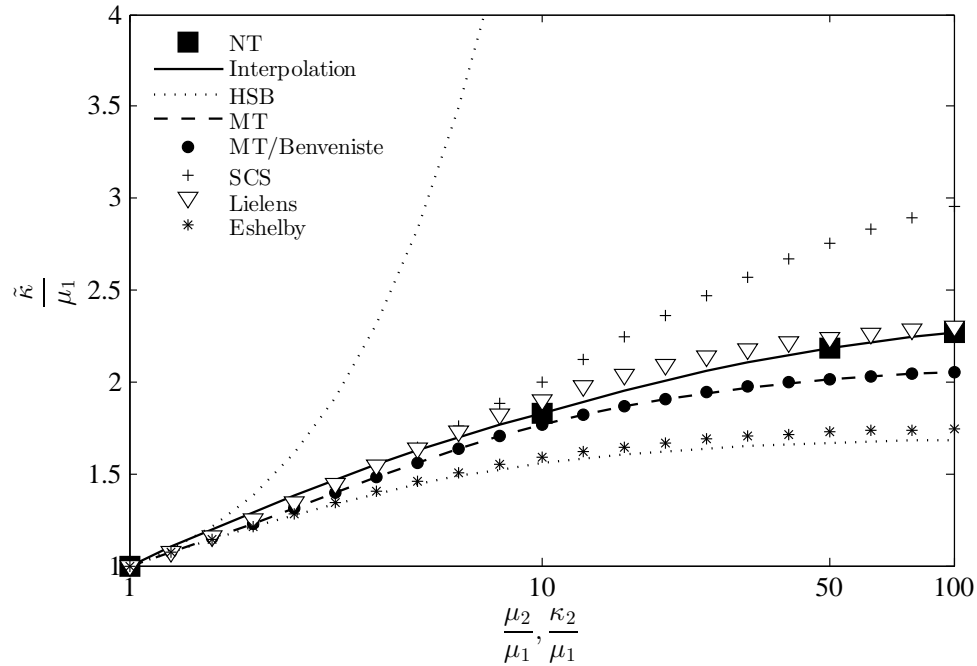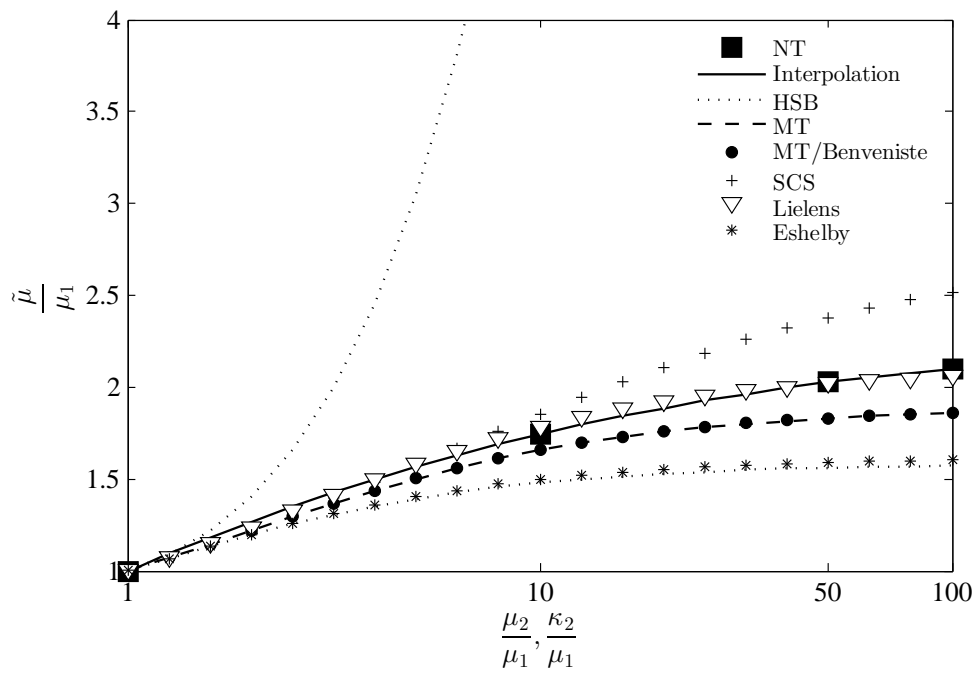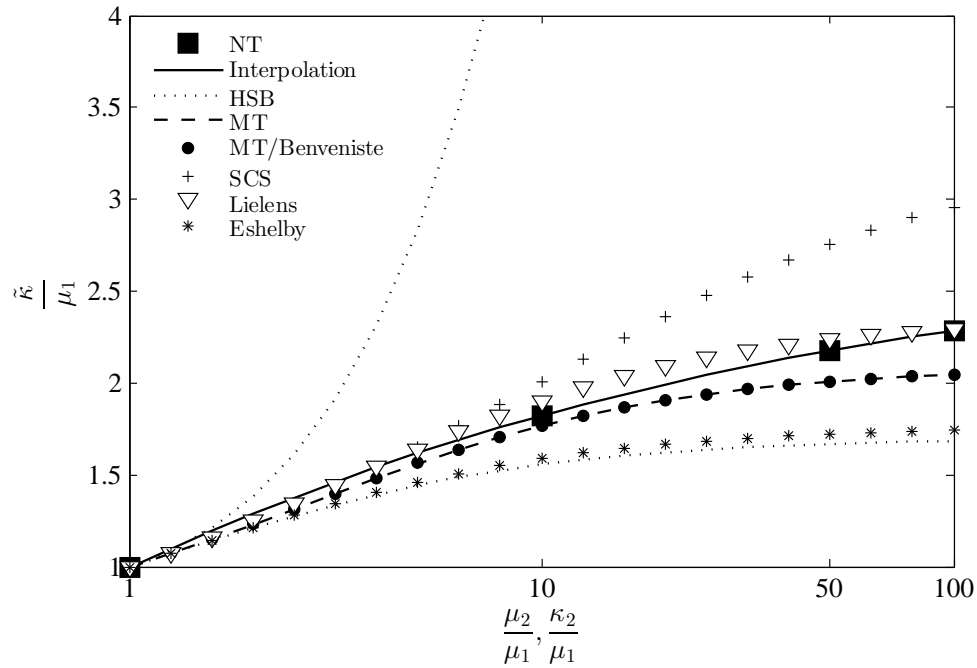
(a)
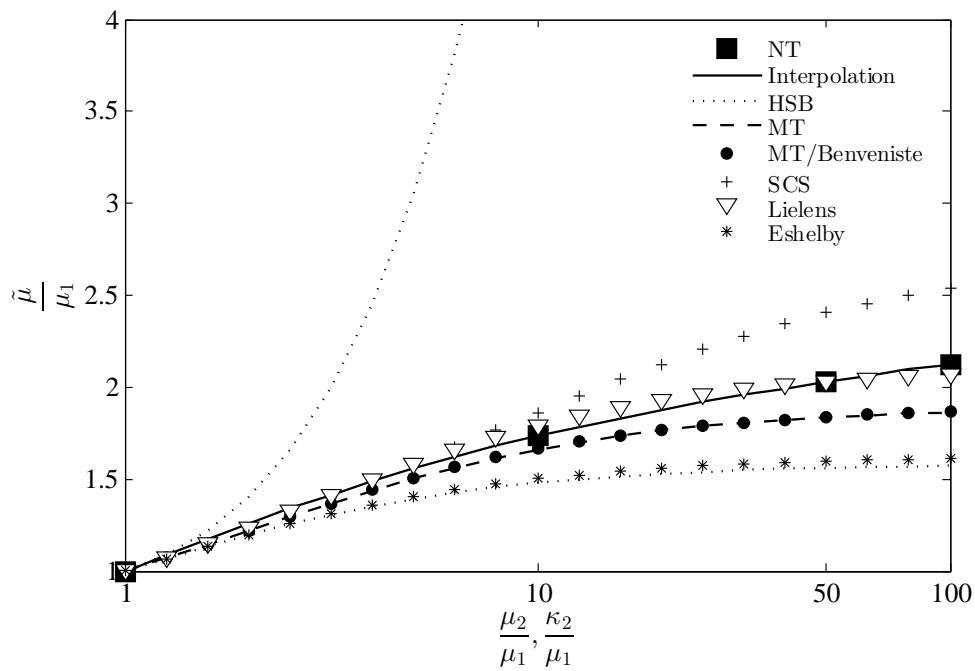
(b)

Figure 6.10 Comparison between the mechanical properties obtained with the numerical tool (NT) and those predicted by the analytical models: Hashin-Shtrikman Bounds (HSB), Mori-Tanaka (MT), Benveniste model (MT/Benveniste), self-consistent scheme (SCS), Lielens and the dilute solution of Eshelby (Eshelby). Volume fraction = 30%. $R_1 = 2$, $R_2 = 1$. $\kappa_1 = \mu_1 = 1$. (a) Normalized effective bulk modulus. (b) Normalized effective shear modulus.
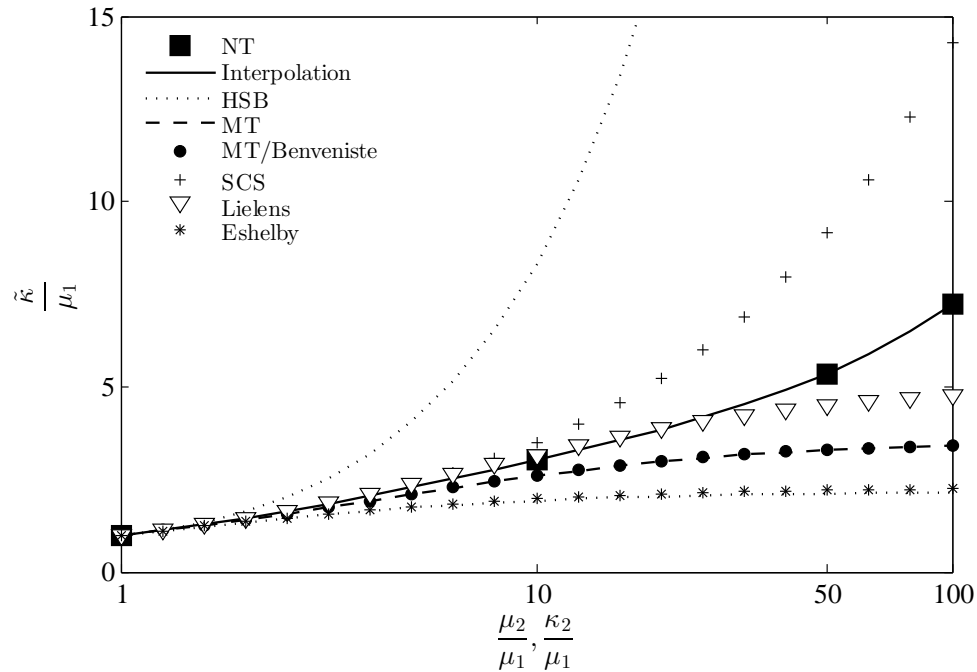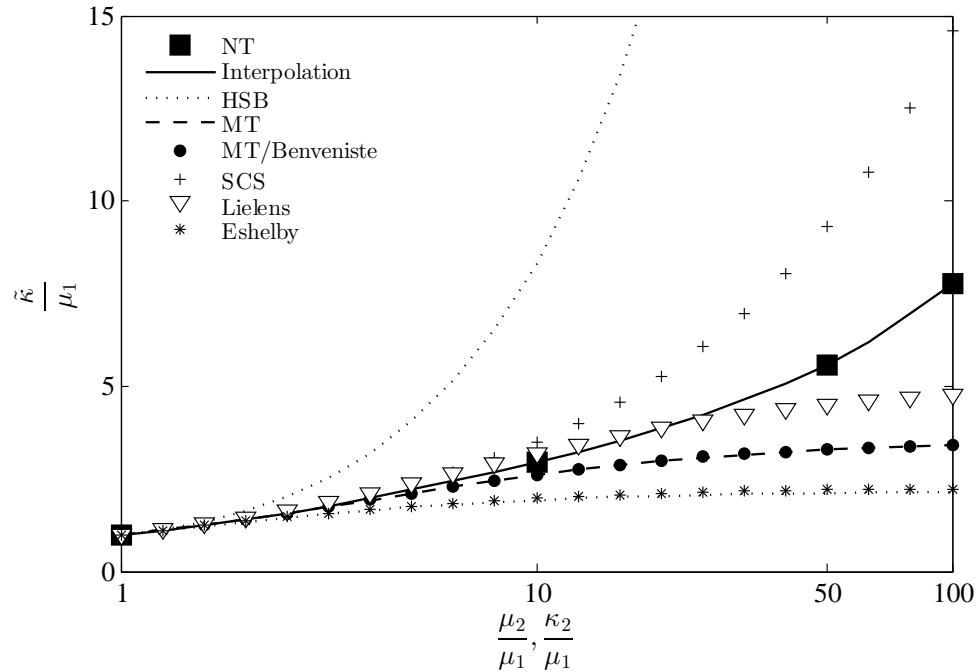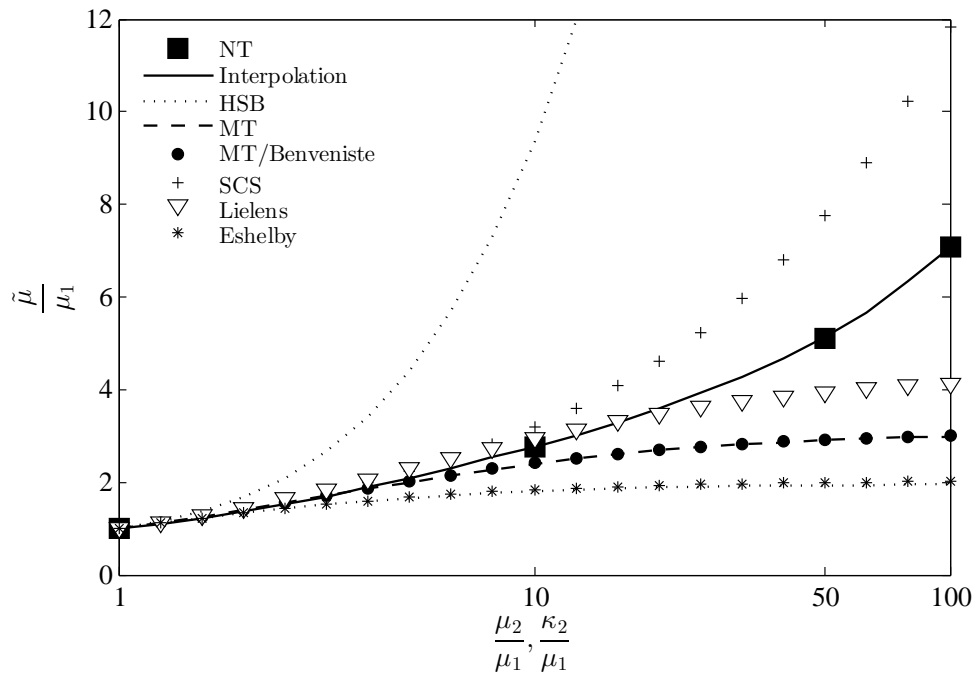
Figure 6.11 Comparison between the mechanical properties obtained with the numerical tool (NT) and those predicted by the analytical models: Hashin-Shtrikman Bounds (HSB), Mori-Tanaka (MT), Benveniste model (MT/Benveniste), self-consistent scheme (SCS), Lielens and the dilute solution of Eshelby (Eshelby). Volume fraction = 50%. $R_1 = 2$, $R_2 = 1$. $\kappa_1 = \mu_1 = 1$. (a) Normalized effective bulk modulus. (b) Normalized effective shear modulus.
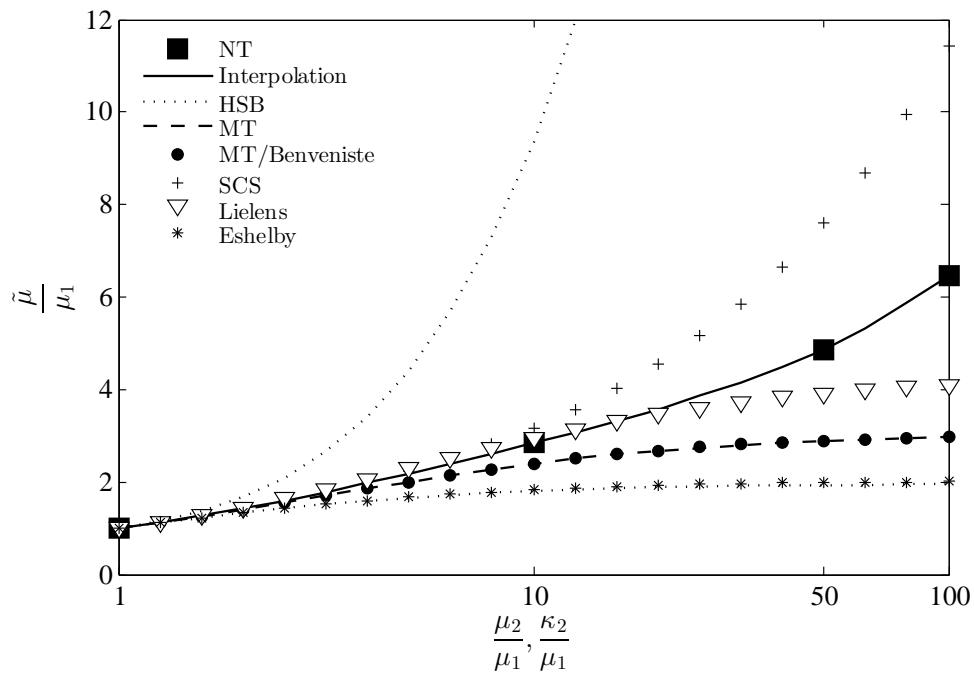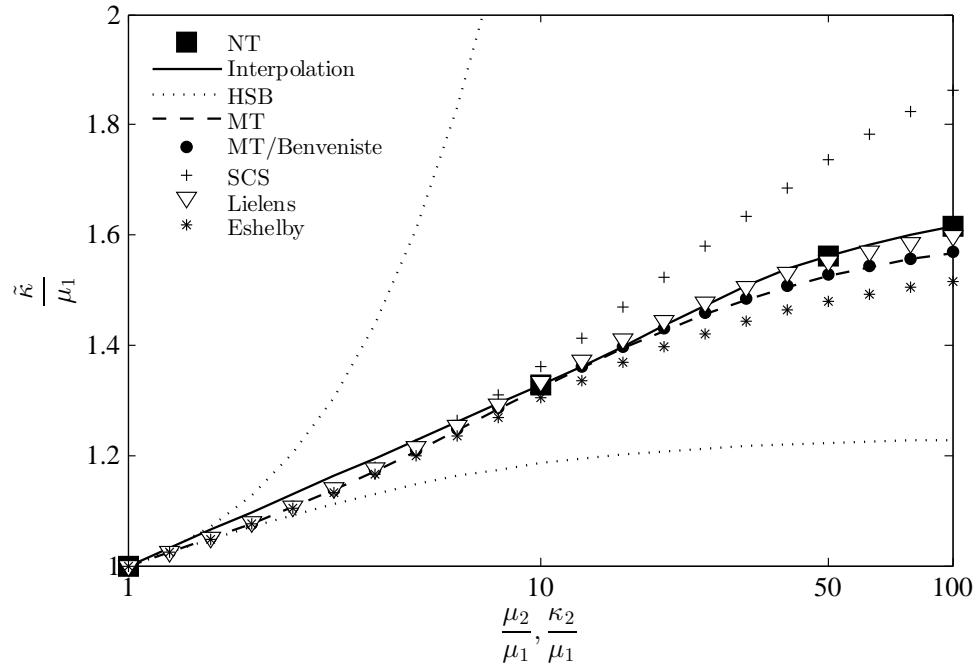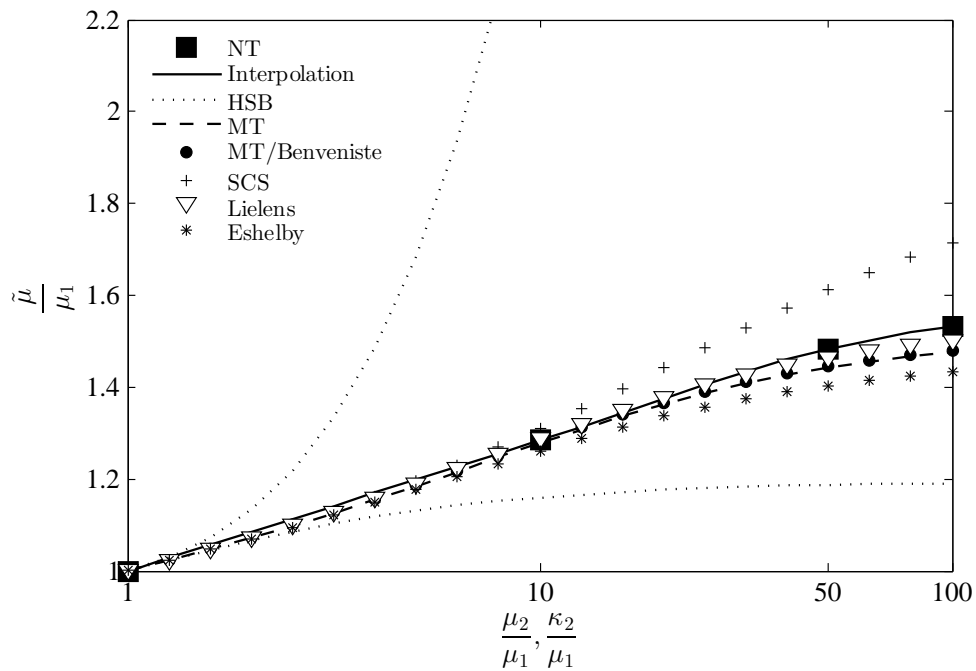
Figure 6.12 Comparison between the mechanical properties obtained with the numerical tool (NT) and those predicted by the analytical models: Hashin-Shtrikman Bounds (HSB), Mori-Tanaka (MT), Benveniste model (MT/Benveniste), self-consistent scheme (SCS), Lielens and the dilute solution of Eshelby (Eshelby). Volume fraction = 10%. $R_1 = 10$, $R_2 = 1$. $\kappa_1 = \mu_1 = 1$. (a) Normalized effective bulk modulus. (b) Normalized effective shear modulus.
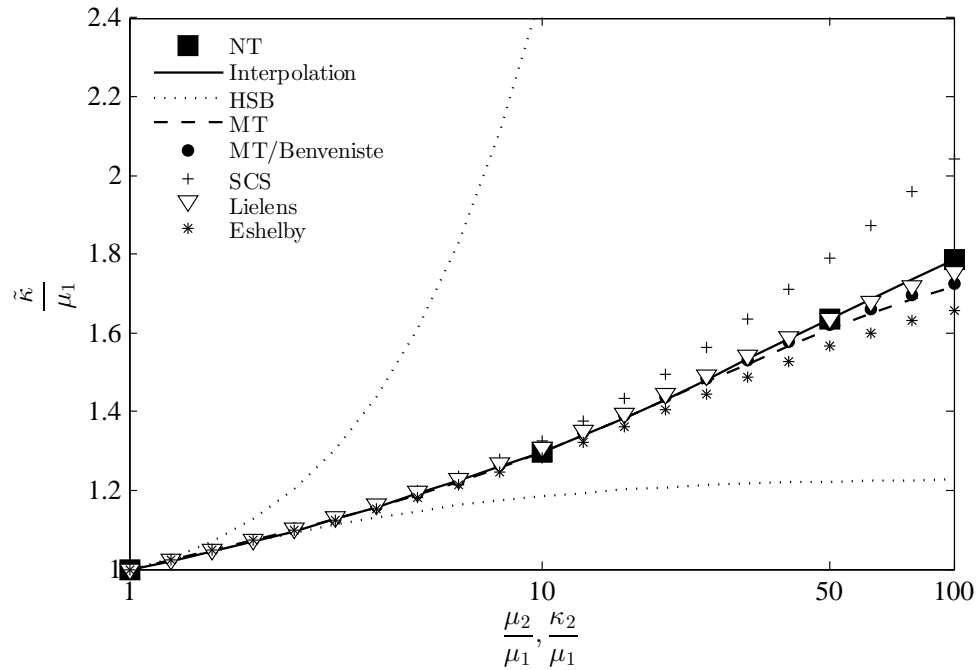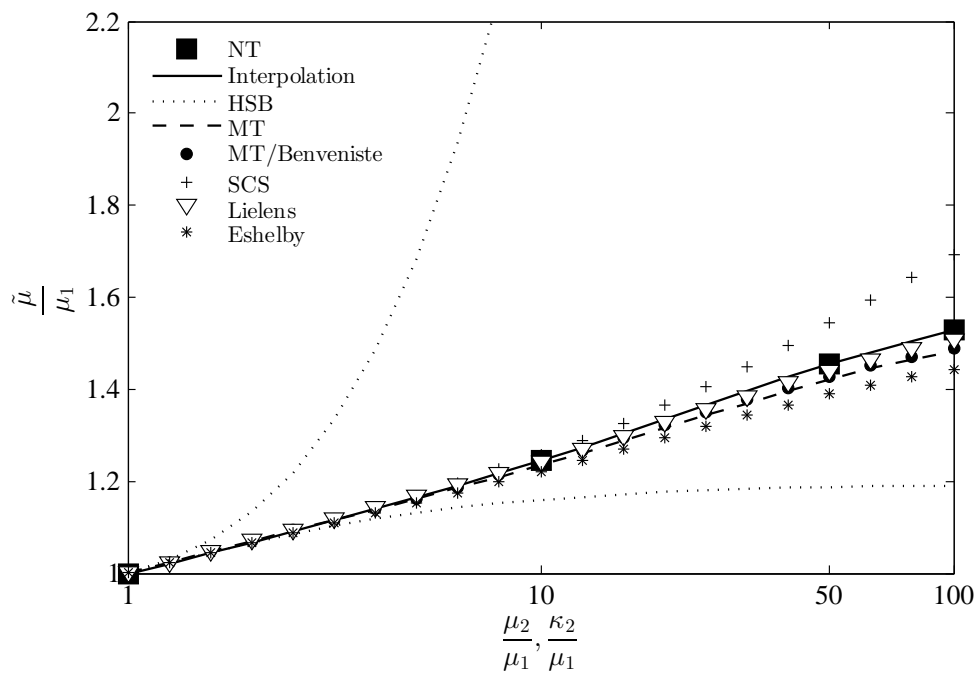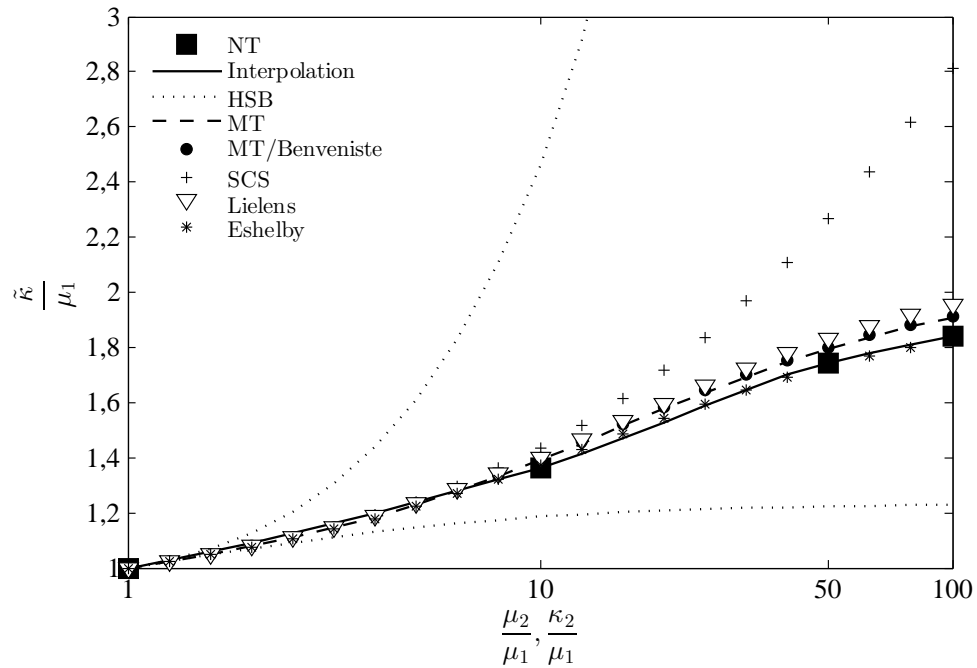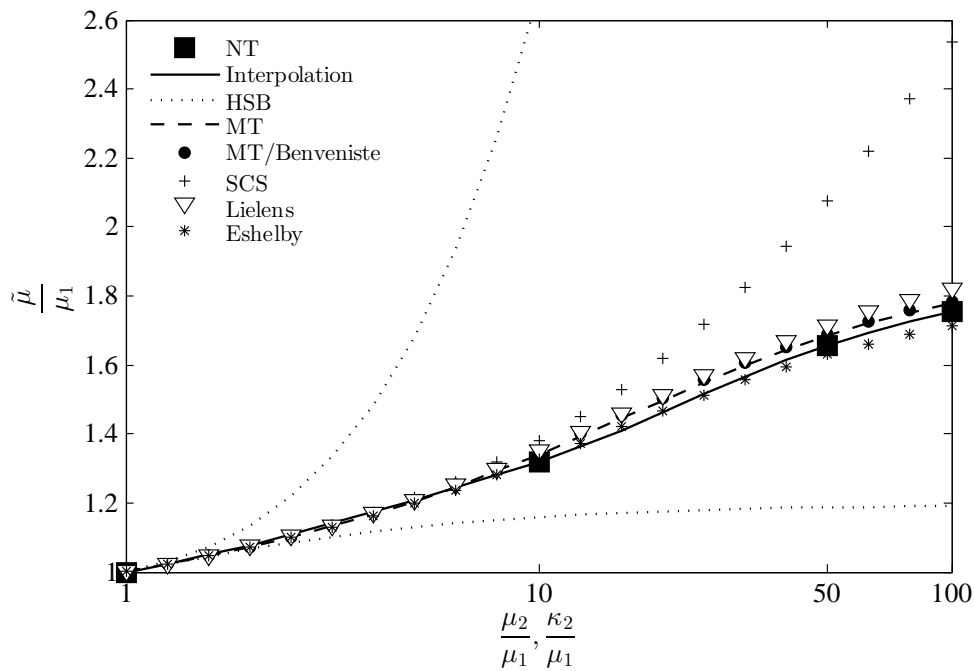
Figure 6.13 Comparison between the mechanical properties obtained with the numerical tool (NT) and those predicted by the analytical models: Hashin-Shtrikman Bounds (HSB), Mori-Tanaka (MT), Benveniste model (MT/Benveniste), self-consistent scheme (SCS), Lielens and the dilute solution of Eshelby (Eshelby). Volume fraction = 10%. $R_1 = 20$, $R_2 = 1$. $\kappa_1 = \mu_1 = 1$. (a) Normalized effective bulk modulus. (b) Normalized effective shear modulus.

CHAPTER 7

ARTICLE 4: HOMOGENIZATION MODELS FOR PREDICTING LOCAL
FIELD STATISTICS IN ELLIPSOIDAL FIBERS REINFORCED
COMPOSITES: COMPARISONS AND VALIDATIONS

E. Ghossein and M. Lévesque. Submitted to the *International Journal of Solids and Structures* on July 16, 2014.

7.1 Abstract

This paper validates the performance of analytical homogenization models at predicting the local field statistics in randomly distributed and oriented ellipsoidal fibers reinforced composites. The numerical validation was based on a newly introduced load independent metric, which allowed to formulate general conclusions. A large validation campaign was conducted and the Representative Volume Element (RVE) was rigorously determined for each combination of phases mechanical properties, fibers volume fraction and aspect ratio. The load independent properties computed numerically were compared to those predicted by a range of analytical models. The study revealed that the original Benveniste's interpretation of the Mori-Tanaka scheme led to the most accurate first order moments and intra-matrix second order moments, provided that the mechanical properties contrast between fibers and matrix are low. For higher contrasts, Lielens' model delivers the most accurate estimates. The self-consistent scheme is the most suited model to predict the intra-fiber second order moments when the fibers aspect ratio is low. For fibers with high aspect ratio, Lielens' model could be an alternative to the self-consistent scheme. Furthermore, an interpolation model has been developed and it has been shown to predict accurately the mean and covariance tensors of the intraphase stress fields.

7.2 Introduction

Homogenization models predict the effective mechanical behavior of heterogeneous materials using the properties and the statistical description of their constituents. Several micromechanical models have been developed in the literature (Eshelby, 1957; Hashin, 1962; Hashin and Shtrikman, 1963; Budiansky, 1965; Hill, 1965; Mori and Tanaka, 1973; Christensen and Lo, 1979; Benveniste, 1987; Torquato, 1991; Castaneda and Willis, 1995; Torquato, 1998) and their capacities at accurately evaluating effective properties of linearly elastic materials

have been rigorously evaluated (Ghossein and Levesque, 2012; Ghossein and Lévesque, 2014). Homogenization models can also compute first order moments (spatial average) and second order moments (related to the standard deviation and co-variance) of local stress or strain fields. It has been shown by numerous authors (Castañeda, 1991, 1996, 2002a,b; Castaneda and Suquet, 1998; Idiart and Castaneda, 2007a,b; Lahellec and Suquet, 2007a,b; Rekik *et al.*, 2007, 2012) that adding first and second order moments information into nonlinear homogenization schemes can significantly improve their performances. It would therefore be of interest to evaluate the performances of existing homogenization schemes at predicting local field fluctuations.

The capabilities of analytical homogenization models at predicting local field moments have been studied by a limited number of authors. The approach typically consisted of computing local fields with detailed models where the microstructure was explicitly represented, computing scalar equivalent stresses/strains for specific load cases and compare them with those predicted from analytical models. For example, Moulinec and Suquet (2003b); Brenner and Masson (2005); Idiart and Castaneda (2007b); Rekik *et al.* (2007); Buryachenko (2011); Doghri *et al.* (2011); Corcolle *et al.* (2012); Lahellec and Suquet (2013) studied composites while Idiart *et al.* (2006); Idiart and Castaneda (2007b); Rekik *et al.* (2007); Idiart *et al.* (2009); Rekik *et al.* (2012) were interested in rigidly reinforced and porous composites. Other studies dealt with the computation of intragranular field fluctuations in polycrystals (Lebensohn *et al.*, 2004, 2005b,a, 2007; Castelnau *et al.*, 2006, 2008; Brenner *et al.*, 2009; Montagnat *et al.*, 2013).

All of the above-mentioned studies focused on very specific microstructures submitted to very specific load cases, which led to load dependent conclusions. Such analyses cannot, therefore, be used to draw general conclusions regarding the accuracy of specific models at predicting local fields statistical moments.

The aim of this paper is to compare and validate the accuracy of analytical homogenization models at predicting the intraphase field fluctuations in randomly oriented and distributed ellipsoidal fibers reinforced composites. The approach relies on a new load independent metric that allows for drawing general conclusions. The load independent properties are first defined. A numerical technique is then implemented to compute these specific properties for a single microstructure. Finally, a large validation campaign is conducted by sweeping a wide range of phases mechanical and geometrical properties, and by comparing the properties obtained numerically to those predicted by analytical homogenization models.

The paper is structured as follow: Section 7.3 recalls the fundamental equations for determining the first and second order moments, and summarizes the different numerical techniques for computing the local fields in two-phase composites. The numerical approach used

in this work to compute the load independent properties is detailed in Section 7.4 while Section 7.5 describes the numerical validation campaign. Section 7.6 performs a thorough assessment of several analytical homogenization models by comparing their local field statistics estimations to those obtained numerically. A discussion and an analysis conclude the paper.

Scalars and vectors are respectively denoted by letters (e.g., s, S, σ, Σ) and boldfaced lower case Latin letters (e.g., $\boldsymbol{s}$); second and fourth order tensors are respectively denoted by boldfaced Greek letters (e.g., $\boldsymbol{\sigma}$, $\boldsymbol{\Sigma}$) and boldfaced upper case Latin letters (e.g., $\mathbf{S}$). Einstein summation convention has been adopted, unless specified otherwise.

7.3 Background

7.3.1 Governing equations

Suppose that a two-phase composite is subjected to a macroscopic stress $\boldsymbol{\Sigma}$ or a macroscopic strain $\mathbf{E}$. The purpose of homogenization is to compute the composite's effective stiffness tensor $\widetilde{\mathbf{C}}$ or compliance tensor $\widetilde{\mathbf{S}}$ such that:

$$\boldsymbol{\Sigma} = \widetilde{\mathbf{C}} : \mathbf{E} \tag{7.1a}$$

$$\mathbf{E} = \widetilde{\mathbf{S}} : \boldsymbol{\Sigma} \tag{7.1b}$$

It is possible to show that (Böhm, 1998):

$$< \boldsymbol{\varepsilon}(\boldsymbol{x}) > = \mathbf{E} \tag{7.2a}$$

$$< \boldsymbol{\sigma}(\boldsymbol{x}) > = \boldsymbol{\Sigma} \tag{7.2b}$$

where $\boldsymbol{\varepsilon}(\boldsymbol{x})$ and $\boldsymbol{\sigma}(\boldsymbol{x})$ are the local strain and stress fields, respectively, and $< \cdot >$ denotes an average over the volume. The relationship between the micro- and the macroscopic scale is given by the following equations:

$$\boldsymbol{\varepsilon}(\boldsymbol{x}) = \mathbf{A}(\boldsymbol{x}) : \mathbf{E} \tag{7.3a}$$

$$\boldsymbol{\sigma}(\boldsymbol{x}) = \mathbf{B}(\boldsymbol{x}) : \boldsymbol{\Sigma} \tag{7.3b}$$

where $\mathbf{A}(\boldsymbol{x})$ and $\mathbf{B}(\boldsymbol{x})$ denote the strain localization tensor and the stress concentration tensor, respectively. The first moment of strains and stresses in phase "i" ($i = 1$ for the matrix and $i = 2$ for the fibers) can be expressed as:

$$< \boldsymbol{\varepsilon} >_i = < \mathbf{A}(\boldsymbol{x}) >_i : \mathbf{E} = \mathbf{A}_i : \mathbf{E} \tag{7.4a}$$

$$< \boldsymbol{\sigma} >_i = < \mathbf{B}(\boldsymbol{x}) >_i : \boldsymbol{\Sigma} = \mathbf{B}_i : \boldsymbol{\Sigma} \tag{7.4b}$$

where $< \cdot >_i$ denotes the volume averaging over phase "i" and $\mathbf{A}_i$ and $\mathbf{B}_i$ refer respectively to the average strain localization tensor and stress concentration tensor within the phase.

For the very specific case of two-phase composites, tensors $\mathbf{A}_i$ and $\mathbf{B}_i$ are related since:

$$< \mathbf{A}(\boldsymbol{x}) > = c_1 \mathbf{A}_1 + c_2 \mathbf{A}_2 = \mathbf{I} \tag{7.5a}$$

$$< \mathbf{B}(\boldsymbol{x}) > = c_1 \mathbf{B}_1 + c_2 \mathbf{B}_2 = \mathbf{I} \tag{7.5b}$$

where $\mathbf{I}$ is the fourth order identity tensor and c_i is the volume fraction of phase "i". In addition, by using Eqs. (7.1) and (7.4), one can write:

$$< \boldsymbol{\sigma} >_i \; = \; \mathbf{B}_i : \boldsymbol{\Sigma} = \mathbf{B}_i : \left(\widetilde{\mathbf{C}} : \mathbf{E} \right) = \left(\mathbf{B}_i : \widetilde{\mathbf{C}} \right) : \mathbf{E} \tag{7.6a}$$

$$= \; \mathbf{C}_i : < \boldsymbol{\varepsilon} >_i = \mathbf{C}_i : \left(\mathbf{A}_i : \mathbf{E} \right) = \left(\mathbf{C}_i : \mathbf{A}_i \right) : \mathbf{E} \tag{7.6b}$$

Eqs. (7.6a) and (7.6b) lead to:

$$\mathbf{B}_i : \widetilde{\mathbf{C}} = \mathbf{C}_i : \mathbf{A}_i \quad \Longleftrightarrow \quad \mathbf{B}_i = \mathbf{C}_i : \mathbf{A}_i : \widetilde{\mathbf{S}} \tag{7.6c}$$

where $\mathbf{C}_i$ refers to the stiffness tensor of phase "i". Eqs. (7.5) and (7.6c) show that $\mathbf{A}_1$, $\mathbf{B}_1$ and $\mathbf{B}_2$ can be deduced from $\mathbf{A}_2$. Thus, the accuracy of homogenization models for evaluating the intraphase first moment of stresses and strains depends solely on their performance at predicting $\mathbf{A}_2$. The latter depends only on the microstructure properties and is independent of the loading. The expression of $\mathbf{A}_2$ for different analytical models can be found in (Ghossein and Lévesque, 2014).

Castaneda and Suquet (1998) showed that:

$$< \boldsymbol{\varepsilon} \otimes \boldsymbol{\varepsilon} >_i = \frac{1}{c_i} \mathbf{E} : \frac{\partial \widetilde{\mathbf{C}}}{\partial \mathbf{C}_i} : \mathbf{E} \tag{7.7a}$$

$$< \boldsymbol{\sigma} \otimes \boldsymbol{\sigma} >_i = \frac{1}{c_i} \boldsymbol{\Sigma} : \frac{\partial \widetilde{\mathbf{S}}}{\partial \mathbf{S}_i} : \boldsymbol{\Sigma} \tag{7.7b}$$

The stiffness and compliance tensors of an isotropic material can be expressed as:

$$\mathbf{C}_i = 3\kappa_i \mathbf{J} + 2\mu_i \mathbf{K} \tag{7.8a}$$

$$\mathbf{S}_i = \frac{1}{3}\kappa_i^{-1}\mathbf{J} + \frac{1}{2}\mu_i^{-1}\mathbf{K} \tag{7.8b}$$

where κ_i and μ_i denote the bulk and shear moduli of phase "i", respectively, and $\mathbf{J}$ and $\mathbf{K}$ are the classical spherical and deviatoric projection tensors. Combination of Eqs. (7.7) and

(7.8), and use of the chain rule leads to (Castaneda and Suquet, 1998):

$$\frac{1}{c_i}\mathbf{E}:\frac{\partial\widetilde{\mathbf{C}}}{\partial\kappa_i}:\mathbf{E}\ =\ 3<\boldsymbol{\varepsilon}\otimes\boldsymbol{\varepsilon}>_i::\mathbf{J} \tag{7.9a}$$

$$\frac{1}{c_i}\mathbf{E}:\frac{\partial\widetilde{\mathbf{C}}}{\partial\mu_i}:\mathbf{E}\ =\ 2<\boldsymbol{\varepsilon}\otimes\boldsymbol{\varepsilon}>_i::\mathbf{K} \tag{7.9b}$$

$$\frac{1}{c_i}\boldsymbol{\Sigma}:\frac{\partial\widetilde{\mathbf{S}}}{\partial\kappa_i^{-1}}:\boldsymbol{\Sigma}\ =\ \frac{1}{3}<\boldsymbol{\sigma}\otimes\boldsymbol{\sigma}>_i::\mathbf{J} \tag{7.9c}$$

$$\frac{1}{c_i}\boldsymbol{\Sigma}:\frac{\partial\widetilde{\mathbf{S}}}{\partial\mu_i^{-1}}:\boldsymbol{\Sigma}\ =\ \frac{1}{2}<\boldsymbol{\sigma}\otimes\boldsymbol{\sigma}>_i::\mathbf{K} \tag{7.9d}$$

Eqs. (7.9) show that second order moments are directly related to the first derivative of the effective tensors with respect to the phases properties. These derivatives solely depend on the microstructure and are therefore load independent.

7.3.2 Computation of local fields in heterogeneous materials

The Finite Element Method (FEM) has been the most commonly used technique for computing the local fields in heterogeneous materials (Llorca *et al.*, 2000; Bohm *et al.*, 2002; Segurado and Llorca, 2002; Kari *et al.*, 2007b; Barello and Lévesque, 2008; Klusemann and Svendsen, 2010; Cojocaru and Karlsson, 2010; El-Mourid *et al.*, 2012; Pahlavanpour *et al.*, 2013; Moussaddy *et al.*, 2013b). The method consists of meshing a unit cell and computing the local fields when it is submitted to an external load. Despite its robustness, FEM cannot be fully automated since the meshing operation usually requires user input, especially for fibers with high volume fractions and/or aspect ratios.

Moulinec and Suquet (1998) have proposed an alternative technique based on Fast Fourier Transforms (FFT). The technique consists of discretizing the microstructures into voxels and solving, in each voxel, the constitutive law in Fourier space. The main advantage of this approach is that it does not require meshing, and therefore has the potential to be completely automated. The details of this technique can be found in (Ghossein and Levesque, 2012).

7.4 Computation of load independent properties for a single microstructure

Load independent properties related to first and second order moments have been defined in Section 7.3.1. The following section describes how these properties were computed numerically for a single microstructure. It should be noted that local stress and strain fields were computed in this study using the FFT-based technique.
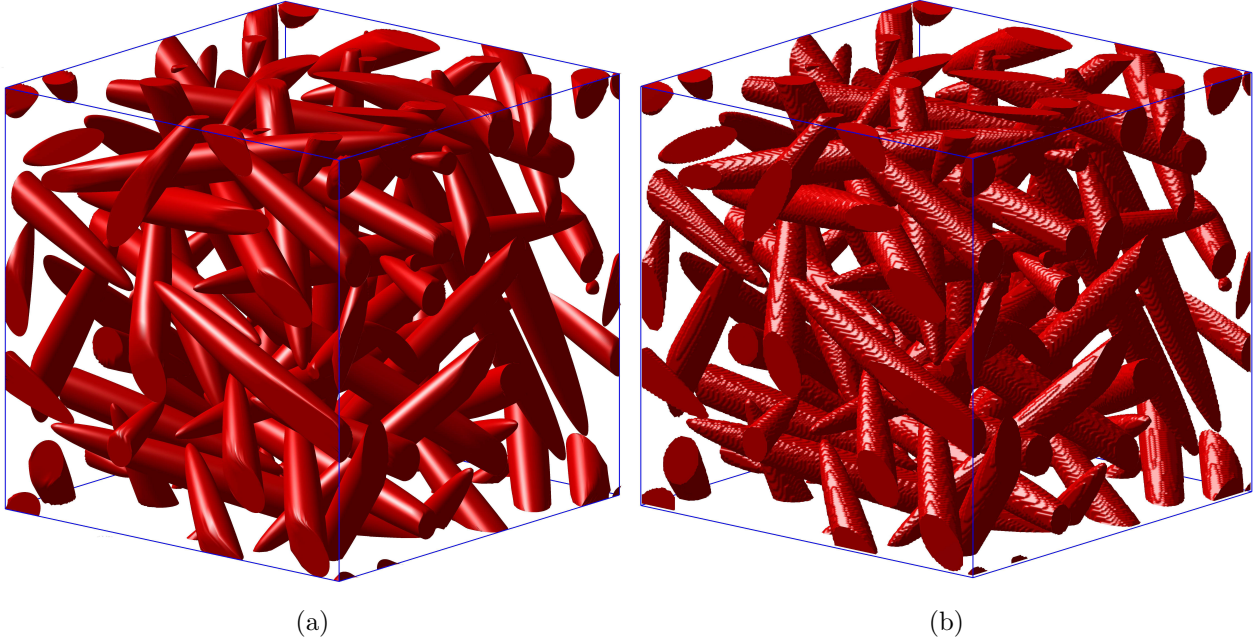
Figure 7.1 Generation and discretization of a single microstructure on a grid of $256 \times 256 \times 256$ voxels. Number of prolate fibers = 45. Volume fraction = 20%. Aspect ratio = 10. (a) Generated microstructure. (b) Discretized microstructure.

7.4.1 Generation and discretization of a random microstructure

Each microstructure was randomly generated by using the molecular dynamics algorithm proposed by Ghossein and Levesque (2013). Each microstructure was then discretized into $N \times N \times N$ cubic voxels, each of which had 9 points evenly distributed. The stiffness tensor of each voxel, denoted by $\mathbf{C}(\boldsymbol{x}_p)$, was obtained by adopting the following rules of arbitration:

$$\mathbf{C}(\boldsymbol{x}_p) = \begin{cases} \mathbf{C}_1 & \text{if 5 points or more belonged to a fiber} \\ \mathbf{C}_2 & \text{otherwise} \end{cases} \tag{7.10}$$

Figure 7.1a shows an example of a generated random microstructure containing 45 prolate ellipsoidal fibers with an aspect ratio of 10 and a volume fraction of 20%. The aspect ratio of an axisymmetric ellipsoidal fiber is defined as the ratio between the length of its radius along the symmetry axis and the length of its equatorial radius. Figure 7.1b shows the discretization of the same microstructure on a grid of $256 \times 256 \times 256$ voxels.

7.4.2 Load independent properties related to the first order moments

Assuming that the generated microstructure is isotropic , $\mathbf{A}_2$ is also isotropic and can be

written as:

$$\mathbf{A}_2 = \alpha \mathbf{J} + \beta \mathbf{K} \qquad (7.11)$$

Therefore, Eq. (7.4a) becomes:

$$< \boldsymbol{\varepsilon} >_2 = \left(\alpha \mathbf{J} + \beta \mathbf{K} \right) : \mathbf{E} = \alpha \mathbf{J} : \mathbf{E} + \beta \mathbf{K} : \mathbf{E} \qquad (7.12a)$$

Then

$$< \boldsymbol{\varepsilon} >_2 = \alpha \frac{\left(\mathrm{E}_{11} + \mathrm{E}_{22} + \mathrm{E}_{33} \right)}{3} \begin{bmatrix} 1 & 0 & 0 \\ 0 & 1 & 0 \\ 0 & 0 & 1 \end{bmatrix}$$

$$+ \frac{\beta}{3} \begin{bmatrix} 2\mathrm{E}_{11} - \mathrm{E}_{22} - \mathrm{E}_{33} & 3\mathrm{E}_{12} & 3\mathrm{E}_{13} \\ 3\mathrm{E}_{12} & 2\mathrm{E}_{22} - \mathrm{E}_{11} - \mathrm{E}_{33} & 3\mathrm{E}_{23} \\ 3\mathrm{E}_{13} & 3\mathrm{E}_{23} & 2\mathrm{E}_{33} - \mathrm{E}_{11} - \mathrm{E}_{22} \end{bmatrix} \qquad (7.12b)$$

A unit macroscopic axial strain field was applied along the first principal direction (i.e., $\mathrm{E}_{ij} = 1$ for $i = j = 1$ and $\mathrm{E}_{ij} = 0$ otherwise). Let $\boldsymbol{\varepsilon}^\dagger$ be the intra-fiber first moment of strains obtained under this specific loading, i.e., the average of the strain field over all the voxels belonging to the fibers. Since the microstructure was assumed to be isotropic, the intra-fiber average shear strains were almost null (i.e., $\varepsilon_{ij}^\dagger \approx 0$ for $i \neq j$). Therefore, Eq. (7.12b) becomes:

$$\begin{bmatrix} \varepsilon_{11}^\dagger & 0 & 0 \\ 0 & \varepsilon_{22}^\dagger & 0 \\ 0 & 0 & \varepsilon_{33}^\dagger \end{bmatrix} = \frac{\alpha}{3} \begin{bmatrix} 1 & 0 & 0 \\ 0 & 1 & 0 \\ 0 & 0 & 1 \end{bmatrix} + \frac{\beta}{3} \begin{bmatrix} 2 & 0 & 0 \\ 0 & -1 & 0 \\ 0 & 0 & -1 \end{bmatrix} \qquad (7.13)$$

α and β can be deduced from Eq. (7.13):

$$\alpha = \varepsilon_{11}^\dagger + \varepsilon_{22}^\dagger + \varepsilon_{33}^\dagger \qquad (7.14a)$$

$$\beta = \varepsilon_{11}^\dagger - \frac{\varepsilon_{22}^\dagger + \varepsilon_{33}^\dagger}{2} \qquad (7.14b)$$

Given that the microstructure was almost isotropic, the same values of α and β would have been obtained if the macroscopic strain field was applied along the second or third principal direction. Indeed, a maximum variation of 0.6% was observed between two different principal directions, for both α and β.

7.4.3 Load independent properties related to the second order moments

Writing the effective tensors as:

$$\widetilde{\mathbf{C}} = 3\widetilde{\kappa}\mathbf{J} + 2\widetilde{\mu}\mathbf{K} \tag{7.15a}$$

$$\widetilde{\mathbf{S}} = \frac{1}{3}\widetilde{\kappa}^{-1}\mathbf{J} + \frac{1}{2}\widetilde{\mu}^{-1}\mathbf{K} \tag{7.15b}$$

the first-order derivatives that appear in Eqs. (7.9) become:

$$\frac{\partial \widetilde{\mathbf{C}}}{\partial \kappa_i} = 3\frac{\partial \widetilde{\kappa}}{\partial \kappa_i}\mathbf{J} + 2\frac{\partial \widetilde{\mu}}{\partial \kappa_i}\mathbf{K} \tag{7.16a}$$

$$\frac{\partial \widetilde{\mathbf{C}}}{\partial \mu_i} = 3\frac{\partial \widetilde{\kappa}}{\partial \mu_i}\mathbf{J} + 2\frac{\partial \widetilde{\mu}}{\partial \mu_i}\mathbf{K} \tag{7.16b}$$

$$\frac{\partial \widetilde{\mathbf{S}}}{\partial \kappa_i^{-1}} = \frac{1}{3}\frac{\partial \widetilde{\kappa}^{-1}}{\partial \kappa_i^{-1}}\mathbf{J} + \frac{1}{2}\frac{\partial \widetilde{\mu}^{-1}}{\partial \kappa_i^{-1}}\mathbf{K} \tag{7.16c}$$

$$\frac{\partial \widetilde{\mathbf{S}}}{\partial \mu_i^{-1}} = \frac{1}{3}\frac{\partial \widetilde{\kappa}^{-1}}{\partial \mu_i^{-1}}\mathbf{J} + \frac{1}{2}\frac{\partial \widetilde{\mu}^{-1}}{\partial \mu_i^{-1}}\mathbf{K} \tag{7.16d}$$

In this study, only the derivatives that appear in Eqs (7.16c) and (7.16d) were computed since the derivatives in Eqs (7.16a) and (7.16b) can be easily deduced. Indeed, using the chain rule, one can show that:

$$\begin{aligned}
\frac{\partial y}{\partial x} &= \left(\frac{\partial y}{\partial y^{-1}}\right)\left(\frac{\partial y^{-1}}{\partial x^{-1}}\right)\left(\frac{\partial x^{-1}}{\partial x}\right) \\
&= \left(-y^2\right)\left(\frac{\partial y^{-1}}{\partial x^{-1}}\right)\left(-\frac{1}{x^2}\right) \qquad \text{with} \qquad \begin{cases} y \in \{\widetilde{\kappa}, \widetilde{\mu}\} \\ x \in \{\kappa_i, \mu_i\} \end{cases} \\
&= \left(\frac{y}{x}\right)^2 \frac{\partial y^{-1}}{\partial x^{-1}}
\end{aligned} \tag{7.17}$$

Define δ_x^y as:

$$\delta_x^y = \frac{\partial y^{-1}}{\partial x^{-1}} \tag{7.18}$$

The evaluation of Eqs. (7.16c) and (7.16d) therefore required computing:

$$\delta_{\kappa_i}^{\widetilde{\kappa}} = \frac{\partial \widetilde{\kappa}^{-1}}{\partial \kappa_i^{-1}} \quad , \quad \delta_{\kappa_i}^{\widetilde{\mu}} = \frac{\partial \widetilde{\mu}^{-1}}{\partial \kappa_i^{-1}} \quad , \quad \delta_{\mu_i}^{\widetilde{\kappa}} = \frac{\partial \widetilde{\kappa}^{-1}}{\partial \mu_i^{-1}} \quad , \quad \delta_{\mu_i}^{\widetilde{\mu}} = \frac{\partial \widetilde{\mu}^{-1}}{\partial \mu_i^{-1}}$$

These derivatives were obtained numerically as follows. First, the FFT-based algorithm was implemented for computing the effective properties of a single microstructure. The

algorithm took as inputs the phases moduli and outputted the effective moduli (see (Ghossein and Levesque, 2012) for more details about this algorithm). It can be represented by a black-box function, such as:

$$\left[\widetilde{\kappa}^{-1}, \widetilde{\mu}^{-1}\right] = \mathcal{F}\left(\kappa_i^{-1}, \mu_i^{-1}\right) \tag{7.19}$$

The derivatives were then computed according to a second order central finite difference scheme:

$$\left[\delta_{\kappa_i}^{\widetilde{\kappa}}, \delta_{\kappa_i}^{\widetilde{\mu}}\right] = \frac{\mathcal{F}\left(\kappa_i^{-1} + h, \mu_i^{-1}\right) - \mathcal{F}\left(\kappa_i^{-1} - h, \mu_i^{-1}\right)}{2h} \tag{7.20a}$$

$$\left[\delta_{\mu_i}^{\widetilde{\kappa}}, \delta_{\mu_i}^{\widetilde{\mu}}\right] = \frac{\mathcal{F}\left(\kappa_i^{-1}, \mu_i^{-1} + h\right) - \mathcal{F}\left(\kappa_i^{-1}, \mu_i^{-1} - h\right)}{2h} \tag{7.20b}$$

where h is the modulus step. It was found after trials and errors that $h = 10^{-4}$ provided accurate and converged results.

According to Eqs. (7.20), the FFT-based algorithm had to be called 8 times in total (4 times per phase) in order to compute the load-independent derivatives for a single microstructure.

7.4.4 Convergence in terms of number of voxels

Let Φ be a vector containing the load-independent properties that have been defined and computed in the previous sections:

$$\Phi = \left\{\alpha, \beta, \delta_{\kappa_i}^{\widetilde{\kappa}}, \delta_{\kappa_i}^{\widetilde{\mu}}, \delta_{\mu_i}^{\widetilde{\kappa}}, \delta_{\mu_i}^{\widetilde{\mu}}\right\} \qquad \text{with} \qquad i \in \{1, 2\} \tag{7.21}$$

The procedure for computing Φ was repeated for an increasing number of voxels until convergence. Starting with $N = 32$, the value of N was doubled until the following inequality was satisfied:

$$\max_{\Phi}\left(\frac{\Phi^{2N} - \Phi^N}{\Phi^N}\right) \leq 0.02 \tag{7.22}$$

where Φ^N refers to the set of properties computed with N^3 voxels. A tolerance of 2% was used as a convergence criterion.

7.5 Validation campaign

7.5.1 Studied microstructures

A wide range of mechanical and geometrical properties was studied for randomly ori-

Table 7.1 Studied combinations of aspect ratios and volume fractions for prolate and oblate fibers.

Aspect ratios	Volume fractions (%)	
	Prolate fibers	Oblate fibers
1	{10, 20, 30, 40, 50}	
2	{10, 20, 30, 40, 50}	{10, 20, 30, 40, 50}
5	{10, 20, 30, 40}	{10, 20, 30}
10	{10, 20}	{10, 20}
20	{10}	{10}

ented and distributed isotropic ellipsoidal fibers into an isotropic matrix. Prolate and oblate ellipsoidal fibers with different aspect ratios and volume fractions were considered. All combinations of geometrical properties are summarized in Table 7.1.

For each combination of volume fraction and aspect ratio, the mechanical properties contrast $\rho = \frac{\kappa_2}{\kappa_1} = \frac{\mu_2}{\mu_1}$ was varied and took the values of {1, 10, 50, 100}.

7.5.2 Representative Volume Element determination

The load-independent properties were evaluated as follows. For each combination of contrast, aspect ratio and volume fraction, the size of the Representative Volume Element (RVE) was determined according to the methodology of Kanit *et al.* (2003). For the same number of represented fibers, Φ was computed for several random realizations. The number of simulations n was considered sufficient when the half width of a 95% confidence interval over each item of Φ was less than 2% of the corresponding property average, as per:

$$\max_{\Phi} \frac{T_{1-\alpha/2}^{n-1} S_{\Phi}}{\bar{\bar{\Phi}} \sqrt{n}} \leq 0.02 \quad , \quad n \geq 6 \tag{7.23}$$

where T is the Student distribution quantile with $(n-1)$ degrees of freedom, $(1-\alpha)$ is the confidence level (i.e., $1-\alpha = 0.95$) and S_{Φ} is an estimate of the standard deviation of Φ.

The procedure was repeated for an increasing volume element size (or number of fibers). Starting with volume elements having the same size as the RVE obtained by Ghossein and Lévesque (2014) when computing the effective moduli $\widetilde{\kappa}$ and $\widetilde{\mu}$ (for the same combination of contrast, aspect ratio and volume fraction), 15 fibers were added between each volume element size. The RVE was reached when Φ converged with less than 2% variation from one

volume element size to the next.

7.6 Results and discussion

The numerical predictions of the intraphase first and second order moments were compared to the predictions of the dilute solution of Eshelby (Eshelby), the model of Mori-Tanaka, the self-consistent scheme (SCS), Lielens' model and the model of Benveniste (MT/Benveniste). The numerical results were interpolated using a MATLAB built-in cubic spline interpolation. Results are only shown for the case of prolate fibers since similar predictions were obtained for oblate fibers. For all cases, κ_1 and μ_1 were set to 1 and contrast ρ was varied from 1 to 100.

7.6.1 Prediction of the intra-fiber first order moments

Figure 7.2 shows the predictions of the spherical and deviatoric components of the localization tensor $\mathbf{A}_2$ (α and β, respectively) for a volume fraction of 10% and an aspect ratio of 1 (spherical particles). Every analytical model provided accurate predictions for both components, even for high mechanical properties contrasts. The difference between numerical and analytical predictions is negligible. However, significant discrepancies were observed for volume fractions of 50%. It can be seen in Figure 7.3 that the dilute solution of Eshelby underestimates α and β while they are overstimated by the SCS. It seems that neither model is suitable for predicting the intraphase first order moments for composites with high fibers volume fractions. For low contrasts (i.e., $\rho \leq 10$), MT and MT/Benveniste models deliver the most accurate predictions. For high contrasts (i.e., $\rho \geq 10$), Lielens' model is the most accurate.

Figure 7.4 shows the results for an aspect ratio of 20 and a volume fraction of 10%. In the studied range of contrasts, all analytical models deliver accurate estimates for α and β. The SCS deviates slightly from the numerical predictions when $\rho \geq 10$. However, its accuracy remains acceptable, even when $\rho = 100$.

From the results shown in Figures 7.2, 7.3 and 7.4, it seems that the fibers volume fraction is the most influent parameter on the analytical models accuracy when predicting the intraphase first order moments. Indeed, when the volume fraction is low (i.e., 10%), the analytical homogenization models provide accurate estimates for α and β, even for high aspect ratios and contrasts. Moreover, independently of the fibers aspect ratio and volume fraction, MT and MT/Benveniste estimates are the closest to the numerical predictions when $\rho \leq 10$, while Lielens' model has the highest accuracy when $\rho \geq 10$.

7.6.2 Prediction of the intra-matrix second order moments

Figure 7.5 shows the predictions for $\delta_{\kappa_1}^{\widetilde{\kappa}}$, $\delta_{\kappa_1}^{\widetilde{\mu}}$, $\delta_{\mu_1}^{\widetilde{\kappa}}$ and $\delta_{\mu_1}^{\widetilde{\mu}}$ for spherical particles with a volume fraction of 10%. For $\rho \leq 10$, every model predicts accurately $\delta_{\kappa_1}^{\widetilde{\kappa}}$ and $\delta_{\kappa_1}^{\widetilde{\mu}}$, except the dilute solution of Eshelby (Figures 7.5a and 7.5b). For $\rho \geq 10$, only the SCS and Lielens' model provide acceptable estimates for $\delta_{\kappa_1}^{\widetilde{\kappa}}$ and $\delta_{\kappa_1}^{\widetilde{\mu}}$. It is important to note that $\delta_{\kappa_1}^{\widetilde{\mu}}$ is negligible when compared to $\delta_{\kappa_1}^{\widetilde{\kappa}}$ ($\delta_{\kappa_1}^{\widetilde{\kappa}} \approx 100\, \delta_{\kappa_1}^{\widetilde{\mu}}$). The same behavior is observed in Figures 7.5c and 7.5d. Indeed, $\delta_{\mu_1}^{\widetilde{\kappa}}$ follows a similar trend as $\delta_{\kappa_1}^{\widetilde{\mu}}$, while $\delta_{\mu_1}^{\widetilde{\mu}}$ and $\delta_{\kappa_1}^{\widetilde{\kappa}}$ have the same tendency. The only difference is that the SCS is slightly more accurate than Lielens' model when predicting $\delta_{\mu_1}^{\widetilde{\mu}}$ for high contrasts ($\rho \geq 10$).

For an aspect ratio of 1 and a volume fraction of 50%, Figure 7.6 shows that the SCS underestimates $\delta_{\kappa_1}^{\widetilde{\kappa}}$, $\delta_{\mu_1}^{\widetilde{\kappa}}$, and $\delta_{\mu_1}^{\widetilde{\mu}}$, while they are overstimated by Lielens' model. Except for $\delta_{\kappa_1}^{\widetilde{\mu}}$, the predictions of MT and MT/Benveniste are the most accurate when $\rho \leq 10$. When $\rho \geq 10$, Lielens' model delivers the most accurate predictions. For $\delta_{\kappa_1}^{\widetilde{\mu}}$ (Figure 7.6b), it seems that the dilute solution of Eshelby is the closest to the numerical predictions. However, for the same range of contrasts, the values of $\delta_{\kappa_1}^{\widetilde{\mu}}$ are low when compared to those of $\delta_{\kappa_1}^{\widetilde{\kappa}}$, $\delta_{\mu_1}^{\widetilde{\kappa}}$, and $\delta_{\mu_1}^{\widetilde{\mu}}$. Therefore, the contribution of $\delta_{\kappa_1}^{\widetilde{\mu}}$ in the evaluation of the intra-matrix second order moments is negligible when compared to the contribution of the other derivatives.

Figure 7.7 shows that every analytical model predicts accurately the four derivatives when $\rho \leq 10$, for ellipsoidal particles with an aspect ratio of 20 and a volume fraction of 10%. For high contrasts, the SCS deviates from the numerical solution, especially for $\delta_{\kappa_1}^{\widetilde{\mu}}$ and $\delta_{\mu_1}^{\widetilde{\kappa}}$. The accuracy of the other models remains acceptable, Lielens' model being the most accurate.

As observed for the first order moments, the homogenization models accuracy is more sensitive to the fibers volume fraction than to their aspect ratio when predicting $\delta_{\kappa_1}^{\widetilde{\kappa}}$, $\delta_{\kappa_1}^{\widetilde{\mu}}$, $\delta_{\mu_1}^{\widetilde{\kappa}}$ and $\delta_{\mu_1}^{\widetilde{\mu}}$. For low contrasts, MT and MT/Benveniste are the most suited models to predict the intra-matrix second order moments. For high contrasts, it seems that Lielens' model provides the most accurate estimates.

7.6.3 Prediction of the intra-fiber second order moments

Figure 7.8 shows the numerical and analytical estimates for $\delta_{\kappa_2}^{\widetilde{\kappa}}$, $\delta_{\kappa_2}^{\widetilde{\mu}}$, $\delta_{\mu_2}^{\widetilde{\kappa}}$ and $\delta_{\mu_2}^{\widetilde{\mu}}$ for a volume fraction of 10% and an aspect ratio of 1. Every analytical model provided accurate predictions when $\rho \leq 10$, except the dilute solution of Eshelby, for $\delta_{\kappa_2}^{\widetilde{\kappa}}$ and $\delta_{\mu_2}^{\widetilde{\mu}}$. No analytical model predicts accurately $\delta_{\kappa_2}^{\widetilde{\kappa}}$ and $\delta_{\mu_2}^{\widetilde{\mu}}$ when $\rho \geq 60$ and $\rho \geq 20$, respectively. However, in both cases, the predictions of the SCS are the closest to the numerical solution. It should be noted that all models reached a plateau for high contrasts, which is not the case for the numerical solution. On the other hand, according to Figures 7.8b and 7.8c, only the SCS

estimates accurately $\delta_{\kappa_2}^{\widetilde{\mu}}$ and $\delta_{\mu_2}^{\widetilde{\kappa}}$ when $\rho \leq 10$. For all other models, $\delta_{\kappa_2}^{\widetilde{\mu}} = \delta_{\mu_2}^{\widetilde{\kappa}} \approx 0$ for the studied range of contrasts. However, the SCS deviates from the numerical predictions when $\rho \geq 20$, but remains the most accurate among the studied models.

When the volume fraction of the spherical particles reaches 50%, Figures 7.9a and 7.9d show that MT and MT/Benveniste models are the most accurate for predicting $\delta_{\kappa_2}^{\widetilde{\kappa}}$ and $\delta_{\mu_2}^{\widetilde{\mu}}$ when $\rho \leq 10$. Nevertheless, the estimates of the SCS and Lielens' model are still within acceptable margins. For higher contrasts, all analytical models reached a plateau, except the SCS. The latter follows the same trend as the numerical solution and is the only model that provides acceptable estimates of $\delta_{\kappa_2}^{\widetilde{\kappa}}$ and $\delta_{\mu_2}^{\widetilde{\mu}}$. The same observation can be made in Figures 7.9b and 7.9c. It can be seen that the SCS provides the most accurate predictions of $\delta_{\kappa_2}^{\widetilde{\mu}}$ and $\delta_{\mu_2}^{\widetilde{\kappa}}$ among all the studied models.

When the fibers aspect ratio reaches 20 (with a volume fraction of 10%), all analytical models except the SCS predict the four derivatives with a high accuracy and for the entire range of mechanical properties contrasts. Among these models, Lielens' is slightly the most accurate. The SCS predictions for $\delta_{\kappa_2}^{\widetilde{\kappa}}$, $\delta_{\kappa_2}^{\widetilde{\mu}}$, $\delta_{\mu_2}^{\widetilde{\kappa}}$ and $\delta_{\mu_2}^{\widetilde{\mu}}$ are acceptable for $\rho \leq 40$. Significant discrepancies are observed when $\rho \geq 40$.

According to these results, and as observed in Sections 7.6.1 and 7.6.2, the influence of the fibers aspect ratio on the analytical models accuracy is negligible when compared to that of the fibers volume fraction. Moreover, for fibers with low aspect ratio, the SCS seems to be the most suitable model to predict the intra-fiber second order moments. This is valid for the entire range of volume fractions. For ellipsoidal particles with high aspect ratio, Lielens' model provided the most accurate estimates.

7.6.4 Prediction of the stress fields using the interpolation model

The objective of this section is to evaluate the accuracy of the interpolation model at predicting the stress fields in a composite subjected to a given complex loading. Two composites were studied. The first (composite A) was reinforced with ellipsoidal fibers having an aspect ratio of 3 and a volume fraction of 35%. The mechanical properties contrast was $\rho = 80$. In the second (composite B), the fibers had an aspect ratio of 15 and a volume

Table 7.2 Mechanical and geometrical properties of composites A and B.

	Number of fibers	Volume fraction	Aspect ratio	Contrast ρ
Composite A	90	35%	3	80
Composite B	120	15%	15	40

fraction of 15%. For this composite, $\rho = 40$. For each composite, the size of the RVE was determined according to the methodology described in Section 7.5.2. It was found that the RVE of composite A contained 90 fibers while that of composite B contained 120 fibers. The properties of both composites are summarized in Table 7.2.

A complex loading was represented by a macroscopic strain field. It was randomly chosen and is given by:

$$\mathbf{E} = \begin{bmatrix} 3 & -5 & -2 \\ -5 & 1 & 2 \\ -2 & 2 & 0.5 \end{bmatrix} \tag{7.24}$$

The intraphase stress fields were computed numerically. A microstructure having the same size as the RVE was randomly generated for each composite, namely microstructures A and B. The stress fields were computed with the FFT-based technique and the first and second order moments were simply deduced in each phase (i.e., $< \boldsymbol{\sigma} >_i^{\mathrm{num}}$ and $< \boldsymbol{\sigma} \otimes \boldsymbol{\sigma} >_i^{\mathrm{num}}$, where "num" stands for "numerical").

The intraphase first and second order moments of the stress fields were also determined analytically, as follows. First, the load-independent properties Φ were computed for each composite by using the interpolation model. $\mathbf{A}_2$ was computed using Eq. (7.11) and $\mathbf{A}_1$ was deduced from Eq. (7.5a). Knowing $\mathbf{A}_1$ and $\mathbf{A}_2$, the first moment of stress in each phase was computed as:

$$< \boldsymbol{\sigma} >_i^{\mathrm{ana}} = \mathbf{C}_i : \left(\mathbf{A}_i : \mathbf{E} \right) \tag{7.25}$$

where "ana" stands for "analytical".

In a second step, the intraphase second moment of stresses was computed using Eq.(7.7b), which can be written as (see Appendix 7.A):

$$< \sigma_{mn} \otimes \sigma_{op} >_i^{\mathrm{ana}} = \frac{1}{c_i} \boldsymbol{\Sigma} : \left[\frac{1}{3} \left(\frac{3\delta_{\kappa_i}^{\widetilde{\kappa}}}{\mathrm{J}_{mnop}} + \frac{2\delta_{\mu_i}^{\widetilde{\kappa}}}{\mathrm{K}_{mnop}} \right) \mathbf{J} + \frac{1}{2} \left(\frac{3\delta_{\kappa_i}^{\widetilde{\mu}}}{\mathrm{J}_{mnop}} + \frac{2\delta_{\mu_i}^{\widetilde{\mu}}}{\mathrm{K}_{mnop}} \right) \mathbf{K} \right] : \boldsymbol{\Sigma} \tag{7.26}$$

where $\boldsymbol{\Sigma}$ is the macroscopic stress that can be deduced from the applied macroscopic strain $\mathbf{E}$ and the effective stiffness tensor $\widetilde{\mathbf{C}}$ (see Eq. (7.1a)). $\widetilde{\mathbf{C}}$ was computed by using the interpolation model developed in (Ghossein and Lévesque, 2014), which provides the effective moduli for any given combination of mechanical properties contrast, fibers volume fraction and aspect ratio.

Knowing the first and second order moments in each phase, it was possible to obtain the mean ($\mathbf{M}_i$) and covariance ($\mathbf{V}_i$) tensors of the intraphase stress fields, both numerically and analytically:

Table 7.3 Relative errors (in %) between the mean ($\mathbf{M}_i$) and covariance ($\mathbf{V}_i$) tensors obtained numerically for microstructures A and B and those predicted analytically by the interpolation model.

		Error on $\mathbf{M}_i$ ($\epsilon_{\mathbf{M}_i}$)	Error on $\mathbf{V}_i$ ($\epsilon_{\mathbf{V}_i}$)
Microstructure A	Matrix	1.7%	2.0%
	Fibers	1.5%	2.1%
Microstructure B	Matrix	1.3%	2.6%
	Fibers	1.9%	2.3%

$$\mathbf{M}_i^{\mathrm{num/ana}} = <\boldsymbol{\sigma}>_i^{\mathrm{num/ana}} \tag{7.27a}$$

$$\mathbf{V}_i^{\mathrm{num/ana}} = <\boldsymbol{\sigma}\otimes\boldsymbol{\sigma}>_i^{\mathrm{num/ana}} - <\boldsymbol{\sigma}>_i^{\mathrm{num/ana}} \otimes <\boldsymbol{\sigma}>_i^{\mathrm{num/ana}} \tag{7.27b}$$

Table 7.3 provides the relative errors between tensors $\mathbf{M}_i$ and $\mathbf{V}_i$ obtained numerically for microstructures A and B and those predicted analytically by the interpolation model. This errors were computed as:

$$\epsilon_{\mathbf{M}_i} = \max_{\{m,n\}\in\{1,2,3\}} \left| \frac{\mathrm{M}_{mn/i}^{\mathrm{num}} - \mathrm{M}_{mn/i}^{\mathrm{ana}}}{\mathrm{M}_{mn/i}^{\mathrm{num}}} \right| \tag{7.28a}$$

$$\epsilon_{\mathbf{V}_i} = \max_{\{m,n,o,p\}\in\{1,2,3\}} \left| \frac{\mathrm{V}_{mnop/i}^{\mathrm{num}} - \mathrm{V}_{mnop/i}^{\mathrm{ana}}}{\mathrm{V}_{mnop/i}^{\mathrm{num}}} \right| \tag{7.28b}$$

where $\epsilon_{\mathbf{M}_i}$ and $\epsilon_{\mathbf{V}_i}$ denote the relative error for tensors $\mathbf{M}_i$ and $\mathbf{V}_i$, respectively.

Table 7.3 shows that the interpolation model predicted accurately the intraphase stress fields for both microstructures. Indeed, the maximum error on tensor $\mathbf{M}_i$ was 1.9% while that on tensor $\mathbf{V}_i$ was 2.6%.

Although one complex loading and two microstructures were considered in this study, it should be noted that similar results were obtained for any loading and for any microstructure within the studied range of mechanical and geometrical properties.

7.6.5 Effect of Poisson's ratio on the analytical models accuracy

The validation campaign was performed by fixing $\frac{\kappa_2}{\kappa_1} = \frac{\mu_2}{\mu_1}$. In this case, fibers and matrix have the same Poisson's ratio, which is not representative of real composites. Two new composites of varying Poisson's ratios were studied so as to cover a range of potentially realistic applications. The first composite (composite C) was reinforced with ellipsoidal particles hav-

ing an aspect ratio of 2 and a volume fraction of 50% (fibers with high volume fraction) while the second composite (composite D) was reinforced with ellipsoidal particles having an aspect ratio of 20 and a volume fraction of 10% (fibers with high aspect ratio). For both composites, the mechanical properties contrasts were fixed as follows: $\mu_2/\mu_1 = 131.8$, $\kappa_1/\mu_1 = 9.7$ and $\kappa_2/\mu_1 = 120.8$. These values were chosen so that fibers and matrix had a Poisson's ratio of 0.1 and 0.4, respectively.

The load independent properties were computed numerically and compared to the analytical models predictions for both composites and the relative error induced by each analytical model was determined as follows:

$$\epsilon_p = \left| \frac{p^{\mathrm{ana}} - p^{\mathrm{num}}}{p^{\mathrm{num}}} \right| \tag{7.29}$$

where p denotes one of the load independent properties included in Φ. The obtained results are shown in Tables 7.4a and 7.4b, respectively for composites C and D. The relative errors are rounded to the unit.

Tables 7.4a and 7.4b show that Lielens' is the most accurate model to predict the first order moments as well as the intra-matrix second order moments, for both composites C and D. By assuming that $\delta_{\kappa_1}^{\widetilde{\mu}}$ is negligible when compared to the other derivatives (see Section 7.6.2), the maximum error induced by Lielens' model was 10%. These results agree well with those obtained in Sections 7.6.1 and 7.6.2, where it has been shown that Lielens' is the most suitable model for predicting the first order moments and the intra-matrix second order moments for high mechanical properties contrasts.

Table 7.4a Relative error (in %) induced by each analytical model when predicting the first and second order moments of ellipsoidal particles reinforced composites. Aspect ratio = 2. Volume fraction = 50%. Mechanical properties: $\mu_2/\mu_1 = 131.8$, $\kappa_1/\mu_1 = 9.7$, $\kappa_2/\mu_1 = 120.8$.

Models	First order moments		Intra-matrix second order moments				Intra-fiber second order moments			
	α	β	$\delta_{\kappa_1}^{\widetilde{\kappa}}$	$\delta_{\kappa_1}^{\widetilde{\mu}}$	$\delta_{\mu_1}^{\widetilde{\kappa}}$	$\delta_{\mu_1}^{\widetilde{\mu}}$	$\delta_{\kappa_2}^{\widetilde{\kappa}}$	$\delta_{\kappa_2}^{\widetilde{\mu}}$	$\delta_{\mu_2}^{\widetilde{\kappa}}$	$\delta_{\mu_2}^{\widetilde{\mu}}$
MT	6	5	18	15	38	24	43	100	100	63
MT/Ben.	6	5	18	15	38	24	43	100	100	63
SCS	94	95	98	76	73	82	22	9	11	24
Lielens	3	4	6	31	8	8	36	100	100	58
Eshelby	24	21	221	12	98	166	70	100	100	79

Table 7.4b Relative error (in %) induced by each analytical model when predicting the first and second order moments of ellipsoidal particles reinforced composites. Aspect ratio = 20. Volume fraction = 10%. Mechanical properties: $\mu_2/\mu_1 = 131.8$, $\kappa_1/\mu_1 = 9.7$, $\kappa_2/\mu_1 = 120.8$.

Models	First order moments		Intra-matrix second order moments				Intra-fiber second order moments			
	α	β	$\delta_{\kappa_1}^{\widetilde{\kappa}}$	$\delta_{\kappa_1}^{\widetilde{\mu}}$	$\delta_{\mu_1}^{\widetilde{\kappa}}$	$\delta_{\mu_1}^{\widetilde{\mu}}$	$\delta_{\kappa_2}^{\widetilde{\kappa}}$	$\delta_{\kappa_2}^{\widetilde{\mu}}$	$\delta_{\mu_2}^{\widetilde{\kappa}}$	$\delta_{\mu_2}^{\widetilde{\mu}}$
MT	4	3	5	13	12	4	7	7	8	7
MT/Ben.	3	3	4	11	11	4	7	6	8	7
SCS	14	16	72	58	62	48	27	41	40	49
Lielens	2	2	3	9	10	4	6	4	6	6
Eshelby	7	5	6	15	16	6	9	9	9	9

Tables 7.4a and 7.4b show that the SCS provides the most accurate predictions for the intra-fiber second order moments in composite C, with a maximum error of 24%. Lielens' model delivers the most accurate estimates with a maximum error of 6% for the same quantities in composite D. These results are consistent with those obtained in Section 7.6.3. Indeed, the SCS has the highest accuracy when the fibers aspect ratio is low (e.g., composite C) while Lielens' is the most suitable model for fibers with high aspect ratio (e.g., composite D).

Thus, the same conclusions were obtained even if fibers and matrix had significantly different Poisson's ratios.

7.7 Conclusion

The main conclusions of this study are:

⊙ The accuracy of analytical homogenization models is more sensitive to the fibers volume fraction than to their aspect ratio when predicting the first and second order moments.

⊙ For low mechanical properties contrasts, MT and MT/Benveniste are the most suitable models to predict the first order moments as well as the intra-matrix second order moments. Lielens' model provides the most accurate predictions for high contrasts.

⊙ The predictions of the SCS are the most accurate at predicting the intra-fiber second order moments in the investigated range of contrasts and volume fractions, provided that the fibers aspect ratio is low. For fibers with high aspect ratio, Lielens' model

has the highest accuracy among the studied models.

Moreover, an interpolation model has been developed. This model delivers accurate estimates of the mean and covariance tensors of the intraphase stress fields, and that for any microstructure subjected to a complex loading.

Acknowledgments

Appendix 7.A   Demonstration of Equation (7.26)

Eq. (7.7b) can be written as:

$$< \sigma_{mn} \otimes \sigma_{op} >_i = \frac{1}{c_i} \boldsymbol{\Sigma} : \frac{\partial \widetilde{\mathbf{S}}}{\partial \mathrm{S}_{mnop/i}} : \boldsymbol{\Sigma} \tag{7.30}$$

Since:

$$\widetilde{\mathbf{S}} = \frac{1}{3} \widetilde{\kappa}^{-1} \mathbf{J} + \frac{1}{2} \widetilde{\mu}^{-1} \mathbf{K} \ , \tag{7.31}$$

it is possible to write:

$$\frac{\partial \widetilde{\mathbf{S}}}{\partial \mathrm{S}_{mnop/i}} = \frac{1}{3} \frac{\partial \widetilde{\kappa}^{-1}}{\partial \mathrm{S}_{mnop/i}} \mathbf{J} + \frac{1}{2} \frac{\partial \widetilde{\mu}^{-1}}{\partial \mathrm{S}_{mnop/i}} \mathbf{K} \tag{7.32a}$$

$$= \frac{1}{3} \left(\frac{\partial \widetilde{\kappa}^{-1}}{\partial \kappa_i^{-1}} \frac{\partial \kappa_i^{-1}}{\partial \mathrm{S}_{mnop/i}} + \frac{\partial \widetilde{\kappa}^{-1}}{\partial \mu_i^{-1}} \frac{\partial \mu_i^{-1}}{\partial \mathrm{S}_{mnop/i}} \right) \mathbf{J}$$

$$\qquad + \frac{1}{2} \left(\frac{\partial \widetilde{\mu}^{-1}}{\partial \kappa_i^{-1}} \frac{\partial \kappa_i^{-1}}{\partial \mathrm{S}_{mnop/i}} + \frac{\partial \widetilde{\mu}^{-1}}{\partial \mu_i^{-1}} \frac{\partial \mu_i^{-1}}{\partial \mathrm{S}_{mnop/i}} \right) \mathbf{K} \tag{7.32b}$$

$$= \frac{1}{3} \left(\delta_{\kappa_i}^{\widetilde{\kappa}} \frac{\partial \kappa_i^{-1}}{\partial \mathrm{S}_{mnop/i}} + \delta_{\mu_i}^{\widetilde{\kappa}} \frac{\partial \mu_i^{-1}}{\partial \mathrm{S}_{mnop/i}} \right) \mathbf{J}$$

$$\qquad + \frac{1}{2} \left(\delta_{\kappa_i}^{\widetilde{\mu}} \frac{\partial \kappa_i^{-1}}{\partial \mathrm{S}_{mnop/i}} + \delta_{\mu_i}^{\widetilde{\mu}} \frac{\partial \mu_i^{-1}}{\partial \mathrm{S}_{mnop/i}} \right) \mathbf{K} \tag{7.32c}$$

Since:

$$\mathrm{S}_{mnop/i} = \frac{1}{3} \kappa_i^{-1} \mathrm{J}_{mnop} + \frac{1}{2} \mu_i^{-1} \mathrm{K}_{mnop} \quad \Longrightarrow \quad \begin{cases} \dfrac{\partial \kappa_i^{-1}}{\partial \mathrm{S}_{mnop/i}} = \dfrac{3}{\mathrm{J}_{mnop}} \\[3mm] \dfrac{\partial \mu_i^{-1}}{\partial \mathrm{S}_{mnop/i}} = \dfrac{2}{\mathrm{K}_{mnop}} \end{cases} \tag{7.33}$$

Eq. (7.32c) becomes:

$$\frac{\partial \widetilde{\mathbf{S}}}{\partial \mathrm{S}_{mnop/i}} = \frac{1}{3} \left(\frac{3 \delta_{\kappa_i}^{\widetilde{\kappa}}}{\mathrm{J}_{mnop}} + \frac{2 \delta_{\mu_i}^{\widetilde{\kappa}}}{\mathrm{K}_{mnop}} \right) \mathbf{J} + \frac{1}{2} \left(\frac{3 \delta_{\kappa_i}^{\widetilde{\mu}}}{\mathrm{J}_{mnop}} + \frac{2 \delta_{\mu_i}^{\widetilde{\mu}}}{\mathrm{K}_{mnop}} \right) \mathbf{K} \tag{7.34}$$

Therefore, Eq. (7.30) can be written as:

$$< \sigma_{mn} \otimes \sigma_{op} >_i = \frac{1}{c_i} \boldsymbol{\Sigma} : \left[\frac{1}{3} \left(\frac{3\delta_{\kappa_i}^{\widetilde{\kappa}}}{\mathrm{J}_{mnop}} + \frac{2\delta_{\mu_i}^{\widetilde{\kappa}}}{\mathrm{K}_{mnop}} \right) \mathbf{J} + \frac{1}{2} \left(\frac{3\delta_{\kappa_i}^{\widetilde{\mu}}}{\mathrm{J}_{mnop}} + \frac{2\delta_{\mu_i}^{\widetilde{\mu}}}{\mathrm{K}_{mnop}} \right) \mathbf{K} \right] : \boldsymbol{\Sigma} \quad (7.35)$$

which corresponds to Eq. (7.26).
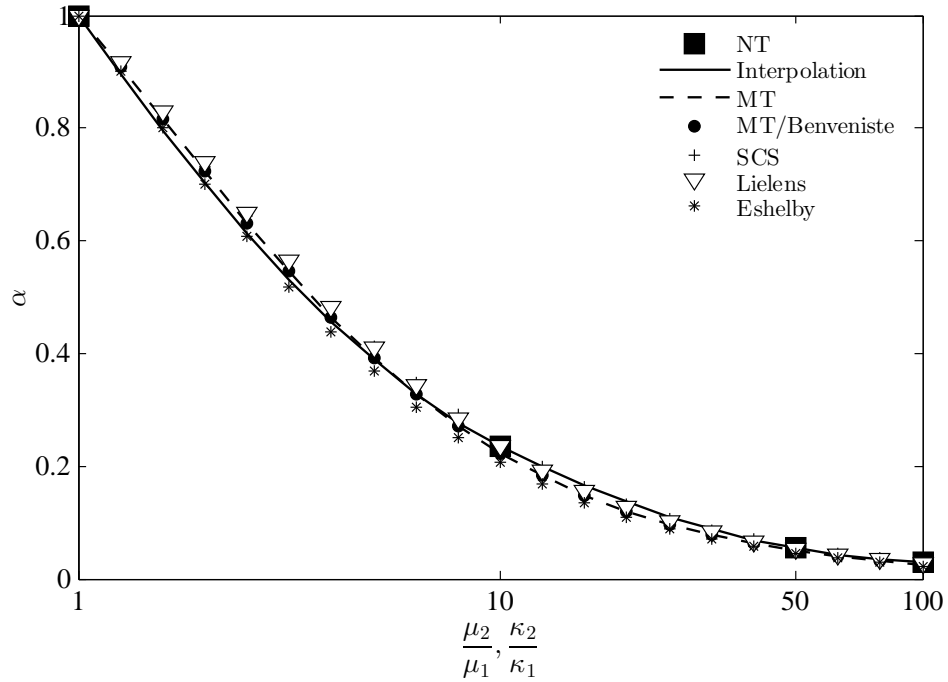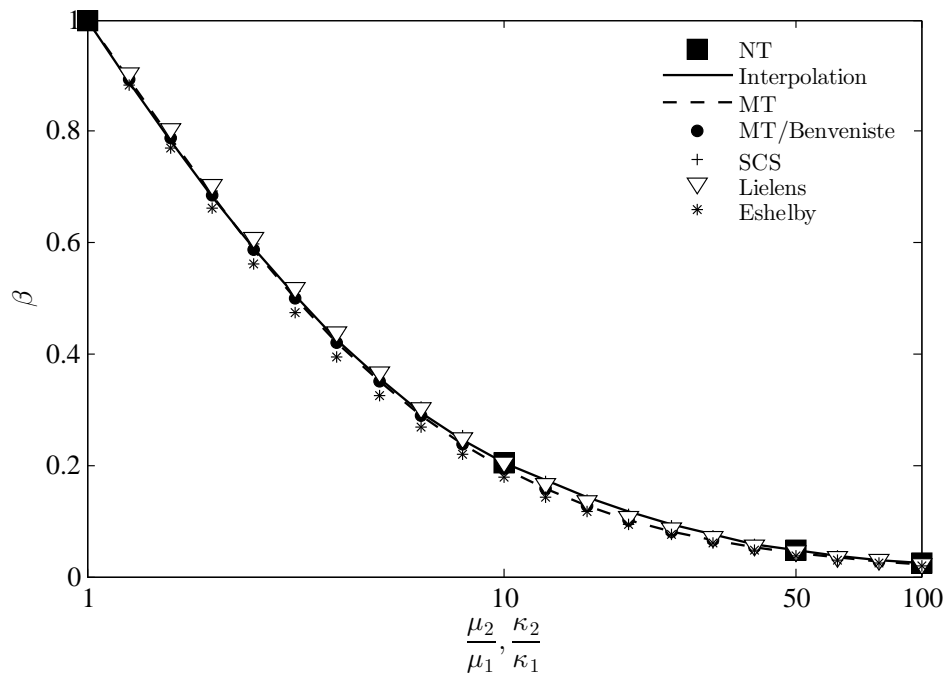
Figure 7.2 Comparison between the intra-fiber first order moments obtained with the numerical tool (NT) and those predicted by the analytical models: Mori-Tanaka (MT), Benveniste model (MT/Benveniste), self-consistent scheme (SCS), Lielens and the dilute solution of Eshelby (Eshelby). Volume fraction = 10%. Aspect ratio = 1 (prolate ellipsoids). $\kappa_1 = \mu_1 = 1$. (a) Spherical component of tensor $\mathbf{A}_2$ (α). (b) Deviatoric component of tensor $\mathbf{A}_2$ (β).

Figure 7.3 Comparison between the intra-fiber first order moments obtained with the numerical tool (NT) and those predicted by the analytical models: Mori-Tanaka (MT), Benveniste model (MT/Benveniste), self-consistent scheme (SCS), Lielens and the dilute solution of Eshelby (Eshelby). Volume fraction = 50%. Aspect ratio = 1 (prolate ellipsoids). $\kappa_1 = \mu_1 = 1$. (a) Spherical component of tensor $\mathbf{A}_2$ (α). (b) Deviatoric component of tensor $\mathbf{A}_2$ (β).

Figure 7.4 Comparison between the intra-fiber first order moments obtained with the numerical tool (NT) and those predicted by the analytical models: Mori-Tanaka (MT), Benveniste model (MT/Benveniste), self-consistent scheme (SCS), Lielens and the dilute solution of Eshelby (Eshelby). Volume fraction = 10%. Aspect ratio = 20 (prolate ellipsoids). $\kappa_1 = \mu_1 = 1$. (a) Spherical component of tensor $\mathbf{A}_2$ (α). (b) Deviatoric component of tensor $\mathbf{A}_2$ (β).

Figure 7.5 Comparison between the intra-matrix second order moments obtained with the numerical tool (NT) and those predicted by the analytical models: Mori-Tanaka (MT), Benveniste model (MT/Benveniste), self-consistent scheme (SCS), Lielens and the dilute solution of Eshelby (Eshelby). Volume fraction = 10%. Aspect ratio = 1 (prolate ellipsoids). $\kappa_1 = \mu_1 = 1$. (a) $\delta_{\kappa_1}^{\widetilde{\kappa}}$. (b) $\delta_{\kappa_1}^{\widetilde{\mu}}$. (c) $\delta_{\mu_1}^{\widetilde{\kappa}}$. (d) $\delta_{\mu_1}^{\widetilde{\mu}}$.

Figure 7.6 Comparison between the intra-matrix second order moments obtained with the numerical tool (NT) and those predicted by the analytical models: Mori-Tanaka (MT), Benveniste model (MT/Benveniste), self-consistent scheme (SCS), Lielens and the dilute solution of Eshelby (Eshelby). Volume fraction = 50%. Aspect ratio = 1 (prolate ellipsoids). $\kappa_1 = \mu_1 = 1$. (a) $\delta_{\kappa_1}^{\widetilde{\kappa}}$. (b) $\delta_{\kappa_1}^{\widetilde{\mu}}$. (c) $\delta_{\mu_1}^{\widetilde{\kappa}}$. (d) $\delta_{\mu_1}^{\widetilde{\mu}}$.
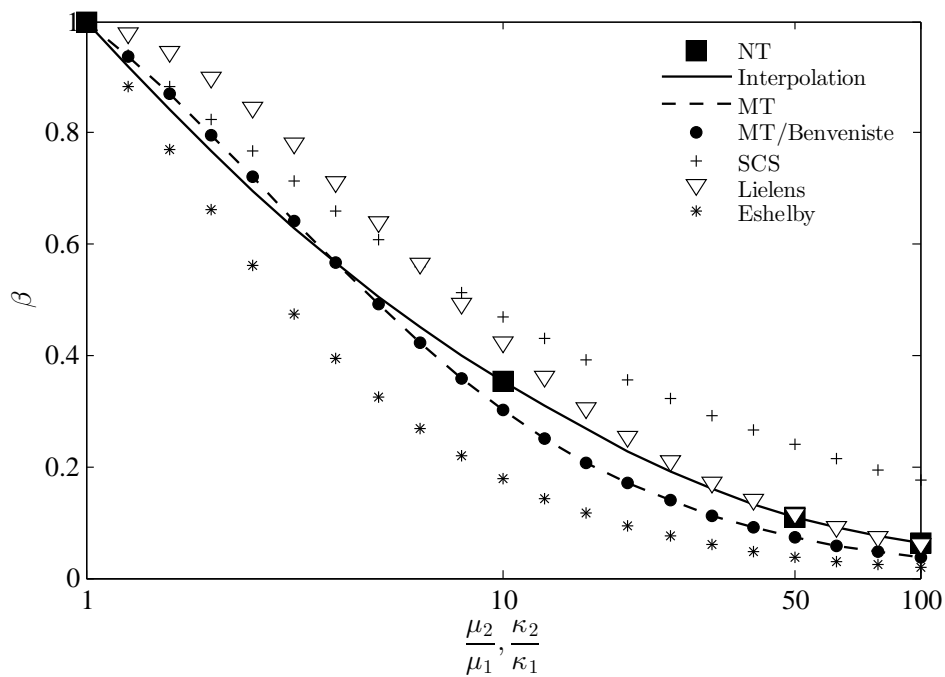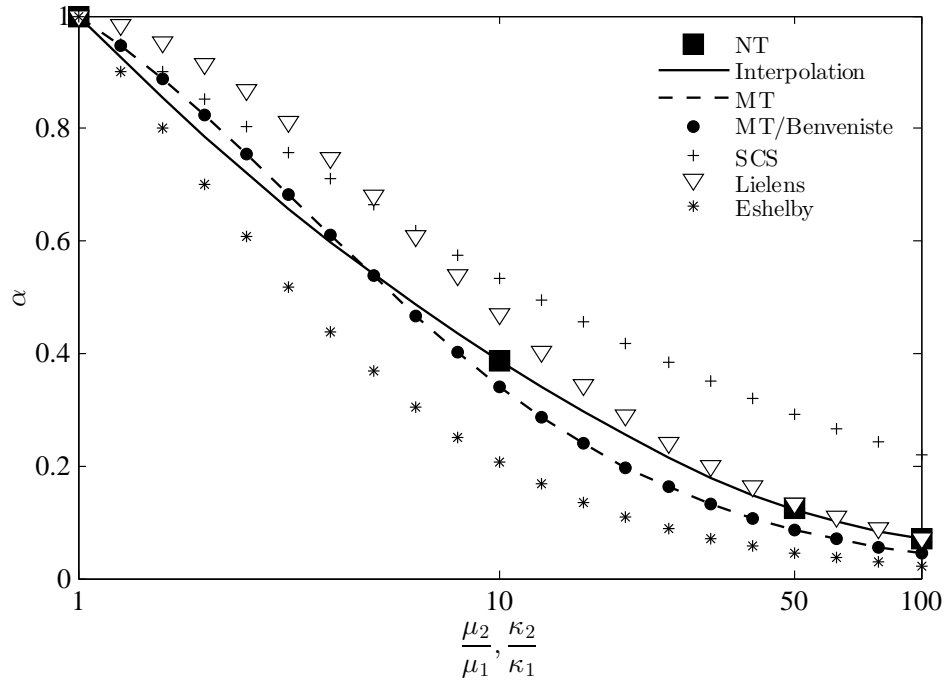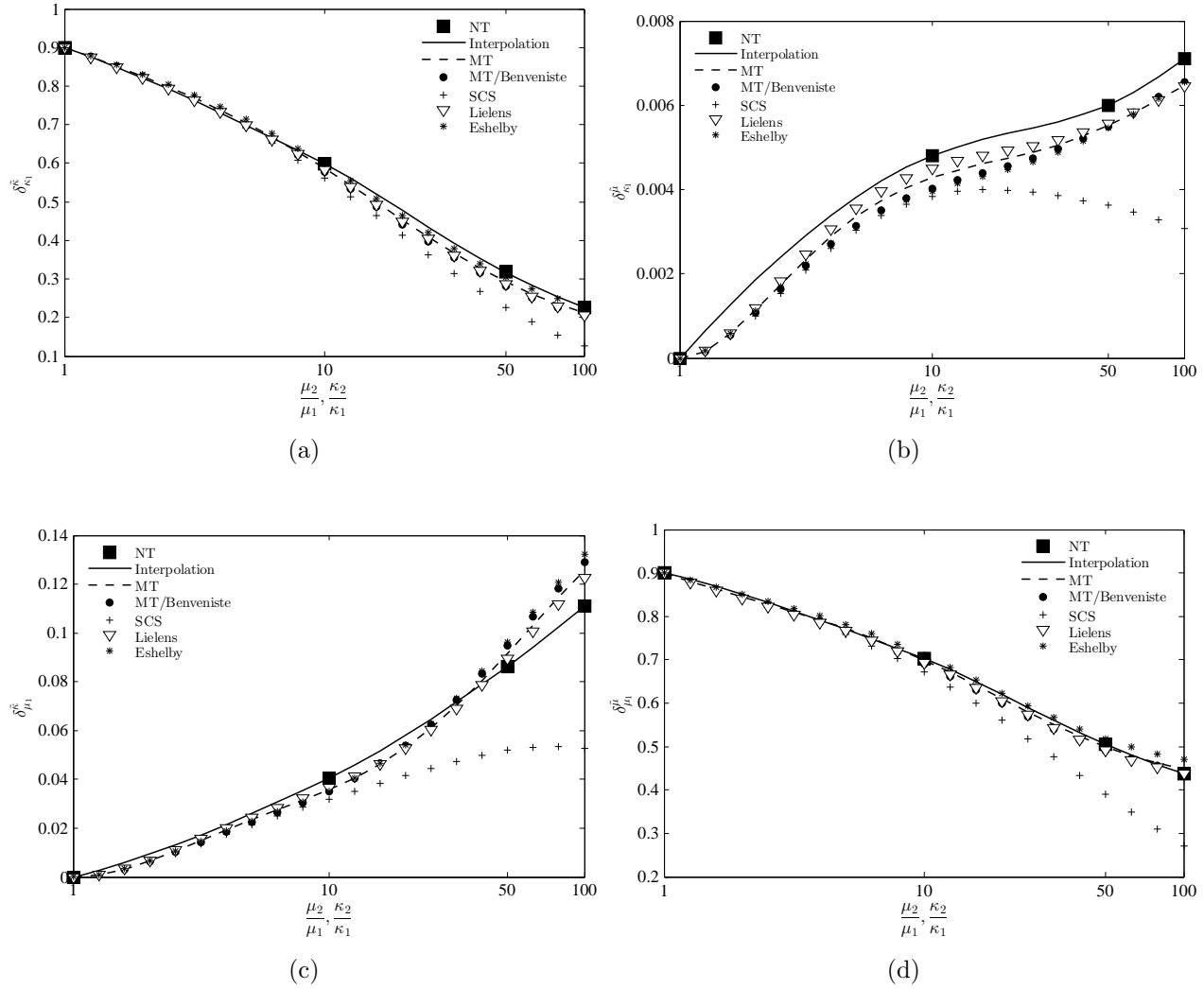
Figure 7.7 Comparison between the intra-matrix second order moments obtained with the numerical tool (NT) and those predicted by the analytical models: Mori-Tanaka (MT), Benveniste model (MT/Benveniste), self-consistent scheme (SCS), Lielens and the dilute solution of Eshelby (Eshelby). Volume fraction = 10%. Aspect ratio = 20 (prolate ellipsoids). $\kappa_1 = \mu_1 = 1$. (a) $\delta_{\kappa_1}^{\widetilde{\kappa}}$. (b) $\delta_{\kappa_1}^{\widetilde{\mu}}$. (c) $\delta_{\mu_1}^{\widetilde{\kappa}}$. (d) $\delta_{\mu_1}^{\widetilde{\mu}}$.
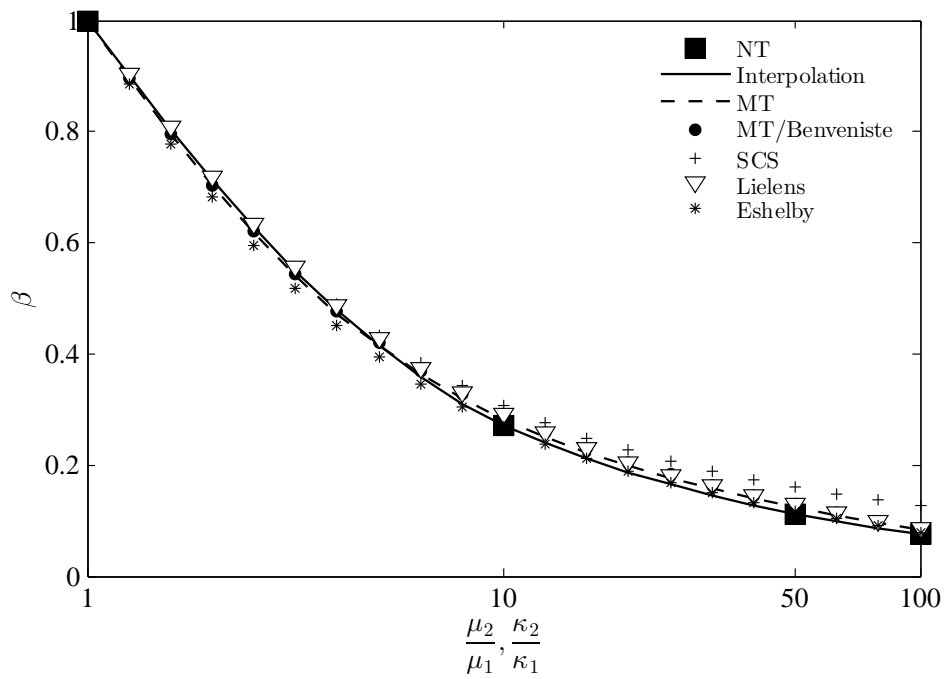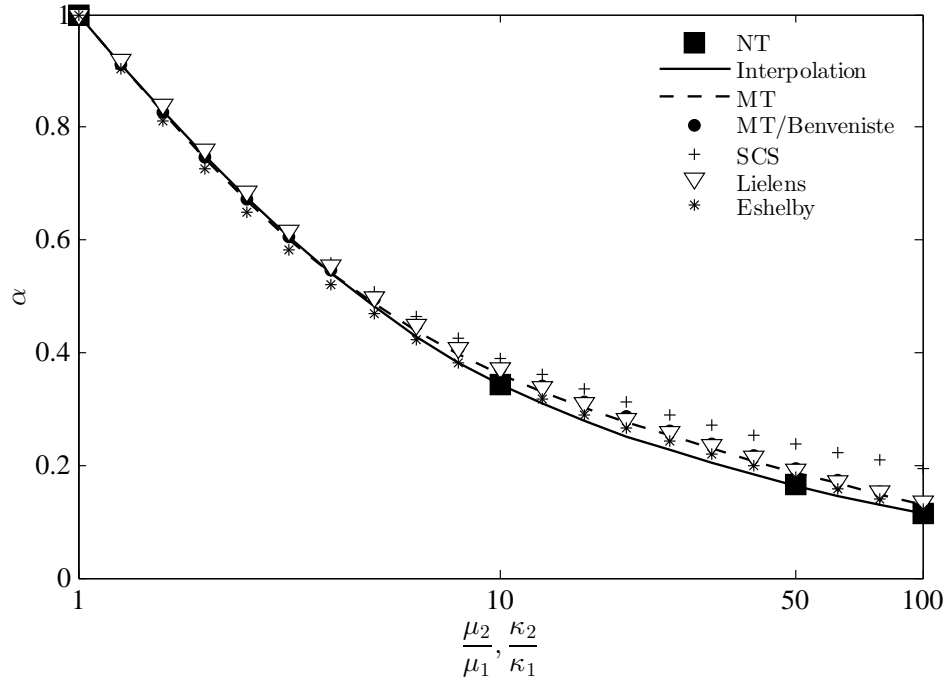
Figure 7.8 Comparison between the intra-fiber second order moments obtained with the numerical tool (NT) and those predicted by the analytical models: Mori-Tanaka (MT), Benveniste model (MT/Benveniste), self-consistent scheme (SCS), Lielens and the dilute solution of Eshelby (Eshelby). Volume fraction = 10%. Aspect ratio = 1 (prolate ellipsoids). $\kappa_1 = \mu_1 = 1$. (a) $\delta_{\kappa_2}^{\widetilde{\kappa}}$. (b) $\delta_{\kappa_2}^{\widetilde{\mu}}$. (c) $\delta_{\mu_2}^{\widetilde{\kappa}}$. (d) $\delta_{\mu_2}^{\widetilde{\mu}}$.

Figure 7.9 Comparison between the intra-fiber second order moments obtained with the numerical tool (NT) and those predicted by the analytical models: Mori-Tanaka (MT), Benveniste model (MT/Benveniste), self-consistent scheme (SCS), Lielens and the dilute solution of Eshelby (Eshelby). Volume fraction = 50%. Aspect ratio = 1 (prolate ellipsoids). $\kappa_1 = \mu_1 = 1$. (a) $\delta_{\kappa_2}^{\widetilde{\kappa}}$. (b) $\delta_{\kappa_2}^{\widetilde{\mu}}$. (c) $\delta_{\mu_2}^{\widetilde{\kappa}}$. (d) $\delta_{\mu_2}^{\widetilde{\mu}}$.
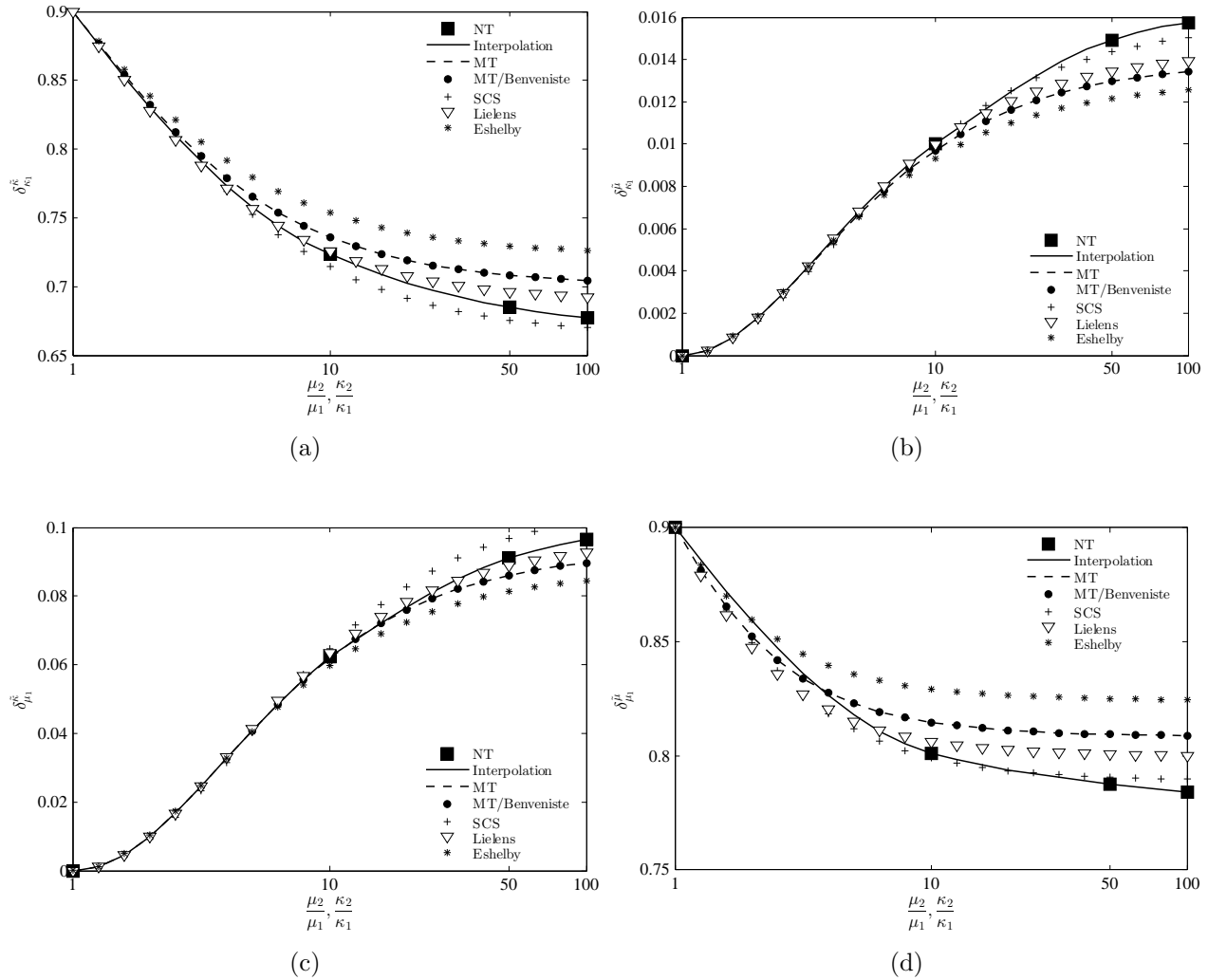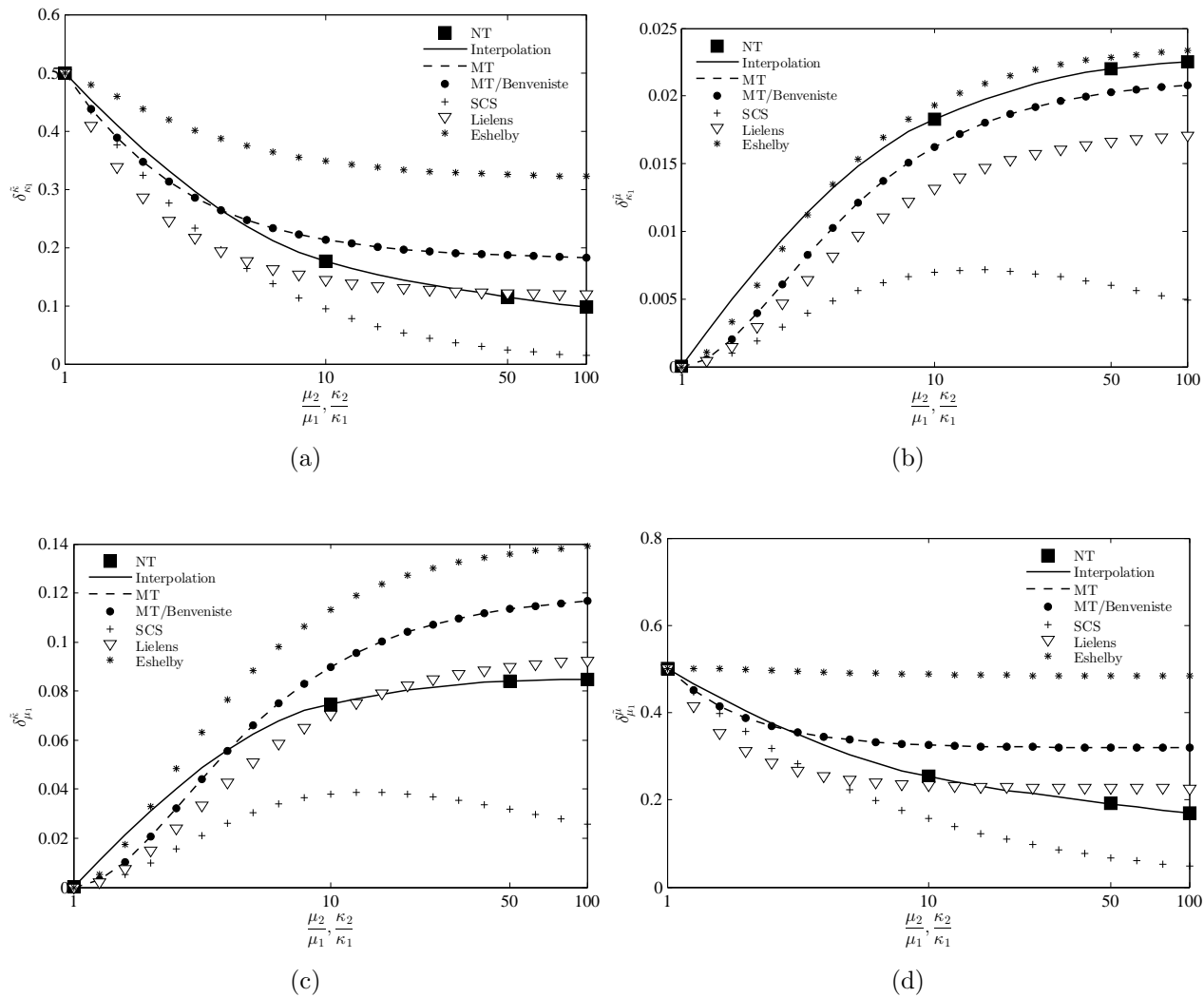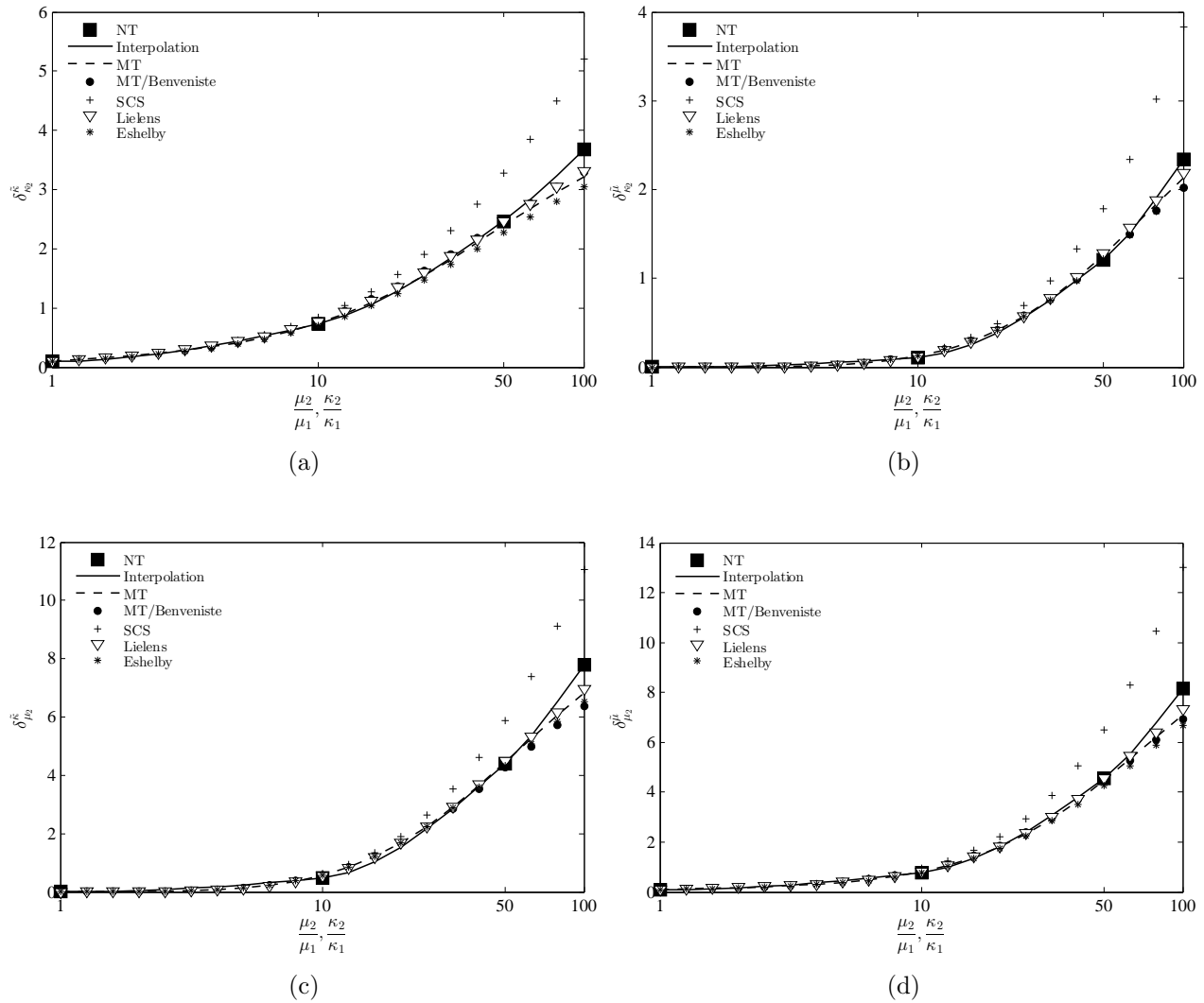
Figure 7.10 Comparison between the intra-fiber second order moments obtained with the numerical tool (NT) and those predicted by the analytical models: Mori-Tanaka (MT), Benveniste model (MT/Benveniste), self-consistent scheme (SCS), Lielens and the dilute solution of Eshelby (Eshelby). Volume fraction = 10%. Aspect ratio = 20 (prolate ellipsoids). $\kappa_1 = \mu_1 = 1$. (a) $\delta_{\kappa_2}^{\widetilde{\kappa}}$. (b) $\delta_{\kappa_2}^{\widetilde{\mu}}$. (c) $\delta_{\mu_2}^{\widetilde{\kappa}}$. (d) $\delta_{\mu_2}^{\widetilde{\mu}}$.
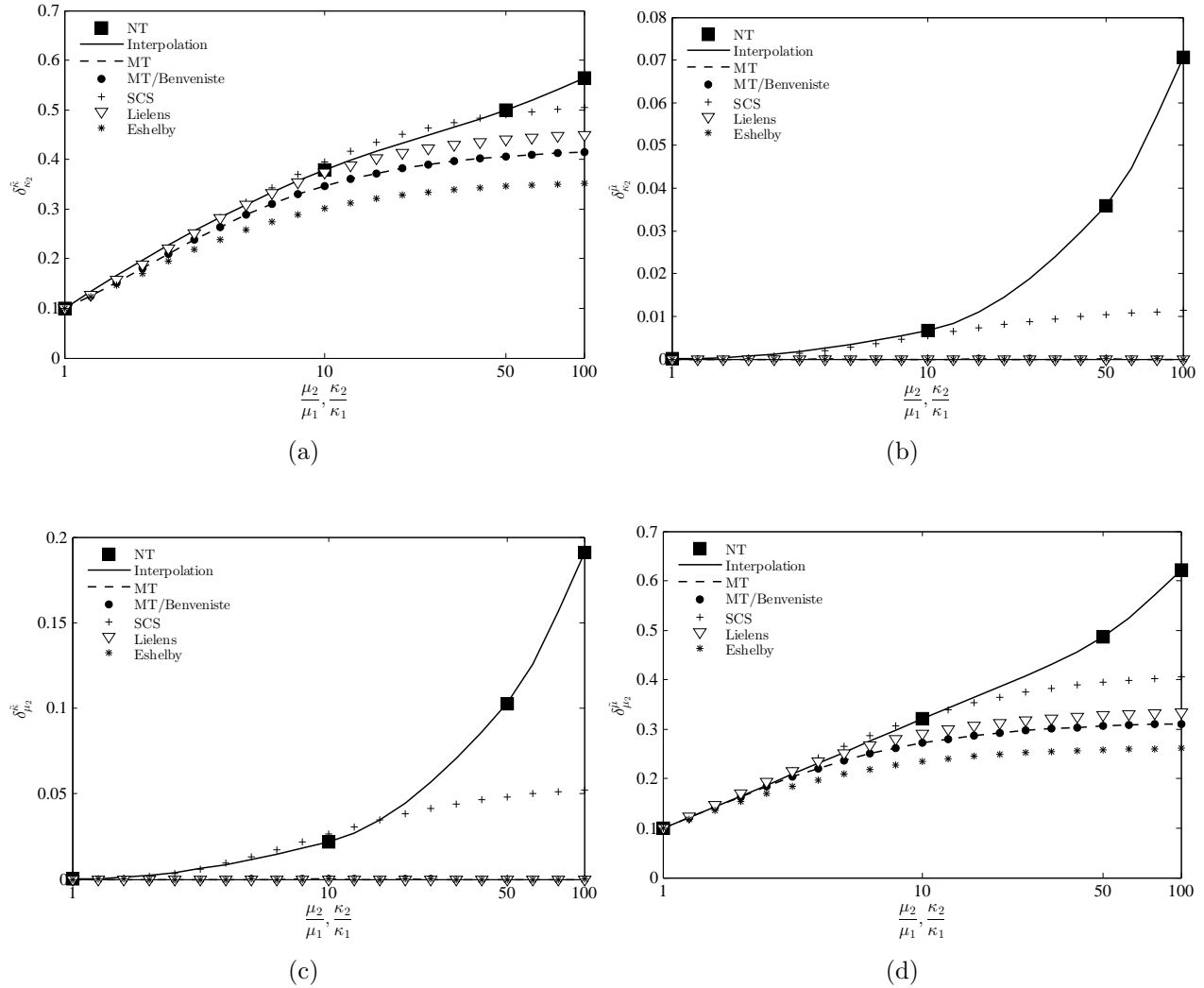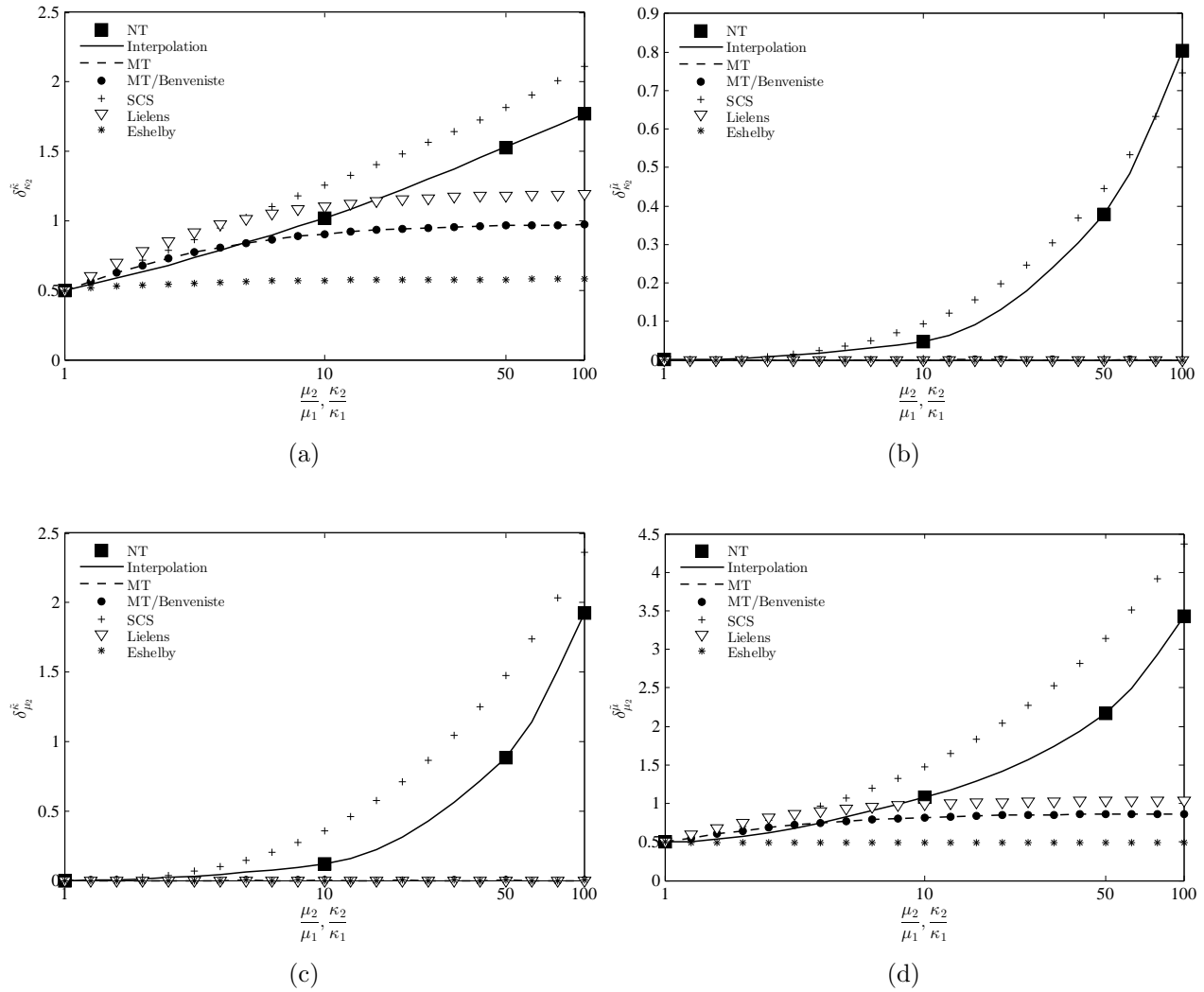
CHAPTER 8

GENERAL DISCUSSION

8.1 Clarification on some aspects

Following the jury's comments, this section aims to provide further clarification and explanations on the difference between exact solution and numerical solution as well as on the validation of homogenization models using experimental data.

8.1.1 Exact solution vs numerical solution

An exact solution of a physical problem can be obtained only in simple cases (simple microstructures and boundary conditions). For the case of randomly distributed and oriented fibers reinforced composites, it is not possible to obtain the exact solution for the effective properties. Therefore, a numerical model should be used. It can be shown that once the convergence is reached, the numerical solution approaches the exact solution within an acceptable tolerance for engineering applications. Since the difference between both solutions is relatively low, it is possible to consider the numerical solution as an exact solution and use it as a benchmark for computing the accuracy of analytical models. However, from a mathematical point of view, a numerical solution is not an exact solution. It would therefore be more appropriate to use the term "accurate solution" or "converged solution" to designate the numerical solution.

8.1.2 Validation of homogenization model using experimental data

To validate an analytical model, one should compare its predictions to experimental observations. However, analytical homogenization models studied in this thesis rely on certain assumptions including:

⊙ The fibers are perfectly ellipsoidal;

⊙ The fibers orientations distribution is perfectly random;

⊙ The fibers are perfectly bonded to the matrix (perfect interphase).

In an experimental model, it is not possible to guarantee that these assumptions are met. For instance, the fibers may not be perfectly ellipsoidal and randomly oriented into the matrix. Therefore, comparison between analytical models and experimental observations

could led to erroneous conclusions. In this case, a numerical model would be more appropriate to establish comparisons and conclusions since it can reproduce the same assumptions made for analytical models.

The word "validation" may bring confusion in this thesis since no experimental data were used. To avoid any ambiguity, it should be noted that by "validating a model", the author's main objective was to compute its accuracy and validity domain in terms of mechanical properties contrasts, fibers volume fraction and fibers aspect ratio.

8.2   The most suitable analytical homogenization model

This study presented a rigorous and comprehensive evaluation of the performance of analytical models at predicting the effective mechanical properties and local field statistics of randomly distributed and oriented ellipsoidal particles reinforced composites, for a broad range of phases mechanical properties, fibers volume fractions and aspect ratios.

For the specific case of spherical particles reinforced composites, it has been shown that Lielens' model delivers the most accurate predictions of the effective moduli, provided that the spheres are completely stiffer than the matrix (i.e., $\kappa_2 \geq \kappa_1$ and $\mu_2 \geq \mu_1$). If the particles are not completely stiffer than the matrix, the self-consistent scheme is the most accurate model for low spheres volume fractions (i.e., $< 20\%$). For higher volume fractions, the generalized self-consistent model provides the most accurate estimates.

For the general case of ellipsoidal fibers, Lielens' is the most accurate homogenization model for predicting the effective properties, provided that the fibers are completely stiffer than the matrix. Otherwise, the model of Benveniste could be an alternative to the Lielens' model, especially when predicting the effective shear modulus of microstructures with high ellipsoids aspect ratios.

On the other hand, it was found that none of the tested analytical models predicts accurately the local field statistics for the whole investigated range of phases mechanical and geometrical properties. Regarding the first order moments and the intra-matrix second order moments, the Mori-Tanaka model and the Benveniste's model have the highest accuracy for low rigidity contrasts while Lielens' is the most accurate model for high contrasts. As to the intra-fiber second order moments, the self-consistent scheme is the most suitable model for fibers with low aspect ratios whereas Lielens' model provides the most accurate estimates for fibers with high aspect ratios.

The results obtained in this thesis highlighted the fact that no analytical homogenization model stands out of the others as being more accurate over the investigated range of mechanical properties contrasts, fibers volume fractions and aspect ratios. However, if a single model

was to be chosen for predicting the effective properties and the local field statistics of ellipsoidal fibers reinforced composites, this study suggests that it should be Lielens' model. Although it is a simple nonlinear interpolation between the Hashin-Shtrikman-Walpole bounds, it was found that Lielens' model provides the most accurate predictions in most cases.

8.3   The interpolation models

All numerical results generated during this project were saved into a database. Approximately, 1800 different ellipsoidal fibers reinforced composites were studied. These numerical results were used to build two interpolation models. The first model predicts the effective properties while the second model predicts the local field statistics. These interpolation models can be seen as a substitute to analytical homogenization models. Their numerical execution is as quick as analytical models but their accuracy is the highest published so far, provided that the properties of the phases are within the investigated range of mechanical and geometrical properties:

- ⊙   A phases mechanical properties contrast between 1 and 100;

- ⊙   A fibers volume fraction between 0% and 50%;
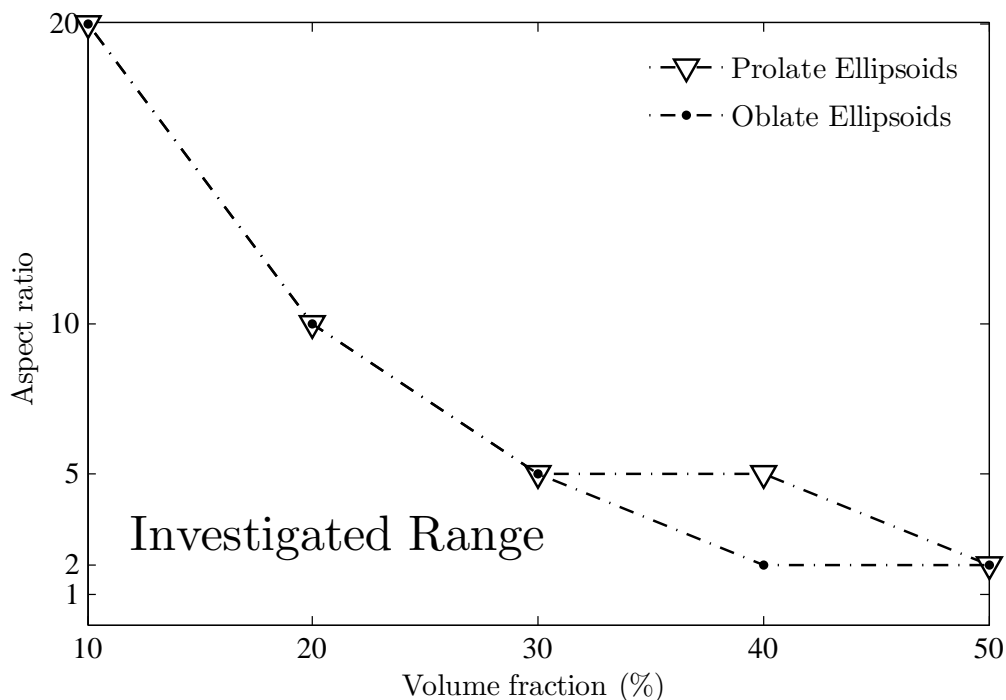
Figure 8.1 Investigated range of geometrical properties for prolate and oblate ellipsoidal fibers: ellipsoids aspect ratio as a function of the ellipsoids volume fraction.

⊙ A fibers aspect ratio between 1 and 20 (prolate or oblate fibers).

More specifically, the investigated range of geometrical properties is illustrated in Figure 8.1, for both prolate and oblate ellipsoidal particles. The figure shows the ellipsoids aspect ratio as a function of the ellipsoids volume fraction.

8.4   A fully automated numerical tool

Besides the validation of analytical homogenization models, this project led to the development of a fully automated numerical tool able to compute accurate local fields and effective properties of linearly isotropic composites reinforced by randomly distributed and oriented ellipsoidal fibers. The user inputs the phases mechanical properties, the fibers volume fraction, the fibers aspect ratio as well as the confidence level (for computing confidence intervals). The numerical tool generates random microstructures representatitve of the studied composite and computes the effective properties and local field statistics using a rigorous RVE determination process. More specifically, the numerical tool can:

⊙ Compute the mechanical properties as well as the stress and strain fields of a single microstructure submitted to a given loading. The microstructure can be either generated randomly or provided by the user by specifying the position and orientation of each fiber.

⊙ Compute the effective mechanical properties and local field statistics of a given composite. The tool generates as many microstructures required to reach the RVE. Convergence analysis in terms of number of realizations and volume element size is performed automatically. The tool outputs the required properties with their confidence interval.

This numerical tool can be used by other researchers who wish to compute the effective properties of specific composites and/or validate their homogenization models.

CHAPTER 9

COMPLEMENTARY WORK: EXTENSION TO THE CASE OF CYLINDRICAL FIBERS

This chapter presents the modifications that should be made in the numerical tool to deal with cylindrical fibers reinforced composites. The only difference lies in the random generation process since the technique for computing the effective properties and local field statistics remains the same. In the following, two molecular dynamics algorithms are proposed. The first algorithm generates randomly distributed unidirectional cylindrical fibers while the second algorithm generates randomly distributed and oriented cylindrical fibers.

9.1   Randomly distributed unidirectional cylindrical fibers

The algorithm is based on that proposed in Chapter 4. The cylinders are generated in a cube of side L oriented along the $e_1 e_2 e_3$-axes. It is assumed that the cylinders remain parallel during the simulation and their longitudinal axis is oriented along the e_2-axis. At each step of the simulation, each cylinder A has the following parameters: a position vector $(\boldsymbol{r}^A)$, a velocity vector $(\boldsymbol{v}^A)$, a radius (R^A) and its growth rate (R_0^A), a length (l^A) and its growth rate (l_0^A). The ratio $l_0^A/(2R_0^A)$ must be equal to the aspect ratio provided by the user.

Three subroutines need to be modified: computation of binary collisions (Algorithm 4.2), computation of collisions with the cell faces (Algorithm 4.3) and update of post-collision particles velocities (Algorithm 4.4).

9.1.1   Computation of binary collisions

Let A and B be two cylinders in space. Two types of binary collisions can occur: an out-of-plane collision, i.e., along the e_2-axis, and an in-plane collision, i.e., in the $e_1 e_3$-plane. Two parameters δ_1 and δ_2 must be computed, both being a function of the time t. The first is the distance between the two cylinders in the $e_1 e_3$-plane. It is calculated as follows:

$$\delta_1(t) = \sqrt{\left(r^A[1] - r^B[1] + \left(v^A[1] - v^B[1]\right)t\right)^2 + \left(r^A[3] - r^B[3] + \left(v^A[3] - v^B[3]\right)t\right)^2}$$
$$- \left(R^A + R^B + \left(R_0^A + R_0^B\right)t\right) \quad (9.1a)$$

where $r^A[k]$ and $v^A[k]$ refer respectively to the kth term of vectors $\boldsymbol{r}^A$ and $\boldsymbol{v}^A$. δ_2 represents

the distance between the two cylinders along e_2-axis. It is given by:

$$\delta_2(t) = \left| r^A[2] - r^B[2] + \left(v^A[2] - v^B[2]\right)t \right| - \left(\frac{l^A + l^B + \left(l_0^A + l_0^B\right)t}{2} \right) \qquad (9.1b)$$

The next collision time between cylinders A and B is the smallest positive value t_c such that $\delta_1(t_c) \leq 0$ and $\delta_2(t_c) \leq 0$. To find the time t_c, the roots of $\delta_1(t)$ and $\delta_2(t)$ should be computed first, i.e., find t_1 and t_2 such that $\delta_1(t_1) = 0$ and $\delta_2(t_2) = 0$. If the quadratic equation $\delta_1(t_1) = 0$ has no solution, there will never be a collision between the two cylinders. Otherwise, if t_1 exist, three cases must be considered. If $t_1 > t_2$ and $\delta_2(t_1) \leq 0$, an in-plane collision occurs at time $t_c = t_1$. If $t_1 \leq t_2$ and $\delta_1(t_2) \leq 0$, an out-of-plane collision occurs at time $t_c = t_2$. In all other cases, there is no collision between the cylinders.

9.1.2 Computation of collisions with the cube cell faces

For each cylinder A, a collision time with each cube face should be calculated. The six collision times are obtained as follows:

$$t_k = \begin{cases} \left(r^A[2k-1] - R^A\right)\left(R_0^A - v^A[2k-1]\right)^{-1} & k = \{1,2\} \quad (e_1 = 0\,,\, e_3 = 0) \\[2mm] \left(L - r^A[2k-5] - R^A\right)\left(R_0^A + v^A[2k-5]\right)^{-1} & k = \{3,4\} \quad (e_1 = L\,,\, e_3 = L) \\[2mm] \left(r^A[2] - l^A/2\right)\left(l_0^A/2 - v^A[2]\right)^{-1} & k = 5 \qquad (e_2 = 0) \\[2mm] \left(L - r^A[2] - l^A/2\right)\left(l_0^A/2 + v^A[2]\right)^{-1} & k = 6 \qquad (e_2 = L) \end{cases} \qquad (9.2)$$

The next collision time between cylinder A and a cube face corresponds to the smallest value of t_k obtained from Eq. (9.2).

9.1.3 Velocities update after a binary collision

The update of velocities depends on the type of collision. If an in-plane collision occurs, the velocities update procedure is the same as for a collision between two circles or spheres (see Algorithm 4.4). If an out-of-plane collision occurs, only the e_2-component of the velocities is affected. The respective e_2-components of the two cylinders are exchanged while considering the length growth rate. The computation of the post-collision velocities is performed as follows:

$$v^{A+}[2] = v^{B-}[2] + \left(\frac{l_0^A + l_0^B}{2}\right)u^{AB} \qquad (9.3a)$$

$$v^{B+}[2] \;=\; v^{A-}[2] - \left(\frac{l_0^A + l_0^B}{2}\right)u^{AB} \tag{9.3b}$$

where

$$u^{AB} \;=\; \frac{r^A[2] - r^B[2]}{\left|r^A[2] - r^B[2]\right|} \;=\; 1 \;\text{ or }\; (-1) \tag{9.3c}$$

It should be noted that v^- and v^+ denote respectively the velocities before and after the binary collision.

9.1.4 Example of a random packing

Figure 9.1 shows an example of a random packing containing 30 randomly distributed unidirectional cylindrical particles with an aspect ratio of 6 and a volume fraction of 50%.

9.2 Randomly distributed and oriented cylindrical fibers

Generating randomly distributed and oriented cylindrical fibers using a molecular dynamics algorithm is not obvious. Indeed, computing binary collisions between two particles under translational and rotational motions is more complex for cylinders than for ellipsoids. This is due to the fact that the surface gradient of an ellipsoid is continuous, which is not the case for a cylinder.
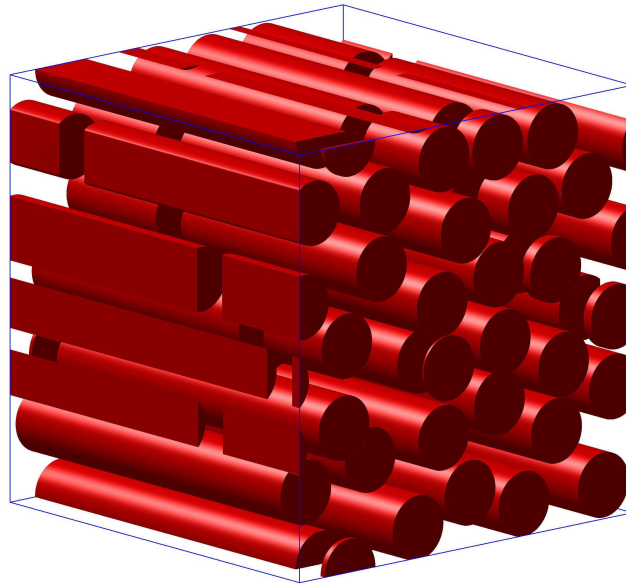
Figure 9.1 30 unidirectional cylindrical particles randomly distributed in a periodic unit cell. Volume fraction = 50%. Aspect ratio = 6.

It is possible to overcome this issue by generating first a packing containing randomly distributed and oriented axisymmetric ellipsoidal fibers (prolate or oblate) using the algorithm developed in Chapter 5. Once the simulation is complete, the cylinders particles are then embedded in the generated ellipsoids. This ensures that there is no overlapping between the cylinders. However, the bounding ellipsoids must occupy the smallest possible space for performance matters. In other words, each cylinder must occupy the highest possible volume in its bounding ellipsoid.

Figure 9.2 shows a 2D representation of a cylinder embedded in an axisymmetric ellipsoid. The ellipsoid and the cylinder are coaxial. The equation of the ellipsoid in its local coordinate system $Oxyz$ is given by:

$$\frac{x^2}{a^2} + \frac{y^2}{b^2} + \frac{z^2}{b^2} = 1 \tag{9.4}$$

where a refers to the length of the ellipsoid's first semi-principal axis and b refers to the length of the ellipsoid's second and third semi-principal axis (axisymmetric ellipsoid).

For a given length l, the cylinder's cross section corresponds to the ellipsoid's cross section at $x = l/2$. The equation of this cross section can be obtained from Eq. (9.4):

$$y^2 + z^2 = b^2 \left(1 - \frac{l^2}{4a^2} \right) \tag{9.5}$$
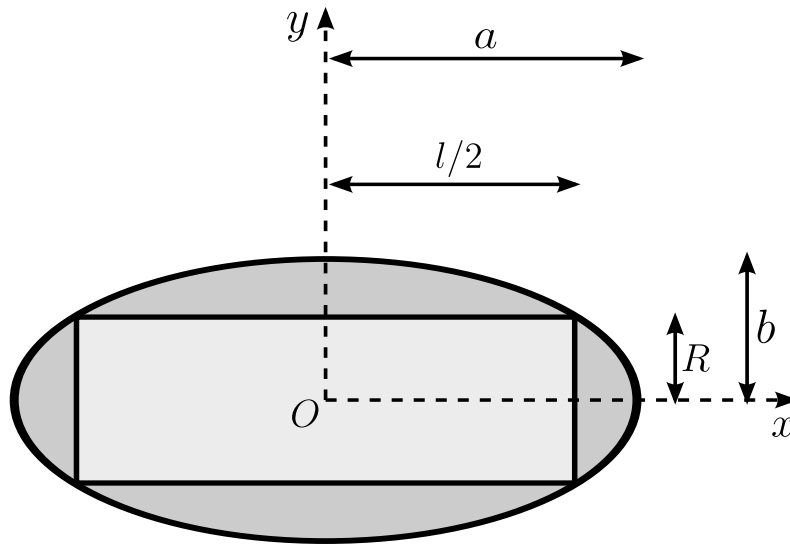
Figure 9.2 2D representation of a cylinder embedded in an axisymmetric ellipsoid. The ellipsoid and the cylinder are coaxial and $Oxyz$ denotes their local coordinate system (z is not shown). The maximum volume that the cylinder can have represents approximately 77% of the ellipsoid's volume.

From Eq. (9.5), one can deduce the radius of the cylinder:

$$R = b\sqrt{1 - \frac{l^2}{4a^2}} \tag{9.6}$$

The volume of the cylinder for a given length l is expressed as follows:

$$V(l) = \pi R^2 l = \pi b^2 l \left(1 - \frac{l^2}{4a^2}\right) \tag{9.7}$$

The aim is to find the value of l, denoted by l^*, for which $V(l)$ is maximal. This can be done by finding the value of l for which the derivative of $V(l)$ is zero:

$$\left.\frac{\mathrm{d}V(l)}{\mathrm{d}l}\right|_{l=l^*} = \pi b^2 \left[\left(1 - \frac{l^{*2}}{4a^2}\right) - \frac{l^{*2}}{2a^2}\right] = 0 \quad \Longleftrightarrow \quad l^* = \frac{2a\sqrt{3}}{3} \tag{9.8}$$

The radius, aspect ratio and volume of the optimal cylinder can be deduced from Eqs. (9.6), (9.7) and (9.8):

$$R^* = b\sqrt{1 - \frac{l^{*2}}{4a^2}} = \frac{b\sqrt{6}}{3} \tag{9.9a}$$

$$\frac{l^*}{2R^*} = \frac{\sqrt{2}}{2}\frac{a}{b} \tag{9.9b}$$

$$V^* = V(l^*) = \pi b^2 l^* \left(1 - \frac{l^{*2}}{4a^2}\right) = \frac{4\sqrt{3}}{9}\pi ab^2 \tag{9.9c}$$

Eqs. (9.9) state that the aspect ratio of the optimal cylinder is equal to 70.7% ($\sqrt{2}/2$) of the ellipsoid's aspect ratio. Furthermore, the volume of the optimal cylinder represents 77.0% ($4\sqrt{3}/9$) of the ellipsoid's volume.

For example, in order to generate randomly distributed and oriented cylindrical fibers with an aspect ratio of 10 and a volume fraction of 45%, the following methodology should be adopted. First, a packing containing randomly distributed and oriented ellipsoidal fibers with an aspect ratio of 14.1 ($10 \times 2/\sqrt{2}$) and a volume fraction of 58.5% ($45 \times 9/4\sqrt{3}$) must be generated using the algorithm developed in Chapter 5. Knowing the length of the ellipsoids, the length and radius of the cylinders can be computed using Eqs. (9.8) and (9.9). The cylinders are then optimally embedded in the generated ellipsoids, so that they have the desired aspect ratio and volume fraction.

CONCLUSION AND RECOMMENDATIONS

A through and exhaustive study was performed to validate the performance of analytical homogenization models at predicting the mechanical behavior of randomly distributed and oriented ellipsoidal fibers reinforced composites. The validation was performed at two levels. First, the accuracy of analytical models at predicting the effective mechanical properties was evaluated. In a second step, this study assessed the performance of analytical models at estimating the local field statistics, and more specifically the first and second order moments of stresses and strains.

A fully automated numerical tool was developed. The representative microstructures were randomly generated using a molecular dynamics algorithm. For the specific case of spherical particles, the algorithm of Lubachevsky and Stillinger was used. As for the case of ellipsoidal particles, a new computationally-efficient algorithm was developed since the available algorithms in the literature have a high computational cost. The originality of the new developed algorithm lies in the fact that binary collision times between two moving ellipsoids are computed by simply finding the roots of a nonlinear function. The algorithm can generate all types of ellipsoids packings (prolate, oblate and scalene) with very high aspect ratios.

The effective properties and local field statistics of the generated microstructures were obtained by using a Fast Fourier Transforms (FFT) based technique. A wide range of phases mechanical properties, fibers volume fractions and aspect ratios was swept, and approximately 1800 different ellipsoidal fibers reinforced composites were studied. For each combination of phases mechanical and geometrical properties, the size of the Representative Volume Element (RVE) was determined rigorously.

The predictions of the numerical tool were compared to those of the best known analytical homogenization models: the dilute solution of Eshelby, the self-consistent scheme, the generalized self consistent scheme, the Mori-Tanaka model, the Benveniste's model, the Third Order Approximation and the Lielens' model. Comparisons between numerical and analytical predictions allowed to attribute a validity domain for each analytical model. Furthermore, the influence of the phases mechanical properties contrast, fibers volume fraction and fibers aspect ratio on the analytical models accuracy was investigated.

It was found that Lielens' model delivers the most accurate effective properties predictions, provided that the inclusions are completely stiffer than the matrix. If this condition is not met, the self-consistent and the generalized self-consistent schemes are the most accurate models for the case of spherical particles, respectively for low and high volume fractions. For

the case of ellipsoidal fibers, the model of Benveniste provides the most accurate estimates, especially for high aspect ratios.

As for the local field statistics, a novel and original load independent approach was proposed to evaluate the accuracy of analytical models. This approach was based on the computation of load independent properties directly related to the first and second order moments. It was found that the Mori-Tanaka and Benveniste's models provide the most accurate predictions of the first order moments and intra-matrix second order moments, provided that the mechanical properties contrast is low. For high contrasts, Lielens's is the most accurate model. On the other hand, the self-consistent scheme is the most suitable model to predict the intra-fiber second order moments, provided that the fibers aspect ratio is low. For high aspect ratios, Lielens' model delivers the most accurate estimates.

Although no analytical model stands out of the others as being more accurate over the investigated range of mechanical and geometrical properties, this study suggests that Lielens' model remains the best suitable model since it delivers the most accurate predictions in most cases. This study also reveals that the mechanical properties contrast is the most influential parameter on the analytical models accuracy, followed by the fibers volume fraction. Indeed, the models accuracy is not very sensitive to the fibers aspect ratio.

Finally, two interpolation models were developed in this thesis. The first models predicts the effective moduli while the second model estimates the local field statistics. It has been shown that both models have the highest accuracy published so far and can be seen as a substitute to analytical homogenization models.

Limitations and recommendations for future studies

This thesis was limited to the case of two-phase linearly elastic composites reinforced by axisymmetric and monodisperse ellipsoidal fibers. It was also assumed that the reinforcements were perfectly bonded to the matrix. The following lines suggest some recommendations for future studies.

- ⊙ **Take into consideration the interphase between fibers and matrix**
  It would be interesting to evaluate the performance of analytical homogenization models by taking into account the interphase between fibers and matrix. One could study the influence of the thickness and mechanical properties of the interphase on the analytical models accuracy. A new numerical tool could be developed for the case of coated inclusions and validity domains could be computed for the different analytical three-phase models available in the literature.
  For this purpose, the FFT-based technique should be modified to take into consider-

ation the presence of a third phase. A rigorous rule of arbitration should be defined during the discretization process, so that the correct properties are assigned to each voxel.

⊙ **Investigate the case of scalene and/or polydisperse ellipsoidal fibers**
Only the case of axisymmetric ellipsoidal particles were considered in this study (spheres, prolate ellipsoids and oblate ellipsoids). Investigating the case of scalene ellipsoidal particles could be interesting. It should be noted that there is no analytical expression of Eshelby's tensor for scalene ellipsoids. It must be computed numerically using the methodology of Gavazzi and Lagoudas (1990). Therefore, the numerical execution of analytical homogenization models becomes slower, making the use of interpolation models more attractive.
Furthermore, one could study the case of polydisperse particles. The effect of the particles size distribution on the analytical models accuracy could be investigated. It would also be possible to consider the case of microstructures where each particle has a random aspect ratio (see Figure 5.5).

⊙ **Extension of the numerical tool to the case of cylindrical fibers**
Extend the numerical tool for computing the effective mechanical properties of randomly distributed and oriented cylindrical fibers. The only difference with the current tool lies in the random generation process (see Chapter 9). Generating randomly distributed and oriented cylindrical particles using a molecular dynamics algorithm is more complex than generating ellipsoidal particles. Indeed, computing binary collisions between two cylindrical particles under translational and rotational motions is not trivial since the surface gradient of a cylinder is not continuous (unlike an ellipsoid).
Using this numerical tool, one could study the aspect ratio threshold from which ellipsoidal and cylindrical fibers would have the same mechanical behavior.

⊙ **Extension to other families of composites**
This thesis was limited to linearly elastic composites with isotropic phases. As part of future studies, it would be interesting to investigate other types of material symmetries (e.g., transverse isotropy, orthotropy, cubic symmetry, etc.) with linear and nonlinear viscoelastic phases. In fact, many composite structures used in aerospace have a viscoelastic behavior (e.g., polymer matrix composites used in engine components). Validating the performance of analytical models for these different families of composites could be of interest to the industry since it can incorporates these models in early stages of design.

⊙ **Investigate the higher order moments**

This thesis was limited to the computation of the first and second order moments. The interpolation model developed in Chapter 7 can predict the intraphase first and second order moments, but cannot provide the intraphase stress and strain field distributions. Indeed, since the latter are not Gaussian, higher order moments are required to reconstruct the real distributions. Further studies are needed to investigate the higher order moments and thus to develop a model able to predict the intraphase field distributions. This model could be very useful to predict damage in composites.

REFERENCES

ADVANI, S. and TUCKER, C. (1987). The use of tensors to describe and predict fiber orientation in short fiber composites. *Journal of Rheology*, <u>31</u>, 751–784.

ALLEN, M., FRENKEL, D. and TALBOT, J. (1989). Molecular dynamics simulation using hard particles. *Computer physics reports*, <u>9</u>, 301–353.

BARELLO, R. B. and LÉVESQUE, M. (2008). Comparison between the relaxation spectra obtained from homogenization models and finite elements simulation for the same composite. *International Journal of Solids and Structures*, <u>45</u>, 850 – 867.

BASU, S., POLLACK, R. and ROY, M. (2006). *Algorithms in real algebraic geometry*, vol. 10. Springer-Verlag New York Inc.

BENVENISTE, Y. (1987). A new approach to the application of Mori-Tanaka's theory in composite materials. *Mechanics of Materials*, <u>6</u>, 147 – 157.

BENVENISTE, Y. (2008). Revisiting the generalized self-consistent scheme in composites: Clarification of some aspects and a new formulation. *Journal of the Mechanics and Physics of Solids*, <u>56</u>, 2984 – 3002.

BENVENISTE, Y., DVORAK, G. and CHEN, T. (1991). On diagonal and elastic symmetry of the approximate effective stiffness tensor of heterogeneous media. *Journal of the Mechanics and Physics of Solids*, <u>39</u>, 927–946.

BEZRUKOV, A. and STOYAN, D. (2006). Simulation and statistical analysis of random packings of ellipsoids. *Particle & Particle Systems Characterization*, <u>23</u>, 388–398.

BOHM, H., ECKSCHLAGER, A. and HAN, W. (2002). Multi-inclusion unit cell models for metal matrix composites with randomly oriented discontinuous reinforcements. *Computational Materials Science*, <u>25</u>, 42 – 53.

BOHM, H. and HAN, W. (2001). Comparisons between three-dimensional and two-dimensional multi-particle unit cell models for particle reinforced metal matrix composites. *Modelling and Simulation in Materials Science and Engineering*, <u>9</u>, 47 – 65.

BÖHM, H. J. (1998). A short introduction to basic aspects of continuum micromechanics. *Cdl-fmd Report*, <u>3</u>.

BORNERT, M., BRETHEAU, T. and GILORMINI, P. (2001). *Homogénéisation en mécanique des matériaux, Tome 2 : Comportements non linéaires et problèmes ouverts*. Hermes science.

BOURGEOIS, N. (1994). *Caractérisation et modélisation micromécanique du comportement et de l'endommagement d'un composte à matrice métallique Al/SiCp*. Ph.D thesis.

BRENNER, R., LEBENSOHN, R. and CASTELNAU, O. (2009). Elastic anisotropy and yield surface estimates of polycrystals. *International Journal of Solids and Structures*, 46, 3018–3026.

BRENNER, R. and MASSON, R. (2005). Improved affine estimates for nonlinear viscoelastic composites. *European Journal of Mechanics-A/Solids*, 24, 1002–1015.

BRENT, R. (2002). *Algorithms for minimization without derivatives*. Dover Pubns.

BUCATARU, I. and SLAWINSKI, M. A. (2009). Invariant properties for finding distance in space of elasticity tensors. *Journal of Elasticity*, 94, 97–114.

BUCHALTER, B. and BRADLEY, R. (2007). Orientational order in amorphous packings of ellipsoids. *EPL (Europhysics Letters)*, 26, 159.

BUDIANSKY, B. (1965). On the elastic moduli of some heterogeneous materials. *Journal of the Mechanics and Physics of Solids*, 13, 223 – 227.

BURYACHENKO, V. (2011). Inhomogeneity of the first and second statistical moments of stresses inside the heterogeneities of random structure matrix composites. *International Journal of Solids and Structures*, 48, 1665–1687.

CASTANEDA, P. and WILLIS, J. (1995). The effect of spatial distribution on the effective behavior of composite materials and cracked media. *Journal of the Mechanics and Physics of Solids*, 43, 1919 – 51.

CASTAÑEDA, P. P. (1991). The effective mechanical properties of nonlinear isotropic composites. *Journal of the Mechanics and Physics of Solids*, 39, 45 – 71.

CASTAÑEDA, P. P. (1996). Exact second-order estimates for the effective mechanical properties of nonlinear composite materials. *Journal of the Mechanics and Physics of Solids*, 44, 827–862.

CASTAÑEDA, P. P. (2002a). Second-order homogenization estimates for nonlinear composites incorporating field fluctuations: I. theory. *Journal of the Mechanics and Physics of Solids*, 50, 737–757.

CASTAÑEDA, P. P. (2002b). Second-order homogenization estimates for nonlinear composites incorporating field fluctuations: Ii. applications. *Journal of the Mechanics and Physics of Solids*, 50, 759–782.

CASTANEDA, P. P. and SUQUET, P. (1998). *Nonlinear composites*, vol. 34. 172 – 302.

CASTELNAU, O., BLACKMAN, D., LEBENSOHN, R. and PONTE CASTAÑEDA, P. (2008). Micromechanical modeling of the viscoplastic behavior of olivine. *Journal of Geophysical Research*, 113.

CASTELNAU, O., BRENNER, R. and LEBENSOHN, R. (2006). The effect of strain heterogeneity on the work hardening of polycrystals predicted by mean-field approaches. *Acta materialia*, 54, 2745–2756.

CHOI, Y., CHANG, J., WANG, W., KIM, M. and ELBER, G. (2009). Continuous collision detection for ellipsoids. *Visualization and Computer Graphics, IEEE Transactions on*, 15, 311–325.

CHOI, Y., WANG, W. and KIM, M. (2003). Exact collision detection of two moving ellipsoids under rational motions. *2003 IEEE International Conference on Robotics and Automation*. IEEE, vol. 1, 349–354.

CHRISTENSEN, R. M. and LO, K. H. (1979). Solutions for effective shear properties in three phase sphere and cylinder models. *Journal of the Mechanics and Physics of Solids*, 27, 315 – 330.

CHUNG, D. and BUESSEM, W. (1967). The elastic anisotropy of crystals. *Journal of Applied Physics*, 38, 2010–2012.

COJOCARU, D. and KARLSSON, A. (2010). On the effective elastic properties of macroscopically isotropic media containing randomly dispersed spherical particles. *Journal of Engineering Materials and Technology, Transactions of the ASME*, 132, 0210111 – 02101111.

CORCOLLE, R., PRÉAULT, V. and DANIEL, L. (2012). Second order moments in linear smart material composites. *IEEE Transactions on Magnetics,*, 48, 663–666.

DOGHRI, I., BRASSART, L., ADAM, L. and GÉRARD, J.-S. (2011). A second-moment incremental formulation for the mean-field homogenization of elasto-plastic composites. *International Journal of Plasticity*, 27, 352–371.

DONEV, A. (2006). *Jammed Packings of Hard Particles*. Ph.D thesis.

DONEV, A., TORQUATO, S. and STILLINGER, F. H. (2005a). Neighbor list collision-driven molecular dynamics simulation for nospherical hard particles. i. algorithmic details. *Journal of computational physics*, 202, 737–764.

DONEV, A., TORQUATO, S. and STILLINGER, F. H. (2005b). Neighbor list collision-driven molecular dynamics simulation for nospherical hard particles. ii. applications to ellipses and ellipsoids. *Journal of computational physics*, 202, 765–793.

DRUGAN, W. and WILLIS, J. (1996). A micromechanics-based nonlocal constitutive equation and estimates of representative volume element size for elastic composites. *Journal of the Mechanics and Physics of Solids*, 44, 497–524.

DUSCHLBAUER, D., BÖHM, H. J. and PETTERMANN, H. E. (2006). Computational simulation of composites reinforced by planar random fibers: homogenization and localization by unit cell and mean field approaches. *Journal of composite materials*, 40, 2217–2234.

EBERLY, D. (2002). Rotation representations and performance issues. *Magic Software*, 6006.

EL-MOURID, A. E., GANESAN, R. and LÉVESQUE, M. (2012). Comparison between analytical and numerical predictions for the linearly viscoelastic behavior of textile composites. *Mechanics of Materials*, 58, 69–83.

ESHELBY, J. (1957). The determination of the elastic field of an ellipsoidal inclusion, and related problems. *Proceedings of the Royal Society of London. Series A, Mathematical and Physical Sciences*, 241, 376–396.

EYRE, D. and MILTON, G. (1999). A fast numerical scheme for computing the response of composites using grid refinement. *European Physical Journal, Applied Physics*, 6, 41 – 47.

FERRARI, M. (1991). Asymmetry and the high concentration limit of the mori-tanaka effective medium theory. *Mechanics of Materials*, 11, 251–256.

FIGIEL, L. and BUCKLEY, C. (2009). Elastic constants for an intercalated layered-silicate/polymer nanocomposite using the effective particle concept–a parametric study using numerical and analytical continuum approaches. *Computational Materials Science*, 44, 1332–1343.

GAVAZZI, A. and LAGOUDAS, D. (1990). On the numerical evaluation of eshelby's tensor and its application to elastoplastic fibrous composites. *Computational Mechanics*, 7, 13–19.

GHOSSEIN, E. and LEVESQUE, M. (2012). A fully automated numerical tool for a comprehensive validation of homogenization models and its application to spherical particles reinforced composites. *International Journal of Solids and Structures*, <u>49</u>, 1387 – 1398.

GHOSSEIN, E. and LEVESQUE, M. (2013). Random generation of periodic hard ellipsoids based on molecular dynamics: A computationally-efficient algorithm. *Journal of Computational Physics*, <u>253</u>, 471 – 490.

GHOSSEIN, E. and LÉVESQUE, M. (2014). A comprehensive validation of analytical homogenization models: the case of ellipsoidal particles reinforced composites. *Mechanics of Materials*, <u>75</u>, 135–150.

GRAY, C., GUBBINS, K. and GUBBINS, K. (1984). *Theory of molecular fluids*, vol. 1. Clarendon Press Oxford.

GUSEV, A. A. (1997). Representative volume element size for elastic composites: A numerical study. *Journal of the Mechanics and Physics of Solids*, <u>45</u>, 1449 – 1459.

HAN, W., ECKSCHLAGER, A. and BOHM, H. (2001). The effects of three-dimensional multi-particle arrangements on the mechanical behavior and damage initiation of particle-reinforced mmcs. *Composites Science and Technology*, <u>61</u>, 1581 –1590.

HASHIN, Z. (1962). The elastic moduli of heterogeneous materials. *Journal of Applied Mechanics*, <u>29</u>, 143 – 150.

HASHIN, Z. and SHTRIKMAN, S. (1961). Note on a variational approach to the theory of composite elastic materials. *Journal of the Franklin Institute*, <u>271</u>, 336–341.

HASHIN, Z. and SHTRIKMAN, S. (1962a). On some variational principles in anisotropic and nonhomogeneous elasticity. *Journal of the Mechanics and Physics of Solids*, <u>10</u>, 335–342.

HASHIN, Z. and SHTRIKMAN, S. (1962b). A variational approach to the theory of the elastic behaviour of polycrystals. *Journal of the Mechanics and Physics of Solids*, <u>10</u>, 343–352.

HASHIN, Z. and SHTRIKMAN, S. (1963). A variational approach to the theory of the elastic behaviour of multiphase materials. *Journal of the Mechanics and Physics of Solids*, <u>11</u>, 127 – 140.

HBAIEB, K., WANG, Q., CHIA, Y. and COTTERELL, B. (2007). Modelling stiffness of polymer/clay nanocomposites. *Polymer*, <u>48</u>, 901–909.

HILL, R. (1963). Elastic properties of reinforced solids: some theoretical principles. *Journal of the Mechanics and Physics of Solids*, 11, 357–372.

HILL, R. (1965). A self-consistent mechanics of composite materials. *Journal of the Mechanics and Physics of Solids*, 13, 213 – 222.

HU, G. and WENG, G. (2000). Some reflections on the mori-tanaka and ponte castaneda-willis methods with randomly oriented ellipsoidal inclusions. *Acta mechanica*, 140, 31–40.

HUA, Y. and GU, L. (2013). Prediction of the thermomechanical behavior of particle-reinforced metal matrix composites. *Composites Part B: Engineering*, 45, 1464–1470.

HUET, C. (1990). Application of variational concepts to size effects in elastic heterogeneous bodies. *Journal of the Mechanics and Physics of Solids*, 38, 813–841.

IDIART, M. and CASTANEDA, P. (2007a). Field statistics in nonlinear composites. i. theory. *Proceedings of the Royal Society of London, Series A (Mathematical, Physical and Engineering Sciences)*, 463, 183 – 202.

IDIART, M. and CASTANEDA, P. (2007b). Field statistics in nonlinear composites. ii. applications. *Proceedings of the Royal Society of London, Series A (Mathematical, Physical and Engineering Sciences)*, 463, 203 – 22.

IDIART, M., DANAS, K. and CASTANEDA, P. (2006). Second-order theory for nonlinear composites and application to isotropic constituents. *Comptes Rendus de l'Academie des Sciences Serie II b/Mecanique*, 334, 575 – 81.

IDIART, M. I., WILLOT, F., PELLEGRINI, Y.-P. and PONTE CASTANEDA, P. (2009). Infinite-contrast periodic composites with strongly nonlinear behavior: effective-medium theory versus full-field simulations. *International Journal of Solids and Structures*, 46, 3365–3382.

IORGA, L., PAN, Y. and PELEGRI, A. (2008). Numerical characterization of material elastic properties for random fiber composites. *J. Mech. Mater. Struct*, 3, 1279–1298.

JIA, X., CHOI, Y., MOURRAIN, B. and WANG, W. (2011). An algebraic approach to continuous collision detection for ellipsoids. *Computer Aided Geometric Design*.

KANIT, T., FOREST, S., GALLIET, I., MOUNOURY, V. and JEULIN, D. (2003). Determination of the size of the representative volume element for random composites: statistical and numerical approach. *International Journal of Solids and Structures*, 40, 3647 – 3679.

KARI, S., BERGER, H. and GABBERT, U. (2007a). Numerical evaluation of effective material properties of randomly distributed short cylindrical fibre composites. *Computational materials science*, 39, 198–204.

KARI, S., BERGER, H., RODRIGUEZ-RAMOS, R. and GABBERT, U. (2007b). Computational evaluation of effective material properties of composites reinforced by randomly distributed spherical particles. *Composite Structures*, 77, 223 – 231.

KLUSEMANN, B. and SVENDSEN, B. (2010). Homogenization methods for multi-phase elastic composites: Comparisons and benchmarks. *Technische Mechanik*, 30, 374–386.

KOLAFA, J. and NEZBEDA, I. (1987). Monte carlo simulations on primitive models of water and methanol. *Molecular Physics*, 61, 161–175.

KRÖNER, E. (1972). *Statistical continuum mechanics*. Springer-Verlag.

LAHELLEC, N. and SUQUET, P. (2007a). On the effective behavior of nonlinear inelastic composites: I. incremental variational principles. *Journal of the Mechanics and Physics of Solids*, 55, 1932 – 1963.

LAHELLEC, N. and SUQUET, P. (2007b). On the effective behavior of nonlinear inelastic composites: Ii: A second-order procedure. *Journal of the Mechanics and Physics of Solids*, 55, 1964–1992.

LAHELLEC, N. and SUQUET, P. (2013). Effective response and field statistics in elasto-plastic and elasto-viscoplastic composites under radial and non-radial loadings. *International Journal of Plasticity*, 48, 1–30.

LEBENSOHN, R., CASTELNAU, O., BRENNER, R. and GILORMINI, P. (2005a). Study of the antiplane deformation of linear 2-d polycrystals with different microstructures. *International journal of solids and structures*, 42, 5441–5459.

LEBENSOHN, R., LIU, Y. and CASTAÑEDA, P. P. (2004). Macroscopic properties and field fluctuations in model power-law polycrystals: full-field solutions versus self-consistent estimates. *Proceedings of the Royal Society of London. Series A: Mathematical, Physical and Engineering Sciences*, 460, 1381–1405.

LEBENSOHN, R., TOMÉ, C. and CASTAÑEDA, P. P. (2007). Self-consistent modelling of the mechanical behaviour of viscoplastic polycrystals incorporating intragranular field fluctuations. *Philosophical Magazine*, 87, 4287–4322.

LEBENSOHN, R., TOMÉ, C. and PONTE CASTAÑEDA, P. (2005b). Improving the self-consistent predictions of texture development of polycrystals incorporating intragranular field fluctuations. <u>495</u>, 955–964.

LIELENS, G., PIROTTE, P., COUNIOT, A., DUPRET, F. and KEUNINGS, R. (1998). Prediction of thermo-mechanical properties for compression moulded composites. *Composites Part A: Applied Science and Manufacturing*, <u>29</u>, 63 – 70.

LLORCA, J., ELICES, M. and TERMONIA, Y. (2000). Elastic properties of sphere-reinforced composites with a mesophase. *Acta Materialia*, <u>48</u>, 4589 – 4597.

LUBACHEVSKY, B. (1991). How to simulate billiards and similar systems. *Journal of Computational Physics*, <u>94</u>, 255–283.

LUBACHEVSKY, B. and STILLINGER, F. (1990). Geometric properties of random disk packings. *Journal of statistical physics*, <u>60</u>, 561–583.

LUBACHEVSKY, B., STILLINGER, F. and PINSON, E. (1991). Disks vs. spheres : Contrasting properties of random packings. *Journal of statistical physics*, <u>64</u>, 501–523.

LUSTI, H. R. and GUSEV, A. A. (2004). Finite element predictions for the thermoelastic properties of nanotube reinforced polymers. *Modelling and Simulation in Materials Science and Engineering*, <u>12</u>, S107.

MAN, W., DONEV, A., STILLINGER, F., SULLIVAN, M., RUSSEL, W., HEEGER, D., INATI, S., TORQUATO, S. and CHAIKIN, P. (2005). Experiments on random packings of ellipsoids. *Physical review letters*, <u>94</u>, 198001.

MARUR, P. (2004). Estimation of effective elastic properties and interface stress concentrations in particulate composites by unit cell methods. *Acta Materialia*, <u>52</u>, 1263 – 1270.

MICHEL, J., MOULINEC, H. and SUQUET, P. (1999). Effective properties of composite materials with periodic microstructure: a computational approach. *Computer Methods in Applied Mechanics and Engineering*, <u>172</u>, 109 – 143.

MICHEL, J., MOULINEC, H. and SUQUET, P. (2000). A computational method based on augmented lagrangians and fast fourier transforms for composites with high contrast. *Computer Modeling in Engineering Sciences*, <u>1</u>, 79 – 88.

MICHEL, J. C., MOULINEC, H. and SUQUET, P. (2001). A computational scheme for linear and non-linear composites with arbitrary phase contrast. *International Journal for Numerical Methods in Engineering*, <u>52</u>, 139–160.

MONTAGNAT, M., CASTELNAU, O., BONS, P., FARIA, S., GAGLIARDINI, O., GILLET-CHAULET, F., GRENNERAT, F., GRIERA, A., LEBENSOHN, R., MOULINEC, H., ROESSIGER, J. and SUQUET, P. (2013). Multiscale modeling of ice deformation behavior. *Journal of Structural Geology.*

MORI, T. and TANAKA, K. (1973). Average stress in matrix and average elastic energy of materials with misfitting inclusions. *Acta Metallurgica*, 21, 571 – 574.

MORTAZAVI, B., BANIASSADI, M., BARDON, J. and AHZI, S. (2013). Modeling of two-phase random composite materials by finite element, mori–tanaka and strong contrast methods. *Composites Part B: Engineering*, 45, 1117–1125.

MOULINEC, H. and SUQUET, P. (1998). A numerical method for computing the overall response of nonlinear composites with complex microstructure. *Computer Methods in Applied Mechanics and Engineering*, 157, 69 – 94.

MOULINEC, H. and SUQUET, P. (2003a). Comparison of fft-based methods for computing the response of composites with highly contrasted mechanical properties. *Physica B*, 338, 58 – 60.

MOULINEC, H. and SUQUET, P. (2003b). Intraphase strain heterogeneity in nonlinear composites: a computational approach. *European Journal of Mechanics, A/Solids*, 22, 751 – 70.

MOUSSADDY, H. (2013). *A New Definition of the Representative Volument Element in Numerical Homogenization Problems and its Application to the Performance Evaluation of Analytical Homogenization Models.* Ph.D thesis, École Polytechnique de Montréal.

MOUSSADDY, H., PAHLAVANPOUR, M., THERRIAULT, D. and LEVESQUE, M. (2013a). Evaluation of analytical homogenization models for randomly oriented and high aspect ratio fiber reinforced composites. *Submitted to Composites Part B: Engineering.*

MOUSSADDY, H., THERRIAULT, D. and LÉVESQUE, M. (2013b). Assessment of existing and introduction of a new and robust efficient definition of the representative volume element. *International Journal of Solids and Structures*, 50, 3817–3828.

MURA, T. (1987). General theory of eigenstrains. *Micromechanics of defects in solids*, Kluwer Academic Publishers. 1–73.

NORRIS, A. (1985). A differential scheme for the effective moduli of composites. *Mechanics of materials*, 4, 1–16.

ODEGARD, G., GATES, T., WISE, K., PARK, C. and SIOCHI, E. (2003). Constitutive modeling of nanotube–reinforced polymer composites. *Composites science and technology*, 63, 1671–1687.

OSTOJA-STARZEWSKI, M. (1999). Scale effects in materials with random distributions of needles and cracks. *Mechanics of Materials*, 31, 883–893.

OSTOJA-STARZEWSKI, M. (2002). Microstructural randomness versus representative volume element in thermomechanics. *Journal of Applied Mechanics*, 69, 25–35.

OSTOJA-STARZEWSKI, M. (2006). Material spatial randomness: From statistical to representative volume element. *Probabilistic Engineering Mechanics*, 21, 112–132.

PAHLAVANPOUR, M., HUBERT, P. and LÉVESQUE, M. (2014). Numerical and analytical modeling of the stiffness of polymer–clay nanocomposites with aligned particles: One-and two-step methods. *Computational Materials Science*, 82, 122–130.

PAHLAVANPOUR, M., MOUSSADDY, H., GHOSSEIN, E., HUBERT, P. and LÉVESQUE, M. (2013). Prediction of elastic properties in polymer–clay nanocomposites: Analytical homogenization methods and 3d finite element modeling. *Computational Materials Science*, 79, 206–215.

PERRAM, J., RASMUSSEN, J., PRæSTGAARD, E. and LEBOWITZ, J. (1996). Ellipsoid contact potential: Theory and relation to overlap potentials. *Physical Review E*, 54, 6565–6572.

PERRAM, J. and WERTHEIM, M. (1985). Statistical mechanics of hard ellipsoids. i. overlap algorithm and the contact function. *Journal of Computational Physics*, 58, 409–416.

PIERARD, O. (2006). *Micromechanics of inclusion-reinforced composites in elasto-plasticity and elasto-viscoplasticity: modeling and computation*. Ph.D thesis.

PIERARD, O., FRIEBEL, C. and DOGHRI, I. (2004). Mean-field homogenization of multiphase thermo-elastic composites: a general framework and its validation. *Composites Science and Technology*, 64, 1587 – 1603.

RANGANATHAN, S. I. and OSTOJA-STARZEWSKI, M. (2008). Universal elastic anisotropy index. *Physical Review Letters*, 101, 055504.

REDENBACH, C. and VECCHIO, I. (2011). Statistical analysis and stochastic modelling of fibre composites. *Composites Science and Technology*, 71, 107–112.

REKIK, A., AUSLENDER, F., BORNERT, M. and ZAOUI, A. (2007). Objective evaluation of linearization procedures in nonlinear homogenization: A methodology and some implications on the accuracy of micromechanical schemes. *International journal of solids and structures*, 44, 3468–3496.

REKIK, A., BORNERT, M. and AUSLENDER, F. (2012). A critical evaluation of local field statistics predicted by various linearization schemes in nonlinear mean-field homogenization. *Mechanics of Materials*, 54, 1–17.

RINTOUL, M. D. and TORQUATO, S. (1997). Reconstruction of the structure of dispersions. *Journal of Colloid and Interface Science*, 186, 467 – 476.

SAB, K. (1992). On the homogenization and the simulation of random materials. *European journal of mechanics. A. Solids*, 11, 585–607.

SEGURADO, J. and LLORCA, J. (2002). A numerical approximation to the elastic properties of sphere-reinforced composites. *Journal of the Mechanics and Physics of Solids*, 50, 2107 – 2121.

SEGURADO, J. and LLORCA, J. (2006). Computational micromechanics of composites: The effect of particle spatial distribution. *Mechanics of Materials*, 38, 873 – 883.

SHENG, N., BOYCE, M. C., PARKS, D. M., RUTLEDGE, G., ABES, J. and COHEN, R. (2004). Multiscale micromechanical modeling of polymer/clay nanocomposites and the effective clay particle. *Polymer*, 45, 487–506.

SPOOR, P., MAYNARD, J. and KORTAN, A. (1995). Elastic isotropy and anisotropy in quasicrystalline and cubic alculi. *Physical review letters*, 75, 3462.

STROEVEN, M., ASKES, H. and SLUYS, L. (2004). Numerical determination of representative volumes for granular materials. *Computer Methods in Applied Mechanics and Engineering*, 193, 3221–3238.

SUN, C., SAFFARI, P., RANADE, R., SADEGHIPOUR, K. and BARAN, G. (2007). Finite element analysis of elastic property bounds of a composite with randomly distributed particles. *Composites Part A (Applied Science and Manufacturing)*, 38, 80 – 86.

TERADA, K., HORI, M., KYOYA, T. and KIKUCHI, N. (2000). Simulation of the multiscale convergence in computational homogenization approaches. *International Journal of Solids and Structures*, 37, 2285–2311.

TORQUATO, S. (1991). Random heterogeneous media: Microstructure and improved bounds on effective properties. *Applied Mechanics Reviews*, <u>44</u>, 37 – 76.

TORQUATO, S. (1998). Effective stiffness tensor of composite media: II. applications to isotropic dispersions. *Journal of the Mechanics and Physics of Solids*, <u>46</u>, 1411 – 1440.

TORQUATO, S. (2002). *Random heterogeneous materials: microstructure and macroscopic properties*, vol. 16. Springer Verlag.

TRIAS, D., COSTA, J., TURON, A. and HURTADO, J. (2006). Determination of the critical size of a statistical representative volume element (srve) for carbon reinforced polymers. *Acta Materialia*, <u>54</u>, 3471–3484.

TUCKER, C. L. and LIANG, E. (1999). Stiffness predictions for unidirectional short-fiber composites: Review and evaluation. *Composites Science and Technology*, <u>59</u>, 655 – 671.

WALPOLE, L. (1966). On bounds for the overall elastic moduli of inhomogeneous systems—i. *Journal of the Mechanics and Physics of Solids*, <u>14</u>, 151–162.

WANG, W., WANG, J. and KIM, M. (2001). An algebraic condition for the separation of two ellipsoids. *Computer aided geometric design*, <u>18</u>, 531–539.

WENG, G. (1984). Some elastic properties of reinforced solids, with special reference to isotropic ones containing spherical inclusions. *International Journal of Engineering Science*, <u>22</u>, 845–856.

WENG, G. (1990). The theoretical connection between mori-tanaka's theory and the hashin-shtrikman-walpole bounds. *International Journal of Engineering Science*, <u>28</u>, 1111–1120.

WENG, G. (1992). Explicit evaluation of willis' bounds with ellipsoidal inclusions. *International journal of engineering science*, <u>30</u>, 83–92.

WILLIAMS, S. and PHILIPSE, A. (2003). Random packings of spheres and spherocylinders simulated by mechanical contraction. *Physical Review E*, <u>67</u>, 051301.

WILLIS, J. (1977). Bounds and self-consistent estimates for the overall properties of anisotropic composites. *Journal of the Mechanics and Physics of Solids*, <u>25</u>, 185–202.

ZENER, C. M. and SIEGEL, S. (1949). Elasticity and anelasticity of metals. *The Journal of Physical Chemistry*, <u>53</u>, 1468–1468.

ZHAO, J., LI, S., ZOU, R. and YU, A. (2012). Dense random packings of spherocylinders. *Soft Matter*, <u>8</u>, 1003–1009.

ZHENG, Q.-S. and DU, D.-X. (2001). An explicit and universally applicable estimate for the effective properties of multiphase composites which accounts for inclusion distribution. *Journal of the Mechanics and Physics of Solids*, <u>49</u>, 2765 – 2788.

APPENDIX A

ORIENTATION AVERAGING OF A TENSOR

The orientation averaging of a given tensor $\mathbf{X}$ is given by:

$$\langle X_{mnop} \rangle \;=\; \frac{1}{2\pi^2} \int\limits_{-\pi}^{\pi} \int\limits_{0}^{\pi} \int\limits_{0}^{\pi/2} \omega_{mq}\omega_{nr}\omega_{os}\omega_{pt} X_{qrst} \sin(\phi)\mathrm{d}\theta\mathrm{d}\phi\mathrm{d}\psi \qquad (A.1)$$

where θ, ϕ and ψ refer to the Euler angles and $\boldsymbol{\omega}$ denotes the rotation tensor. Norris (1985) and Benveniste (1987) have shown that Eq. (A.1) can be computed analytically. If all possible orientations are considered, $\langle \mathbf{X} \rangle$ is isotropic and can be expressed as:

$$\langle \mathbf{X} \rangle \;=\; \alpha\mathbf{J} + \beta\mathbf{K} \qquad (A.2)$$

where $\mathbf{J}$ and $\mathbf{K}$ refer to the classical spherical and deviatoric projection tensors, respectively. α and β are given by:

$$\alpha \;=\; \frac{1}{3}X_{mmnn} \qquad (A.3a)$$

$$\beta \;=\; \frac{1}{5}(X_{mnmn} - \alpha) \qquad (A.3b)$$

APPENDIX B

ESHELBY'S TENSOR FOR SPHERICAL AND ELLIPSOIDAL INCLUSIONS

B.1 Eshelby's tensor for a spherical inclusion

The Eshelby's tensor for a spherical inclusion embedded in an infinite medium is given by (Bourgeois, 1994):

$$\mathbf{S}^{\mathrm{E}} = \frac{3\kappa_0}{3\kappa_0 + 4\mu_o}\mathbf{J} + \frac{6(\kappa_0 + 2\mu_0)}{5(3\kappa_0 + 4\mu_0)}\mathbf{K} \tag{B.1}$$

where κ_0 and μ_0 refer respectvely to the bulk and shear moduli of the infinite medium, while $\mathbf{J}$ and $\mathbf{K}$ are the classical spherical and deviatoric projection tensors.

B.2 Eshelby's tensor for an ellipsoidal inclusion

The Eshelby's tensor for an ellipsoidal inclusion embedded in an infinite medium and oriented along the third principal direction is given by (Bourgeois, 1994):

$$S^{\mathrm{E}}_{1111} = S^{\mathrm{E}}_{2222} = \frac{3R^2}{8(1-\nu_0)(R^2-1)} + \frac{1}{4(1-\nu_0)}\left[1 - 2\nu_0 - \frac{9}{4(R^2-1)}\right]\gamma(R) \tag{B.2a}$$

$$S^{\mathrm{E}}_{3333} = \frac{1}{2(1-\nu_0)}\left\{1 - 2\nu_0 + \frac{3R^2-1}{R^2-1} - \left[1 - 2\nu_0 + \frac{3R^2}{R^2-1}\right]\gamma(R)\right\} \tag{B.2b}$$

$$S^{\mathrm{E}}_{1122} = S^{\mathrm{E}}_{2211} = \frac{1}{4(1-\nu_0)}\left\{\frac{R^2}{2(R^2-1)} - \left[1 - 2\nu_0 + \frac{3}{4(R^2-1)}\right]\gamma(R)\right\} \tag{B.2c}$$

$$S^{\mathrm{E}}_{1133} = S^{\mathrm{E}}_{2233} = -\frac{R^2}{2(1-\nu_0)(R^2-1)} + \frac{1}{4(1-\nu_0)}\left[\frac{3R^2}{R^2-1} - (1-2\nu_0)\right]\gamma(R) \tag{B.2d}$$

$$S^{\mathrm{E}}_{3311} = S^{\mathrm{E}}_{3322} = -\frac{1}{2(1-2\nu_0)}\left\{\left[1 - 2\nu_0 + \frac{1}{R^2-1}\right] + \left[1 - 2\nu_0 + \frac{3}{2(R^2-1)}\right]\gamma(R)\right\} \tag{B.2e}$$

$$S^{\mathrm{E}}_{1212} = \frac{1}{4(1-\nu_0)}\left\{\frac{R^2}{2(R^2-1)} + \left[1 - 2\nu_0 - \frac{3}{4(R^2-1)}\right]\gamma(R)\right\} \tag{B.2f}$$

$$S^{E}_{3131} = S^{E}_{3232} = \frac{1}{4(1-\nu_0)}\left\{1 - 2\nu_0 - \frac{R^2+1}{R^2-1} - \frac{1}{2}\left[1 - 2\nu_0 - \frac{3(R^2+1)}{R^2-1}\right]\gamma(R)\right\} \qquad (B.2g)$$

where ν_0 is the Poisson's ratio of the infinite medium and R is the aspect ratio of the ellipsoidal inclusion. R is defined as the ratio between the length of the radius along the symmetry axis and the length of the equatorial radius. $\gamma(R)$ is expressed as:

$$\gamma(R) = \begin{cases} \dfrac{R}{(R^2-1)^{3/2}}\left[R(R^2-1)^{1/2} - \cosh^{-1}(R)\right] & \text{if} \quad R > 1 \\[4mm] \dfrac{R}{(1-R^2)^{3/2}}\left[\cos^{-1}(R) - R(1-R^2)^{1/2}\right] & \text{if} \quad R < 1 \end{cases} \qquad (B.3)$$

It should be noted that $\mathbf{S}^{E}$ has the minor symmetry property (i.e., $S^{E}_{mnop} = S^{E}_{nmop} = S^{E}_{mnpo} = S^{E}_{nmpo}$.

APPENDIX C

NORMALIZATION OF THE FIRST AND SECOND ORDER MOMENTS

The aim of this appendix is to show that the first and second order moments can be normalized (i.e., load independent) only for very specific load cases. The proof is developed for 2D microstructures but the same reasoning applies for 3D microstructures.

Suppose that a 2D microstructure is subjected to a macroscopic strain $\mathbf{E}$. Define:

⊙ $\boldsymbol{\sigma}^{11}$ the stress field obtained under a unit uniaxial loading in the first principal direction (i.e., $E_{11} = 1$ and $E_{22} = E_{12} = 0$);

⊙ $\boldsymbol{\sigma}^{22}$ the stress field obtained under a unit uniaxial loading in the second principal direction (i.e., $E_{22} = 1$ and $E_{11} = E_{12} = 0$);

⊙ $\boldsymbol{\sigma}^{12}$ the stress field obtained under a unit pure shear loading (i.e., $E_{12} = 1$ and $E_{11} = E_{22} = 0$).

Under an arbitrary loading $E_{11} = \gamma_{11}$, $E_{22} = \gamma_{22}$ and $E_{12} = \gamma_{12}$, the stress field can be obtained using the superposition principle:

$$\boldsymbol{\sigma} = \gamma_{11}\boldsymbol{\sigma}^{11} + \gamma_{22}\boldsymbol{\sigma}^{22} + \gamma_{12}\boldsymbol{\sigma}^{12} \tag{C.1}$$

The stress first order moment in phase "i" is given by:

$$<\boldsymbol{\sigma}>_i = <\gamma_{11}\boldsymbol{\sigma}^{11} + \gamma_{22}\boldsymbol{\sigma}^{22} + \gamma_{12}\boldsymbol{\sigma}^{12}>_i \tag{C.2a}$$

$$= \gamma_{11}<\boldsymbol{\sigma}^{11}>_i + \gamma_{22}<\boldsymbol{\sigma}^{22}>_i + \gamma_{12}<\boldsymbol{\sigma}^{12}>_i \tag{C.2b}$$

Eq. (C.2b) shows that the intraphase stress first order moment can be normalized (i.e., obtain a metric that depends only on $<\boldsymbol{\sigma}^{11}>_i$, $<\boldsymbol{\sigma}^{22}>_i$ and $<\boldsymbol{\sigma}^{12}>_i$) only for the following specific load cases:

⊙ $\gamma_{22} = \gamma_{12} = 0$ or $\gamma_{11} = \gamma_{12} = 0$ (uniaxial loading);

⊙ $\gamma_{11} = \gamma_{22} = 0$ (pure shear loading);

⊙ $\gamma_{11} = \gamma_{22} = \gamma_{12}$;

⊙ $\gamma_{11} = \gamma_{22}$ and $\gamma_{12} = 0$ or $\gamma_{11} = \gamma_{12}$ and $\gamma_{22} = 0$ or $\gamma_{22} = \gamma_{12}$ and $\gamma_{11} = 0$.

In all other cases, the stress first order moment cannot be normalized and is therefore load

dependent.

The intraphase stress second order moment is given by:

$$< \boldsymbol{\sigma} \otimes \boldsymbol{\sigma} >_i \ = \ < \left(\gamma_{11} \boldsymbol{\sigma}^{11} + \gamma_{22} \boldsymbol{\sigma}^{22} + \gamma_{12} \boldsymbol{\sigma}^{12} \right) \otimes \left(\gamma_{11} \boldsymbol{\sigma}^{11} + \gamma_{22} \boldsymbol{\sigma}^{22} + \gamma_{12} \boldsymbol{\sigma}^{12} \right) >_i \qquad \text{(C.3a)}$$

$$\begin{aligned}
= \ & \gamma_{11}^2 < \boldsymbol{\sigma}^{11} \otimes \boldsymbol{\sigma}^{11} >_i \ + \ \gamma_{22}^2 < \boldsymbol{\sigma}^{22} \otimes \boldsymbol{\sigma}^{22} >_i \ + \ \gamma_{12}^2 < \boldsymbol{\sigma}^{12} \otimes \boldsymbol{\sigma}^{12} >_i \\
& + \ \gamma_{11} \gamma_{22} < \boldsymbol{\sigma}^{11} \otimes \boldsymbol{\sigma}^{22} >_i \ + \ \gamma_{11} \gamma_{12} < \boldsymbol{\sigma}^{11} \otimes \boldsymbol{\sigma}^{12} >_i \\
& + \ \gamma_{22} \gamma_{11} < \boldsymbol{\sigma}^{22} \otimes \boldsymbol{\sigma}^{11} >_i \ + \ \gamma_{22} \gamma_{12} < \boldsymbol{\sigma}^{22} \otimes \boldsymbol{\sigma}^{12} >_i \\
& + \ \gamma_{12} \gamma_{11} < \boldsymbol{\sigma}^{12} \otimes \boldsymbol{\sigma}^{11} >_i \ + \ \gamma_{12} \gamma_{22} < \boldsymbol{\sigma}^{12} \otimes \boldsymbol{\sigma}^{22} >_i \qquad \text{(C.3b)}
\end{aligned}$$

Eq. (C.3b) shows that the intraphase stress second order moment can be normalized only for the following specific load cases:

⊙ $\gamma_{22} = \gamma_{12} = 0$ or $\gamma_{11} = \gamma_{12} = 0$ (uniaxial loading);

⊙ $\gamma_{11} = \gamma_{22} = 0$ (pure shear loading).

Indeed, normalization is possible if one can obtain a metric that depends only on $< \boldsymbol{\sigma}^{11} \otimes \boldsymbol{\sigma}^{11} >_i$, $< \boldsymbol{\sigma}^{22} \otimes \boldsymbol{\sigma}^{22} >_i$ and $< \boldsymbol{\sigma}^{12} \otimes \boldsymbol{\sigma}^{12} >_i$ (without the coupled terms, i.e., $< \boldsymbol{\sigma}^{mn} \otimes \boldsymbol{\sigma}^{op} >_i$ with $m \neq o$ or $n \neq p$).

In conclusion, the stress first and second order moments can be normalized only for uniaxial and pure shear loadings. In all other cases, the stress first and second order moments cannot be normalized and are therefore load dependent. It should be noted that this statement also applies for the strain first and second order moments.